VIOLENT PHREATOMAGMATIC ERUPTIONS THAT FORMED MAARS IN AN INTRA-MOUNTAIN BASIN AT ARXAN-CHAIHE VOLCANIC FIELD, INNER MONGOLIA, CHINA

A thesis presented in partial fulfilment of the requirements for the degree of

Masters in Earth Science

School of Agriculture and Environment

Massey University

Palmerston North, New Zealand

Boxin Li

2018

Look up at the stars and not down at your feet. Try to make sense of what you see and wonder about what makes the universe exist. Be curious. And however difficult life may seem, there is always something you can do and succeed at. It matters that you don't just give up.

– Stephen Hawking

Acknowledgements

The author would like to show great thanks to all who gave their strength to help him participate in this project for a Master's degree in Earth Science. Their inspiration and patience will always be the guide for the author, not only for the spirit of science but also in their attitude of a way of life.

First, the author shows great respect, appreciation and thanks to his supervisor – Prof. Karoly Nemeth. Your project designing, dedication, enthusiasm, encouragement and wisdom have represented the spirit of science, and will always be a guide for the author's life. The inspiration and excitement of the author are from your teaching, advice and humour.

Next, the author also has great respect and would like to thank other professors – Julie Palmer, Alan Palmer, Georg Zellmer and Christopher Anderson. Their immense knowledge and wisdom were the lights for each step of the author's thesis. Your advice and recommendations have become the fruit of the thesis.

During the sample preparation, Dr. Szabolcs Kósik presented his professional skills in order to teach the author how to proceed with the sample analyses and evaluations. Your knowledge and skill were a helpful indication for each step of the sample assessments. Also the author's best friend, Callum Rees, is thanked as he gave and recommended many ideas and sedimentary aspects in relation to the author's logic for the thesis.

Last, but not least, the author gives many thanks to Dr. Anja Moebis. Your laboratory work and skills are very professional for every student who is involved in Earth Science at Massey University. The author's geochemistry data is the fruit of your skills and patience.

There are others who were involved the procedures of the author's thesis and his appreciation and thanks belong to them all.

More importantly, the author gives sincere thanks, respect and love to his parents as they are the flagships of his life. Your strength, intelligence, wisdom, patience and love have become part of the author's spirit. These will always be his light and guidance throughout his life.

Additionally, there are other professors that the author would like to show thanks to – Prof. Jiaqi Liu and Prof. Ge Sun. Although these two professors are in China, your encouragement and care in the author's past will be the strength and confidence of the author's path. Thank you to all of the people mentioned above, as you shall be the lights for the author's future research.

Index

Index....1
Abstract....3
Introduction....5
Outline of the geological interest of Tongxin Crater and Wusulangzi Lake....5
Outlines of the study area....5
The objectives of this study....7
The principles and tech used in this research....10
Monogenetic volcanism....14
Definitions of monogenetic volcanism....14
Definitions of monogenetic volcanic landforms....20
Definitions of maar-diatreme volcano....26
Calderas and maar volcanoes....28
Maar-diatreme crater formations....33
Role of phreatomagmatism....36
Geological settings and volcanic conditions in Eastern Inner Mongolia, China....39
Basement geology of Inner Mongolia, China....39
Geo-tectonic context of Inner Mongolia, China....39
Intra-plate volcanism in Inner Mongolia and its adjacent areas in NE China....44
Introduction to the ACVF....54
Volcanic landforms of ACVF....56
Maps of vents....59
Vent distribution....63
Wusulangzi volcano....64
Volcanic architecture....64
Field observations....64
Tongxin volcano....67
Volcanic rock distribution....68
Preliminary sedimentary/stratigraphy log....79
Microtextural analysis of Wusulangzi (AX1) and Tongxin (AX2) pyroclastic units....84
Granulometry....85
Optical light microscopy....88

Petrographic microscopy and thin sections 91
Back-scattered Electron Microscopy (2D) 94
Scanning Electron Microscopy (3D) 101
Geochemistry of Wusulangzi and Tongxin pyroclastic units 104
Major element chemistry 106
Trace element chemistry 121
Discussion and conclusions 136
Discussion 136
Conclusions 141
References: 142

Abstract

Two large depressions contain Wusulangzi Lake and Tongxin Lake in the Arxan-Chaihe Volcanic Field (ACVF), which preserves at least 27 volcanoes in NE China in about a 1000 km^2 area. Due to the preliminary research on both Wusulangzi and Tongxin, two sample groups (Sample 1 and Sample 2) were collected and field observations were held on both sites. Sample 1, representing Wusulangzi, was collected from the SE part of the lake where the lava flow is suspected to cover and preserve medial to distal sections of the tuff ring. Sample 2, representing Tongxin, was collected from the SW rim of the crater from the proximal area, as well as the eastern side in regard to the distal region. Specifically at Tongxin Lake, the pyroclastic successions and beddings contain a series of horizontal and laminated structures, with dune beddings, cross-beddings, as well as a chute-and-pool structure. Pyroclastic deposits of the tuff rings can be traced from the crater rim about 3 km. The various methods of microscopy reveal that glass shards are distributed differently in both sample groups. Mineral diversity is shown to a large extent, and the mineralogical alteration can be observed under petrographic microscopy. SEM and BSE for 2D and 3D images indicate a relatively high fragmentation of juvenile particles. The grain-size distribution also implies medium-to-high explosive energy. Geochemistry data of both major and trace elements reveals a diversity of magma in relation to fractional crystallisation (olivine, clinopyroxene and plagioclase crystallisation) and magma evolution processes, which are depicted by Harker variation diagrams. The AFM plot reveals a primitive stage of magma evolution. The multi-element diagram shows uranium as abnormal, which is suspected to be a U-rich mantle source.

Keywords: phreatomagmatic eruption, maar crater, major and trace elements, SEM, BSE, petrographic microscopy, grain-size distribution, ternary plot, Harker diagram

Introduction

Outline of the geological interest of Tongxin Crater and Wusulangzi Lake

Tongxin Crater and Wusulangzi Lake are located in NE China as one of the largest explosive volcanic edifices of the Pliocene in the recent alkaline basaltic volcanic field. The Arxan-Chaihe Volcanic Field (ACVF) in NE China consists of about 30 young scoria cones with pahoehoe to aa-type basaltic lava flows and at least four maars, together covering an area of c. 1000 km^2. Volcanism was initiated in the Pliocene and continued through the Late Pleistocene to the Holocene with eruptions as young as c. 2000 cal yrs BP age. Recently recovered tephra layers in crater lakes provide further evidence of young Quaternary volcanism in the region by having a tephra of 14,200 cal yrs BP age preserved in the Moon Lake, a crater lake formed on top of a perfectly circular scoria cone crater. The discovery of such locally-sourced tephra suggests a Holocene violent phreatomagmatic explosive eruption from an unknown source (Sun et al., 2016). This newly-identified young tephra layer showed textural evidence that a violent phreatomagmatic explosion must have taken place in the ACVF. This has intensified the search for potential phreatomagmatic volcanoes in the ACVF. Tongxin volcano (that has a similar pattern with hearts) in the eastern ACVF forms a steep-walled, flat-floored basin filled with a lake that is suspected to be a maar. The Wusulangzi Lake in the western end of the volcanic site presents a flat and shallow lake within a geographic depression. The Tongxin Depression is surrounded by a c. 400 m high escarpment of Mesozoic crystalline rocks, e.g. Cambrian granite that gradually drops toward the south. Dune-bedded base surge dominated successions are at least 40 m thick in the south and diminish toward the higher cliffs in the north. Abundant accretionary lapilli beds, accidental lithic-rich tuffs with impact sags, cored bombs, blocky pyroclasts, as well as glassy, non-to-low vesicular juvenile particles, all point to a sustained and energetic phreatomagmatic explosive eruption forming this volcano. The uniform basaltic composition of the juvenile pyroclasts indicates that phreatomagmatism played a key role in the eruption and the volcano was likely capable of producing a large volume of ash, which could have accumulated in other craters and maar lakes in the ACVF. The pyroclastic deposit characteristics, stratigraphy and micro-textures suggest that Tongxin Tianchi is a maar volcano. However, the present-day depression is not necessarily identical to the structural margin of the maar crater.

Outlines of the study area

The ACVF is located in NE China, near the national boundary between present-day China and Mongolia. This volcanic field geographically belongs to the Great Xing'An Mountain Belt (Fig 14) with a NE-SW orientation (1200 km long and 200-300 km wide, c. 2000 m at the highest point). With the post-eruptive erosion to the Mesozoic crystalline basement rocks, the present-day elevation of this area is about 1500 m above the sea level. The ACVF provides a habitat for extended forests in cold temperate climates, with a strong monsoon effect and an extremely low winter temperature, which is approximately -25 degrees on average in winter (Németh et al., 2017). Within such a geoenvironmental conditions the deposits of volcanism

can be present in a variety of structures and textures commonly affected by strong surface weathering. The vegetation cover also prevents access to outcrops while the long winter season (about four months), commonly associated with deep snowpack (4-7 m in thickness), prevents fieldwork for most of the year. Geologically, the ACVF is part of the Tianshan-Xing'an Orogenetic Belt (Fig 11) (Chao, 1992; Huang et al., 1980; Zhang et al., 1999), which lies on a thick continental lithosphere. The volcanic chain is aligned with the NE orientation, which follows the major fault orientation of the region. This means that this volcanic field is dominantly controlled by the regional tectonic settings, which follows the structural pattern of a Mesozoic Rift system (Fig 13, 14) (Decker and Decker, 1999; Liu et al., 2001). The volcanism approximately occurred near the Cenozoic era, especially in the Late Pleistocene, i.e. 14200 BP (Sun et al., 2016). Some lesser-known and lesser-studied volcanic structures express the remains of older volcanism in the region in the form of preserved remnants of columnar jointed basaltic rocks inferred to be a remnant of ponded basaltic lava flows (Németh et al., 2017).

The majority of the volcanic landforms of the ACVF are typically composed of variable eroded scoria or cinder cones, lava spatter cones, tephra surrounded maars, and large and flattened scoria cone preserving crater lakes such as the Moon Lake. These characteristics indicate that the ACVF is a typical intra-continental monogenetic volcanic field producing an overall volume of eruptive products of a few km^3. The lava flows that overlap and accumulate on each other express the temporal evolution of the volcanic field through well-distinguished episodes.

The most extended lava flow of the ACVF is more than 5 km in length and with over more than 10 m in thickness (Fig 23) (Németh et al., 2017). But near the valley shoulders, the thickness of the lava flow drops to a few metres in thickness. The major type of lava surface texture of the ACVF is the typical pahoehoe lava. Due to the lava flow surface texture changes, the inflation and deflation of lava flows can be recorded in the field in the form of the appearance of specific lava surface textures such as tumuli, lava pits, hummocky whalebacks (turtle skin), as well as various size of hornitos, i.e. the few metres high lava domes are developed from the rootless cones, for instance, the Etna volcano in Italy (source from www.volcanodiscovery.com/photoglossary/hornito.html and (Németh et al., 2017)).

In addition to lava flow fields and scoria cones, there are some maars in the ACVF that represent geoenvironmental conditions where a series of magma-water interactions, namely phreatomagmatic eruptions, took place. The ACVF has a high volcanic geodiversity in terms of monogenetic volcanism with extended volcano distribution, which is formed in a fluvial-lacustrine environment enclosed by loose crystalline basement rocks (Németh et al., 2017). This high geodiversity alongside the surrounding area's great human traditions and natural beauty forms the foundation of two volcanic geoparks in the region administered by local and central governmental organisations (Németh et al., 2017; Wang et al., 2014; Zhao et al., 2015; Zhizhong et al., 2015).

The objectives of this study

Trying to understand how a volcano works can increase the ability of human society to utilise its natural resources and develop strategies for managing the hazards they pose to the environment and society. To understand volcanic hazards and define the geoheritage values that could be used for geotouristic reasons, detailed geological research to determine the eruption styles, magma fragmentation modes, pyroclasts transportation, deposition and reworking is needed, as well as an understanding of the overall development of individual volcanoes and the volcanic field as a whole. This study aims to provide geological information to establish the eruption history of one of the largest eruptive centers of the ACVF in NE China, with the aim to characterise its deposits, define its eruption style, document its geochemical features, and highlight the potential petrological origins in the light of the subsequent assessments and evaluations of the regional volcanism. This thesis will explore the main topics listed below, applying extensive literature data available through the public domain, limited fieldwork provided in previous field campaigns since 2015, and some descriptive work of collected samples from key outcrops.

1) Document the volcanic rock types in relation to the Tongxin and Wusulangzi volcanoes

This part is the initial step of the whole journey. As recent research interest has intensified to search for potential source volcanoes of tephra layers recovered from closed crater lakes of the ACVF, detailed investigation of potential sources can contribute to our ability to trace such tephra layers across the field preserved in various lakes. By observing petrographical thin sections under the petrological light microscope, in order to record the characteristics of the pyroclastic samples and the bulk texture of volcanic rock's thin sections with the aim of defining the mineralogical assemblages of coherent volcanic rocks and the origin of individual pyroclasts, several technologies and analytical methods will be utilised. Standard binocular light microscopy was used to identify specific rock textures that can be linked to specific magma fragmentation styles. Also with precise geochemical measurements to define the compositions of both individual pyroclasts and the whole rock composition of pyroclasts, coherent rock varieties have been applied. Various chemical discrimination diagrams are then applied to determine the petrogenetic assemblages of the studied rocks.

2) Determine the magma fragmentation types of Tongxin and Wusulangzi volcanoes

As always, just like other studies, understanding the type of magma fragmentation is the key to providing supporting evidence to establish magma-water explosive fragmentation vs pure magmatic volatile-driven explosive fragmentations of ascending magma (Cashman et al., 2000; Morrissey et al., 2000). Phreatomagmatic explosive processes have defined those where rising magma interacts with the ground-water table (Németh and Kereszturi, 2015; White and Ross, 2011) through molten fuel-coolant interaction (MFCI) that transfers thermal energy to kinetic energy and fragments the magma itself and disrupts the surrounding wall rocks (Morrissey et al., 2000; Zimanowski, 1998). This process results in two sets of pyroclasts in the accumulating pyroclastic deposits:

- specific textured, chilled glassy juvenile pyroclasts, and
- a various accidental lithic population that is derived from country rocks (Németh and Martin, 2007).

The interactions between ascending magma batches and shallow surface water and various levels of the ground-water table can result in a great diversity of pyroclasts textures, making it a challenging job to link such textures to a specific level of magma and water interactions. To clarify this, the accidental lithic clast population has also been examined. Identification of various rock types among accidental lithic populations can help to characterise the maximum depth clasts that might have been excavated. However, their appearance in the tephra layers is not necessarily linked to the depth of fragmentation assumed to produce the tephra layer of pyroclasts recovered (Graettinger et al., 2016; Graettinger et al., 2015; Valentine et al., 2015). While a conventional view of country rock excavation and their link to the depth of fragmentation is still considered as a potential mechanism of how wall rocks are excavated by individual explosive outbursts (Lorenz, 1986a), here in this study the information on country rock population and type is used to define the potential depth where fragmentation of ascending magma can take place regardless that the clasts have been exploded straight from that level in a single explosive outburst or through multiple explosive actions in a growing diatreme (Valentine and White, 2012).

As will be described later in this thesis, both the Tongxin and Wusulangzi volcanos are under debate as being defined as maar volcanoes. If this is so, the explosive magma-water eruption must have a remarkable role in the evolution of the Tongxin and Wusulnagzi volcanoes and highlights the important role of phreatomagmatism in the ACVF. By utilising Scanning Electronic Microscope (SEM) and Back-scatter Electron Microscopy (BSE), the 3D, as well as 2D, images of juvenile pyroclasts can be obtained and analysed by the geometrical parameters of the pyroclasts to determine the fragmentation type the magma went through. It can clearly depict the details of the pyroclast's shape and the vesicularity in each grain so the possible magma fragmentation style can be determined.

3) *Establish a volcanic evolution model consistent with the rock and mineral textures documented from the recovered volcanic deposits*

The contents and composition of the whole rocks of juvenile pyroclasts and coherent magmatic bodies, as well as their specific mineral composition, can provide information on the initial melt that drove the eruptions. The texture of minerals depicts when and how the crystallisation took place and in what way secondary alteration processes change them through time. By observing them through the light-optical microscope, and capturing images from SEM and BSE juvenile pyroclasts, textures can be well characterised. Utilisation of these methods can also help to depict immediate alteration processes such as palagonitisation (Stroncik and Schmincke, 2002), which is an essential feature in tephra formed through phreatomagmatic explosive eruptions.

4) *Establish the brief petrological constraints on the volcanic eruptions in order to compare them with other sites in the same volcanic field*

There are only a few types of research that have emerged recently that can reveal some limited details of the petrogenesis of volcanic rocks in the ACVF (Bai et al., 2012; Németh et al., 2017; Sun et al., 2016). Based on these previous studies (Figs 24, 29), the geochemical data from adjacent areas of the Tongxin and Wusulangzi volcanoes can provide a relative constraint for evaluating the majority of the rock type compositions. These parameters may reveal the possible processes of the petrology in the Tongxin and Wusulangzi volcano rocks and a hypotheses of their volcanic evolutions. As with traditional ways, the background of the petrology commonly provides the details that explain the very specific procedures of the mineralisation and crystal fractionation, as will be discussed in the following sections.

5) *Determine the eruptive environment and relative age of the Tongxin and Wusulangzi volcanoes*

Reconstruction of the paleo-environments is always a significant focus in geology. However, this thesis concentrates on the volcanology of the studied site, so this part will provide a relative limitation as to the age of the Tongxin and Wusulangzi volcanoes. Due to sampling issues, such as a large number of accidental lithics in cored volcanic bombs, it made it difficult to design an absolute age determination of the rocks (K-Ar or Ar-Ar method) and hence there was no attempt to perform such age datings during this research. For establishing the eruptive environment, however, information was collected from literature alongside some observation on field data. One can only hope that using this way we can demonstrate the conditions of the paleo-environments of the contemporary eruptions of the Tongxin and Wusulangzi volcanoes, but this part is another story which this thesis will not describe.

6) *Provide evidence to demonstrate the geological processes responsible for the formation and present-day appearance of the geographic depressions at the Tongxin and Wusulangzi volcanoes*

The fieldwork in geology can usually present the formation of an outcrop, which provides a range of implications for post-eruptive processes. Commonly, it is defined as a degradation landscape modification or in broader sense erosion. Erosional forces are likely to act upon the freshly-deposited tephra deposits and, under humid climatic conditions, remobilisation of tephra likely takes place quickly after the eruption. In this aspect, the present-day depression is assumed to be the source (e.g. crater) of many tephra deposits as a result of a combination of volcanic processes and post-volcanic erosion. In the areas around the Tongxin volcano, the climate is relatively semi-humid (-2.7°C per year on average; 450 mm precipitation from June to September, source from (Németh et al., 2017)). This implies the degradation and erosion process must play a significant role during the post-eruptive period. With the amount of occurrence of vegetation and a large crater lake, the quantities of precipitation must be high in volume. Combined with the observations from the surrounding outcrops, the processes are responsible in the present time of this volcano and can be well illustrated. A similar scenario

and link between geomorphology and the presence of a geomorphic depression at Wusulangzi is hypothetised.

7) *Provide a critical review of the volcanic features forming the ACVF in the available Chinese and Western literature*

Always remember that the science will only be promoted by taking previous studies as the foundation of every step for one's research. This part will largely and comprehensively present previous research in ACVF, including recent Chinese and Western outcomes. Also, it will show the geological background to this study area, so that the readers can have an entire picture and expression of the importance of this research.

8) *Provide a global comparison of the Tongxin and Wusulangzi volcanoes and ACVF with other similar volcanic fields around the world*

The ACVF is located on the NW margin of the Pacific-East Asian plates and this area is established in an intra-continental setting (Liu et al., 2001; Németh et al., 2017). With the amount of continental alkaline basaltic rocks in the NE China territory, Arxan-Chaihe volcanism is inferred to be similar in a volcanological and petrochemical sense to other intra-plate volcanism in the region. It is also assumed that the ACVF may show similarities to other intra-plate monogenetic volcanic fields that formed over/under similar magmatological, lithospheric or surface geo-environments as the ACVF. Compared to data and geological settings with typical patterns, this thesis will choose data for comparison from Auckland, New Zealand; Harrat Hutaymah, Saudi Arabia; Taupo, New Zealand; Inner Mongolia, China (Duncan et al., 2016; McGee et al., 2013; Sun et al., 2016; Zhao et al., 2014a) in respect of the potential geological settings and geochemical contents.

9) *Outline research strategies for future work in the region*

After one year of study for a Master of Science, a series of systematic works including laboratory and field sections have been carried out. Trying to cover all aspects of the sample evaluation and data analyses is the essence of this study, however further detailed research is needed for the next cycle of the work. This part will briefly present the gaps in recent work in order to imply future study plans.

The principles and tech used in this research

In terms of the above-mentioned objectives, a range of methodologies and analytical methods are applied throughout the entire study. In this part, this thesis will present the detailed theories and technologies used in the data collection, analyses and conclusions. Please note that the field observation and sample collection was carried out by Associate Professor Karoly Nemeth who is the chief supervisor of the author. Due to the time schedule and other irreversible circumstances, it is a shame that the author could not participate in this critical part. Associate Professor Nemeth did the fieldwork in October 2015 and October 2016 alongside researchers of the Chinese Academy of Sciences, Beijing (Dr Jing Wu and Dr Chunqing Sun). During the fieldwork, key volcanological sites were visited across the ACVF

and samples were collected in the key sections associated with the main tephra ring successions of the Tongxin and Wusulangzi volcanoes. The samples collected were dry sieved at the Massey University sedimentology laboratory and sample preparation facilities. The dry sieved samples were carefully analysed in each grain-size fraction with the aim to characterise the componentry of such sections by utilising conventional point counting. Further, juvenile and accidental lithic pyroclasts (terminology is followed by (Fisher and Schmincke, 1984)) were selected from ash and lapilli-size fractions with the aim to determine their textural as well as chemical characteristics.

The following approaches were taken into account:

1) *Detailed literature review of our current knowledge on monogenetic volcanism, volcanic fields and maar-diatreme volcanism*

This section is based on an extensive literature review to establish our understanding of volcanic fields, monogenetic volcanism and maar-diatreme volcanism from a global perspective. This section also provides an overview to put this information into context from a Chinese geological perspective.

2) *Field campaign to establish 3D facies architecture*

This section is the whole view of the studied territory (Fig 27, 29). Briefly summarising the geological and tectonic settings associated with the satellite photo (GoogleEarth based) in order to present the basic conditions and environments of this area is the focus of this section. Photos of the fieldwork collected during the 2015 and 2016 field campaigns illustrate the structures of the sediments, which can bring expressions to readers about the sedimentary circumstances and surrounding area's conditions. 3D facies architecture can be directly depicted by the cross-sections of the Tongxin volcano so that it can be described in detail vertically and laterally. Due to limited outcrop availability and time in the field, similar stratigraphical sections are not described for the Wusulangzi volcano. It should be noted that most of this part will be presented from the previous research and relevant aspects of the Chinese geographical evaluations.

3) *Newly-collected and existing samples analyses*

Sample preparation has a critical role in the process of data collection. Following the preparation role, each type for both pyroclastic and bulk rock samples should be treated in different ways. For volcanic clasts from pyroclastic samples, the selected grain-size fractions after dry sieving were triple washed with 10% hydrochloric acid in order to clean the varieties of secondary minerals such as carbonates. Such sample preparation was essential to open up the original surface textures to be visible for subsequent SEM studies and for preparing a suitable set of grains for BSE studies. Textural analyses of these clasts is presented under the light-optical microscope first hand in the light to identify the surface structures, vesicularity, shapes, size and surface alteration features of individual pyroclasts. By identification of end-member textural classes of pyroclasts, standard point counting was utilised to express the

relative ratio between identified textural classes, with the aim to be able to define various processes that may be responsible for the formation of such classes. For the coherent volcanic rocks represented as large lava bombs in pyroclastic successions, thin sections were prepared to characterise their mineralogy and microtexture. Each of them was observed under the petrographic microscope with cross-polarised light in order to recognise the groundmass textures and minerals structures.

4) Grain-size analyses

The distribution of the grain sizes in a differentiated manner is one of the volcanic evolutionary evaluations in terms of the magma processes. As mentioned, the point counting that was undergone through light-microscopy (Fig 44, 45) is held on the different clastic samples for different grain sizes (approximately from 4 ϕ to -4.5 ϕ). The proportion of the juvenile and non-juvenile (accidental lithics derived from country rocks (Németh and Martin, 2007) particles can clearly depict the processes of the eruption style and explosive conditions (phreatomagmatic vs magmatic explosive). It also can provide information about magma compositions and the relative role of the magmatic volatiles in the fragmentation (e.g. vesicularity). By sieving and separating various grain sizes (Fig 39), it is easy to get access to juvenile and non-juvenile particle populations. In particular, separating the different contents for both juvenile and non-juvenile particles must be operated under the light microscope, especially for clasts with smaller sizes.

5) Shapes of juvenile particles

Phreatomagmatic volcanism is common and can be recognised in the pyroclast's texture level by specific textural elements preserved on the juvenile pyroclasts (Buttner et al., 1999; Dürig et al., 2012; Németh, 2010b; Otterloo et al., 2015; Pardo et al., 2009; Zimanowski et al., 2003). Evaluating and estimating the styles of the juvenile particle types can give access to the detailed intelligence of the processes of magma-water interactions. With the aim to determine magma fragmentation in volcanic evolutions, observing pyroclastic rocks under the light microscope in varieties of grain sizes is essential. The point counting tech concentrates on assessing the pyroclasts' sizes to determine their mineral compositions in percentages. Different shapes of the clasts can present the different type of magma fragmentation procedures and depict the magnitude of this fragmentation. This part will be discussed in the following sections.

6) Vesicle density and population of juvenile clasts

The roles of phreatomagmatic eruption are dominated throughout by a monogenetic volcano life expectancy. Analysing the vesicle density and populations of the juvenile clasts of the samples can provide an insight into the vesiculation history of the juvenile clasts and the timing of phreatomagmatic eruption. The magnitude of water-magma interaction controls the amount of vesicle and void spaces in juvenile particles. Evaluating the vesicle density can provide evidence of how much energy during the phreatomagmatic eruption has taken place.

The population of the juvenile clasts is controlled by the volumes of magma batches during the magma ascent interacting with the shallow water or aquifer systems. Depending on when the magma and shallow water contacted each other in a specific depth, the time of the magma batches' ascent and fragmentation into the vesicular particles can be evaluated. The average compositions of the juvenile clasts is preserved in the adjacent deposits. Based on the estimated ascending velocity, the timing and even the history of the fragmentations can be determined.

7) Chemical compositions of the juvenile particles

The origin of the volcanic rocks is a treasure for all geologists. The petrology that can precisely describe the forming processes of a specific volcanic rock is always a treasure map which can lead to the treasure. Major and trace elements evaluations are the two major ways of illustrating the juvenile particles' origins. It is possible that through X-ray fluorescence (XRF), the whole rock's major elements contents can be collected, as well as the trace elements. In the methodology part, this thesis will demonstrate the principles and diagrams in terms of major elements and trace element assessments respectively.

8) Accidental lithic clasts analyses

During volcano evolutions, the materials of wall rocks have been accompanied by juvenile particles. The proportion of accidental lithics may not occupy a large volume, however they can provide important information about fragmentation depth and rock fracturing during eruption processes (Németh and Martin, 2007). Through the above-mentioned XRF analytic technology, the geochemical data may present the wall rock assimilation which occurred at a specific depth. It is then possible to determine the extent of how many volumes of wall rocks interacted or have been melted into the melt. In the geochemistry assessments, this part will be fully discussed.

To sum up, this part presents the general expressions of this thesis. More details and study processes will be discussed and interpreted. Basically, the Tongxin and Wusulangzi volcanoes are parts of the entire ACVF and are obviously monogenetic volcanoes, which are suspected to be maar volcanoes, and it is important to illustrate the principles of monogenetic volcanism followed by the regional geology settings. The following contents will show the initial portion of this thesis – monogenetic volcanism.

Monogenetic volcanism

Definitions of monogenetic volcanism

There are many continental volcanoes in the world (e.g. volcanoes erupted through a typical continental lithosphere in a region typically far from the direct influence of convergent plate boundary processes). These volcanoes commonly form a field of volcanoes that are individually short-lived and erupted in a singular event, hence they are defined as monogenetic individually, and the monogenetic volcanic fields are defined as a group of volcanoes (Smith and Németh, 2017). In the last decade, many types of research have revealed a range of small-volume basaltic volcanism volcanologically, geochemically, structurally and tectonically. The areas of studies include Udo volcano in Jeju Island, South Korea (Brenna et al., 2011), Mt Gambier of the Newer Volcanic Province in Australia (Demidjuk et al., 2007; Otterloo et al., 2014), Paricutin in Mexico (Cebriá et al., 2011; Erlund et al., 2010), the Wudalianchi Volcanic Field in China (Gao et al., 2013; Xiao and Wang, 2009; Zhao et al., 2014a; Zou et al., 2003), the Anatolian Volcanic Field in Turkey (Ersoy et al., 2010; Ersoy and Palmer, 2013; Ersoy et al., 2012a; Ersoy et al., 2012b), and also contain territories with large scale, for example the volcanic belt in Germany (Haase et al., 2004), Hungary in the western Pannonia Basin (Harangi et al., 2015; Németh, 2010a; Németh et al., 2012), the Central European Volcanic Province (Cajz et al., 2009) and the Auckland Volcanic Field (AVF) in New Zealand (Cook et al., 2005).

Figure 1: These two pictures give a general view of monogenetic volcanoes around the world. However, these maps do not include the entire monogenetic volcanism, for instance, volcanism in Central Asia, the East African Rift System, Ethiopia, the Andes mountain system containing Chile, Colombia and Argentina, as well as in SW USA. Also, keep in mind that these two pictures do not include the correlations of large-scale island volcanism, for example, in Azores, Iceland and Hawaii (Smith and Németh, 2017).

This kind of volcano contains small-volume scoria cone volcanoes, which are formed by mild explosive eruption processes and are composed of large varieties of chemical compositions (Gutmann, 1979; Gutmann, 2002; Luhr et al., 1993; Martin and Németh, 2006; Valentine et al., 2005; Valentine et al., 2007; Valentine et al., 2006; Wood, 1980). Some volcanic fields are also associated with either extensive lava fields, e.g. in the western Arabian Peninsula (Murcia et al., 2014), or small lava shield volcanoes, or even chains of shields (Hughes et al., 2002; Kuntz et al., 1986).

In recent studies, many types of research reveal that monogenetic volcanoes as small volumes of magma or small volcanoes, which highlights the necessary size to reach the definition of a monogenetic volcano (Valentine and Gregg, 2008; Valentine et al., 2006). Typically, in relation to the term small eruption, it is recognised by two features; one is a small volume which is characteristically less than 1 km^3, another is the relatively short duration of the eruption and usually it can persist over 10 years (Németh and Kereszturi, 2015). In order to adapt the varieties of complex volcanic patterns, the definition of monogenetic volcanoes is represented as "*a volcanic edifice with a small cumulative volume (typically less than 1 km^3) that has been built up by one continuous, or many discontinuous, small eruptions occurring in*

a short time-scale (typically less than 10 years) and fed from one or multiple magma batches through a relatively simple, closely spaced feeder dyke (and sill) system with no well-developed magma chambers associated with it" (Németh and Kereszturi, 2015). Based on this definition, it is easier to recognise a continuous trend between monogenetic volcanoes and polygenetic volcanoes. The accumulated volumes are the essence, not the complexity, of physical and chemical developments. As mentioned in many concepts, small-scale magma clusters in monogenetic systems usually present on the surface of the Earth. They express the ascent of small batches of magma emplaced into the spatial and temporal domains of the sub-surface (Smith and Németh, 2017). Also, others (Kereszturi et al., 2013) suggested that monogenetic basalt volcanoes contain a series of characteristics of spatial and temporal distributions as well as variabilities, and these factors include magma outputs, magma influxes and eruptive frequencies. Therefore, monogenetic volcanoes can also be defined as small volumes of magma, with short eruption time periods, and wide distributive plumbing systems, even if these conduits are preserved for a very long time.

In general, there are five types of volcanoes and each type is defined by its original category: central volcanoes, lava shield volcanoes, stratovolcanoes, flood basalts and monogenetic volcanoes. The first four of them are long-lived, large volume volcanic systems, hence commonly defined as polygenetic volcano systems (Wei et al., 1999). Recent notions however encountered with lava fields that are about a magnitude smaller than a typical flood basalt province, still produce tens of km^3 volume of lava fields but are essentially fed from small volcanic cones that apparently were active in short pulses over a few weeks' time, eg. Harrat Rahat (Kereszturi et al., 2016; Murcia et al., 2014).

In some *sensu stricto* concepts, monogenetic volcanoes are commonly expressed by their small volume and dispersed distribution characteristics. Every individual volcano has undergone a single eruptive event. Even if it experienced a series of eruption phases, the time interval between these phases may be approximately more than 1000 years (Wei et al., 1999). In another type of description, eruptions occurring in monogenetic volcanism are featured by episodic short terms of activity, which commonly persist for days to years, and each new eruption might happen in different locations rather than from or near the same destination (Kereszturi et al., 2013). In the observation of monogenetic volcanoes, the unconformities of pyroclastic layers and successions can prove that one single monogenetic volcano might undergo a number of eruption phases. These phases are associated with eruption episodes and a potential number of eruption breaks (Németh and Kereszturi, 2015). Specifically, eruptive phases depend on how large the magma supply can be to provide enough magma volumes. In monogenetic volcanism, the eruptive volumes reaching the surface are associated with magma supplies in high-pressure locations and can be generated by individual or multiple magma clusters, which commonly erupt through a single and well-formed volcanic conduit (Németh and Kereszturi, 2015).

Various types of volcanic landforms associated with monogenetic volcanism and generally defined as a maar, tuff ring, tuff cone or scoria cone are the most common landforms. Most

of the monogenetic volcanoes are wholly or in part formed by magma-water interactions while they explode (Valentine and Gregg, 2008). The behaviour of monogenetic volcanism is controlled by regional tectonic forces, which contain the geology and hydrology of subaerial settings, as well as the processes of magma sources (Brenna et al., 2012; Jankovics et al., 2012; Smith et al., 2008; Valentine and Gregg, 2008). People can commonly observe tuff rings, tuff cones (scoria cones), as well as maar structures. These volcanic structures that are associated with some sort of magma and water explosive interactions were built when the eruptive vents were in the area with abundant ground-water sources, near coastlines or became closer to lacustrine territories (Wei et al., 1999). In recent research, the "competition" between magma ascent and the surrounding environmental conditions became a new concept to interpret the spatial distribution of various types of monogenetic volcanoes in a volcanic field (Kereszturi et al., 2017; Kereszturi et al., 2014). It has been verified that volcanic eruption styles depend on a variety of inner magmatically-controlled parameters (magmatic volatiles, chemical compositions and magma viscosity), as well as natural environment factors (availability and/or presence of external water systems, physical settings and fractures of pre-eruptive sediments) (Németh, 2010a; Németh and Kereszturi, 2015). As some articles have mentioned, the volume of magma batches that generate a monogenetic volcano is commonly less than 1 km^3. With this quantity, the degree of interplay between magmatism and the surrounding environments can be very sensitive (Kereszturi et al., 2014). Put simply, if the magmatic forces are dominant (e.g. large magma output rate, voluminous magma supply) over the surrounding environments with increasing thermal energy and some potential in the ascent magma, the eruption styles will be prevailed by a magmatic (Hawaiin-Strombolian) type, which can form a range of spatter and scoria cones (Fig 4, 25) (Kereszturi and Németh, 2012; Kereszturi et al., 2014). On the contrary, if volcanism contains a lower magmatic flux and a smaller volume of magma clusters, the surrounding environmental factors will dominate and alter the eruptive style, which will become a phreatomagmatic eruption type with large quantities of pyroclast ejecta (Kereszturi et al., 2014). Such an eruption type will eventually produce a series of tuff cones, tuff rings, as well as maars (Fig 5, 6, 16).

Basically, small-scale volcanoes can be separated into monogenetic or polygenetic volcanoes utilising two major characteristics: (1) petrogenetic characteristics, and (2) volcanic architectures (Smith and Németh, 2017). Conceptually, one of the differences between monogenetic volcanoes and polygenetic volcanoes is the plumbing system. In monogenetic volcanism, volumes of magma ascend rapidly to the surface via a simple conduit system. The magma undergoes little interaction with the surrounding rocks which stand in its way. On the contrary, the conduit systems in polygenetic volcanism contain a range of complex interactions between magma and the surrounding rocks in a magma chamber. Usually, crystal fragmentation occurs in such conditions (Smith and Németh, 2017). As mentioned, the volcanic conduit locations can shift over long periods of time and shape a series of dispersed volcanoes, volcano groups, linear volcanic structures, as well as random distributions of volcanoes. Furthermore, in monogenetic volcanism, the location of conduits keep changing, whereas the polygenetic volcanoes generate edifices and relatively fixed conduit systems

(Németh and Kereszturi, 2015). In some of the latest research, plumbing systems have become one of the major differences between monogenetic and polygenetic volcanism. Due to the rapid ascent rate of magmatism in monogenetic volcanoes, there are few interactions between magma and the surrounding lithic rocks. This could be evidence of a correlation between a magma source and eruptive magma on the surface (Smith and Németh, 2017). Relatively primitive basalt magma samples have proven this concept above (McGee and Smith, 2016).

The styles of eruption-processes of monogenetic volcanism are distinct for each eruptive course. During these events, each of them is linked by many transitions of the eruption. In order to predict the hazard magnitude, evaluations of the eruptive styles, alterations of eruptive styles, as well as the bulk volume of ejecta, may play important roles in assessments of volcanism hazard (Kereszturi et al., 2014). Based on the principles and theories of morphology, there are six sourced classifications which can distinguish the broad ranges of monogenetic volcanoes: eruptive fissures, spatter cones, scoria and cinder cones, maar and maar-diatremes, tuff rings, as well as tuff cones (Head et al., 1981; Kereszturi and Németh, 2012; Németh, 2010a; Valentine and Gregg, 2008; Wohletz and Sheridan, 1983; Wood, 1979b). These categories can be correlated with a range of eruptive events. Usually, the eruption sequences are initially dominated by phreatomagmatism if the magma contacts with the shallow water-saturated beds or subterranean aquifers. In this eruption phase, the ground-water or water-saturated conditions are the dominant factors that control the eruptive type. In general, phreatomagmatic eruptions can create maars, tuff rings and tuff cones. When the eruption processes continue, the ground-water or water-saturated sediments are no longer the dominant factors of the eruption style. In other words, long-lived monogenetic volcanic eruptions can quickly consume the water supply from the surrounding substrate or proximal surface water source, thus the eruption processes gradually become “dry” eruptions, even effusive eruptions (Kósik et al., 2016), for instance, Sag-hegy in western Hungary (Fig 2B) (Martin and Németh, 2004), Crosa de Sant Dalmai maar in NE Spain (Fig 2C) (Pedrazzi et al., 2014), as well as the Motukorea tuff ring in the AVF in New Zealand (Fig 2A) (Agustín-Flores et al., 2015).

Figure 2: Three volcanoes: A: Motukorea tuff ring in the AVF, NZ; B: Sag-hegy in western Hungary; C: Crosa de Sant Dalmai maar in NE Spain. Sources from https://es.wikiloc.com/rutas-senderismo/el-volca-de-la-crosa-st-dalmai-13395495/photo-8302761; https://scribblesnz.com/2013/10/11/among-the-volcanoes/; and https://hogsheadwine.wordpress.com/2012/09/11/the-tiny-production-of-peter-wetzer/.

Therefore, during this phase, the eruptive types depict as a "dry" character and express lava-fountains or a Strombolian eruption type (Courtland et al., 2013; Head and Wilson, 1989; Németh et al., 2011; Parfitt, 2004; Valentine and Gregg, 2008). These eruption types can lead to the formation of scoriaceous pyroclastic sediments near the vents and form scoria or cinder cones as well as spatter cones (Head and Wilson, 1989; Martin and Németh, 2006; Riedel et al., 2003; Valentine and Gregg, 2008). Lava-fountaining and/or Strombolian eruptions styles commonly operate with low explosive energy and produce tephra falls and lava flows (Houghton et al., 2006; Németh et al., 2012).

Figure 3: This diagram depicts the eruption sequences. By utilising the binary code "yes" and "no", it is obvious that the different morphology of monogenetic volcanoes is controlled by various eruption sequences. Note that ph.=phreatomagmatic phase; mag.=magmatic eruption phase; eff.=effusive eruption phase (Kereszturi et al., 2014).

In this section of the thesis, the monogenetic volcanism is characterised by small-volume volcanoes with a single eruption or multiple events which contain large intervals of periods. Monogenetic volcanism commonly creates spatter cones, scoria or cinder cones, tuff rings, tuff cones, as well as maars. These classifications are dependent on the interaction between magma and water which can dominate the eruption types, and these types include phreatomagmatic eruptions, lava-fountaining, Strombolian styles and effusive eruptions. As mentioned, the interactions between internal and external parameters play a critical role in forming small-scale volcanoes with various shapes. The internal factors include the physical and chemical features of magmatism, and the external parameters are composed of subterranean water flow or water-saturated sediments and substrate structures or topography. The term "monogenetic volcano" means an expression of specific volcanic types that the volcanic edifice is small scale, specifically less than 1 km^3, and formed by one single eruption or many discontinuous, small eruptive events supported by one or multiple magma batches (Németh and Kereszturi, 2015).

Definitions of monogenetic volcanic landforms

As mentioned, due to the various eruption types and eruptive processes changing, the monogenetic volcanic landforms and their pyroclastic facies architectures with different

styles have emerged. Four major characteristics of monogenetic landforms can be recognised in the field-scale: tuff rings, maars, tuff cones, and scoria or cinder cones. For the first three types, they are commonly formed by magma-water interacted eruptions, namely phreatomagmatic eruptions. Scoria cones or cinder cones are typically created by water-depleted and magma volume overwhelmed eruptive phases, which express lava-fountaining or Hawaiian eruption styles and subsequently change into the effusive eruption type with lava flows. This part will discuss the main features of these volcanic architectures, in terms of their compositions, shapes or morphologies, degradations and formations.

1) Scoria or cinder cones

Basically, a cinder or scoria cone (Fodor and Broz, 2015; Vespermann and Schmincke, 2000) is formed by a single eruption episode of monogenetic volcanism (Fig 4). The eruptive episode may persist for a few hours, or a few years, but eventually the eruption will be stopped. Once the eruption ceases, the plumbing system which connected the vent with the magma source will be closed forever (Francis and Oppenheier, 2004). A volcanologist (Macdonald, 1972) suggested a definition for cinder cones which defined them as a range of small-scale, truncated and cone-shaped volcanoes (Figure 4). This kind of volcano is composed of scoriaceous and loose cinder and other pyroclastic sediments which commonly form a circular-shaped cone. If these sediments are near a fissure-fed vent, the shape could be elongated (Fodor and Broz, 2015).

The geomorphological characteristics of cinder cones are similar but distinctive. In general, the basal diameter of cinder cones approximately ranges from 800 m to 2.5 km. The spatial volume observed by field-scale is 40×10^6 m^3 (Wood, 1979b; Wood, 1980). The altitude may be more than 100 m (usually more than 200 to 300 m) above sea level. Their shapes are nearly asymmetrical, for instance, the elongated shape originated through fissure eruptions on one side higher than the downwind side by the time of the erosion process. The major characteristic of cinder cones is its angle of repose. Almost all cinder cones have nearly 33 degrees of angle of repose (Francis and Oppenheier, 2004). As mentioned, cinder cones commonly exist less than one year, and half of them erupt less than 30 days into the eruption phase (Wood, 1980). In previous worldwide studies, about 800 cones in the Andino-Cuyano Basaltic Province of Argentina have been observed. It was shown that the ratio of cone height to basal diameter would consistently shorten because of external erosional processes. This ratio might demonstrate the relationship between cone size and the extent of the edifice. In terms of this concept, with the cone morphology changing, scientists can relatively and quantitatively estimate the age of cones as well as erosional processes (Hooper and Sheridan, 1998).

In monogenetic volcanism, a cinder cone has commonly undergone a series of simultaneous and/or frequent mafic lava eruptive phrases. Low-viscosity magma with different explosive styles can generate cinder cones. These eruptive styles include Strombolian, Hawaiian, sub-Plinian and even phreatomagmatic types (Fornaciai et al., 2012), for instance, the eruption

style of volcanoes has been reported from the northern Tibetan Volcanic Field (commonly referred to as the Kunlun Volcanic Field) in China (Deng, 1978) and the AVF in New Zealand (Kereszturi and Németh, 2016). Some cinder cones are formed by fissure eruptions, like Laki in Iceland (Thordarson and Self, 1993) and Tolbachik in Russia (Inbar et al., 2011). Cinder cones in the intra-plate plate systems can be grown within a few days despite their final size (Wood, 1980).

Figure 4: This is a cinder cone situated in the Lassen Volcanic National Park, California, USA. With about 213 m of altitude, this cinder cone is formed by loose scoria. Double rims present on the top of the cone, indicating there might be two eruptions occurring at least during its late formation processes. In this picture, the red circle marks the crater rim; the purple dash line and solid line depict the margin of the cone bottom; the double blue lines represent the cone flank; the yellow dash line indicates the crater depth; and the green dash line shows the cone height (sourced from www.roadtrippers.com).

2) *Maar*

A cinder or scoria cone is built by the "dry" conditions and short periods of basaltic monogenetic volcanism (Németh and Kereszturi, 2015). Sometimes, when magma batches ascended through water-saturated sediments or aquifers, the eruptive style became the magma-water interactive explosions, namely phreatomagmatic eruptions (Francis and Oppenheier, 2004). With such short-lived but violent processes, a maar will be generated. A maar crater expresses a circular depression landform which is surrounded by low profiles of ejected materials (DeHon, 2015). The most important characteristic of a maar crater is that its crater floor is below the syn-eruptive surface, e.g. it looks like a hole in the ground landform (Christenson et al., 2015; White and Ross, 2011). After the eruptions, a maar can quickly build circular walls around the centre vent, but because of the properties of its eject materials, the walls will rapidly be eroded away (approximately 80 m high eroded in 19 days, source from (Németh and Cronin, 2007)). Since then, the maar vent presents on the ground rather than being built above the surface (similar to cinder cones), and subsequently a maar vent will be filled with water to be a maar lake (Figure 5). According to the samples found in the surrounding maar deposits, a mixture of accidental and juvenile materials compose the rim deposits (DeHon, 2015). Depending on the environmental conditions, if the eruption can last

long enough, the maars can be covered by cinder or scoria on its floor and the craters can be filled with basaltic ejecta. The eject materials may contain varieties of accidental liths which are transported by the eruption and possibly composed of deep crustal rocks, pre-eruptive sediments, volcanic ash, lapilli, scoriaceous basalts and sparse mantle xenoliths, such as peridotites, kimberlites or lamproites (Fisher and Schmincke, 1984; Fisher and Schmincke, 1994). Specifically, mantle-derived peridotites, kimberlites and lamproites may indicate times of multiple eruptive phases associated with magma injection to the lower crustal level (DeHon, 2015).

Figure 5: This is the Krafla Viti Crater located in Iceland, which is actually a maar volcano of 300 m in diameter. It erupted in 1724, which was known as the Mývatn Fires. As shown in this photo, the crater rim is composed of wall rocks (dark brown) and pyroclastic deposits (grey to black) (sourced from www.zigzagonearth.com/krafla-viti-crater-iceland).

3) *Tuff rings*

The major distinction between tuff rings and maars is that maar-diatremes can excavate below the surface and go deep into the surrounding rocks, but tuff rings are formed just above the surface (Broz and Nemeth, 2015). Generally, maars involve a range of explosive eruptions with minor juvenile materials, and on the contrary tuff rings may contain huge quantities of highly-fragmented juvenile basalts (Francis and Oppenheier, 2004).

A tuff ring usually involves the ring-shaped, low-rim and small-volume volcanic edifice. The crater floor is above the syn-eruptive surface (Broz and Nemeth, 2015). The dip of the crater surrounding pyroclast sediments presents at a low angle approximately less than 25 degrees from the surface (Figure 6). Their extent is commonly less than a kilometre from the crater rim (Kereszturi and Németh, 2012; Németh, 2010a; Vespermann and Schmincke, 2000;

Wohletz and Sheridan, 1983). The crater rim deposits of tuff rings are predominantly composed of a range of dune-bedded, laminated tuff beds which are inter-bedded by coarsely-grained tuff breccias and lapilli tuffs near the vent position (Heiken, 1971; Kereszturi et al., 2013; Németh et al., 2012; Wohletz and Sheridan, 1983). In contrast with a maar, a tuff ring usually doesn't have diatreme structures below its crater floor. Nevertheless, some volcanic debris or solidified lava bodies can be observed below the floor of the crater (Affleck et al., 2001; Cassidy et al., 2007; Lorenz, 1986a; Vespermann and Schmincke, 2000).

Figure 6: The Jabal Bayda tuff ring in the Harrat Khaybar Volcanic Field is composed of comenditic lava and is about 50 m high. It is one of the largest volcanic fields in Saudi Arabia and covers about 14000 km^2. The Jabal Bayda tuff ring has a flat and shallow bottom. The gullies can be observed on its flank. In the centre of this tuff ring a small dome is well preserved (sourced from https://volcano.si.edu/volcano.cfm?vn=231060; (Moufti and Németh, 2016)).

Just as with the categories of volcanic eruption styles, tuff rings are formed by phreatomagmatic eruptions which are featured by magma-water interactions. From this point of view, the conditions of water or water-saturated sediments in the past can be implied from the presence of tuff rings, such as lakes, rivers, swamps or small and shallow ponds/streams. Sometimes, tuff rings may represent the geological settings of coastal plains, alluvial fans, as well as lacustrine basins at the time of formation (Heiken, 1971; Martin and Nemeth, 2005; Németh, 2010a; Németh, 2010b; Németh et al., 2010; Rottas and Houghton, 2012).

As mentioned, the coarse tuff breccias and tuff lapillus-formed crater tuff rings may be deposited from the base surges with a low concentration of particles at the ring rims, and it can be observed that with the gradual changes between different grain sizes within the laterally accumulated deposits. These deposits may indicate the changes in particle

concentrations, consistent depositions, and reduced speed of base surges away from the eruption (Allen et al., 1996; BD et al., 2004; Dellino et al., 2004b; Dellino et al., 2004a; Lajoie et al., 1992; Schmincke et al., 1973; Vazquez and Ort, 2006; Wohletz and Sheridan, 1983).

4) Tuff cones

Tuff cones have a similar composition of pyroclastic deposits, but from their morphology they are commonly small and steep-sided (Brand and Broz, 2015). The composition of deposits is generally composed of volcanic ash beddings, lapilli, as well as blocks. If a range of cross-sections can be observed, the tuff cone deposits contain a number of layers that are centimetres to tens of centimetres in average thickness, and each layer represents the time of eruptive phase powered by phreatomagmatic eruptions (Brand and Broz, 2015). Grain-size distribution is also showing as its varies from each layer, and depicts the intensity of magmatic fragmentation which implies the magma-water interaction in its frequencies.

Figure 7: Damond Head tuff cone in Hawaii, a world-famous landmark, was built approximately c. 200000 years ago with typical hydro-magmatic eruptions. Because of the eruptive loci, the deposit of this cone is composed of a mixture of coral and basalts which are the components of tuff and magmatic debris. Based on its morphology features, this tuff cone today is nearly symmetrical and it is assumed that it must have undergone an eruptive phase that lasted a few days to a month. Considering its monogenetic properties, Diamond Head tuff cone is listed as a dormant volcano (sourced from www.volcanocafe.wordpress.com and www.commons.wikimedia.org).

As mentioned, tuff cones have often undergone a series of phreatomagmatic eruption phases when the intrusive magma batches intersect into the shallow water systems such as a lake or sea (Morrissey et al., 2000; Sheridan and Wohletz, 1983). Distinguishing differences between tuff rings and tuff cones are judged by how long an eruptive phase can last. Due to the deposits observed from rings and cones, relatively high eruption columns and mass eruptive rates can cause tephra to widely distributive, thus a tuff ring should be built. On the contrary, a tuff cone must have been formed through less violent but more prolonged eruption phases. For slumping, it does occur with a very low possibility. However, due to the hot, wet pyroclastic material cooling and drying so rapidly, the settings could be as hard as concrete, thus the tuff cone's tephra layers are stable, preventing the slump (Francis and Oppenheier, 2004).

The composition of tuff cone deposits range from armoured lapilli, vesicular scoriaceous tuff, to soft sedimentary structures, ballistic bedding sags and palagonitic glassy textures. These characteristics list the evidence of the abundance of external water, typically liquid water involved at the time of depositional process. It is necessary to mention that the palagonite, a result of ash alteration due to hydrothermal processes, can be formed during the syn-eruptive periods in phreatomagmatism. Because of the heat and water steam, the palagonite can occur even shortly after an eruptive phase (Brand and White, 2007; Farrand and Singer, 1992). Finally, note that the difference between tuff rings and tuff cones is judged by the crater depth; for a shallow depth of the crater, a tuff ring will be defined.

Definitions of maar-diatreme volcano

A maar is formed by a range of hydrovolcanic and explosive eruptions, and the maar crater is commonly above dykes which have interactions with shallow water or aquifers (Mège and Masson, 1996). In morphology, the rims of maars depict a low profile with an extended but "not so deep" crater. Specifically, the crater floor is below the surrounding surface (Rittmann, 1962). Generally, the morphometry of maars on Earth ranges from a few hundred metres to a few kilometres in their diameter (DeHon, 2012). Based on previous research, the basement diameters of maars average 1.38 km. The ratio between cone height and basement diameter is approximately 0.02. The volume of a maar is often about 25×10^6 m^3 (Wood, 1979a).

As always, the external interactions between magma and water should be frequently mentioned as the most important factor in assessing maar volcanoes. When melting materials meet the water-contained sediments or aquifers, externally-driven fragmentation will occur and lead to phreatomagmatism or Surtseyan-type eruptions (Lorenz, 1985; Németh et al., 2008; White, 1996; Zimanowski and Buttner, 2002; Zimanowski et al., 1997). In other words, the phreatomagmatic volcanism (or hydro-magmatism) is defined as magma encountering ground-water (Rittmann, 1962). There is, however, something exceptional. Mantle peridotites, kimberlites and lamproites involved in maar deposits indicate that the eruption mechanisms might be in relation to deep sources which are more efficient than ground-water. The maar volcanoes differ from the scoria (cinder) cones by more violent and explosive eruptions. The batches of magma are ground into small pieces and ejected into higher

eruptive plumes, leaving a broader cone than scoria cones. Subsequently, the syn-eruptive cone will become a wide and deep crater with low rim properties due to the post-erosions and degradations.

In maar volcanic structures, the most typical one is the diatreme. Diatremes are the sub-surficial structures of maar volcanoes (Blaikie et al., 2014; Delpit et al., 2014; Graettinger et al., 2014; Lefebvre et al., 2013; Lorenz, 1986b; Lorenz et al., 2017; Muirhead et al., 2016; Ross et al., 2017; Valentine and White, 2012). A maar-diatreme presents a reverse cone-shaped architecture up to 2.5 km deep and approximately 2 km in diameter (Martin et al., 2007). The diatreme cuts into the pre-eruptive surrounding rocks, and is filled with clastic debris which comes from the surrounding rocks, juvenile particles as well as slumping wall rocks. Usually, it is hard to get a? direct evaluation of a diatreme's volume due to the technology limitations. However, assessing the volumes of thinly-bedded tephra rings as well as distal ejected deposits, a volume of maar-diatreme can be estimated. At the bottom of a maar-diatreme, the root zone lies within. The shape of the root zone in a diatreme often depicts its irregular morphology. Under the root zone, a range of feeder dykes gets in touch with it. Feeder dykes are the magma sources which engine a maar system.

Because of the properties of phreatomagmatic eruptions in maar systems, the deposits from the sub-surface are majorly composed of peperite, a mixed in-situ rock type of mixed intrusive coherent magmatic body and host sediment (Skilling et al., 2002), which represent the interactions and mingling between magma and wet beddings. The peperite commonly indicates the synchronous occurrence of volcanism and sedimentation. It also can provide the evidence of magma transportation in a shallow sub-surface, magma fragmentation, surrounding sediment properties, as well as the mechanisms of fuel-coolant interactions (Skilling et al., 2002; White et al., 2000). With the eruptive sequences finally to the end, the water will fill in the crater and form an enclosed maar lake. The maar lake is characterised by pillow lavas, hyaloclastite breccias, as well as tuffisitic peperite breccias. Due to the relative isolated conditions (surrounding ejected deposits), the depth of a maar lake is commonly in terms of its diameter. This feature may affect the lake shape and the sediment structures and compositions, and the sediments in the maar crater often catch materials in a very small catchment area (Martin et al., 2007). Usually, the local sediment on the bottom of a maar lake may be affected by the algal bloom inhabiting it. Effective alternations between algal bloom and local background clasts will produce a range of well-laminated beddings. The characters of tephra deposits in maar volcanoes are very similar to the ones generated by a Surtseyan eruption style (interactions between abundant water sources and fluid magma fluxes) in subaerial conditions. For the mechanisms of maar volcanic eruptions, it is clear that the Surtseyan style eruptions preserve the glassy fragments but lack the components of country rocks characteristics. Based on such differences, it is assumed that the Surtseyan eruptions may occur at very shallow ground levels in a volcanic edifice (Martin et al., 2007). As always, with the eruptive processes progressing, in the constantly ascending magma with less or no

water conditions a Surtseyan style eruption will transform to a Strombolian-style eruption and the maar forms may turn into the spatter cones.

Figure 8: This figure depicts the cross-section of a maar system with its geomorphic characteristics. Note that there are two principally different conditions which represent the hard-rock substrate and soft-rock substrate. Each of them is with respect to the source of subterranean water interacting with the dyke-fed magma (Kereszturi and Németh, 2012; Lorenz, 2003a).

Calderas and maar volcanoes

The characteristics of calderas and maars always have ambiguous concepts and similar morphologies (Németh et al., 2009; Palladino et al., 2015). Scientists have been researching the differences in geomorphologies and differentiations in processes and evolutions in order to present a spectrum of distinctions between calderas and maars. Maar-diatreme volcanoes and explosive collapse calderas mark the two completely different volcanic types which similarly penetrate into the pre-eruptive beddings and sediments. Regardless of their difference in size and other features, they commonly display a range of similarities (Lorenz and Suhr, 2012).

The definitions of maar volcanoes have been discussed in previous chapters, which were obviously concentrating on caldera volcanoes and their characteristics. Calderas and their complexes are significantly recognised in the entire volcanic landforms on Earth or even in the solar system (Cole et al., 2005). The most extended caldera that humanity has identified is Olympus Mons on Mars. This super-huge caldera contains six collapsed centres which measure about 80 × 65 km in diameter (Mouginis-Mark and Robinson, 1992). On Earth, the Yellowstone Caldera is the most world's famous caldera and volcanic territory. There are three major eruptions documented in geological history: 2.1 million years ago, 1.2 million years ago and 0.64 million years ago. The magnitudes of these three eruptions were approximately 6000, 700 and 2500 times more intense than the eruption of Mt. St. Helen's in 1980 respectively (sourced from www.yellowstonepark.com). With the last eruption of the Yellowstone caldera (0.64 million years ago), the extensive rhyolitic lava flows have covered as much as 340 km^2 of the syn-eruptive collapse in the eruption area (sourced from

https://volcanoes.usgs.gov). The collapse processes created a giant subsidence depression of nearly 3900 km^2. Calderas also represent the highest activities of thermal energies, thus electricity generation and mineral exploration can be sited in these regions. Generally, a caldera is defined as "*a volcanic structure, generally large, which is principally the result of collapse or subsidence into the top of a magma chamber during or immediately following eruptive activity*" (Cole et al., 2005).

Calderas on the surface of the Earth vary in many types of volcanic fields. In the intra-oceanic plate boundaries, as well as mid-ocean ridges (MOR), basaltic calderas represent the localities of the Hot Spot, such as Hawaii and the Atlantic MOR (Walker, 1988). Island arcs commonly indicate the convergent plate margins, and andesite-dacite calderas are typically in relation to these regions, for instance, Tonga Islands (Baker et al., 1971). In the Eastern African Rift zone, peralkaline calderas are the implications of a massive extension (Acocella et al., 2002), and also can be found in where high rates of extension in convergent boundaries take place, such as in New Zealand (Houghton et al., 1992). The rhyolitic calderas that indicate the most violent explosions mark in continental or continental boundary regions, and also convergent margins, for example, Mount Changbai on the boundary between China and North Korea and the Taupo volcano in New Zealand (Wilson et al., 1995). Specifically, the rhyolitic calderas can also be found in the territories of continental rifting zones such as in the southern central USA (Elston, 1984).

Calderas are often called super-volcanoes due to their massive destructive behaviour and being the cause of fatalities. For instance, the catastrophic eruption of Mount Pinatubo in the The Philippines in 1991 resulted in about 350 people dying during the eruption and it subsequently triggered hazards causing a total of 722 fatalities, as well as approximately 200000 people being left homeless. In addition to such loss of life, the ash deposits covered about 4000 km^2 in land area. The effects of this eruption impacted not only on the regions surrounding Mt. Pinatubo but also affected global weather. The eruptive column that injected into the stratosphere caused the sunlight to decrease and this led to a global cooling of about 1.5 degrees on average (sourced from www.ngdc.noaa.gov).

Figure 9: Olympus Mons, the most extended caldera in the solar system, is approximately more than 25000 m above sea level and almost three times higher than Mount Everest on Earth, probably because of the low gravity of Mars. With six collapsed calderas on the top of this monstrous volcano, the depression is about 85 km wide on average. Note that the Olympus Mons is a giant shield caldera volcano (sourced from www.space.com and NASA).

The following section will discusse maars and calderas – their differences and similarities – and also point out the main issues around them.

Maar-diatreme volcanoes are small volume and short-lived craters of several tens of metres, and some of them extend to approximately more than 2 km in diameter only due to them being long-lived maars (Lorenz, 2007; Lorenz and Kurszlaukis, 2007). Comparatively, the collapsed small caldera craters may be only a few kilometres wide in contrast to larger ones of about 40-100 km. Despite the difference between maar volcanoes and calderas in their size, another major characteristic is their lava composition types which are dominant in their eruption processes. For maar volcanoes, the majority of lava types are mafic to ultramafic lava, but on the contrary the types of lava generated from calderas are intermediate to acidic compositions. The volume of ejecta and main eruptive types should also be taken into account in considering the differences between maars and calderas. Thinking about their eruptions,

maar-diatreme volcanoes commonly erupt small volumes of tephra, and the eruptive columns often largely distribute to the proximal areas with base surge deposits and to distal ash fallout. Usually, such maar tephra volumes range from 0.1 to 0.2 km^3 (Lorenz and Suhr, 2012). Comparedto the maar-diatreme volcanoes, the volume of proximal or distal base surges or ash deposits formed during an explosive caldera may be up to 1000 km^3 for each large caldera. Both types of volcanoes can be filled with water as crater lakes form during the early period of post-eruptive time. The succession of a maar-diatreme volcano probably underwent intra-crater intrusions and magmatic depositions by the phreatomagmatic processes, especially the magmatic deposits including cinder cones, lava flows and lava lakes. In contrast with maars, an explosive collapsed caldera may have a series of intra-caldera cinder cones, lava flows, domes, as well as ash flow deposits due to the intrusion of plutons which result in ring dykes or even resurgence. Sub-surface structures on each type of volcano can be observed. For a maar volcano, about a several hundred metre, less than a kilometre deep, reversed cone-shaped diatreme underlies the maar crater (Lorenz and Kurszlaukis, 2007). As the counterpart of a maar, a small explosive collapsed caldera may contain a funnel-shaped sub-structure in contrast to a large caldera which consists of a plain-underlain sub-structure (Lipman, 1997). The collapse of country rocks and primitive tephra triggers the enlargement of a maar crater diameter and underlying diatreme. The diatreme fills consist of reworked tephra and country rocks (Lorenz and Kurszlaukis, 2007). In the caldera condition, the infills of a caldera crater commonly contain welded ash flow deposits, collapsed breccias, and collapsed crater wall rocks during the syn-eruptive and post-eruptive periods. These materials can reach several kilometres in thickness (Lipman, 1997). In previous research, the energies that engine the eruptions for both maar volcanoes and calderas are a major distinction, as they are phreatomagmatic eruptions and magmatic volatile-driven eruptions. However, both eruption types for both volcano types can be inter-transitional in some fields. To classify whether or not a volcano is a maar or caldera, it depends on which eruption type dominates in volcanic processes. Sometimes, the deposits that are observed in maar systems depict the feature of volatile-driven magmatism. For instance, the Laacher See depression is defined as a maar with a 3 km diameter. This maar volcano contains an unusually high volume of loose deposits, as well as phonolitic tephra, and the main deposits have been inferred as magmatic volatile-driven processes which usually engine an explosive collapsed caldera (Freundt and Schmincke, 1986). Similarly, recognised caldera deposits often show phreatomagmatic-style eruptions. The juvenile particles from Askja, Iceland and Taupo, New Zealand contain a range of vesicularities which indicate the magma-water interactions, namely phreatomagmatism (Carey et al., 2009; Houghton et al., 2010; Self and Healy, 1987; Self and Sparks, 1978).

The idealised models for maar-diatreme volcanoes are characterised by a series of repeated and incoherent eruptions, which are due to the interactions between magma and shallow water, and the sustained time should be from a couple of days to a few years. The surrounding deposits should be tuff breccias and well-bedded lapilli tuffs derived from pyroclastic base surges. Specifically, the total volume of ejected magma should be small for monogenetic

maars in contrast to polygenetic ones. For a maar volcano, the sub-surface structure is an excavated and cone-shaped diatreme, which is no more than 2 km down from the surface. The infill materials in the diatreme are composed of pyroclastic rocks on the crater floor, tuff breccias, lapilli tuff and parts of intrusions (Delpit et al., 2014; Lefebvre et al., 2013; Ross and White, 2006; Valentine and van Wyk de Vries, 2014). Also last, but not least, almost all maar volcanoes are formed by phreatomagmatic eruptions followed by lava-fountain eruptions.

Compared to maar volcanoes an idealised explosive collapsed caldera is fueled by a massive subsidence, which occurrs due to the magma withdrawing during the high discharge rate eruptions. Usually, most of the calderas are formed by sub-Plinian to Plinian eruptions in the beginning, with massive volatile-saturated magma, pyroclastic ejections that follow the first step of the eruptions fueling the pyroclastic density currents which are erupted from the boundary faults (ring faults), the collapses are accompanied throughout the whole eruptive processes, thus a huge caldera may form (Martí et al., 2009; Palladino et al., 2014). The external crater deposits can be widespread as fallouts with poorly-sorted ignimbrites inserted into the bulk products, and the deposits are predominantly composed of juvenile materials, which are in the form of highly-glassy ash and pumice. Despite the lithic materials there can be a high volume in proximal domains, but still it is overall minor compared to ignimbrites. The distinction between calderas and maars visually is their size, as a caldera can extend to a range of several kilometres to tens of kilometres in diameter, and the depth of subsidence is approximately ranging from 100 m to a few kilometres (Acocella, 2007). The internal deposits underlying beneath the caldera depression are the accumulations of ignimbrites inter-bedded by stratified breccias and megabreccias derived from caldera collapses about 1 km in depth (Lipman, 1976). From a lifespan point of view, a maar-diatreme volcano commonly erupts once or has multiple eruptions during a very short period as is judged as monogenetic volcanism. In contrast with maar systems, an explosive collapsed caldera may have structural or eruptive resurgence for about tens of thousands years after the caldera collapsed. Nevertheless, note that if a caldera formation is generated by a single eruptive phase, the features of this caldera can be as for a maar-diatreme volcano. It is recognised that a caldera complex is formed by multiple, overlapping caldera phases which occurred in different periods (Palladino et al., 2015).

Considering the MFCI is the engine of incoherent explosive phreatomagmatic eruption processes, the mixing prior to the eruptive behaviours is a possible result for maar-diatreme volcanoes (Büttner and Zimanowski, 1998). The MFCI is preferred to the anti-premixing of water and magma with the relatively high-viscosity. Small-magma batches that have properties of the friendly mixing attribution and minor time for degassing and crystallisation in the rapid emplacement. Thus, when magma fluxes contacted with large volumes of shallow water, it will cause phreatomagmatic explosions, and result in magma fragmentation during the interactions of magma and water (Zimanowski et al., 1995). Know that the last factor is the key which can trigger the thermohydraulic explosions. All the above-mentioned is

identified in small, monogenetic, mafic maars and the characteristics and behaviours match such a type.

As classified above, explosive collapsed calderas in relation to the massive volumes of magma in the shallow reservoirs triggered the surrounding rock subsidence that are bounded by ring faults. It is different with high-magma flux charges with relatively high-viscosity melt, and bubbles form a series of pumice and ash structures in caldera end-members in contrast to discrete eruptions in MFCI conditions. The concept of MFCI can simply suit for small volumes of mafic magmas, however it is not so sure that this factor can relate to volatile-fueled fragmentation and vesiculation, the phreato-plinian aspect, as well as the importance of vesiculation for the mixing of water and magma in a given conduit depth (Palladino et al., 2015). Also, the rates of magma ascending from its reservoir are under-addressed.

Maar-diatreme crater formations

In the maar volcanoes, the crater formations are formed by two separate stages: syn-eruptive periods and post-eruptive phase. Each of them presents typical and distinctive patterns to effect and form the formations of a maar crater. More complicated basaltic and kimberlitic compositions can also eventually form the different types of maar crater formations. This section will interpret the maar crater in order to comprehensively cover the whole scenarios.

In the terminology, the word “crater” means a geomorphological feature. In other words, a volcano underwent a series of the eruptions and left significant geographic architecture afterwards. Usually, a crater will be formed at the beginning of the eruption but is filled with materials in the later periods of the eruption. This is why volcanologists distinguish syn-eruptive craters and post-eruptive craters in the terminology. The definition of an syn-eruptive crater is that an open pit emerges during a whole eruption event. Compared to it, the post-eruptive crater is preserved after an eruptive event and is filled with various sediments, even lacustrine deposits (White and Ross, 2011).

In a post-eruptive crater, because of the immediate cease of the volcanic eruption, the sedimentation rapidly occurrs on the crater floor and greatly moderates the depth and width of this post-eruptive crater. Specifically, the rates of sedimentation reflect the crater-wall rock features, crater-wall hydrology and streams, and marine as well as aeolian processes which carry the sediments into the crater. In terms of crater-wall hydrology and stream processes, a maar-diatreme crater commonly traverses the water layers. It is easy for a maar crater to preserve a range of high-resolution sediments and deposits. In the upper part of a post-eruptive maar crater, the crater formations are often composed of relatively coarse-grained deposits, which are formed by the crater-wall failure, and the formation of alluvial fans and debris flows (Pirrung et al., 2008; Rayner et al., 1991; Smith, 1986; White, 1992). In the later stage, a maar crater will consequently be filled with water to become a crater lake. Thus, lacustrine sediments will emerge in the deep centre of the crater floor. Composed of mud and diatomite layers, the maar-lake sediments can be a useful tool for the reconstruction and studies of the paleoclimate and paleoenvironment (Kaiser et al., 2006; Lindqvist and Lee,

2009; Ognjanova-Rumenova and Vass, 1998; Zolitschka, 1992). Actually, the lacustrine sediments are commonly recognised in deposits of maar-diatreme formations (Büchel, 1993; Hack, 1942; Németh and Martin, 1999; Smith, 1986).

The kimberlitic maar-diatreme volcanoes are the specific spectrum of maar volcanoes, typically filled with kimberlites, which moderately form diamonds and preserve highly commercial values. In the southern part of Africa, kimberlitic maar-diatremes are commonly exposed by opening mining processes. A few studies have presented that some of the kimberlitic maar-diatreme volcanoes are filled with breccia rocks due to avalanches, turbidites including pyroclastic flows, debris flows and flood layers, and other materials are derived from talus fans (Field et al., 1997; Gernon et al., 2009a; Gernon et al., 2009b; Gernon et al., 2009c). The formations of post-eruptive craters with kimberlitic derivation often contain granite breccias, redeposited volcaniclastic kimberlitic sediments, kimberlitic turbidites, as well as shales (Stiefenhofer and Farrow, 2004).

The subsidence and slumping is an important part in the evolution of maar-diatreme volcanoes. Based on the phreatomagmatic model (Lorenz, 2003a), the explosive site commonly happens on the top end of a feeder dyke in which the initial water-magma explosion has taken place. When the pyroclasts and fragmented magma erupt out of the crater, the excavation of the diatreme penetrates downward to the deeper places. This leads to the material's deficiency near the root zone of the diatreme and the un-stabilisation of overlying country-rocks, so consequently the collapse and slumping will occur. Since the upper and surface materials are swallowed by such a collapse, a maar crater will form (Lorenz, 2003b). In terms of the above-mentioned, the evidence of a post-eruptive maar crater is identified in many maar volcanoes (Lorenz, 2008; Suhr et al., 2006). The thickness of the crater formation is preserved by the eruptive subsidence and slumping (White, 1991a; White, 1991b). It is recognised that the subsidence and slumping can proceed even after the eruptive phases as a result of a geomorphological feature (Suhr et al., 2006).

An syn-eruptive crater is literally formed during the initial eruption phase. The formation of the syn-eruptive crater is the initial stage of the process of crater formation (Goto et al., 2001; Lorenz, 1970; Ohba et al., 2002). The excavation of the maar-diatreme will make the maar crater wider and deeper, and the rate of the crater growth depends on the rate of the diatreme excavation (Valentine et al., 2011). The excavation processes dominate the whole eruptive phase. While the ejecta materials are burst out of the crater, the excavation occurs deeply into the bottom of the diatreme. Generally, the diatreme excavation is caused by the collapse and slumping of the overlying wall rocks due to the mass deficiency of the underlying materials in the diatreme (Lorenz, 2003a). The details of the excavation processes are due to the decompression, which is the reason for volatile materials being erupted from the diatreme. When the volatile materials become ejecta, the decompression behaviour extends to the whole diatreme and leads to the phenomenon of fluidisation (Clement and Reid, 1989; Hawthorne, 1975; Porritt and Cas, 2009; Reynolds, 1954; Shoemaker et al., 1962; Sparks et al., 2006; Wilson and Head Iii, 2007a). Thus the excavation can proceed until the eruption has

ceased. The excavation leads a maar crater to become deep, and the collapse of the upper-diatreme materials leads a crater becoming wide. In some recent research, the development rates between the excavation and crater widening are different. Due to the lithostatic pressure, rock strength will become stronger if the location of the rocks is deeper (Jaeger and Cook, 1979). The water-magma interaction is more effective within the lower hydrostatic-pressured aquifers. Also, the collapse and slumping occur in the upper part of the country rocks (Valentine and White, 2012). Consequently, the rate of crater widening is higher than the rate of the diatreme excavation.

The crater filling is basically derived from the falling materials during the eruption. When the volcanic debris is ejected through the diatreme, some of them would fall and deposit around the crater, however some would inevitably fall back into the syn-eruptive crater. Sometimes these fallen ejecta will form in beddings and become a portion of the upper diatreme (Lorenz, 1986b). As mentioned above, the deficiency of the lower materials causes the un-equilibrium between the excavation and the upper lying wall rocks (Lorenz and Kurszlaukis, 1997; Lorenz and Kurszlaukis, 2007). The syn-eruptive crater floor must be deposited by a range of pyroclasts, which are composed of tephra fallen materials and density currents. Through the processes of the maar volcano evolution, the phreatomagmatic eruption will eventually become a Strombolian-style eruption. Thus, with a higher magmatic eruption rate, the syn-eruptive crater will be consequently filled up and buried by lava flows or scoria cones (Shoemaker et al., 1962). In the field observations, parts of the maar crater formations are covered by scoria or cinder in the late eruptive phases. Some of the maar volcanoes have a range of scoria formations proceeding to the phreatomagmatic formations (Gutmann, 2002). Simply because the variations of magma flux and water supply distribution constrain the efficiency of the water-magma interaction, the end compositional materials depend on it.

The crater size is controlled by the collapse and slumping of the overlying country rocks. The widening of the crater size is also accompanied by the diatreme excavation processes. Due to the phreatomagmatic eruption phases, the crater widening on the top and the excavation in the bottom are proportional (Lorenz, 1973; Lorenz, 1986b). Some studies suggest that the volumes of maar crater and tephra ring are similar, and this represents the crater size in relation to the volume of ejected materials (Valentine and White, 2012). In recent studies, the size of a maar crater is represented as the most violent eruption during the eruptive phases in respect of crater explosive experiments, e.g. the observations for the Lunar Crater maar in Nevada, USA. However, this assumption probably depicts the paradoxical consequence of magma-water composition during the phreatomagmatic eruption phrases. Other assumptions concluded that the final maar crater size is determined by the multiple eruptive events when the growth of the crater is accompanied by subsidence due to the ejection of materials (Valentine et al., 2011). In this scenario, the eventual crater size and its volume are constrained by magma flux composition, variations of vent location, ejective materials which are erupted through a series of shallow explosions and form the individually small craters, as well as the collapse and slumping of the overlying wall rocks (Valentine and White, 2012).

In the most kimberlitic maar-diatreme volcanoes, the depth of several hundred metres and steepness (approximately 70 degrees) are common in the post- to syn-eruptive craters (Scott Smith, 2008; Skinner and Marsh, 2004; Webb et al., 2004). When a maar crater opens, the subsequent sedimentation will fill the opening crater with re-sedimented volcaniclasts and other clastic materials (Gençalioğlu-Kuşcu et al., 2007). Because during the eruption phases, if the wall rocks are composed of jointed materials, the eruptive explosions can easily destroy the joints and weaken the overall lithostatic strength, thus the potential collapse and instability of the shallow wall rocks is possible (Wayne Peter, 2008).

Role of phreatomagmatism

Phreatomagmatic eruption is seemingly the essence of every kind of monogenetic volcanism. During the volcanic evolution processes, with the magma ascent to the surface, countless interactions between external and internal processes occur in the pre-eruptive phase (Kereszturi and Németh, 2012). For example, the degassing will be in the action during the magma ascent from its source to the surface. While the magma erupted through the vent, explosive or effusive eruption behaviours could be determined by the eruptive conditions, which are represented by the internal factors such as magma chemical composition and external parameters such as the availability of water (Kereszturi and Németh, 2012). The formation of a monogenetic volcano is a very important addition to field observation and data collection. Commonly, the formations are formed by a range of discontinued eruptions and subsequent sedimentation (Kereszturi and Németh, 2012).

In this section, the external interaction between magma and water is discussed. The magma fragmentation usually happens when the melt contacts with the external water supply, triggering the phreatomagmatic or Surtseyan eruptions (Lorenz, 1985; Németh et al., 2008; White, 1996; Zimanowski and Buttner, 2002; Zimanowski et al., 1997). The water supplies can present as surface water or the ground-water aquifers preserved in the porosity or country rock fractures (Buttner et al., 1999; Kokelaar, 1986; Lorenz, 1986b; Lorenz and Kurszlaukis, 2007; Sottili et al., 2012; White, 1996; White and Ross, 2011; Wohletz, 1986; Zimanowski and Wohletz, 2000). Using common sense, the phreatomagmatic explosion must take place in the shallow depth of subterranean water systems. However, if the magma ascent meets the bottom of a lake or the sea, even in the water-saturated sediments, a littoral cone or rootless cone can be formed (Fagents and Thordarson, 2007; Hamilton et al., 2010b; Hamilton et al., 2010a; Jurado-Chichay et al., 1996a; Jurado-Chichay et al., 1996b; Mattox and Mangan, 1997; Thorarinsson, 1953). Due to the conditions of subaerial or surface environments, the volcanic crater size ranging from 0.1 km to 2.5 km in diameter is produced by such phreatomagmatic eruptions (Lorenz et al., 1970). Around the world, those such as the Coragulac maar, Mount Gambier (Newer Volcanics Province), SE Australia and Devil Mountain Maar, Seward Peninsula, Alaska have undergone a series of multiple vents which generate complex craters. Whatever the single eruption or multi-eruptions in a short period, the phreatomagmatic processes must be in relation to the so-called MFCI. Same as smelting processes, the MFCI must be composed of three parameters:

- Producing the premixing between magma and external water, with vapour steam
- Vapour steam leads to the magma fragmentation and explosive shockwaves
- The magma fragmentation of post-eruptive processes (Büttner and Zimanowski, 1998; Wohletz, 1986).

In the initial eruptive processes, the magma fragmentation can trigger the subsequent processes, depending on the surrounding conditions (e.g. the depth of the fragmentation taking place). In some cases, the magma fragmentation does not trigger other eruptive processes (Kokelaar, 1983; Kokelaar, 1986; Sheridan and Wohletz, 1981; White, 1996; Wohletz and McQueen, 1984a; Wohletz and McQueen, 1984b). On the contrary, the excavation of an eruptive crater may play an important role in the topography of the pre-eruptive landforms and form a hole in the surface noting it as a maar crater (Fig 5) (Lorenz, 1985). The explosive location of a maar volcano should lie in relatively deep places. In contrast with the maar, the tuff rings (Fig 6) are formed by the shallow explosive location, and its crater floor is nearly on the pre-eruptive surface (Wohletz and Sheridan, 1983). Both maar volcanoes and tuff rings are the major consequences of phreatomagmatic eruptions. As observed in the field, the tephra accumulations, fallout and pyroclastic density currents, as well as base surges form the ejecta rings around craters (Carrasco-Núñez et al., 2007; Funiciello et al., 2003; Gençalioğlu-Kuşcu et al., 2007; Németh and Cronin, 2011; Németh et al., 2008; Sottili et al., 2012; Sulpizio et al., 2008; Sulpizio and Dellino, 2008; Vazquez and Ort, 2006; White and Ross, 2011). Commonly, the phreatomagmatic eruptions can produce a range of pyroclastic materials and accidental lithics (Fig 10) with a variety and diversity (e.g. shape, grain size, vesicles and microlite compositions) in the maar systems, so the accidental lithics often come from the collapse of the wall rocks (Auer et al., 2007; Kereszturi and Németh, 2011; Németh, 2010b; Pardo et al., 2009; Raue, 2004).

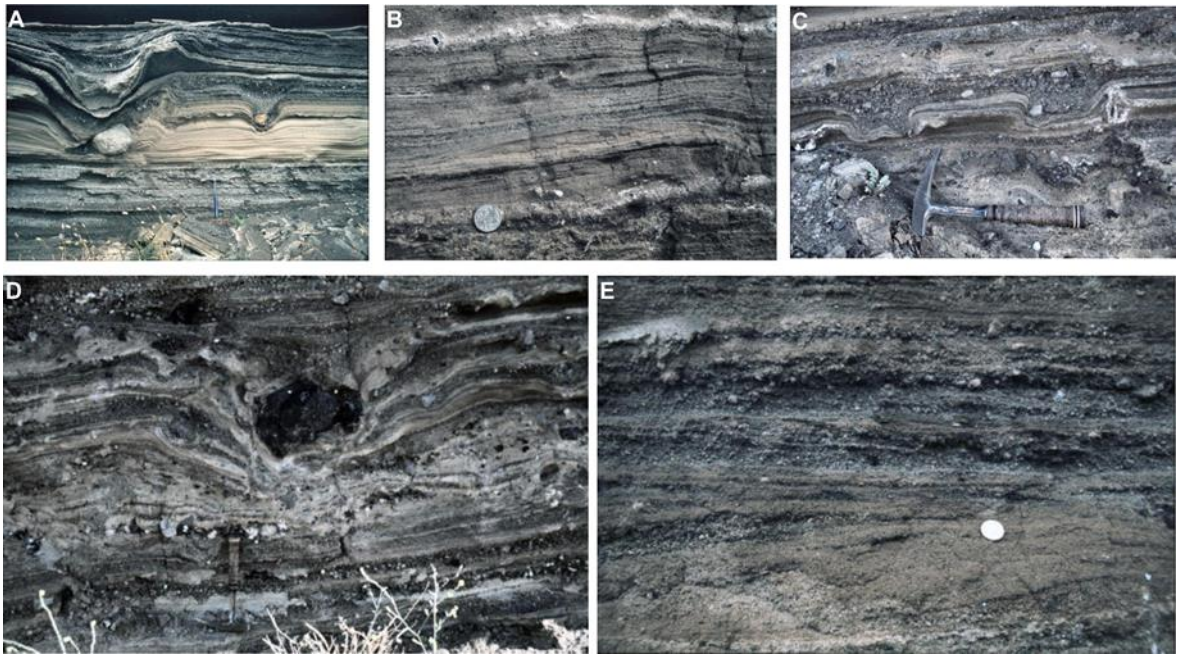

Figure 10: The deposits of pyroclastic density currents at Lake Purdiguluc maar, Western District of Victoria, Australia. A.- ballistic sags (bomb sags); B.- laminated beddings; C.- the decollement fold; D.- bomb in tuff deposits; E.- cross-beddings. As seen in photo E, the dark juvenile lapilli with yellowish brown accidental lithics present a cross-bedding structure. Basically, this series of deposits represent the base surge (sourced from www.members.iinet.net.au).

As Figure 10 depicts, in the phreatomagmatic eruption processes, vent migration and wall-rock collapse can form the coarse-grained breccias, well-bedded lapilli and ash-dominant deposits with different degrees of sorted particles, ballistic bomb sags, as well as angular to sub-rounded accidental lithic blocks (Aranda-Gómez and Luhr, 1996; Chough and Sohn, 1990; Kereszturi et al., 2010; Lorenz, 1974; Lorenz, 2007; Martin and Nemeth, 2005; Németh et al., 2011; Sohn, 1996; White and Schmincke, 1999; Wohletz and Sheridan, 1983). Dune beddings and cross-beddings are in relation to the transportation of the pyroclastic density currents (Alvarado et al., 2011; Auer et al., 2007; Dellino et al., 2004b; Dellino et al., 2004a; Lorenz, 2007; Ngwa et al., 2010; Pardo et al., 2009). Monogenetic volcanoes that undergo a range of phreatomagmatic eruptions must build the columnar joints, as well as the scoria or spatter cones formed by the final stage of the lava effusive eruptions. Either way, these volcano craters will be filled with the post-eruptive products and sediments forming the crater lakes (Aranda-Gómez et al., 1992; Hetényi et al., 2012; Lorenz, 2007; Martí et al., 2011; Németh and White, 2009).

From the aforementioned contents, the low-landform (especially the valleys) are often in association with typical phreatomagmatic volcanism (Lorenz, 1973; Lorenz, 1986b; Lorenz and Büchel, 1980). Identified and recognised phreatomamatism can provide strong evidence for the assessment of the extensive surface and ground-water availability in a territory where the syn-eruptive phases occurr (Németh, 2010a). For instance, geologists concentrate on areas such as the Miocene to Pliocene fields at the western Pannonian Basin (Martin and Németh, 2004) in correlation with the Western Snake River Plain in Idaho (Godchaux et al., 1992; Wood and Clemens, 2004), and with the evaluations of volcanology and

paleogeomorphology. In the fluvial and lacustrine conditions, e.g. Western Snake River Plain (Godchaux and Bonnichsen, 2002; Godchaux et al., 1992), the fields provide a large amount of chances to assess and identify the mechanisms of volcanism under the magma-water interactive patterns, and also for the reconstruction of paleoenvironments, paleohydrology, as well as pre-eruptive landforms (Németh, 2010a).

Geological settings and volcanic conditions in Eastern Inner Mongolia, China

The rim of the Pacific Plate represents the greatest volcanism on the surface of the Earth. On its NW part, the Pacific Plate is in contact with the eastern margin of the Euro-Asian Plate with a subduction zone beneath Japan. Due to this tectonic characteristic, the NE part of China is undergoing the so-called intra-plate or continental volcanism settings.

Basement geology of Inner Mongolia, China

Inner Mongolia is located in the northern part of China. It is a narrow and long strip of land expanding from west to the NE part of North China. The Inner Mongolia region is approximately 2400 km from west to east with 1700 km from north to south. The area of Inner Mongolia is about 1.18 million km^2, which is equal to 12.3% of the total Chinese area.

With the large number of hills, plains, deserts, rivers and lakes, Inner Mongolia is formed by pre-historical geological and tectonic activities with subsequent volcanism. Due to the volcanism and magmatism, Inner Mongolia contains a range of ore belts and has become the most important production area for industrial minerals. Basically, two major structural units can be recognised. Separated by the line of 42°N, one unit is the geosyncline, which is spread from Tianshan Mountain via Inner Mongolia to Xing'an Range in the north of the line of 42°N, and another is the platform of the Huabei region in the south of the line of 42°N. During the Mesozoic to Cenozoic, an N-NE orientated tectonic belt with a distribution of magmatic and volcanic activities has been formed. As mentioned above, this tectonic belt is directly in relation to the ore belts and mineral production.

Geo-tectonic context of Inner Mongolia, China

Inner Mongolia is located in the northern land of China (Fig 11). Actually, there were three major tectonic platforms formed in the Precambrian period in China: North China, Tarim and Yangtze (Chao, 1992; Huang et al., 1980), and definitely Central Inner Mongolia is lain on the North China Platform. The oldest platform of these three is the North China Platform, i.e. up to 3300 to 3800 million years old (Jahn et al., 1987; Liu et al., 1992; Liu et al., 1989). During the Proterozoic and Phanerozoic, the tectonic processes greatly affected the Archean base rocks in the North China Platform (Zhang et al., 1999). Basically, two major geological processes have taken place. One is the Phanerozoic accretion and collision along the north to south of the platform's margin. Another is in relation to the subduction zone, where tectonic magma activities move along the east of the platform's border (Zhang et al., 1999). Notably,

the second process has occurred and replaced the first process during the Jurassic to Cretaceous (Zhang et al., 1999). In Central Inner Mongolia, the northern boundary of the North China Platform is the part of this area where metamorphism, tectonic movements and magma activities are typically active. Because of the tectonic evolutions of Precambrian base-rocks in pre-Triassic and Pacific-Rim tectonism in Mesozoic, the activities are extraordinary in action (Zhang et al., 1999). In terms of the ore and metallogeny, a range of metallic mineralisation, including iron ore deposits, base metals, gold and some rare earth elements (REE), are contributed by the aforementioned magmatism and tectonic activities (Guo, 1992; Li et al., 1990; Miller, 1998; Nie, 1997a; Nie, 1997b; Pei and Nie, 1993; Wang, 1989; Zhang, 1991; Zhang, 1989).

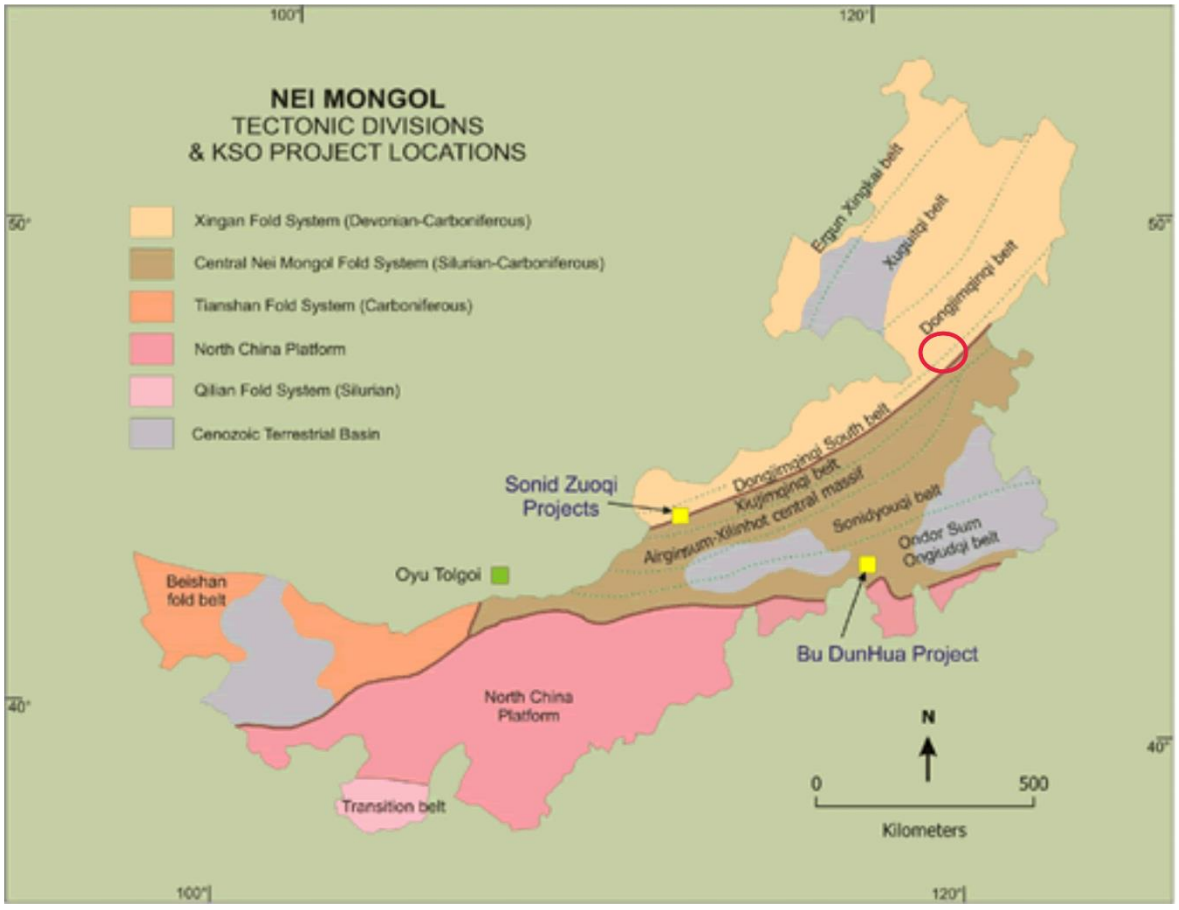

Figure 11: This picture depicts the general tectonic conditions in Inner Mongolia, China. The orange region represents the orogenic belt of Tianshan Mountain, which lies in the western part of Inner Mongolia, the red circle is the essential part of this thesis, which is the eastern part of Inner Mongolia in NE China. The ACVF is located in this area (sourced from www.kingsolomonmines.com/Projects/Exploration_Strategy.aspx).

In the eastern part of Inner Mongolia, especially during the late Cenozoic, the tectonic evolution due to the collision between the Euro-Asian Plate and the Western Pacific Plate, as well as magmatism and basaltic volcanism, have played an important role in this area. This thesis will concentrate on the eastern part of Inner Mongolia.

The Central Asian Orogenic Belt is one of the world's famous tectonic belts, which has built the great extended orogen and ranges from the Ural to the Pacific along with latitude, and

from the Eastern European cratons via North China to the Tarim craton with longitude (Fig 12) (Şengör et al., 1993; Windley et al., 2007). Obviously, Inner Mongolia is lain on this tremendous orogenic belt, especially the central-eastern portion of the Central Asian Orogenic Belt (Zhang et al., 2011a; Zhang et al., 2011b).

Figure 12: The Central Asian Orogenic Belt – the Tianshan Range in the west and the Great Xing'an Range in the east belong to this great orogenic belt. The green line marks the Solonker Suture. The northern pink area is the northern early- to mid-Palaeozoic Orogen, the southern brown area represents the Ondor sum subduction-accretion complex. The eastern margin of this belt probably represents the contact zone between the Euro-Asian Plate and Pacific Plate overlying the East Asian Subduction Zone (sourced from (Kroner and Rojas-Agramonte, 2014; Zhang et al., 2011a).

The Solonker Suture marks the northern margin of the Tarim Craton, which is directly located in Inner Mongolia. This is the most spectacular suture in the world for it eventually closed in the period of the vanishing of the Paleo-Asian Ocean and divided into two continental blocks (Jian et al., 2010). One block is composed of the Hutag Uul Block in the south of Mongolia from the north (Badarch et al., 2002), and another is contained by the Uliastai Block,

Hegenshan accretionary complex and Northern Orogen in the north of China from the south (Jian et al., 2008).

In the north of the Solonker Suture, Southern Mongolia was formed by an islan -arc, a backarc to forearc basin, as well as platform accretion (Badarch et al., 2002). These tectonic evolutions and terranes have been documented as the processes of the northern boundary of the Palaeo-Asian Ocean in Palaeozoic, and they have also been recognised as overlying on the north-trend dipped subduction zone (Windley et al., 2007). These ranges of tectonic activities are the result of the magmatic activities with multiple phases during the Silurian to Late Carboniferous (Blight et al., 2010; Helo et al., 2006; Lamb and Badarch, 2001; Yarmolyuk et al., 2008). The subsequent intrusion of peralkaline granites has occurred during the Late Carboniferous to Early Permian (Blight et al., 2010; Kovalenko et al., 2006; Yarmolyuk et al., 2008). The Uliastai Platform is majorly composed of gneiss, schist and quartzite formed in the Proterozoic, and limestone and siltstone generated in the Cambrian (Xiao et al., 2003; Xiao et al., 2009). A spectrum of metamorphic complex, a supra-subduction zone-type ophiolitic succession, as well as a group of overlying conglomerates formed in the Late Devonian, have dominated the Northern Orogen in North China during the early to middle Palaeozoic (Chen et al., 2009; Jian et al., 2008; Zhang et al., 2009). A variety of foliated calc-alkaline plutons and supra-subduction zone-type ophiolitic rocks formed the Hegenshan ophiolitic accretion complex in the Carboniferous (Bao et al., 2007; Chen et al., 2000; Liu et al., 2009; Miao et al., 2008; Miao et al., 2007). Then, the above-mentioned successions have been intruded by alkaline rocks and granites during the Early Permian (Shi et al., 2004; Wu et al., 2002).

In the northern boundary of the North China Platform, a range of magmatism has occurred during the late Palaeozoic (Zhang and Zhai, 2010), for instance, mafic and alkaline intrusions in the Middle Devonian (Zhang et al., 2009a; Zhang et al., 2009b; Zhang et al., 2010), calc-alkaline pluton intrusion in the Carboniferous (Zhang et al., 2009a; Zhang et al., 2009b), the intrusion of high-K calc-alkaline rocks in the Early Permian (Zhang and Zhai, 2010), and high-K alkaline to alkaline intrusive rocks from the Late Permian to Early Triassic (Zhang et al., 2009a; Zhang et al., 2009b; Zhang et al., 2010). Specifically, during the Permian, the volcanic and sedimentary successions present lavas, tuffs and a series of volcanic pyroclastic rocks of approximately 200 to 1200 m in thickness (Zhang et al., 2011a; Zhang et al., 2011b).

Eastern Inner Mongolia is typically represented by tectonic, magmatic and volcanic activities during Cenozoic. However, this area has undergone multiple tectonics and volcanism during these early periods. The tectonic extension processes have taken place throughout East China and its adjoining regions. The first rifting phase involved in the NE of Asia from Lake Baikal to Sikhot-Alin in the east to west orientation is also from the Mongol-Okhotsk Belt to North China in the NS orientation. This phase took place approximately in the Late Jurassic to Early Cretaceous (Ren et al., 2002). During this rifting process, intra-continental rifts, volcanism, as well as extensional activities involved in large strike-slip faults, are the major phenomena (Ren et al., 2002).

Due to the tectonic activities and ages in relation to the rifting processes, the east of the Euro-Asian plate has undergone a range of tectonic varieties and shifts during the Late Jurassic (Ren et al., 2002). Especially, in the Late Mesozoic rift processes were represented by a series of tectonic basins in terms of basin and range types (Li et al., 1995; Li et al., 1988; Ren et al., 1997). With equally-spaced ranges and medium-sized basins, the NE Asian fault system contains approximately 300 NE-NNE trended grabens within a more than 2 million km^2 area. Subsequently, newly-formed basins covered the Late Mesozoic tectonic basins during the Cenozoic (Ren et al., 2002). In the west of Great Xing'an Mountain, grabens, half-grabens and a fault complex are the major characteristics of this area. In the east of Great Xing'an Mountain, the Songliao Graben containing petroleum and coal is deposited by the thick post-rifting sediments. The widely-distributed rifting features in the NE Asian fault system has similarities to the west of America (Buck, 1991). More than about 100 km of the lithospheric extension with a horizontal trend is beneath NE China, and this probably suggests that extensive stretching and rifting in the lithosphere occurred during the Late Mesozoic (Lin et al., 1997; Ren et al., 1997).

During the Late Mesozoic to Cenozoic, the tectonic activities predominantly present a large amount of volcanism in Eastern Inner Mongolia, i.e. NE China. As mentioned, the geology of NE China is mainly identified by the NE-ENE trend tectonic structures, and varieties of volcanic rocks were distributed during the Cenozoic (Wang et al., 1999). These volcanic rocks contain a spectrum of high-K alkaline basalts (e.g. Wudalianchi), potassium or sodium alkaline basalts to alkaline rhyolites (e.g. Changbaishan Mountain/Caldera), as well as other types of basalts, which are distributed around NE orientation faults in Xialiaohe and Eastern Inner Mongolia (Wang et al., 1999).

The preliminary tectonic settings with NE orientation were formed by the shifting and alteration of tectonic activities in East China during the Middle Jurassic and Late Mesozoic. In the meantime, Songliao Basin, Great Xing'an Mountain, as well as a fault complex in a NE orientation, were generated in NE China (Wang, 1996; Wang, 1998). From the Late Jurassic to Early Cretaceous, a typical event of thermal magmatism contributed to the forming of andesitic volcanism and a massive intrusion of granite. The backarc basin, arc volcanic rocks, as well as faulting and subsidence associated with subduction, may be the main reasons for volcanism during the Late Mesozoic (Wang et al., 1999). From the observations of volcanism with NE orientation, petrology and geochemistry, the volcanic rocks formed in the Late Mesozoic present a feature of assimilation with mantle sources and crust, thus thermal-magmatic processes and remelting of crustal materials must have taken place. Also, the assimilation represents that volcanism had undergone a series of compression and strike-slipping in the Late Mesozoic (Wang et al., 1999).

During the Cenozoic, the tectonic settings were based on the Late Mesozoic settings but with inversed tectonic features (Wang, 1998). These inversed characteristics were represented as widely-distributed normal faults, strike-slipping faults and correlated to basaltic volcanism in Cenozoic (Wang et al., 1999). For another reason, a range of remote stress due to the collision

between the SW China Plates, as well as the tectonic activities at the east margin of the Euro-Asian Plate, may affect the volcanism in NE China during the Cenozoic (Wang et al., 1999). Except for a few of the volcanisms in NE China, the majority of is concentrated from the Great Xing'an Mountain to the west of the Taihang Range, and is distributed as a large plain in the Mid-Cenozoic. In the Late Cenozoic, the volcanism extended to Changbaishan Mountain, Longgang, Jingbohu Lake, Wudalianchi and Great Xing'an Mountain (i.e. ACVF) (Wang et al., 1999). The volcanic activity feature was represented along with a NWW orientation with a NE orientation in some regions (Wang et al., 1999).

Intra-plate volcanism in Inner Mongolia and its adjacent areas in NE China

This part contains the discussion of the intra-plate volcanism which is spreading worldwide, e.g. the East African Rift. The volcanism in NE China, especially the ACVF, was formed by this type of volcanism. With the definition of intra-plate volcanism, each volcanic field in NE China will be briefly mentioned in this section, as well as the distribution of each volcanic field in this area. The world famous Wudalianchi Volcanic Field will have detailed information about it compared to the other parts.

1) The definition of intra-plate volcanism

Intra-plate volcanism is responsible for 5% of volcanoes around the world. Meanwhile, these volcanoes are not involved in plate boundaries. The intra-plate volcanic activities are believed to be in relation to the consistent mantle plumes which are formed by the convention of deep mantle materials with high viscosity (Decker and Decker, 1999). When the hot and solid materials ascend from the deep mantle source, partial melting will occur during their ascent due to the temperature dropping of the pressure-dependent melting point (Decker and Decker, 1999). With the mantle plumes reaching the lithospheric plate, a range of volcanic islands will form. As the plate is moving, the older volcanoes away from the mantle plume will vanish, and newly-formed volcanoes will occur directly following the former volcanoes, thus a volcanic chain emerges, i.e. Hawaii (Fig 13).

Figure 13: The schematic graph of intra-plate volcanism, the conventions forming mantle plumes are from the bottom of the mantle through the entire mantle to the lithospheric plate, eventually become the fuel of volcanic chain. On the right side of this picture, the subduction results in a relative thickening of the overlying plate, thus the under-plating or delamination will lead to subduction-related volcanism (sourced from www.britannica.com/science/volcano/Rift-volcanoes).

Small-scale monogenetic volcanoes formed by intra-plate volcanism are not produced by mantle plumes but by the fractures or faults within the continental plate. As Fig 13 depicts on the right side of the diagram, the small amount of magma batches erupted through the fractures or faults to the surface. The magma batches may generate from the so-called low-velocity layer which is named by the seismic wave transporting lower than in the solidified plate. The physical property of this layer presents hot and plastically deforming. Any magma batches that form from this layer may ascend with their own buoyancy and be facilitated by the plate fissures, fractures or faults (Decker and Decker, 1999).

2) Intra-plate volcanism in Inner Mongolia

The intra-plate volcanism emerges in Eastern Inner Mongolia which contains Wulanchabu, Xilingele and Great Xing'an Mountain (Fig 14). The volcanic belt formed in the Quaternary is expanding thousands of kilometres from the north of Great Xing'an Mountain, i.e. Nuomin River to Wulanhada and with a NE orientation (Bai et al., 2012). This volcanic belt is composed of the Nuomin Volcanic Field, the ACVF, the Xilinhaote-Abaga Volcanic Field and the Wulanhada Volcanic Field, and also it is close to the Datong-Great Xing'an Mountain Volcanic Belt formed in the Cenozoic (Huang et al., 1993). In Eastern Inner Mongolia, extensive volcanism with frequent volcanic eruptions have taken place during the Quaternary, however the apex of volcanism occurred in the Late Pleistocene. The preservation of the volcanoes formed after the Late Pleistocene is well identified with low erosion and degradation, relatively intact structures and precisely geomorphological features, i.e. volcanic cones and craters. A range of studies performed by many geoscientists during the 1980s has been carried out at high levels (Bai et al., 2005; Bai et al., 2008; Liu, 1987; Liu, 1999; LIU, 2000; Luo and Chen, 1990; Yang, 1988; Zhang et al., 2006).

Figure 14: This map depicts the distribution of Cenozoic volcanic rocks. The purple circle marks the Songliao Braben. The light-blue dot is the Longgang Volcanic Field; the red dot indicates the Changbai-Tianchi Caldera; the green dot marks the ACVF; the yellow dot implies the Nuomin Volcanic Field, and the orange dot represents the Wudalianchi Volcanic Field. Black solid lines are the trends of the local fault systems. The volcanism is precisely constrained by the fault trends which disperse between both sides of the Songliao Graben (Liu et al., 2001).

In the early period of the Late Pleistocene, the major eruption style of the volcanism in Eastern Inner Mongolia presented as the phreatomagmatic eruption style, which formed maar-diatreme volcanoes, with subsequent Strombolian to fissure eruption types (Cas and Wright, 1987). The morphology of maar volcanoes is relatively intact, and the maar craters can be clearly observed, although they have undergone a series of degradation and erosional processes (Bai et al., 2012). The relatively low height of Strombolian-style volcanoes with gullies on their flank depict fragmentary crater shapes, which represent older eruptive ages than maar volcanoes. The fluvial gravel beddings formed in the Mid-Pleistocene are overlain by the base surge deposits, which are covered by a group of basalts formed in the late stage of the Late Pleistocene (Bai et al., 2012).

In the late period of the Late Pleistocene, the alkaline basaltic explosive eruptions and lava effusive eruptions dominated the volcanism, which formed a large amount of central, fissure-central and fissure types volcanoes. The landform of these volcanoes is clear with relative height and intact crater formation, and some of the craters are filled with water to be the

crater lakes (i.e. Tianchi) (Bai et al., 2012). The structures of gullies are relatively shallow in relation to the low degree of degradation. The lava flows become as platforms or sediments deposited on the fluvial terraces, for instance, in the Nuomin and Arxan-Chaihe areas the basalts overlie on the gravel beddings formed in the early stage of the Late Pleistocene (Bai et al., 2012).

During the Holocene, the volcanism was relatively lower than it occurred in the Late Pleistocene, however each volcanic field in Eastern Inner Mongolia produced new volcanoes. The newly-formed volcanoes in Holocene include:

- Maanshan of Nuomin in the north of Great Xing'an Mountain (CGS, 2004)
- Yanshan, Gaoshan, Xiaodonggou and Zigongshan in the ACVF (Bai et al., 2012)
- Liandanlu in Wulanhada (CGS, 2004).

Accompanied by Hawaiian and sub-Plinian eruptive styles, the Holocene newly-formed volcanoes were dominated by the Strombolian eruption type (Bai et al., 2012; Liu, 1987; Liu, 1989). Most of the volcanoes formed in the Holocene have undergone a high magnitude of eruptions, although the number of them is still less than in the Late Pleistocene. For example, Yanshan, Maanshan and Gezishan are composed of volcanic cones, pyroclastic rocks, as well as lava flows (Bai et al., 2012). The formations of volcanic cones are mostly formed by multiple phases of ballistic falls and spatter deposits. The widely-distributed pyroclastic materials represent the relatively high eruptive plume forced by the high buoyancy over the vents, also such pyroclastic deposits are suggestive that these volcanoes experienced sub-Plinian-type eruptions with relatively high energy (Bai et al., 2012; Liu, 1989). The outcrops of these Holocene-formed volcanoes are intact due to less of the post-eruptive degradation and erosional processes (e.g. cones, craters and intra-crater domes) (Bai et al., 2012; Liu, 1989). The surface formations of lava flow, such as tumulus without erosional features, represent these lava flows formed during the near pre-historical time. In addition, the trends of the lava flows are constrained by geomorphological characteristics in the adjacent areas, such as valleys and gullies (Bai et al., 2012). Also, these lava flows are underlain by a range of gravels and wind-blowing sand deposits during the Holocene (Bai et al., 2005; Bai et al., 2008).

3) The distribution of volcanoes in Inner Mongolia

Three major volcanic fields have represented the volcanism in the Late-Pleistocene to Holocene. Basically, the distribution of volcanism in Inner Mongolia presents a NE-orientation trend during the Late Quaternary (Fig 14). According to incomplete statistics, there are approximately 300 volcanoes which disperse in Nuomin, Arxan-Chaihe, Xilinhaote-Abaga, as well as the Wulanhada regions (Bai et al., 2012; Németh et al., 2017). The volcanic rocks are composed of alkaline-basaltic pyroclastic rocks and lava flows. The eruptive styles are commonly central or central-fissure types. The types of volcano include maar-diatreme volcanoes, Hawaiian-type volcanoes, Strombolian-style volcanoes, sub-Plinian-style volcanoes and Icelandic eruption-style volcanoes (Williams and McBirney, 1979). Most of the volcanoes in Inner Mongolia belong to Strombolian-type volcanoes and are formed as

monogenetic volcanoes (Wei et al., 1999). In addition, the characteristics of the volcanic activities present as phreatomagmatic eruptions and subsequent lava effusive eruptions during the early stages of the Late Pleistocene and the late stage of the Late Pleistocene to the Holocene respectively (Bai et al., 2012). This section will discuss the Nuomin Volcanic Field, the ACVF and the Wulanhada Volcanic Field.

The Nuomin Volcanic Field is located in the northern Quaternary volcanism belt of Eastern Inner Mongolia, which belongs to the eastern flank of the Nothern Great Xing'an Mountain. The distance between the Nuomin Volcanic Field and Wudalianchi is approximately 160 km. The area of this volcanic field is about 7500 km^2, with only 820 km^2 of volcano-distributive area. The thickness of the lava flow that is composed of basanites and alkali-peridotitic basalts is 15 to 30 m. Approximately 30 volcanoes are dispersed in the upstream areas and branches of the Nuomin River (Li et al., 2003).

Figure 15: Mt. Sifang, the highest crater lake at Great Xing'an Mountain and located in the Nuomin Volcanic Field, has an altitude of about 933.4 m. The cone is composed of loose scoria, spatter deposits and agglutinated or welded scoria. The crater diameter is approximately 500 m with 70 m in depth (sourced from www.chinascenic.com/magazine/water-born-of-fire-discovering-chinas-volcanic-lakes-407.html (Bai et al., 2012; Nemeth et al., 2003).

The ACVF is located in the SW Nuomin Volcanic Field which belongs to the southern part of Great Xing'an Mountain (Liu, 1999). About 46 volcanoes were distributed around the Halahahe, Chaoer River, Chaihe and Ledehe regions during the Late Quaternary. In the early stage of the Late Pleistocene, the major volcanism is represented as phreatomagmatic eruptions, which formed typical base surge deposits and maar-diatreme volcanoes. These features can be found in Wusulangzi Lake, the Tongxin Crater and the Eastern Chaoer River (Bai et al., 2012; Zhao et al., 2008).

Figure 16: The Tongxin Crater, which is the primary concentration and topic of this thesis. The crater was formed by a range of phreatomagmatic eruptions accompanied by a small magnitude of lava-fountain eruptions during the Late Pleistocene to Early Holocene. It is located on the NE side of the ACVF (captured by Karoly, Nemeth in 2016).

In the late period of the Late Pleistocene, the majority of the volcanism presented lava-fountaining or effusive eruption styles which include Strombolian-, Hawaiian-, and Icelandic-eruption types. Note the Strombolian-type eruptions are the most developed. The volcanic rocks are composed of alkali-basaltic clasts and lava flows (Zhao et al., 2008). Most of the craters were filled with water as crater lakes (Tianchi), such as Tuofengling, Shuanghoushan and Jierguoshan (Bai et al., 2012; Bai et al., 2008). Hawaiian-type eruptions are represented by the Chaoer River area which underwent a range of fissure effusive eruptions and was composed of large amounts of lava flows. During the Holocene, the eruption styles are basically the Strombolian-type, with the small scale of the sub-Plinian-type, such as Zigongshan, Yanshan and Xiaodonggou. These volcanoes align with the NE orientation.

The Wulanhada Volcanic Field overlies the plutonic and metamorphic base-rocks formed during the Archean to Neo–Proterozoic, and latter Neogene basalts with intrusive rocks. The total area is about 280 km^2 with various types and scales of 30 volcanoes (Bai et al., 2008). The major eruption styles are dominated by fissure and fissure-central eruptions during the Late Pleistocene. A range of spatter cones, cordas, as well as possible dyke conduits, distribute along a basement rift which is approximately 12 km in a NE orientation. The types of lava flows that overlie the gravel sediments, wind-blowing sand deposits and talus are basically pahoehoe and aa lava flows, as well as tumulus with well-developed fissure structures that are 30 to 80 m in diameter (Bai et al., 2012; Liu, 1999; LIU, 2000).

Figure 17: The bird's-eye view of the Wulanhada Volcanic Field – this picture depicts a range of Cupola volcanoes in this area from the north to south. The names of these volcanoes are in turn North Cupola (red circle), Middle Cupola (purple circle) and South Cupola (quarried and not shown in this picture). These Holocene-formed volcanoes are basically the scoria or cinder cones which were built by the fissure eruptions and lava fountains (sourced from www.chinascenic.com/magazine/inner-mongolia--a-land-of-volcanoes-344).

4) *Introductions of the Wudalianchi Volcanic Field*

In contrast to the adjacent volcanic areas in NE China, the Wudalianchi (Five Connected Pools) Volcanic Field is one of the spectacular volcanic fields in the world (Fig 18). Overall, the Wudalianchi volcanoes were formed during the Holocene about 10000 years ago, and are is located in the NE of China (Fig 14). There are approximately 14 volcanoes identified along the fault complex in a NE to NNE orientation (Gao et al., 2013). Two volcanoes, Laoheoshan and Houshaoshan, erupted during 1719 to 1721 with well-preserved volcanic forms and geomorphology (Li and Guo, 1986; Wang and Guo, 1982; Wang, 1979). Specifically, the Wudalianchi Volcanic Field with the nearby volcanic fields in NE China is set in relation to the intra-continental volcanism which is discussed above, with the distance about 1800 km from the subduction zone collided between the Euro-Asian Plate and the Pacific Plate (Zhao, 2009).

Figure 18: The Wudalianchi Volcanic Field – his map depicts the general distribution of volcanoes in Wudalianchi. Note there are five lakes, which are formed by the Shilong River once dammed by the lava flows. These five connected lakes became the name of Wudalianchi, which are depicted as five colourful stars. The alignments of volcanoes (pink dash lines) mark the trend of the faulting systems, which are the same in a NE orientation (sourced from (Gao et al., 2013; Zhao et al., 2014b).

There are three major fault systems controlling the Wudalianchi area: NE, NW and EW orientated faults. Typically, the NE and NW orientated fault systems predominantly constrain the major tectonic features. Thus, the Wudalianchi is aligned with the NW orientated fault zone, and it also closely associates with the two nearby volcanic fields which are the Erkeshan and Keluo in the SW and NW respectively (Gong, 1997; Shao and Zhang, 2008; Wei et al., 2003).

The Wudalianchi Volcanic Field is in the north of the above-mentioned Songliao Graben which is a continental rifting basin. Generally, the Wudalianchi is fueled by the westward Pacific subduction plate overlain by the Euro-Asian Plate (Zhao, 2009). The volcanic centres are probably shifting in relation to the thinning and rifting of the crust, which leads to the asthenosphere upwelling, and these volcanic centres are also along NE and NW orientations, which are parallel with both sides of the Songliao Graben (Fig 14) (Gao et al., 2013). Large amounts of lava flows were produced due to the mild Strombolian-type eruptions, and large areas of monogenetic volcanic fields were formed by a range of small-scale frequent eruptions, which generated basaltic to intermediate magma flows. It is common worldwide (White, 1991a; White, 1991b). There are 25 volcanoes recognised in this field, and 14 of them have generated lava flows which were covered by the subsequent pyroclastic materials. Another 11 volcanoes formed small-scale volcanic shields and are rarely involved in pyroclastic cones (Gao et al., 2013). The entire number of volcanoes in Wudalianchi are classified as monogenetic volcanoes through the small-scale lava flows and the structures of lava fields (Francis, 1993; Thouret, 1999), such as pahoehoe-type lava flows, ellipsoidal lava flows, blocky lava, aa-type lava, hornitos and lava tube caves (Gao et al., 2013). In addition,

based on the observations in Wudalianchi, a series of central and fissure eruptions have taken place during the Holocene (Ollier, 1988).

Figure 19: The Nangelaquishan cinder cone in the Wudalianchi Volcanic Field was formed during the Pleistocene. Its crater is approximately 500 m in width. There are four cinder cones which were formed during the Holocene and they are aligned with one faulting system in a NE orientation (sourced from https://volcano.si.edu/volcano.cfm?vn=305030; (Feng et al., 1979).

5) *Longgang Volcanic Field*

The Longgang Volcanic Field is located in NE China (Fig 14). In some recent studies the newly-formed volcano – Jinlongdingzi in the Longgang Volcanic Field – is identified due to the second largest volcanism during the past 2000 years (Liu, 1999; Ou and Fu, 1984; Wei et al., 2003). The Longgang Range is a NW branch of the Changbai Range and the monogenetic volcanism is well developed in this area (Wei et al., 1999). According to incomplete statistics, there are more than 160 craters which distribute in an area of about 1700 km^2 (Liu, 1999; Ou and Fu, 1984; Sui et al., 1999; Xie et al., 1993). These volcanoes were formed in the Quaternary. A range of scoria cones, pyroclastic rocks, lava flows and maar-diatreme volcanoes constitute the major features of the volcanic structures. Among these volcanoes, the Jinlongdingzi volcano is the newest and highest volcano on this site (Liu and Xiang, 1997; Wei et al., 1999). As in the Wudalianchi site, the regional tectonic settings and volcanism were shaped by the westward subduction zone between the Pacific Plate and Euro-Asian Plate (Liu, 1999). Most volcanoes in the Longgang Volcanic Field are scoria/cinder cones and less of them are maar-diatreme volcanoes. There are eight maar lakes in the western Longgang Volcanic Field, such as Sihailongwan and Xiaolongwan. These two crater lakes preserving well-developed laminae (Chu et al., 2008; Mingram et al., 2004). The Sihailongwan Lake is located about 20 km in SW Jinlongdingzi volcano. The area of the crater lake is about 0.39 km^2 with 50 m in depth and

the altitude is about 791 m above the sea level (Fig 20). The Xiaolongwan Lake lies in the SW Jinlongdingzi volcano. The crater area is about 0.079 km^2 with a depth of 15 m. Its altitude is approximately 655 m above sea level (Liu et al., 2009).

Figure 20: The Sihailongwan Lake is a maar lake that is located in the Longgang Volcanic Field, NE China. Note the laminated beddings around this maar lake represent the monsoon abilities with a minor artificial disturbance in the past 900 years (sourced from www.gfz-potsdam.de/en/section/climate-dynamics-and-landscape-evolution/projects/completed-projects/east-asian-monsoon-system/sihailongwan (Mingram et al., 2004)).

Basaltic lava flows are widely distributed in the Longgang Volcanic Field. The major types of lava flows are commonly the pahoehoe and aa types. The pahoehoe lava flow in the Longgang Volcanic Field can disperse tens of kilometres away from the vent, however the aa type lava flows can only distribute about in few kilometres near the vent. In the proximal pahoehoe and aa lava flows, the mantle xenoliths are well developed (Wei et al., 1999). The amounts of xenoliths present decrease the trend though away from the vent site. The Songhuajiang Basalt is the typical lava flow in the Longgang Volcanic Field. The flow was formed from the Laoling Shield volcano. Two fault systems constrain this lava flow, which flowed about 60 km toward the NW through the paleo-valley of Songhua River (Wei et al., 1999). One fault is from Hongshi via Laoling to the Tianchi in Changbai Mountain in a NW orientation. Another is from Longgang to Laoling with a NNE orientation. The Songhuajiang lava flow is approximately 5 to 10 km in width. This lava flow was formed about 2.59 to 3.99 Ma during the Late Pliocene (Wei et al., 1998a).

The Jinlongdingzi volcano (Gold Dragon Peak) is the most newly-formed volcano and is still active (Liu et al., 1998; Liu and Xiang, 1997; Wei et al., 1998a; Wei et al., 1998b). This volcano is located in the NW of the Longgang Volcanic Belt in a NE orientation. Typically, the Jinlongdingzi volcano has undergone a range of Strombolian-type eruptions due to the observations of proximal lava flows with surface distortions and striped ballistic bombs. The adjacent volcanoes such as Dalongwan (Big Dragon Bay) and Sanjiaolongwan (Triangular Dragon Bay) present as maar-diatreme volcanoes formed by the phreatomagmatic eruptions.

Figure 21: The Jinlongdingzi Lake – this crater lake is a cinder cone which has experienced a series of eruptions in the past 15000 years. The eruption type is supposed to be the sub-Plinian type, thus it has the potential to harm the adjacent areas (sourced from http://wikimapia.org/8548335/Longgang-Volcano-1000-m; (Williams, 1983); (Bell and House, 2007)).

The Jinlongdianzi volcano presents as a horseshoe-shaped crater which constitutes basaltic scoria and ballistic bombs (Fig 21). At the SW of its foot, a range of lava flows can be identified (Liu et al., 2009). This volcano is composed of the cone, lava flows and pyroclastic rocks. The diameter of its bottom, which covers approximately 33 km^2 in area, is about 650 m, the diameter of the crater lake is about 50 m, and the cone height and crater depth are both 220 m. The altitude of the Jinlongdingzi volcano is about 999 m above sea level (Liu et al., 2009; Wei et al., 1999). The NE part of the cone is intact, however the SW part of the cone is destroyed by the later lava flows. The different colours between the lower cone and upper cone are due to the different velocity of depositions in eruptions. When the deposition velocity is fast, the ejecta can keep the high-temperature conditions which are efficient for oxidation, thus the basaltic scoria presents as a red colour and with elastic properties. On the contrary, if the velocity is low, the scoria will be immediately quenched, thus the black, brittle scoria will be formed. Besides, the agglutination and welding of scoria can resist the post-eruptive degradation and erosional processes. Large fan-shaped pyroclastic deposits represent the prevailing NE wind along with a NE orientation.

Introduction to the ACVF

The ACVF is located in the southern part of the Great Xing'an Mountain, and it is close to the boundary of China and Mongolia within a NE to SW orientation (Fig 22). In Mongolia, the word Arxan (some articles note it as Arshaan or Aershan) means "holy hot water". This is in terms

of large amounts of geothermal water in this region, which is the basis and the very foundation of the local cultures. This thesis will use the "Arxan" to distinguish it from other articles in terms of eliminating misunderstanding and confusion. In respect of the regional geography, the ACVF is located in part of the SW of the Great Xing'an Mountain (Range) (Németh et al., 2017). The climate of this site is sub-arctic (Koppen Dwc). Due to the continental-type conditions, this area experiences extreme cold in winter but is normally warm in summer. The average temperature is below 0°C in over six months of the year, and typically the lowest temperature is about -25.1°C in January, but rises to 16.8°C in July (Németh et al., 2017). The monsoon season ranges from June to September with approximately 450 mm of precipitation per year. Note that some of the Arxan-Chaihe areas have performed limited evaluations, and some places have unknown names (Liu et al., 2001; Sun et al., 2016; Wang et al., 2014; Zhao et al., 2008), and this research is only one of the preliminary studies.

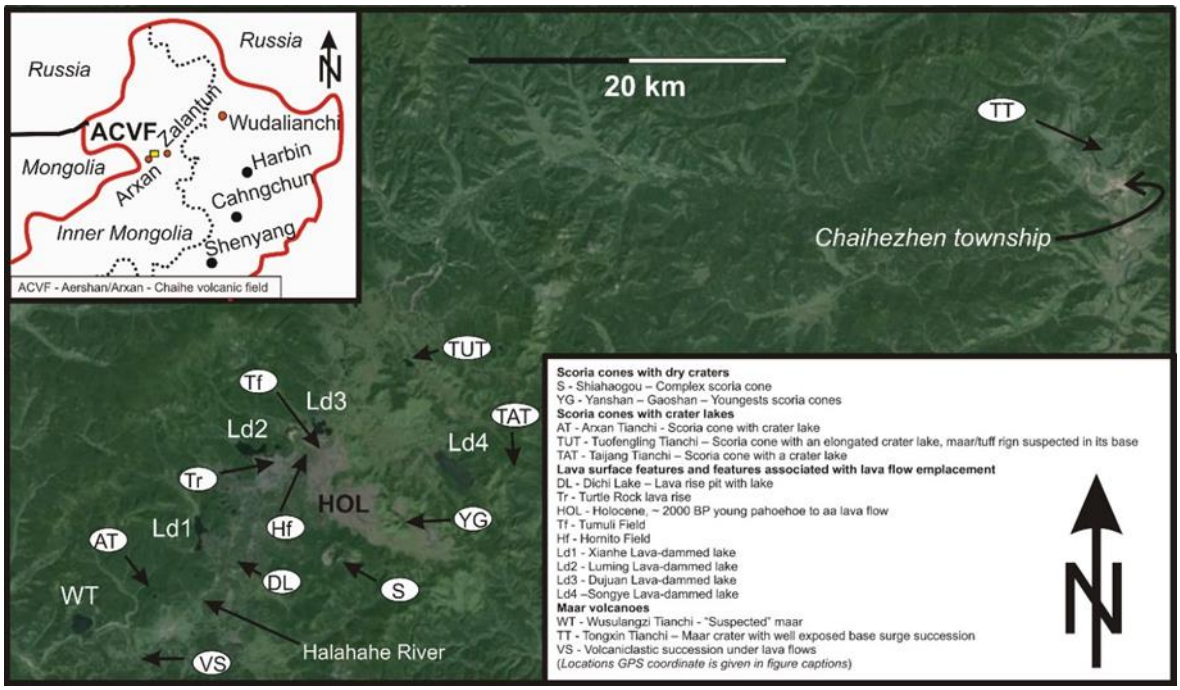

Figure 22: The satellite view of the ACVF. The inlet map in the top-left corner marks the location of this site in NE China. Several crater lakes are labelled on this map, however note the Wusulangzi Lake is under suspicion (sourced from (Németh et al., 2017); GoogleEarth; GoogleMaps).

In general, the country rocks of the ACVF are composed of erosional Mesozoic crystalline and metamorphic rocks with an altitude of 1500 m. As mentioned above, due to the particular monsoon season each year, the vegetation in this site is well developed and covers most areas of the elevated territories (Németh et al., 2017). Because the ACVF belongs to the Tianshan-Xing'an Fold Belt, the volcanism is generally following the trend of the fault orientation. Thus, it is suggested that the ACVF is fueled by the regional tectonic control in association with the Mesozoic rift system, which is discussed above. Based on previous studies, the major volcanism that occurred in the ACVF acted in the Pliocene to the recent period, and some volcanoes probably erupted during the Early Holocene, such as the Yan and Gaoshan scoria

cones (Bai et al., 2005; Bai et al., 2012). Sampling from the bank of the Halahahe River, the eruption ages of Yanshan and Gaoshan are approximately 1990 ± 100a B.P. and 1990 ± 70a B.P. in C^{14} dating from the charcoaled wood and scoria deposits, which cover about 72 km^2 in area (Németh et al., 2017). The major volcanic landforms and topography are composed of scoria cones, lava spatter cones, maar-diatreme volcanoes and crater lakes (Németh et al., 2017). The longest lava flow is about 5 km with 10 m in thickness, and the major type of lava is pahoehoe type with the inflation and deflation surface structures, such as lava rise pits, tumuli, hummocky whaleback (i.e. turtle skin) and hornitos (Németh et al., 2017). In these volcanic landforms, the presence of large-scale maar volcanoes is significant and marks the evidence of magma-water explosive eruptions (i.e. phreatomagmatic eruptions). Pyroclastic materials rich base surge deposits are composed of large amounts of mantle-derived liths. In addition, the ACVF contains a range of eruptive features formed by the fluvial and lacustrine environments, which are surrounded by crystalline and metamorphic basement rocks (Németh et al., 2017).

The major volcanic field covers approximately more than 2000 km^2 in area with about 27 volcanoes lying at the ACVF (Wang et al., 2014). The main type of these volcanoes is monogenetic volcanoes with scoria cones and lava spatter cones. Most of them are highly vegetated, however some volcanoes preserve well-developed outcrops and internal structures which can be precisely observed (Németh et al., 2017).

The lava flow structures are also well developed in the ACVF with respect to the most spectacular pahoehoe lava flows. The lava flows have undergone a range of inflation, which formed the whaleback-type lava shape with subsequent deflation that generated the lava rise pits filled with water. Following the path of the lava flows, the shifting and alteration of the surface of the lava flows can be identified, e.g. smooth-surfaced pahoehoe lava changing into the rubble pahoehoe lava derived from the outbursting of the lava pond (Guilbaud et al., 2007; Murcia et al., 2014). In addition, the ACVF preserved a range of lava tube caves which may indicate the emplacement mechanism during the lava effusive eruption phases (Németh et al., 2017). Many representative structures of lava can be seen in this site, such as hummocky lava surface, lava rise pits, lava tumulus, as well as lava hornitos (Németh et al., 2017). The following section will discuss the detail of the landforms of the ACVF in relation to its vent distributions and erupted volumes from previous studies.

Volcanic landforms of ACVF

As mentioned above, the ACVF has about 27 volcanoes in an area of 2000 km^2 within a NE orientation trend (Wang and Tian, 2013), and this means the distribution of the volcanism is constrained by the major tectonic faulting system. The volcano types are composed of maar-diatreme volcanoes, the Hawaiian-type, the Strombolian-type, the Pinian-type, and Icelandic-type, and specifically the most common type is the Strombolian (White, 1991a; White, 1991b). Ash, lapilli and lava bombs are the main characteristics of the Strombolian-type

eruptions (Chouet et al., 1974; McGreger and Lees, 2004). Many landforms in the ACVF are identified by their derivation, origins and geomorphological features (Table 1) (Tao et al., 1999; Xu et al., 2011; Zhao and Zhao, 2009).

The main volcanic geoheritage in Arxan-Chaihe Volcano Area.

Class	Type	Distribution
Igneous rock profile	Phreatomagmatic and magmatic profile	The southwest and the southeast edge of Tongxin Tianchi, 2.5 km west of Tianchi Forest Department
	Landed and splashdown cone accumulation profile	The three concentric parasitic volcanic cone (vc) northeast of Tongxin Tianchi, Tuofengling Tianchi vc, Yueliang Tianchi vc, Heixiadong vc, 1221 Highland vc, 1132 Highland vc, 1246 Highland vc, Aonier River vc, Yanshan vc
volcano cone landscape	Volcano cone (vc)	The vc of a string of four volcanoes northern of the Dele River, Tianchi vc, Gaoshan vc
	Crater	The 26 crates except Tongxin Tianchi crater
	Caldera	Tongxin Tianchi crater
Lava landscape	Lava plateau	The west bank of the Chaor River of Guangrong Village in Chaihe Town, south of Jiufeng Mountain, along the Dele River
	Lava tube	The larger and smaller lava tube
	Columnar jointing	Along the bank of the Chaor River
	Lava flow	blocky lava, pahoehoe lava and turtleshell-like lava in Xing' an Forest Department, aa lava
	Lava hornito	The western bank of Dujuan lava-dammed lake
	Lava dome	From **Gaoshan to Yanshan**
	Lava collapse	Lava cave and pit in Arxan **Stone Sea**
Pyroclastic seats		Around Yanshan
Mesozoic volcano landscape	Volcano vent	West of Chaiqing Forest Department
	Sub-rhyolite peak forest landform	Jiufeng Mountain
Volcano lake landscape	Crater lake	Tongxin Tianchi Lake(TL), Tuofengling TL, Yueliang TL, Buteha TL, Shuanggoushan TL, Arxan TL, Wusulangzi TL
	Lava collapse lake	Dichi Lake
	Lava-dammed lake(ll)	Songye ll, Dujuan ll, Luming ll, Xianhe ll, Yanjing ll
Spring landscape	Hotspring	Southeast of Tongxin 11, 23 Hot springs in Arxan Nursing Homes, seven hotsprings in Jingjianggou
	Coldspring	Holy coldspring, Wuli coldspring, seven coldsprings in Arxan Nursing Homes

Table 1: The major distributions of landforms in the ACVF (Wang et al., 2014).

Table 1 depicts the major landforms in the ACVF. Due to the volcano type, the volcanoes in the ACVF are monogenetic volcanoes. The signatures of phreatomagmatic and magmatic are the distinct features of maar volcanoes, which are represented by the parallel and cross-beddings of pyroclastic materials (Bitschene and Schüller, 2011). For instance, at the SW and SE sites of the Tongxin Lake, the laminated parallel pyroclastic successions are well preserved. Also, the cross- and parallel-beddings can be observed near the Wusulangzi Lake (Wang et al., 2014).

Most volcanoes in the ACVF are the scoria or cinder cones which produce a series of accumulations of fallen scoria and spattered lava. In the early stages, they may eject pyroclastic materials, such as Tongxin Lake. It is assumed that during the Late Jurassic, this crater experienced sub-Plinian-style eruptions with large quantities of ejected pyroclasts, and these volcanic clasts formed the annular and radial structures (Wang et al., 2014).

Lava-formed landforms in the ACVF are common characteristics and cover large areas around the vent sites. Lava tubes in the ACVF present various shapes and volumes. In the Tuofengling region, the basaltic lava ejected through the vent of Tuofengling crater and interacted with the surrounding water, and subsequent erosional processes formed an SN-trend tube which is approximately 6 km long, 30 to 150 m wide, and 25 to 100 m deep (Wang et al., 2014). On the bank of the Chaoer River, the basaltic columnar jointing is significant. In the ACVF, the vertical columnar jointing dominates both sides of the Chaoer River. Lava flows are the iconic features in the ACVF. A variety of types of lava flow present the various alterations of lava

evolution, such as pahoehoe, aa, blocky, tumuli, hornitos, domes and whaleback (turtle skin). For instance, the lava flows are well developed in the Banyueshan area, and the flows cover an area about 50000 m^2, with almost 1 to 2 m wide of piles of lava blocks (Wang et al., 2014), which formed the Stone Forest in this site. The whaleback lava flows (turtle skin) in the Great Xing'an Mountain are filled with cracks of 5 to 10 cm (Wang et al., 2014). The Arxan Shihai (stone sea) is characterised by the pahoehoe-type flows which preserve the wavy surface (Gao et al., 2013). In Jujuan Dam Lake, the lava hornitos are about 1.5 m in width and 0.2 m in height (Wang et al., 2014). Lava hornitos are formed by the over-pressure of the internal unconsolidated lava within a relatively consolidated shell. When the internal pressure reachs the threshold and subsequently bursts out, a hornito is formed (Ort et al., 2008). In the Yanshan and Gaoshan sites, the lava domes are well preserved and distributed and cover about 40 km^2 with a pillow-like shape which indicates high viscosity. The height and diameter are 2 to 4 m and 5 to 7 m respectively (Gao et al., 2010; Wang et al., 2014).

Mesozoic volcanic landforms can also be observed in the ACVF. A group of columnar jointings about 100 m in height and 300 m in width are preserved in the rhyolitic volcanic vent with 0.5 km^2 area of well-developed vegetation. These Mesozoic landforms indicate the rifting and volcanism were along here and occurred within the continental boundary of Eastern China (Liu et al., 2004; Ren et al., 2002; Tian et al., 1992; Zhang et al., 2011a; Zhang et al., 2011b).

Figure 23: The variations of lava-flow landforms in the ACVF. Pictures A to D depict the lava domes and lava tumulus. Pictures E and F (Chaihe Bank) show blocky lava flows. Photo G represents whaleback (turtle skin) lava flows, and photo H is columnar jointing structures on the Chaoer riverbank (sourced from (Németh et al., 2017); captured by Prof. Karoly Nemeth in 2016).

Maps of vents

Based on Fig 22 and Fig 24, the Arxan-Chaihe Volcanic Field is characterised by five spectacular volcanoes (vents), which are Moon Lake (Arxan Tianchi), Wusulangzi (suspected as a maar), Dichi (Earth Pond), Tuofengling (Camel Hump Mountain) and last, but not least, Tongxin (previously named Woniuhu Lake).

Figure 24: The overview of ACVF, the red dash lines mark the trend of the volcano's distribution. Basically, they are parallel with the NE orientation and corresponding with the regional tectonic fault complex, also each red star represents the location of each vent. Pink dot is Wusulangzi Lake; blue dot is Moon Lake (Arxan Tianchi); green dot is Dichi Lake; yellow dot is Tuofengling Tianchi; and red dot is Tongxin Lake. Also purple complex star marks Jujuan Dam Lake, and brown-yellow complex star indicates Banyueshan lava flows. The inlet map depicts the location of the ACVF (shaded area) (sourced from (Wang et al., 2014)).

1) *Moon Lake – Arxan Tianchi*

Moon Lake is the icon of the ACVF and it is also the first crater lake when tourists enter the geological park (Fig 25, 1a, 1b). This crater is actually a scoria cone with the cone height about 200 m (Németh et al., 2017). The altitude of this lake is approximately 1300 m above sea level. Its shape is an ellipse with a long axis of 450 m and the short axis of 300 m. The crater area is approximately 0.138 km^2. Moon Lake is the third largest crater lake in China following Changbai Tianchi and Tianshan Tianchi. About 3000 years ago, with the magma ascent to the surface and undergoing a series of Strombolian-type eruptions, this crater was formed. However, on the bottom of the cone a group of lapilli tuff and glassy pyroclastic rocks represent the possible phreatomagmatic eruptions which may form the relatively large crater shape (Kereszturi and Németh, 2012).

2) Tuofengling Tianchi

Tuofengling Tianchi is the largest crater lake in the ACVF (Fig 25, 4a, 4b). Its altitude is about 1284 m. The shape of the crater is also an ellipse in association with 800 m on the long axis and 450 m on the short axis. The water depth of this crater lake is the deepest one (Németh et al., 2017). The Tuofengling Tianchi was formed approximately during the mid-Pleistocene. Lapilli to coarse ashes dominate the successions of the pyroclastic beddings. Within the successions, large and basaltic fusiform volcanic bombs can be found in the basement of this

cone. These features also represent the Strombolian-type eruptions during the syn-eruptive phase. Nevertheless, similar to Moon Lake, small amounts of lapilli tuff indicate that small-scale magma-water explosive eruptions might occur during the cone shaping (Németh et al., 2017).

3) Wusulangzi Lake (Sample 1 – ARX1 comes from)

Wusulangzi Lake was formed by the damming of lava flows, which blocked the Halahahe River (Fig 25, 2a, 2b). The depth of this lake is 2.5 m in average and the area of the lake is approximately 1.35 km^2. In recent research, due to the geomorphology and the lake-water distribution, this lake is suspected to be a maar-diatreme volcano and is described in more detail later in the Wusulangzi volcano chapter.

4) Dichi Lake

In the few previous studies, Dichi Lake is suggested as being of maar origin, but this is highly in debate (Fig 25, 3a, 3b). Generally, Dichi Lake is about 170 m in the perimeter and overlies the relatively young lava flows which may derive from the nearby cones with well-developed vegetation (Németh et al., 2017). With an oval shape, this lake has cut into the relatively old lava flow surface. In terms of lacking evidence of tephra, it is suggested that the interaction between magma and water may take place and result in the phreatomagmatic and maar origins (Németh et al., 2017). The water depth of Dichi Lake is less than about 10 m. A small amount of lava boulders can be observed in the surrounding hillside which is highly vegetated. Regardless, this lake seems to be a lava rise pit (Németh et al., 2017).

5) Tongxin Lake

Tongxin Lake in Chaihe Town has preserved the most intact pyroclastic successions in the ACVF (Fig 25, 5a, 5b). This lake is in relation to the violent phreatomagmatic eruptions. In the south of the hilltop, the pyroclastic beddings are well exposed. Tongxin Lake is about 450 m in an EW orientation and 300 m in a SN orientation. The altitude is approximately 1332.3 m. The depression of Tongxin Lake is suspected as the eruptive vent. However, there is no pyroclastic succession in this depression, rather some reworked topsoil with volcanic materials (Németh et al., 2017). In the south of the depression, about 30 m thick, alternating parallel-bedded, grey, accidental lithic ash beds with accretionary lapilli, as well as dune-bedding ash layers, are well observed. Between these ash beds, lapilli beds accompanied with large accidental lithic-lapilli are hosted by coarser-grain ash matrix, also with some ballistic bombs within (Németh et al., 2017). This outcrop section extends about 1 km. Subsequently, about 2 km long, it presents as a spatter pyroclastic unit inter-bedded in a fine-grained grey ash and lapilli sediments. Inside this 2 km long bed, the geometry of ballistic sags and dune structures indicate that base surge may play an important role in bearing these pyroclastic materials from NS along with this same direction (N-S) (Németh et al., 2017). Cauliflower-shaped bombs that are extensively observed are suggested to be the interaction between magma and water (White and Ross, 2011). Inside these cauliflower-shaped bombs, mantle

xenoliths are formed by altered crystalline fragments indicating ascending magma packed such materials at various depths (Murcia et al., 2015). Due to the high degree of degradation and erosional processes, Tongxin Lake formed an intra-mountain basin during the post-eruptive stages (Németh et al., 2017). However, a few amounts of tuff ring are preserved.

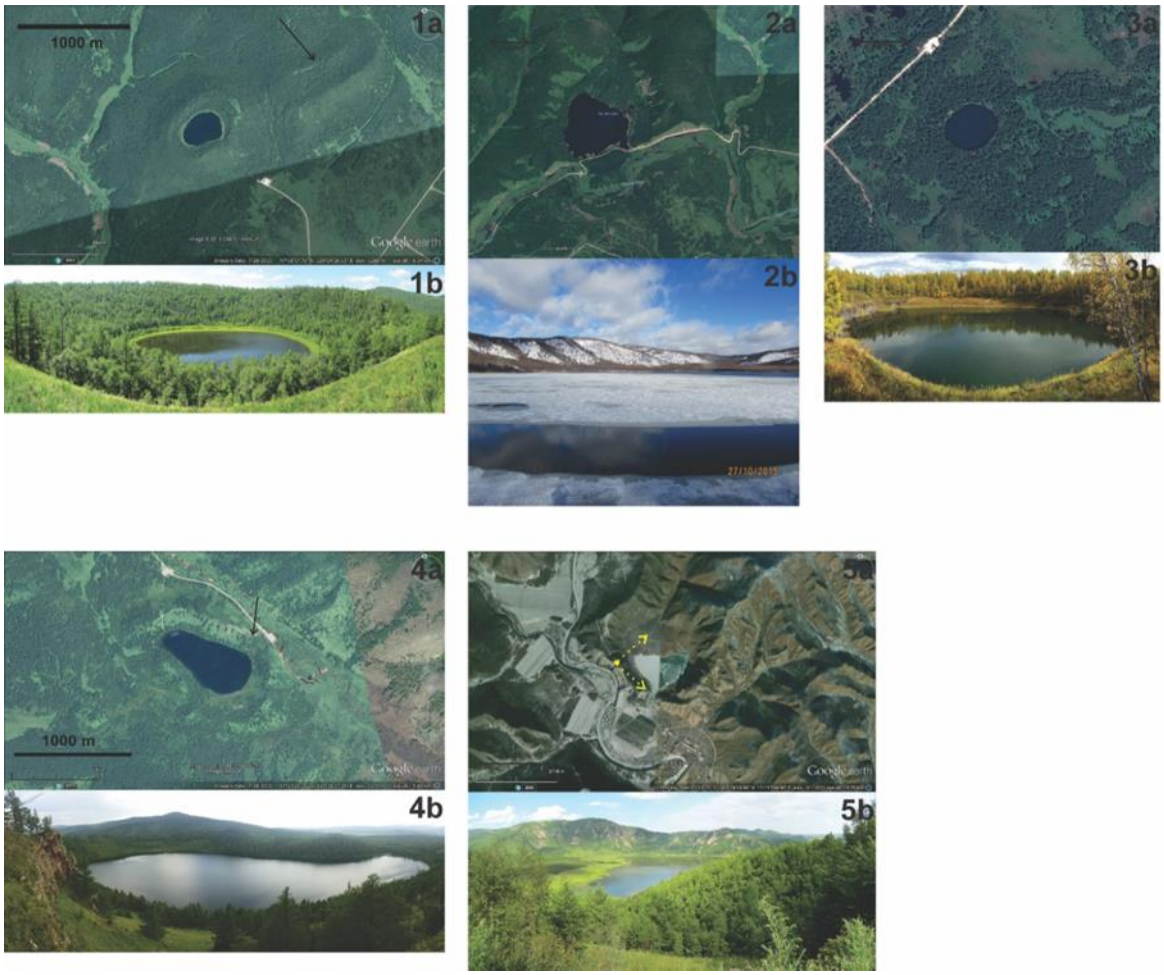

Figure 25: The pictures of the ACVF, 1a and 1b are Moon Lake; 2a and 2b are Wusulangzi Lake; 3a and 3b are DIchi Lake; 4a and 4b are Tuofengling Lake; and 5a and 5b are Tongxin Lake. Note the yellow dot on 5a which marks the viewpoint of 5b (sourced by (Németh et al., 2017); pictures captured by Prof. Karoly Nemeth; GoogleEarth).

Vent distribution

Figure 26: The plot of vent distribution in the ACVF; the colours represent the density of the vents in turn from red (high density) to deep-blue (low density). Basically, the volcanoes in the ACVF are aligned with a NE orientation (sourced from (Wang et al., 2014)).

The vent distribution of the ACVF depicts the major regional tectonic settings which represent the NE-trend fault systems. From this plot, the pattern of the vent distribution represents the regional structures. The trend is aligned with NE orientation which means the faulting system is the same orientation. The major part of the vent marks the belt of the ACVF. Each vent has been labelled by its destination, which is indicated by the abscissa and ordinate. The deep-red zone marks the highest density of the vents. The colour transition zone is sharp, and may indicate the fault systems which enclose the volcanic field. This corresponds with Zhao et al. (2008), in which NE and NW trend faults and NE trend volcanic belts were generated by the rifting events during the Mesozoic and Cenozoic (Zhang et al., 2011a; Zhang et al., 2011b). The rifting led to the upwelling of the asthenosphere, the delamination and under-plating caused the thinning of the crust in the Cenozoic. Thus, the volcanic belt formed (Zhao et al., 2008). The distribution of the volcanoes is constrained by the basement faults (Xu and Bai, 2009). Due to the volcanoes on the fault intersections, the volcanism is along with the NE-trend faulting system, which results in the three parallel trends of the volcanoes (Fig 26, margins of the colour transitional zone) (Wang et al., 2014).

Wusulangzi volcano

Volcanic architecture

Wusulangzi Lake has been suspected to be a maar volcano. However, no detailed investigation has been performed so far. Wusulangzi Lake is located near the valley of the Halahahe River. Due to recent landslides and riverbank erosion, new outcrops formed where an about 20 m thick pyroclastic succession has been exposed. The newly-formed outcrops have been visited briefly in the October 2015 field campaign and this documented its basic textural characteristics. In addition, a representive sample has been collected and investigated in respect of its granulometry, clast population and juvenile pyroclast texture with the aim to understand its origin. Later on this sample and analytical work with its results will be used to compare it to another volcanic crater, Tongxin volcano on the NE edge of the volcanic field (in discussion with Prof. Karoly Nemeth in 2017).

Wusuliangzi is an irregular-shaped lake developed in an intra-mountain basin. In the vicinity of the lake, there are no pyroclastic outcrops known. About 1.5 km to the SE, along with the Halahala riverbank, new pyroclastic outcrops expose a gently dipping and sub-parallel succession of lapilli tuffs and tuff rich in accidental lithic fragments from basement igneous rocks. The tuff beds are intercalated with lapilli tuff layers. The boundary between fine and coarse units is laterally continuous and sharp. Tuff beds show gentle dipping cross-stratification, while lapilli beds are unsorted and weakly stratified. The entire pyroclastic succession is covered by a lava flow. Along the contact between the pyroclastic rocks and the lava flow, thermal alteration forms reddish discolourisation (in discussion with Prof. Karoly Nemeth in 2017).

The pyroclastic rock units have no impact sags which are caused by ballistically-trajected bombs. There is also no accretionary lapilli which have been observed. The pyroclastic rocks, however rich in low vesicles of basaltic lapilli and coarse ash fragments, are commonly angular in shape and show a glassy texture. Advanced palagonitisation is apparent, especially in beds that are richer in juvenile pyroclasts (in discussion with Prof. Karoly Nemeth in 2017).

Note that this section only gives very preliminary observations on the fieldwork and provides the general discussion with Prof. Karoly Nemeth. More detailed research will be carried on in the future.

Field observations

As shown in Fig 24, Wusulangzi Lake is located at the SW corner of the ACVF (pink dot in Fig 24). The position is approximately 47° 18’ N, 120° 20’ E. The altitude of the bottom of the lake is about 1044 m above sea level. The Halahahe River is running through the southern flank of the lake with an ambiguous alluvial fan structure. On the northern side of the lake, a large area of the alluvial fan is covered about 33.3% of the depression’s area (sizeable white curve in Fig 27).

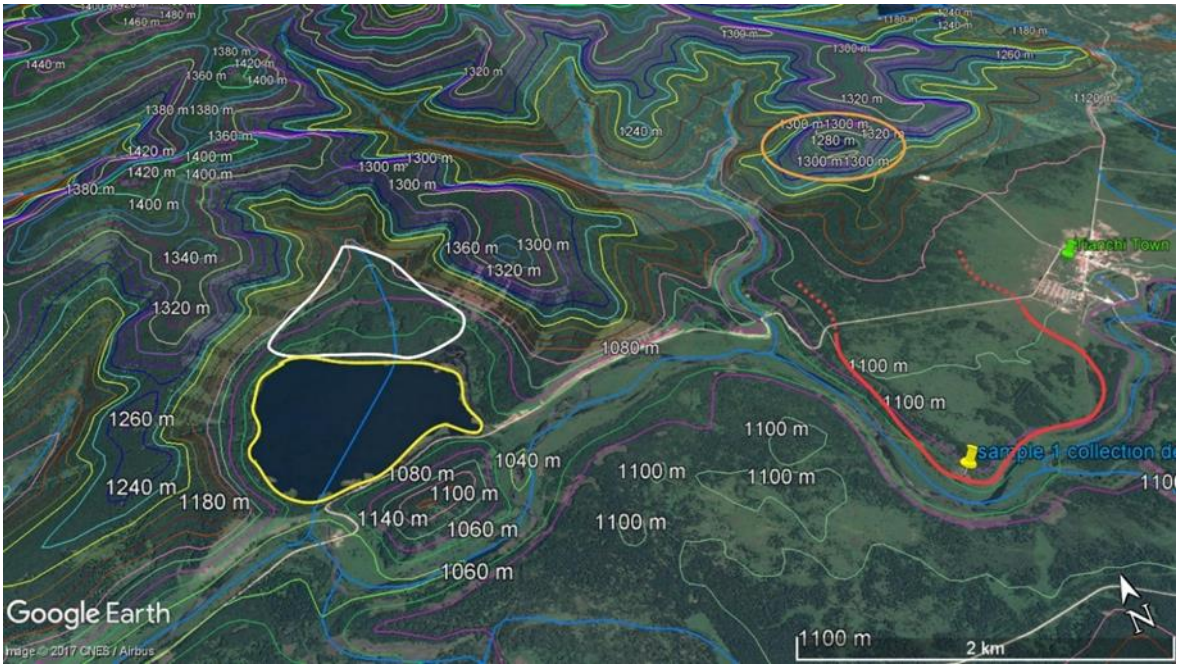

Figure 27: Wusulangzi Lake might be the most massive crater in ACVF. On its NE side, the brown ellipse marks the Moon Lake crater. The yellow label represents the Sample 1 (AX1) collection outcrop (sourced from Google Earth; http://srtm.csi.cgiar.org).

As shown in Fig 27, Wusulangzi Lake has a similar topography with standard maar craters. A large area of the lake (sizeable yellow curve in Fig 27) lies between the Halahahe River and the northern side of the alluvial fan. An arch-shaped rim surrounds the lake with the highest point approximately 1360 m above sea level. The red solid and dash line marks the possible area of lava flow distribution.

The destination of the sample collection is located at 47° 16’ N, 120° 22’ E with the elevation of 1064 m on the SE side of Wusulangzi Lake (yellow label in Fig 27). This site is assumed to be distal deposits from Wusulangzi Crater. However, this hypothesis is still under evaluation. The outcrop of this site is composed of a series of pyrogenetic beddings, including lava flows, tuffs, as well as pyroclastic materials.

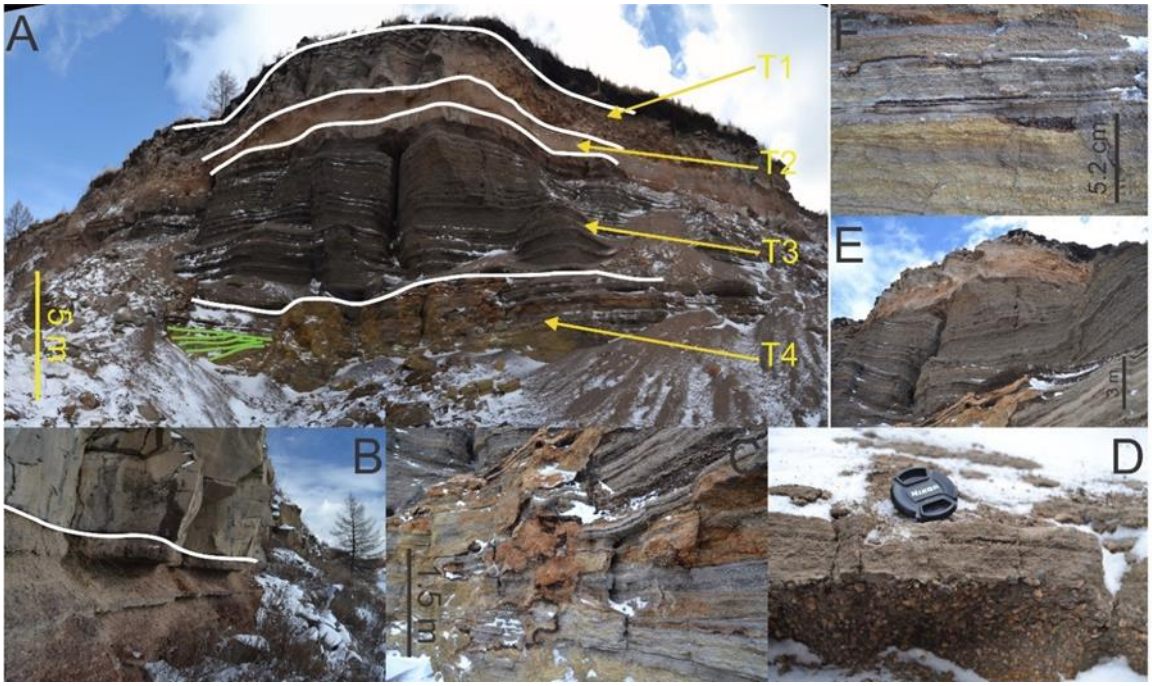

Figure 28: The outcrop of Sample 1 (AX1) is combined with a range of volcanic successions. Note the four varieties of beddings are depicted in photo A, the details are presented via other five photos (captured by Prof. Karoly Nemeth in 2015, China).

As shown in Fig 28, photo A depicts four beddings with various textures of pyrogenetic rocks. Planar beddings are the dominant feature in this site. The small degrees of cross-bedding emerges on the bottom of the T4 layer in photo A. The height of the whole bedding is approximately 13 to 15 m. Beneath the topsoil, the blocky, coherent and jointing-shaped bulk rock layer probably represents the lava flow. Its thickness is about 2.5 to 3 m, which indicates the high outflux of the syn-eruptive lava production (T1 layer in photo B). The underlying layer of T2 is a group of red-brown tuff with dominantly coalescing and dense features and with a thickness of less than 1 m. The inter-bedded thin scoria layers are represented by the small magnitudes of spatter eruptions. The massive T3 layer is composed of a series of coarse-grained lapilli and pyroclasts with planar or laminated beddings about 5.5 m in its thickness. With the poor sorting, this layer is generally a dark-grey colour with an ambiguous reversed grading structure (photo E of Fig 28). The grain-size distribution ranges from 0.5 to 2.5 in the T3 layer. On the bottom of this layer, a very thin bed of lapilli presents the non-bedding textures with approximately -1 to -2.5 phi values of grain size. The lapilli emerge in various colours, but generally dark-brown (photo D of Fig 28). The thickness of this thin lapilli layer is approximately 10 cm. Beneath the layer T3, the T4 layer is full of weathering crust with a dark-red colour, which indicates the iron-rich compositions (photo C of Fig 28). The lamination or parallel beddings are typical and significant. Basically, the coarse-grained and indistinct reverse-grading textures can be recognised within photo F (of Fig 28). However, on the left corner of the layer (photo A of Fig 28), a small degree of cross-beddings can be observed and this is marked by the green lines in photo A of Fig 28. The large-sized clasts that are probably accidental liths disperse throughout this massive layer. The thickness is no more than about 3 m.

Throughout the above-described section, the outcrop location of Sample 1 (AX1) preserves various groups of pyrogenetic lithic beddings. The upper layer of lava flow might imply that volcanism was dominated by Strombolian-style eruptions at the end of eruptive phases. However, this site is relatively near another crater of the ACVF, Moon Lake Crater, which is a crater lake on top of a scoria cone rather than a small-scale maar due to the lack of any deposits indicative of the presence of phreatomagmatic explosive eruptions. Due to the size of Moon Lake volcano, it is suspected that the scoria cone that hosts the crater lake is sitting on top of a lava shield. The basal lava field's exact origin, however, cannot be established at this stage and Wusulangzi volcano could also be a potential source region judging from its complex volcanic facies architecture and size. Still, this field observation is only in a very preliminary stage of research and was carried out by Prof. Karoly Nemeth in 2015 in China. Detailed information needs to be promoted.

Tongxin volcano

As mentioned above, the Tongxin volcano is a suspected maar-diatreme volcano (in relation to the observations in the field and analyses of the samples), which was formed by a series of phreatomagmatic eruptions with subsequent lava-effusive/strombolian-type eruptions (Németh, 2010a; Németh, 2012; Valentine and White, 2012; White and Ross, 2011). The pyroclastic successions are well preserved on the SW range of the crater. In Chinese, the word "Tongxin" means the shape is the same as a heart. The pyroclastic successions around this crater are well preserved and developed. Good outcrops can be traced in its western crater rim, as well as in more distal areas in the township of Chaihe. The pyroclastic rocks exposed and investigated show typical characteristics of a maar-type pyroclastic succession of lapilli tuffs and tuffs rich in accidental lithic clasts. The size of the crater and the type of deposits identified suggest that this volcano must have undergone a range of magma-water explosive eruptions (probably reaching to sub-Plinian-type) with subsequent lava-effusive eruptions. The crater is approximately located at 47°34'N, 121°17'E. The elevation of the depression bottom is about 611 m above sea level. Around this depression, the circular-shaped rim constrains the landform of the Tongxin Depression (crater). The altitude of the highest point of the rim is about 1040 m on the NE side of the rim. On the northern side of the depression, a large area is covered by the alluvial fan (sizeable white curve in Fig 29). On the southern part of the depression, a possible maar lake is adjacent to the alluvial fan (sizeable yellow curve in Fig 29).

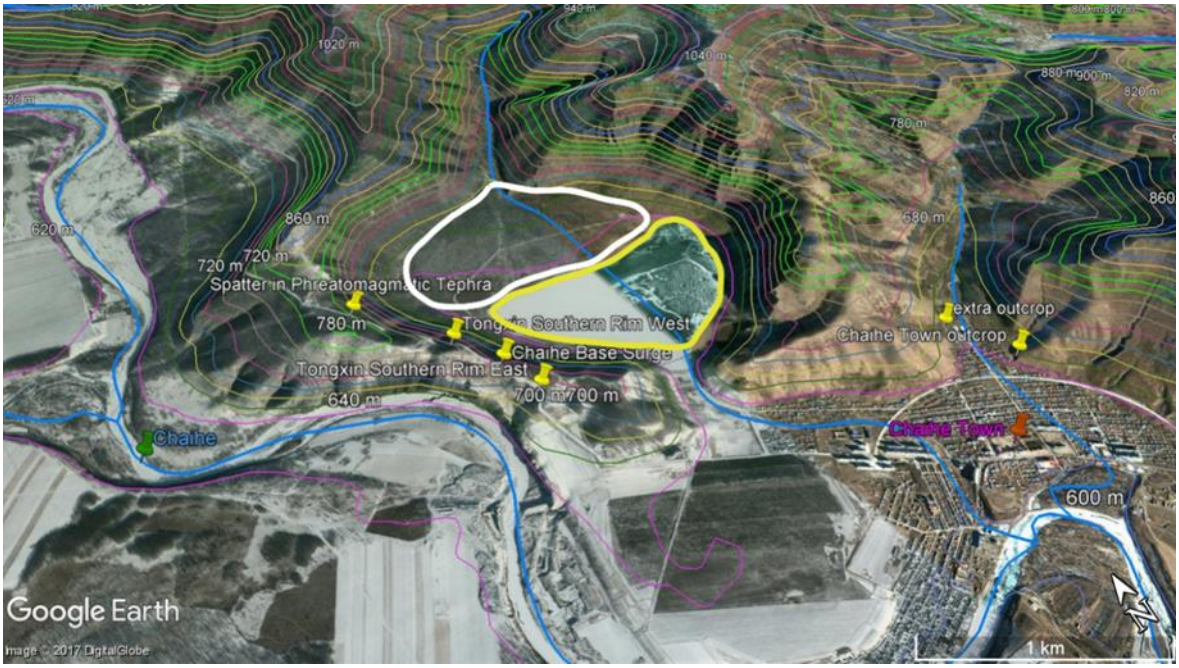

Figure 29: The Tongxin volcano, formerly named Woniupo, is the NE-most crater in the ACVF. Six yellow labels mark the destinations of the fieldwork. The group of colourful solid lines represent the contour lines. The thicker blue lines depict the fluvial systems. The green label on the left is the mark of Chaihe River. The red label on the right marks the location of the Chaihe Town on the SE of the crater. The scale and the direction are on the right-bottom corner of the photo (sourced from Google Earth; http://srtm.csi.cgiar.org/SELECTION/inputCoord.asp).

Due to the massive area of the depression (about 1.7 to 2.2 km in diameter) (Németh et al., 2017), the Tongxin volcano was once considered as a caldera (Németh et al., 2017). However, based on the characteristics between maars and calderas, discussed above, the Tongxin volcano is just a large maar in terms of the typical features of the pyroclastic successions described later. In caldera systems, huge quantities of pumiceous pyroclastic beddings can be produced during Plinian-type eruptions. Generally, the pumiceous pyroclastic successions indicate violent Plinian-type eruptions. Compared to calderas, in the initial stages of maar-type eruptions, explosive products have implied the processes of excavation. Due to no sign of large quantities of pumiceous sediments, and being predominantly composed of basaltic successions, it can be concluded that the Tongxin volcano is just a large maar-diatreme volcano rather than a caldera. In addition, basaltic compositions are rarely produced by calderas (known but not common). The following parts will discuss the details of the observations in the field.

Volcanic rock distribution

As Fig 30 depicts, the SW rim of the Tongxin volcano preserves a range of well-developed, bedded-to-laminated pyroclastic units. Depending on the location and different compositions of the sites, the outcrops of the SW rim are composed of two major parts: the Southern Rim Outcrop west, and the Southern Rim Outcrop east. Between them, a group of very fine grain-sized layers represent the very fine laminated beddings, with a small amount of sags, that also have a series of accidental lithics, accretionary lapilli and angular juvenile clasts with a cauliflowershape. The beds are cross-laminated to cross-bedded, suggesting lateral

transportation. All these textural evidences point to a phreatomagmatic explosive eruption that drove the volcanic activity. The horizontal transport indicators suggest abase surge as the dominant pyroclast transportation during the eruptions. The other locations are in the SW crater. Several outcrops are represented as the similar structures of the pyroclastic density currents or other types of volcanic clastic-textures. The sample collections and field trips are still in the preliminary stage of the whole research due to the time schedule and some irreversible conditions. In this section, limited research will be given and evaluated.

1) The Tongxin Southern Rim Outcrop east

This site is located on the SE rim of the Tongxin volcano (Fig 29), just at the left-hand side of the crater entrance with about 691 m in elevation. The height of this group of beddings is approximately more than 7 m. At the very end of the southern part, a group of light-brown to dark-grey coloured laminated, as well as poorly-sorted, beddings are beneath the topsoils (Fig 30 L1). This site has experienced a high degree of post-eruptive erosional processes and vegetation. As in the photo shown in Fig 30, the collapsed materials, which are possibly formed by degradations and water-influenced, cover most parts of the pyroclastic beddings. The layers between L2 and L3 are mantled (Fig 30). The L3 bedding is thinner than the L2 layer, but due to the erosional material covering its surface, the details cannot be observed. Basically, this bedding is preserved in a range of coarse to fine pyroclastic deposits.

Figure 30: The pyroclastic laminated beddings preserved on the southern flank of the Tongxin volcano. The L1 marks the topsoil layer; L2 and L3 depict the partial outcrops of pyroclastic laminations. The two lapilli present the xenolith of accidental liths enclosed by juvenile materials in photos A and B. The green eclipse on photo A marks a small amount of olivine crystals (photos captured by Prof. Karoly Nemeth in 2016, China).

In this site, the large size of the lapilli are preserved in the beddings with a juvenile crust and with large and intact accidental lithics at its core (xenoliths) (Fig 30 B), as well as the common xenoliths (Fig 30 A). Basically, the lapilli with accidental xenoliths within it are rounded to a sub-rounded shape. The size is medium as Fig 30 depicts. Picture A of Fig 30 shows the accidental xenoliths enclosed by the juvenile matrix with about 10 cm in diameter, and the shape of these xenoliths is nearly sub-rounded, while some of them are rounded. Within it, a small content of olivines or peridotites can be observed (green eclipse in picture A). With observation using the naked eye, the accidental xenoliths occupy approximately 40% of the

whole rock, and they are generally poorly-sorted with size ranging from 1 mm to 3 cm. The vesicle's structures are unambiguous either in accidental xenoliths or a juvenile matrix, but the degree of vesicles is medium to low. Also, the shape of the vesicle's structures is majorly rounded. Photo B in Fig 30 depicts a single and sizeable xenolith cored in the lapillus. The diameter of this lapillus is no more than about 15 cm with the sub-rounded shape. The juvenile on the outer rim of the xenolith is relatively thin. The vesicles is well developed in the outer juvenile crust, but low-to-none in the inner xenolith. The shape of the vesicles structures is almost rounded. The irregular-shaped fractures and the relatively small amount of jointing structures can be seen on the surface of the xenolith. As with photo A in Fig 30, the xenoliths are well developed in the outer rim of the juvenile shell. With observation using the naked eye, the percentage of xenoliths in the outer juvenile crust is about 35% to 40%. The shape of these xenoliths ranges from blocky to sub-sounded shapes.

The following section of this site has a series of well-preserved outcrops which are about 4 to 7 m high, with highly-developed lamination structures, as well as other typical pyroclastic structures (Fig 31).

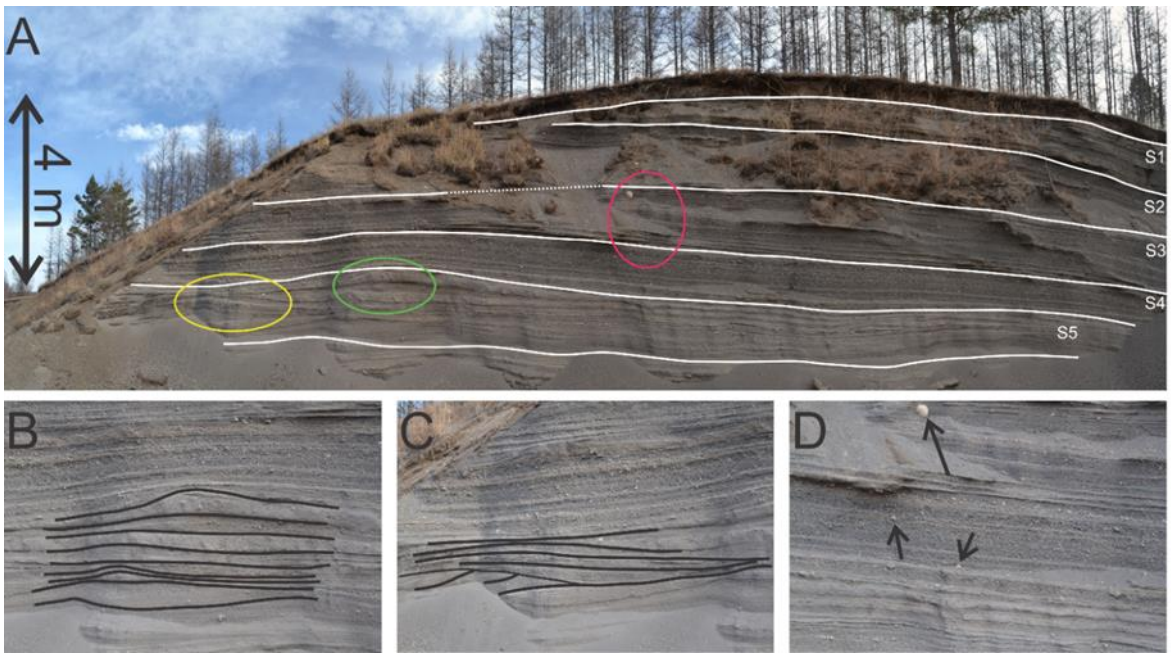

Figure 31: The well-exposed outcrop of pyroclastic beddings in the Tongxin Southern Rim Outcrop east depicts the varieties of structures and grain-size distributions. In photo A, the yellow eclipse marks the location of photo C; the green eclipse represents photo B; and the red eclipse shows the details of photo D. Sections of beddings are indicated by S1 to S5 (captured by Prof. Karoly Nemeth in 2016, China).

This site is composed of a number of pyroclastic beddings and deposits. As shown in photo A of Fig 31, the structure of this group of beddings is dominated by laminations. On the top of the outcrop lies the soil layer. S1 to S4 have similar structures with thin layers of fine volcanic ash beds intersecting in the coarse-grained pyroclastic materials of about 75 cm in thickness. The grain size distributes from -4.5 to 4.5 in phi values. In the S3 layer, the large size of lapilli can be observed in the beddings of approximately 7 to 10 cm in diameter (black arrows in Fig

31 D). These four layers present the typical reverse grading (photo A of Fig 32). Each of the beddings show very poor sorting.

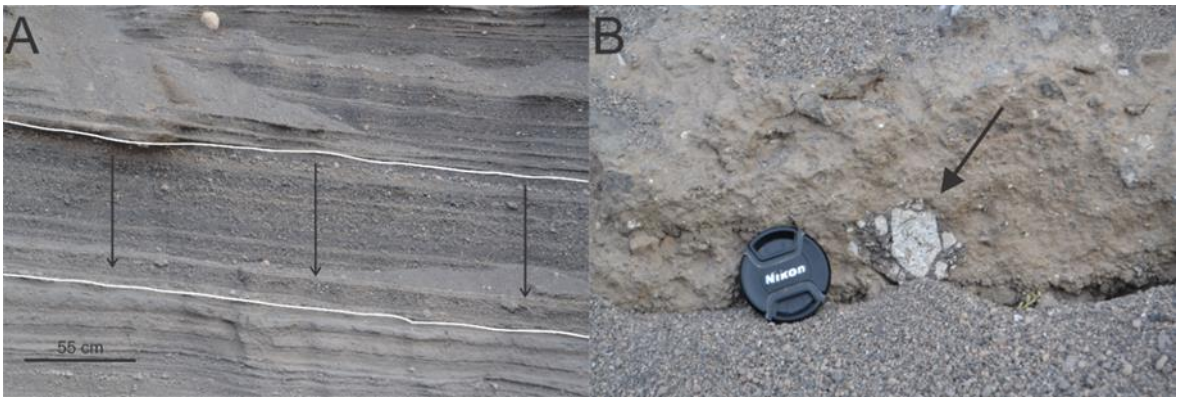

Figure 32: Photo A depicts the reverse grading system. The three black arrows represent the grading direction (i.e. from top to bottom). Photo B shows the large bulk of xenoliths in the basement of this site (captured by Prof. Karoly Nemeth in 2016, China).

Layer S5 is composed of a range of very fine-grain ash beddings with intersected coarse-grained pyroclastic particles. The laminated structures are the major structure in this section, however the medium scale of cross-beddings and dune-shaped structures can be seen in this section. Photo B of Fig 31 depicts the dune-bedding structure. The angles of repose between the right and left of the dune are different. The angle on the left is relatively larger than the right side, which possibly means the transitional direction of pyroclastic flow is from right to left, i.e. away from the crater. Photo C of Fig 31 shows the cross-bedding structures. The contact between S4 and S5 seems to be the chute-and-pool structure whose transitional direction is the same as the dune beddings, however due to the preliminary observations on this site the details are still unknown. In terms of the composition of S5, with the inter-bedding between coarse pyroclastic particles and fine ashes, this section possibly represents the base surges during the phreatomagmatic eruptions. On the bottom of this site, large xenoliths are preserved within the coarse-grained beddings of about 5 cm in diameter (photo B of Fig 32).

Accretionary and compositional lapilli beddings are well developed on this site. The grain size of the lapilli ranges from -4.5 to 4+ in phi value. This site is composed of dark-grey coarse grains with a large size of lapilli and the lamination is well preserved. The overlying layer constitutes dark-brown fine ash beddings with intersecting coarse lapilli layers (Fig 33).

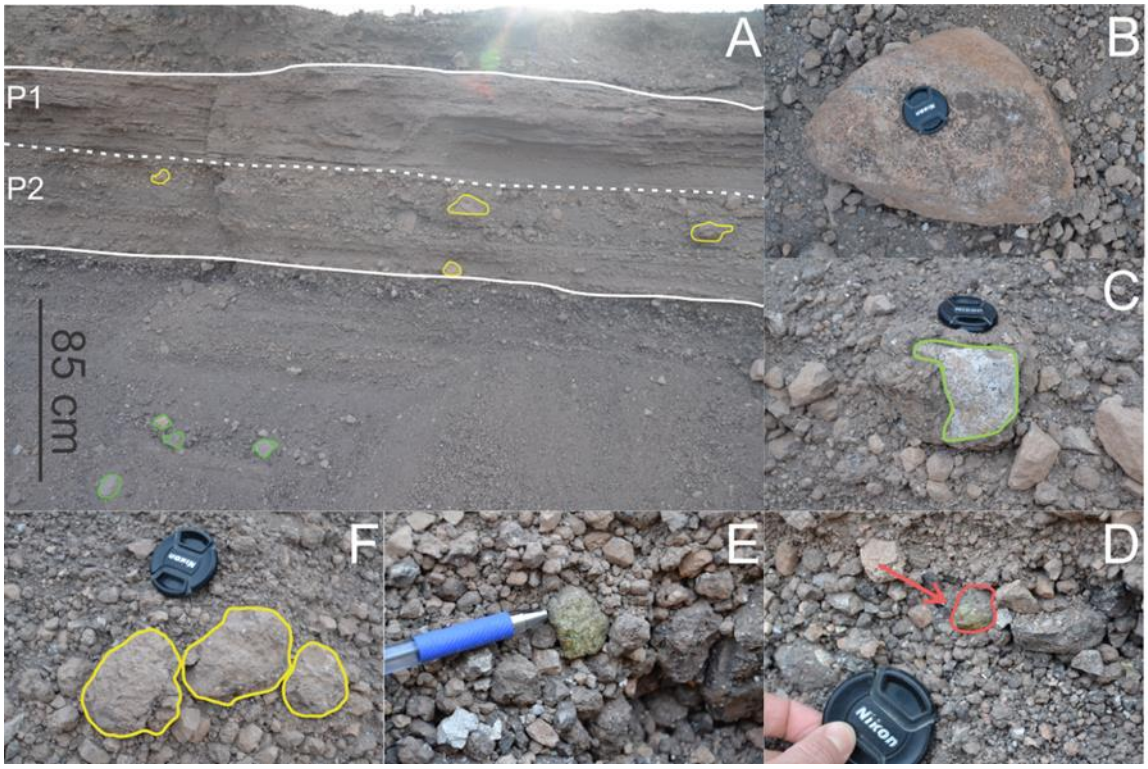

Figure 33: The compositional and accretionary lapilli beddings have various contents and structural feathers. The yellow and deep-green irregular curves mark the large-size lapilli in photo A; the light-green irregular curve depicts the possible shape of xenolith in photo C; the red irregular curve represents the small-sized olivine/peridotite; and three irregular yellow curves label the triple lapilli with a large size (captured by Prof. Karoly Nemeth in 2016, China).

In photo A of Fig 33, bedding P is divided from two sub-layers by a white dash line: P1 and P2. The development of lamination is typical and unambiguous. P1 is predominantly composed of fine ashes with small-to-medium and coarse grain-sized lapilli inter-bedded in them. The texture of P2 is coarser than P1's, but P1 is more sorted than P2. The underlying section constitutes dark-grey and poorly-sorted lapilli beddings, and the laminations are also well developed but not as much as the overlying P-layer. Grain-size distribution is generally from -4 to 3.5 in phi value, except for some large-sized lapilli or bombs which are shown in photos B, C and F of Fig 33. Photo B depicts the large, grey-brown and angular to sub-angular lapillus in this site, with approximately 20 × 30 cm of short axis and long axis respectively. Photo C represents a large cauliflower-shaped bomb of large size (about 15 to 20 cm in diameter) of accidental lithic fragment in its core. Photo F shows three larger lapilli, which are among the coarse lapilli beddings with a sub-rounded shape, and the relatively normal grading can be observed in this picture. Photos E and D capture the rare olivine/peridotite minerals in the accretionary lapilli beddings with a large amount of juvenile and accidental particles; the shape is relatively round, and the slight formations of imbrication are preserved in this site. Basically, the accretionary lapilli beddings are poorly-sorted with typical lamination structures and the reverse grading is the predominant grading trend.

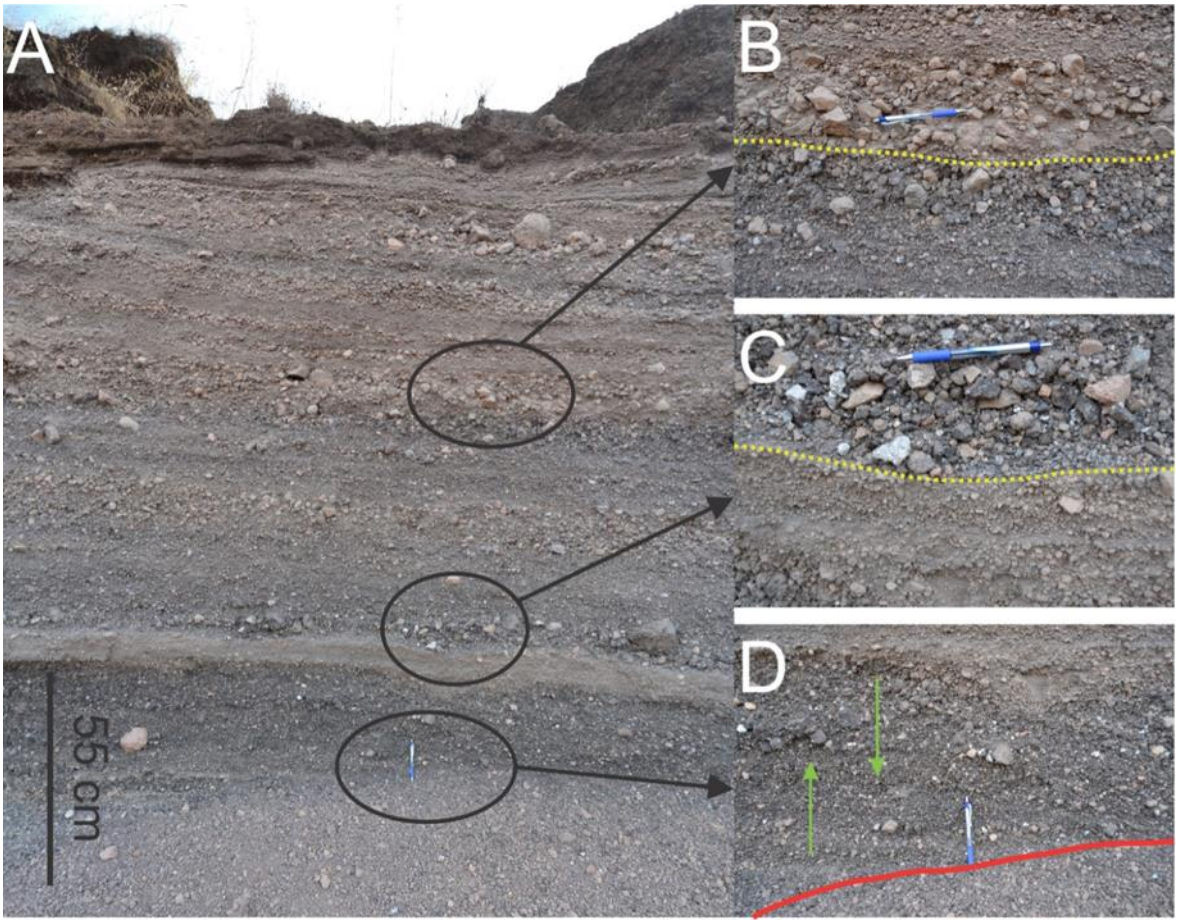

Figure 34: The compositional lapilli beddings with lamination structures are specified by triple black eclipses within the three photos (B, C and D). The two yellow dash lines mark the transitional zones in photos B and C, and the collapsed materials are enclosed below the sizeable red line in photo D (captured by Prof. Karoly Nemeth in 2016, China).

The compositional lapilli beddings are conventional due to the alternations between phreatomagmatic and strombolian eruptions. Fig 34 shows the typical and recognisable compositional lapilli beddings on the rim of the Tongxin Crater. Photos B and C of Fig 34 depict the zones of the transitional phase between phreatomagmatic and strombolian eruptions. Under the transitional zone, the reverse grading is well recognised. In terms of the hydrodynamic properties, the structures of imbrication are slightly developed. Photo D of Fig 34 depicts the ambiguous symmetric grading in turn from the bottom to the upper part (normal to reverse marked with double green arrows). Note there are some collapsed materials (not the beddings) which are under the sizeable red line.

2) The Tongxin Southern Rim Outcrop west

The Tongxin Southern Rim Outcrop west is located on the western flank of the Tongxin Crater Lake. The altitude of this site is approximately 726 m above sea level. Generally, the sedimentation and deposition of this site are more advanced than in the Tongxin Southern Rim Outcrop east due to the typical and unambiguous inter-beddings and particular structures of pyroclastic flows. The deposits of the base surge are well developed and preserved. Possible characteristics of phreatomagmatic explosive eruptions, such as the

presence of small laharic deposits (e.g. mud flow) and mud droplets, can be observed in the outcrops. This section will give a very preliminary observation from this site in terms of outline descriptions.

The very fine grain-sized beddings with intersecting coarse pyroclastic beddings indicate the development and movement of a base surge during the phreatomagmatic explosive eruptions (Fig 35).

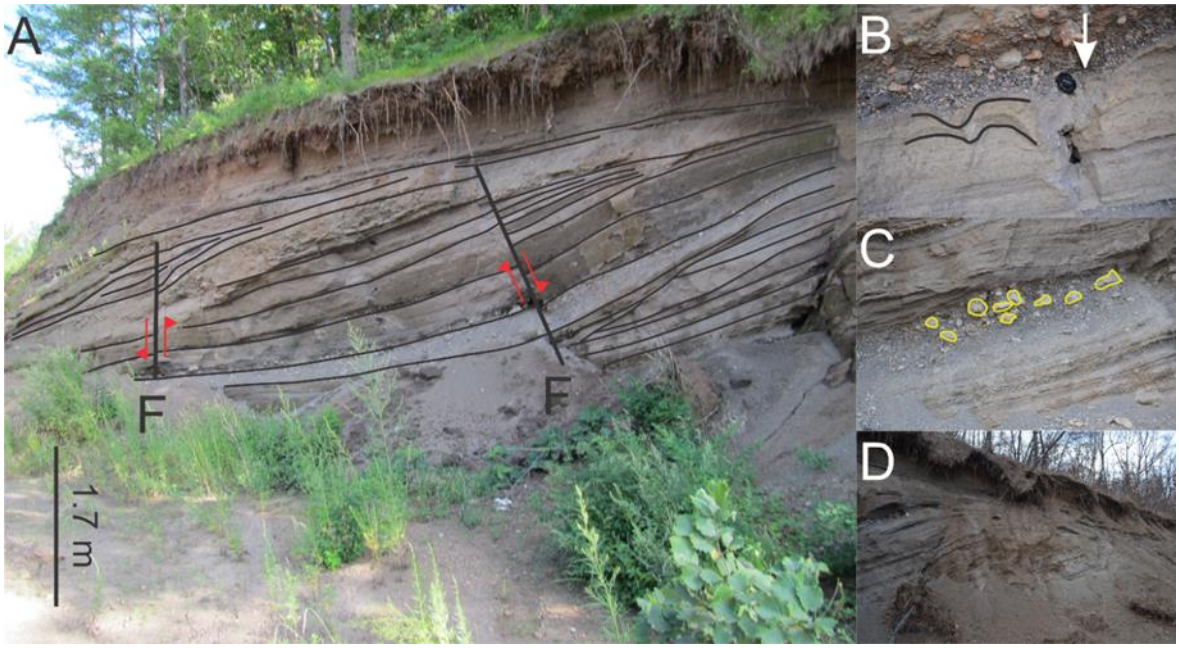

Figure 35: These four photos depict the significant structures and textures at the site of Tongxin Southern Rim Outcrop west. The white arrow in picture B shows the trend of grading; irregular yellow curves represent the large size of volcanic clasts (captured by Prof. Karoly Nemeth in 2016, China).

The outcrop at this site has a range of typical and identified volcanic structures and textures as shown in Fig 35. Photo A depicts the classified structures of chute-and-pool in the beds of base surges which is recognised in most of the volcanic fields around the world. This volcanism structure is defined as cross-beddings changing in lateral directions from relatively large dune structures near the eruptive source to anti-dune structures away from the eruptive source such as in Ubehebe and California (Crowe and Fisher, 1973; Schmincke et al., 1973). The chute-and-pool structures are commonly near the eruptions (Schmincke et al., 1973), which corresponds to this site due to the location of photo A of Fig 35 just behind the Tongxin Crater. As shown in photo A of Fig 35, two faults are penetrating the beddings, and the relative directions of movement are marked by the groups of red arrows. On the right side, the cross-bedding structures are well preserved. This group of base surge beddings is overlain by the soil layers. On the bottom of the chute-and-pool structure, there is a thin layer with coarse-grain size and relatively reverse grading characteristics (photo B of Fig 35). The probable grain size of base beds is approximately 3.5 to 4+ in phi value, and the coarse pyroclastic fallout is about -2 to -3.5 in phi values of grain size, except some large-sized clasts, which are depicted in photos B and C of Fig 35. The underlying base surge deposits represent some small-scale

depressions or sags of about 10 cm wide and 5 cm deep (black curves in photo B of Fig 35), which are possibly formed by the ballistic bombs. However, in this section no sign of large-sized bombs is observed. It is assumed that the bombs must have collapsed from the edge of the beddings or been carried away by some post-eruptive processes. As always, the coarse bedding shows the slightly reversed grading of about 11 to 15 cm in thickness (white arrow in photo B of Fig 35). Photo D of Fig 34 indicates the lateral development of the surge beddings with well-formed laminations and the trend of cross-bedded contact with topsoils.

3) Tongxin lava spatter

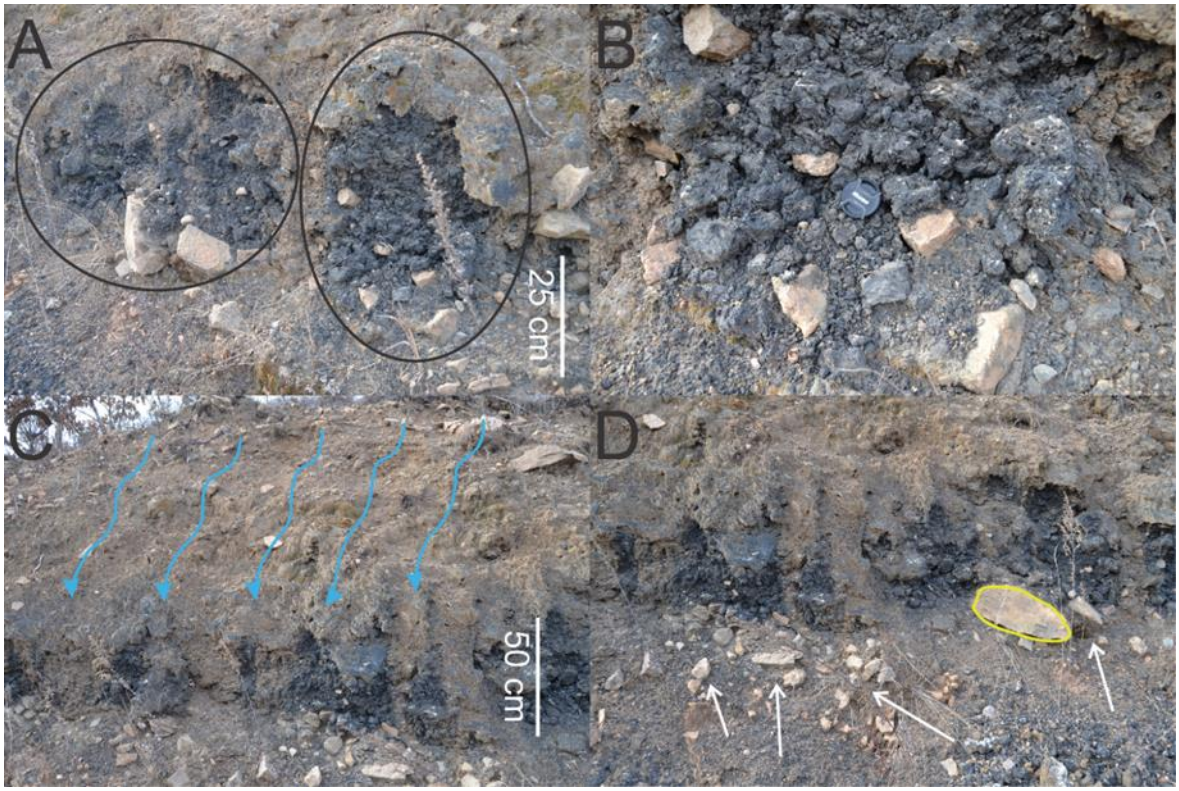

Figure 36: The lava spatter structures on the rim of Tongxin Crater show the ambiguous fluidal eruption potential of lava through mud-rich, wet craters in time as the magma rise and flux increased and/or approached toward the stage when the external water supply became exhausted (captured by Prof. Karoly Nemeth in 2016, China).

Fig 36 depicts the spatter deposits with chaotic structures, as well as the non-bedded system. Photo A of Fig 36 shows the two portions of collapse exposing the inner structures of the spatter lava of no more than about 50 cm thick. Photos B and D present the relatively large accidental lithics within or outside the spatter materials. The accidental lithics within the spatter indicate the mixing between the lava fountain and the wall rocks; the accidental lithics outside the spatter imply the subsequent mud flow or lahar occurred during the post-lava-fountain eruptions. Photo C shows the typical fluidal structures on the top of the lava spatter (blue-curved arrows), which are suspected as mud flow or lahar.

4) Tongxin distal tephras

On the SE side of the Tongxin Crater, there is another outcrop which represents a series of pyroclastic deposits of about 6 to 7 m high. The altitude is about 626 m above sea level. The distance is approximately 1.1 km away from the Tongxin Lake. As shown in Fig 29, this site is marked as the Tongxin Town Outcrop, and on its opposite side another Extra Outcrop is revealed. This section will discuss the details of these two distal outcrops of Tongxin volcano.

The major outcrop of this site is composed of a range of parallel and planar beds of coarse-grain size. The weakly-bedded coarse layers are intersected by the thin and finer grain-sized lapilli sediments.

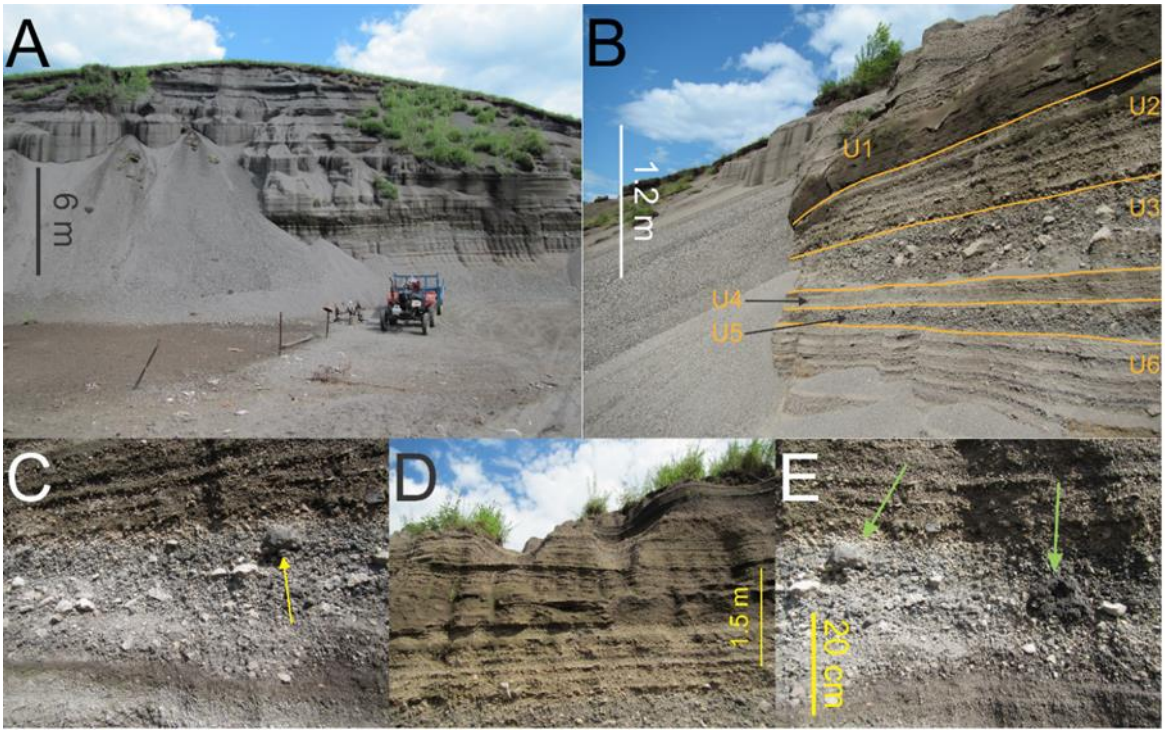

Figure 37: The significant characteristics of the Tongxin distal outcrop have various combinations ranging from tephra to pyroclastic beddings (captured by Prof. Karoly Nemeth in 2016, China).

Fig 37 A depicts the whole view of this site, and several parallel beds with laminations are the main feature of the bedding system. Photo B of Fig 37 is the detailed and close view of this site. Generally, this series of beddings is divided into six layers which are marked as brown lines. On the upper part of the beddings, a dark and moist layer named as U1 presents a relatively fine-grain size with coarse lithic particles, and the lamination is well developed, as well as poor sorting. Due to the collapsed mantling of the lateral successions, other structures are unnoticed. The underlying U2 layer is a grey-dark laminated bed with coarse grains and poorly-sorted structures. The detailed view in photo D of Fig 37 shows the larger size of accidental liths is dispersed within this layer. Layer U3 is the most significant bed in this site, and photos C and E depict that the large-sized juvenile bombs and lithic clasts (green and white arrows in photos C and E) are preserved among the coarse, poorly-sorted and non-bedded matrix. Ambiguous reverse grading can be observed. This layer also represents the medium degree of agglutination and welding, which indicates that Strombolian-style

eruptions intervened in the periods of phreatomagmatic eruptions. The percentage of accidental lithic particles is low. Grain size is probably ranging from -0.5 to -4 in phi values. The thickness of this layer is approximately no more than 20 cm. The U4 layer is a thin, finer-grained and poorly-sorted bed intersecting between U3 and U5, which has similar structures to U3 except for the thickness. The thickness of U4 is about 5 to 7 cm. The grain size is possibly ranging from 0.5 to 2.5 in phi values. No sign of welding or agglutination represents the small magnitude of phreatomagmatic volcanism. As mentioned, the underlying U5 layer has similar structures to U3, which implies the small amount of scoria or cinder generated from the small magnitude of lava-fountain or Strombolian eruptions. The thickness of this layer is about 7 cm. On the bottom of this site, the U6 layer is dominated by a group of parallel beds or laminations. The very thin inter-bedding systems probably represent the density flow (finer layers within the U6) on the bottom of the eruption column moving through the flank of the maar as base surges, which is covered by the fallout particles (coarser layers within the U6). Large-sized lapilli or lithic clasts are well preserved in this bed. This thickness is about 20 cm. The grain size is presumably ranging from -4 to 2.5 in phi values.

The tephra is also well developed on this site. The yellowish and non-bedded tephra deposits represent the distal transportation of the eruptive column during the phreatomagmatic eruptions. The location of this site is on the opposite side of the Tongxin Town Outcrop which is discussed above, and marked as Extra Outcrop in Fig 29.

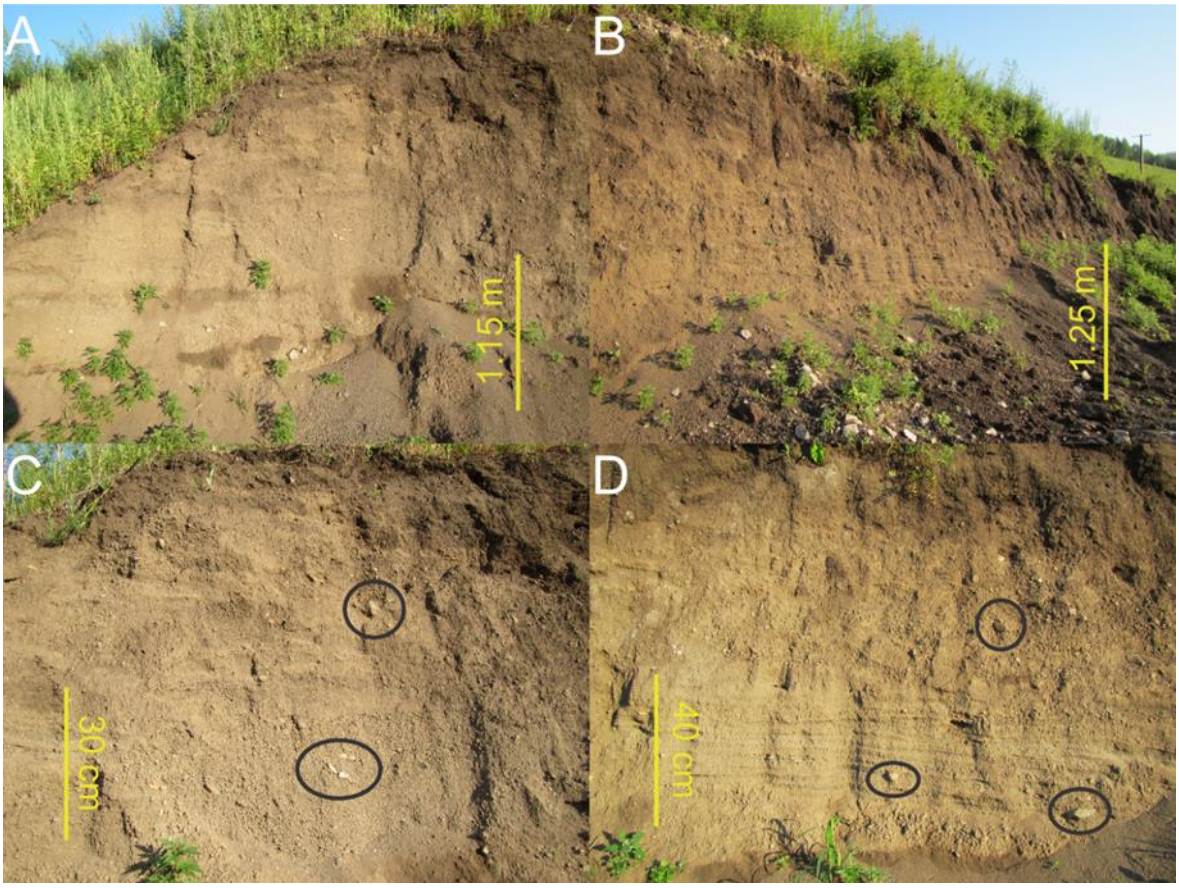

Figure 38: In the photos of the distal tephra deposit the small scale of lamination structures is preserved (captured by Prof. Karoly Nemeth in 2016, China).

As shown in Fig 38, the non-bedding tephra deposits are a yellow to brown colour with a little amount of accidental lithic clasts (black eclipses on photos C and D) as well as a lamination structure. The thickness of this outcrop is approximately no more than 3.3 m. The average grain size ranges from 3 to 4+ in phi value, which means a very fine grain size. Due to the non-bedded structure, there would be no grading alteration, but medium sorting to poor sorting. The grain size of large clasts is probably from -3.5 to -4.5 in phi values. Lamination structure is the exceptional feature in this outcrop with inter-beds between coarse and relatively fine grain layers (photo D of Fig 38). On the bottom of this site, beneath the laminations, a group of non-bedded, coarse and poorly-sorted deposits is preserved with small degrees of fluidal potential, which might be the surface density flow or debris flow.

Preliminary sedimentary/stratigraphy log

In terms of the preliminary observation mentioned above, the stratigraphy of the proximal and distal Tongxin volcano can be established. The successions of the tephra and pyroclastic beddings are evaluated as a preliminary stage of the study, regarding the observations during the field trip and laboratory works. Fig 29 depicts the contour lines which indicate the relatively structural relationship between these beds. Generally, the lithofacies are the non-beddings to beddings with laminations and cross-bedding. The pyroclastic beds typically represent the phreatomagmatic eruption phases intervened by small magnitudes of

Strombolian-type phases. In regard to the ages, the detailed information will be measured during the author's PhD period. This section will give the general sedimentary log around the Tongxin Crater. The absolute age of the Tongxin volcano is still unknown, so this sedimentary log will only be based on topography and regional elevations.

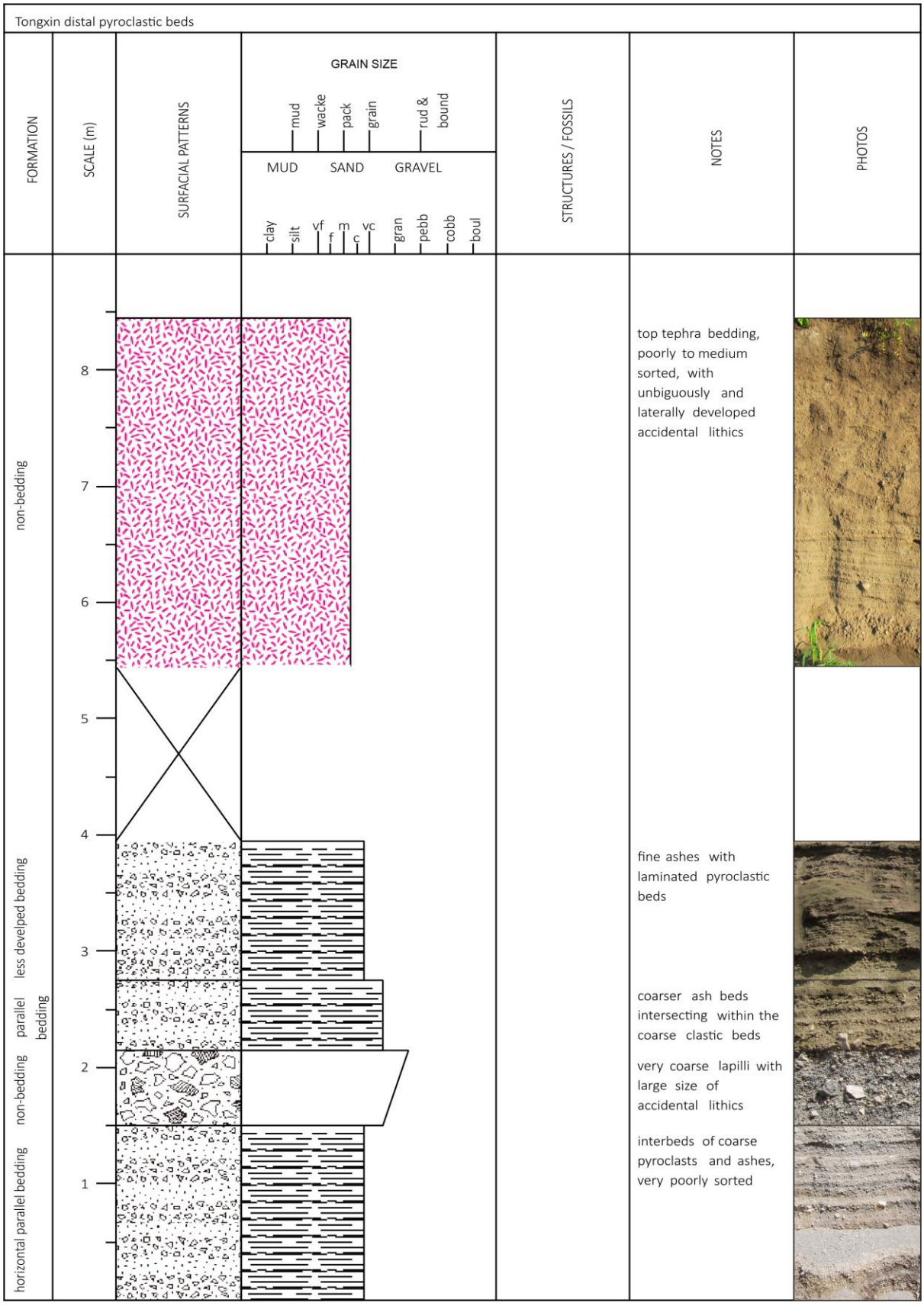

Table 2: The sedimentary log of Tongxin distal outcrop, knowing that the underlying beds of tephra layers are under investigation.

This site represents the tephra and distal fallout deposits (Table 2), and indicates the relative direction of the prevailing wind during the syn-eruptive stage. The pyroclastic beds and clasts with a larger size may imply the intensity of eruption. Due to the similar distance to the Tongxin Crater, the elevation of the tephra site is more than the distal pyroclasts site, so the tephra should be overlying on the latter.

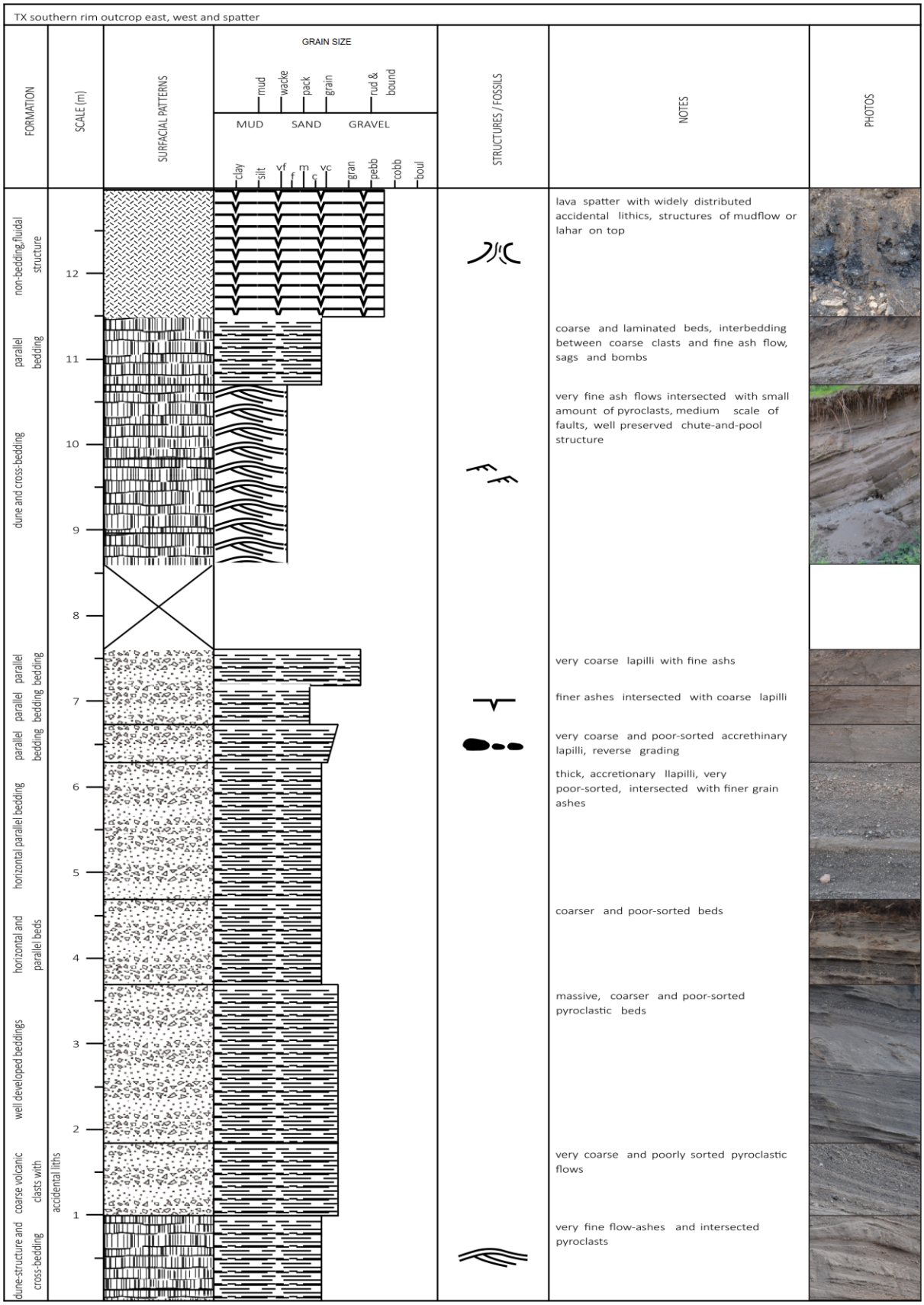

Table 3: The stratigraphic log of the Tongxin southern outcrops from the east to west flanks.

Table 3 depicts the distributions of sedimentary architectures from the Tongxin outcrop east to the Tongxin outcrop west, including the spatter site. As shown in Fig 29, the elevation of the Tongxin spatter site is the highest point, and also these sites are aligned on the SW rim of the Tongxin Crater, which means the relative organisation of the stratigraphy may follow Table 3. Note the underlying layers beneath the spatter site are unknown until the author's PhD period.

Generally, the structures of pyroclastic beds and flows are widely distributed. Although they have less evaluation and estimation, the volume of these volcanic clasts has magnificent quantities. This indicates the Tongxin Crater might be a large maar-diatreme volcano. The fixed age of this volcano is still unknown, however based on the previous research the entire area of the ACVF has undergone volcanism during the late Pleistocene. The Tongxin Crater probably has the same eruption timing at this stage. Also, the lava deposits are found on the western flank of the crater, which means the Tongxin Crater may experience a range of Strombolian-type or lava-fountain phases.

Microtextural analysis of Wusulangzi (AX1) and Tongxin (AX2) pyroclastic units

Two distinct sample groups were recognised and collected from the outcrops as well and named as Sample 1 and Sample 2. These two groups of samples were collected from Wusulangzi Lake and Tongxin Crater respectively. The systematic sieving process can be guaranteed for the concrete size corresponding to each typical value in phi. Basically, due to the quantities and estimation time of each sample, the sieving process was performed from -4 to 4+ in phi values in order to cover the general sizes of pyroclastic materials. The diameter of each sieve was utilised to separate different grain sizes ranging from 16 cm to 63 microns in association with -3.5Φ to 4Φ respectively. As mentioned, Sample 1 from Wusulangzi Lake is limited by a very preliminary field trip, thus this group only contains the pyroclastic materials. Sample 2, which represents the Tongxin Crater, has an amount of bulk rocks which are the lava flow or spatter, thus this group is relatively intact although the research is still in a preliminary stage. For pyroclastic rocks, optical light microscopy, 2D assessment as well as 3D imagery analysis are necessary in terms of their shape, vascularity, as well as the porosity distribution. As for the bulk rocks, thin sections and petrographic microscopy are the essence of the texture evaluation and mineral observation. This section will concentrate on the details of the observations and the techniques for each process.

Figure 39: The sieves of the grain-size analyses in relation to a set of different sieve sizes; the diameters of the sieves are from -4 to 4.5 in ϕ value.

Granulometry

In volcanology, the grain-size distribution represents the relative ratios between various sizes of the particles, and may also imply the eruption intensity. In terms of evaluation for the magnitude of the eruption, Sample 1 and Sample 2 have undergone the same processes of

the sample preparations. The sieves and their diameter were completed following the scheme, which represents the general grain-size distribution of the pyroclastic rocks. After the sieving process, about 18 packs of various grain sizes have been separated for Sample 1. The phi values range from -4 to 4.5 with 0.5 in the interval. Weighing each pack, the variation of weight is obvious.

For the assessment and evaluation of granulometry, the contrast between Wusulangzi Lake and Tongxin Crater is held by grain-size distribution curves and simple weight vs grain size. Both of them can depict the detailed sorting conditions and indicate the possible eruption intensity.

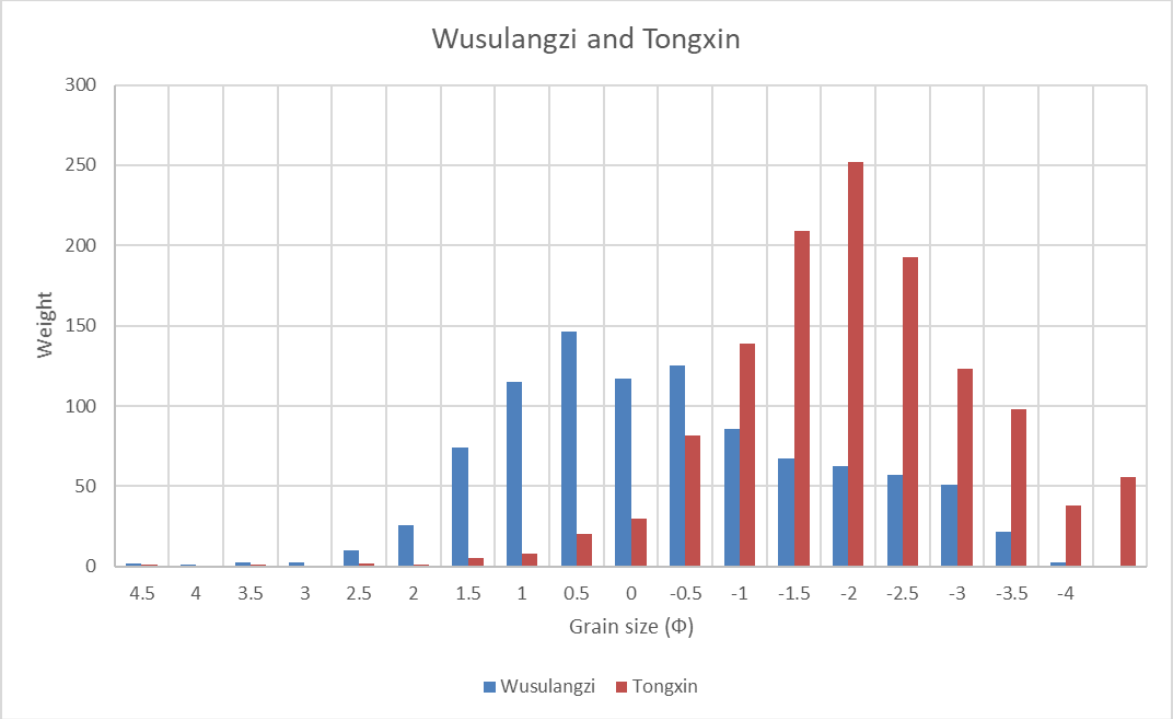

Figure 40: The sample comparisons between Wusulangzi Lake and Tongxin Crater in individual weight vs the corresponding grain size; note each grain size is assessed and collected from the sieving processes.

Fig 40 depicts the grain-size distribution in the concrete weight in association with their corresponding size. Observations from this bar chart, the highest point in the Wusulangzi sample group, occurs at 146.14 with 0.5 in phi value and, on the other side, the highest weight number of Tongxin Crater is 251.93 g with a phi value of -2. The dominant weight of grain sizes ranges from 1.5 to -1 within the Wusulangzi group, but they are less coarse than the Tongxin's, which ranges from -1 to -3.5. Measurements from the total weight for each sample group, due to the Tongxin group (Sample 2) observed, are more detailed than the Wusulangzi group (Sample 1), and the weight of Tongxin's in total is higher than Wusulangzi's. However, each percentage of corresponding grain size still represents the dominance in association with the eruptive intensity and sorting processes. From Fig 40, it is approximately 15.07% at the highest point in the Wusulangzi group with 0.5 in phi value. In contrast with Wusulangzi Lake, the major phi value is -2 with about 20.03% of the total weight in the Tongxin samples. In

regard to the class intervals of grading scales proposed after Wentworth in 1922, the prevailing grain size from Wusulangzi Lake is regarded as coarse sand, even very coarse sand. The dominant grain size that is from the Tongxin rim ranges from very fine gravel to fine gravel (Wentworth, 1922). The outline of each group presents similarly unimodal shape with a totally different potential of skewness. In statistical theories, the Wusulangzi group typically shows positive skewness, otherwise the Tongxin group obviously depicts a negative skewness pattern.

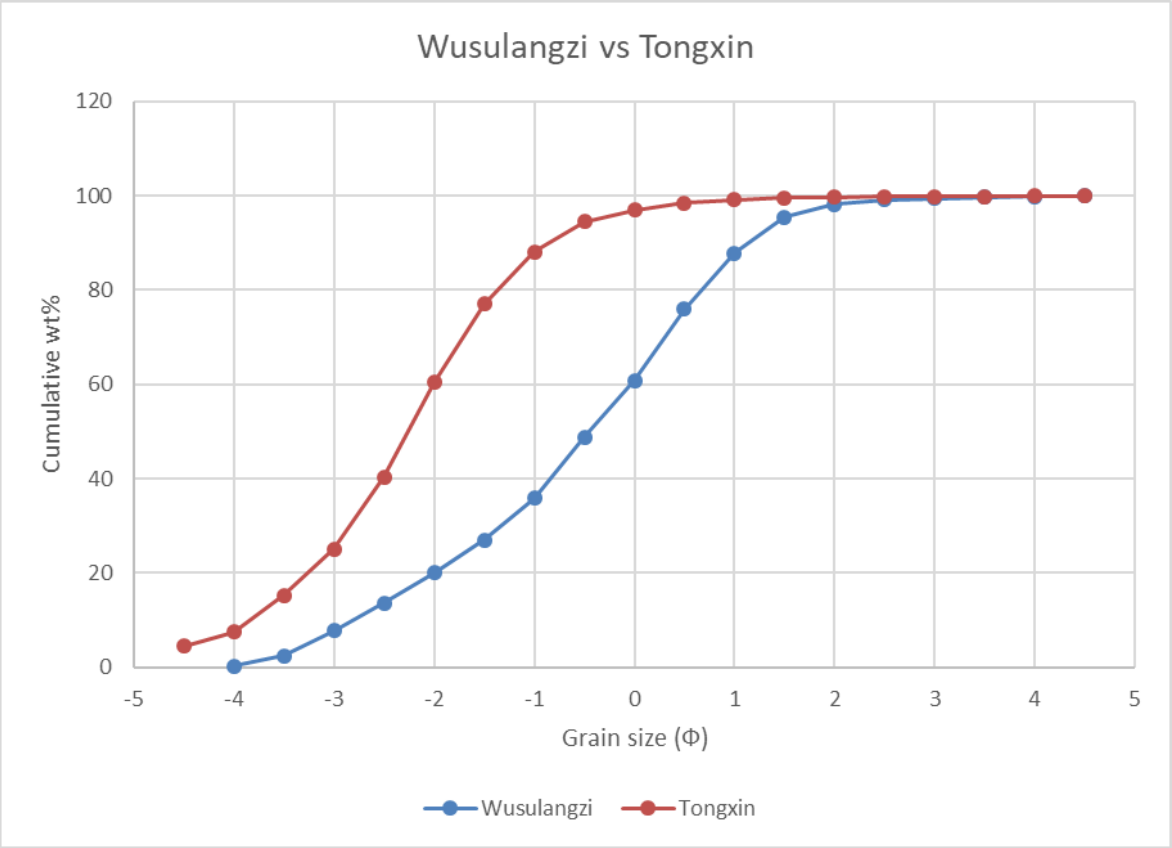

Figure 41: The curves of cumulative weight percentage are plotted by the cumulative weight percentage vs corresponding grain sizes.

The cumulative curves of Wusulangzi Lake and Tongxin Crater reveal the normal probability of grain-size distribution (Fig 41). These two curves depict the similar trend and S-shape potential ranging from coarse gravel to very fine sand textures. The slope of the Tongxin group is steeper than the Wusulangzi group. Also, the obvious grain-size accumulation of the Tongxin group has emerged from -3.5 to -1.5, which is the medium gravel to very fine gravel respectively. The slope of this section is approximately 45^{o}, which means the velocity of accumulation is rapid. Compared to the Tongxin group, the Wusulangzi group shows less cumulative velocity in grain size due to the more progressive trend of the curve. The major change in the Wusulangzi group is represented from -2.5 to 1.5 in phi values, which illustrates a grain size ranging from very fine gravel to medium sand. For each curve, the steepest point is located at -2 and 0.5 in phi values of the Tongxin group and Wusulangzi group respectively. This may imply the most violent timing during the eruption. In statistical theories, the upper-

quartile points and lower-quartile points constrain the inter-quartile section, which indicates the main accumulation process during the syn-eruptive deposition. In observation of Fig 41, the lower-quartile point is lain at 25% in the cumulative weight percentage, otherwise the upper-quartile point is at 75% in the cumulative weight percentage. Corresponding with abscissa values of lower-quartile points, the -3.5 in phi value lies in the Tongxin group and -2 in the Wusulangzi group. The corresponding abscissa values of upper-quartile point are -2 and 0 in phi values of the Tongxin and Wusulangzi groups respectively. Between the lower and upper-quartile points, the inter-quartile section represents the obvious alteration and variation. The inter-quartile section of the Tongxin group ranges from -3.5 to -2, which indicates the medium gravel to fine gravel; in the Wusulangzi group, the inter-quartile section is from -2 to 0, which implies fine gravel to very coarse sand. Thus, judging from the degree of coarseness, it is recognisable that the Tongxin group is coarser than the Wusulangzi group, inferring the possibly eruptive intensity differences between Tongxin and Wusulangzi.

Optical light microscopy

As mentioned, due to the schedule of the field trip the whole bulk rocks were found around the Tongxin Crater, while there were no bulk rocks collected from the surroundings of Wusulangzi Lake. Within each grain size, various colours are separated into different compositions. Generally, dark, dark-grey, grey as well as yellow-brown colours are the majority of the combination. These variations of colours represent juvenile particles, accidental lithics, alkali feldspar or plagioclase in association with intra-plate volcanism. This part will give the microscopy observations for pyroclasts of each sample group (i.e. Wusulangzi-Sample 1 and Tongxin-Sample 2).

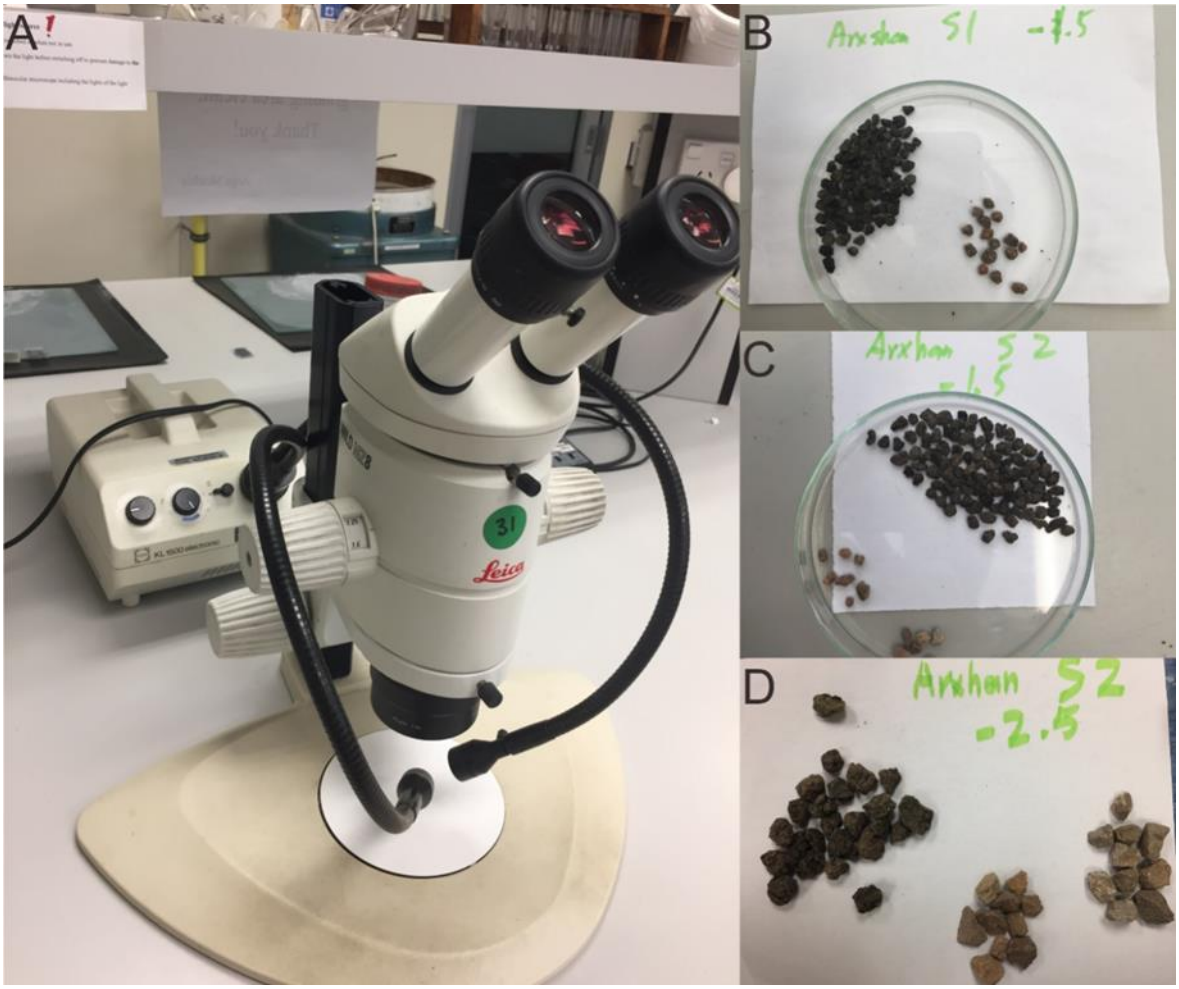

Figure 42: The optical microscope with the pyroclastic samples.

Photos were captured from the very coarse sandy grains with 0 in phi value. The varieties of compositions are obvious under the observations from optical light microscopy-SCHOTT KL 1500 Electronic (Fig 42, photo A). Some photos were captured through a cell phone.

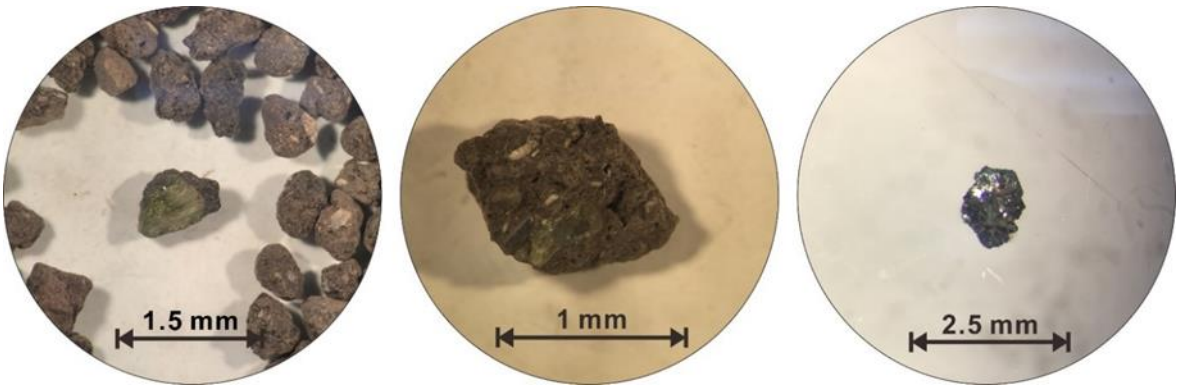

Figure 43: The photos of pyroclasts observed from optical-light microscopy; note the grain size is approximately 1 in phi value, i.e. coarse sand.

Fig 43 depicts the detail of juvenile particles with 1 in phi value. The grain size is simply coarse sand. The average diameter of each grain is about 1 to 1.5 mm. Judging from the outline of these particles, the colour is generally dark with a little bit of grey. This reveals that the

majority of the compositions are juvenile materials. As shown in the first two photos, a juvenile substrate encloses the accidental lithics which are possibly alkali feldspars, and it is occasionally centred with olivine crystal. The shape of the grains range from blocky to sub-rounded outlines with less-developed vesicles. The structure of each particle has abundant mosaic-like cracks and joints, which correspond to typical features of hydroclastic deposits (Fisher and Schmincke, 1984). The third picture reveals a cauliflower-shaped juvenile grain with a high reflection of lustre, a jointing structure, as well as a blocky or sub-rounded shape.

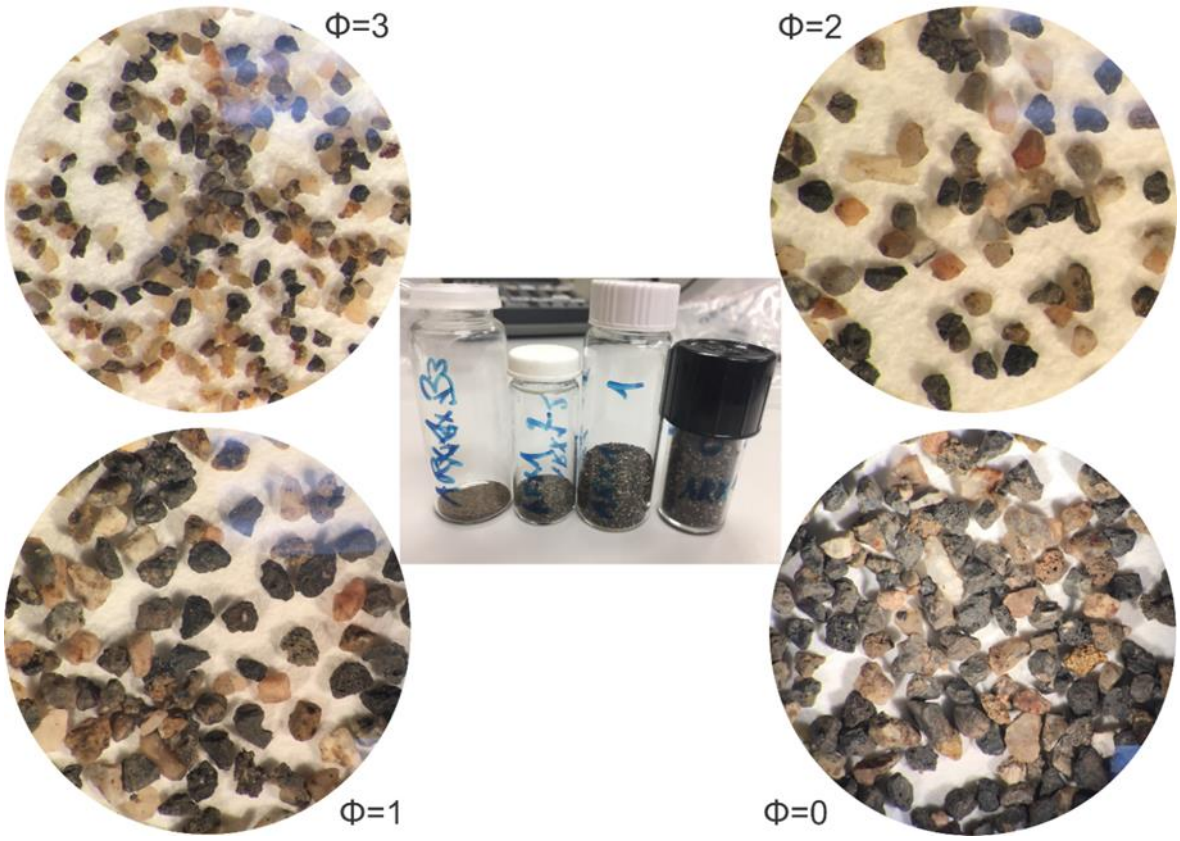

Figure 44: The optical microscopy images of Sample 1, i.e. Wusulangzi Lake.

Fig 44 depicts the observation of Sample 1 from the optical light microscopy-SCHOTT KL 1500 Electronic (Fig 42, photo A). From the four photos representing the four grain sizes (from 0 to 3 in phi values), the juvenile particles dominate the majority with a black colour and the vesicle's structures on the surface are precise and recognisable. The yellow-brown clasts may indicate alkali feldspars. Another type of mineral is represented by the white to grey clasts which are the plagioclase. The glass sharps can rarely be seen. In the photos of φ1 and φ0, the alkali feldspars and plagioclases may transfer into the larger sizes of the granites (brown to grey particles). Some yellow-brown particles with vesicles have low-to-medium compositions, and they may imply the medium intensity of phreatomagmatic eruptions.

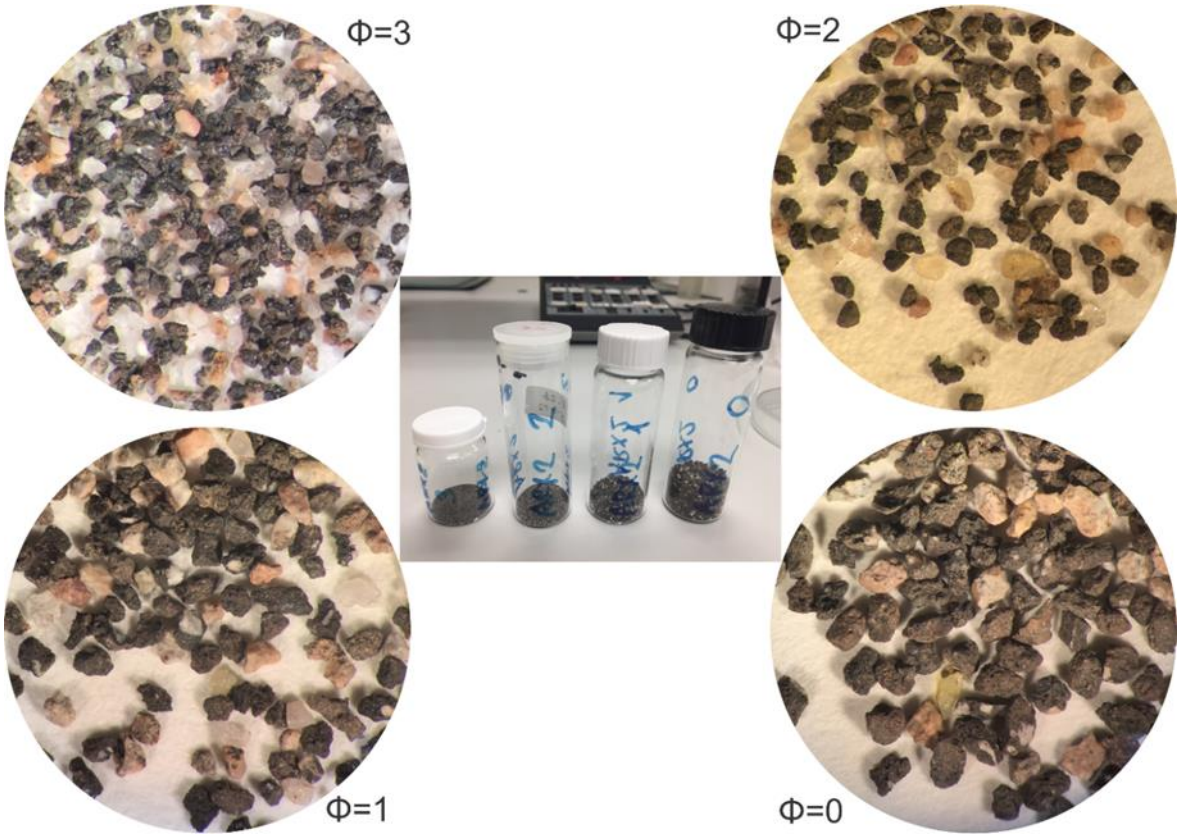

Figure 45: The microscopy images of Sample 2, i.e. Tongxin Crater, with grain size from 0 to 3.

Fig 45 shows the compositional factors of Sample 2, i.e. the Tongxin Crater. From the photo of φ3, large amounts of glass sharps emerge with a relatively high percentage of alkali feldspar. Little amounts of olivine can be observed from photos of φ1 and φ0. Compared to Sample 1, the xenoliths have been increased. Similar to Sample 1, the colours in Sample 2 represent various minerals: juvenile for black colour, alkali feldspar for brown-grey colour, plagioclase for white-grey colour, and green particles implying olivine; also the transparent clasts indicate glass shards.

Generally, the highest amount is juvenile particles which are almost 90%, plagioclase and alkali feldspar occupy approximately 10%, with others including olivine and glass shards being less than about 5%. Xenoliths are commonly observed. The appearance of olivine indicates both of these samples are mafic to ultramafic. Sample 1 preserves the relatively medium vesicles compared to Sample 2 with high vesicles, and both of them represent the medium-to-high intensity of phreatomagmatic eruptions.

Petrographic microscopy and thin sections

The thin section observation is critical for the petrology of pyrogenetic rocks. As mentioned, there are 14 thin sections made for the observation from petrographic microscopy. The details of each section are revealed under a cross-polarised lighting microscope. Due to the absence of bulk rocks from Wusulangzi, this portion will only show the observation details of the Tongxin sample group. By utilising the Nikon Eclipse E600 POL with the LU-Plan 5×0.15

Pol scope (Fig 46 A), the details are revealed as a matrix, with crystal textures as well as lithic compositions. The preparation of the thin sections has undergone a series in the process by utilising the instruments which are shown in Fig 44. Bulk rocks are cut into small dices or pieces and the sample is pasted onto the glass sections. The observation was held under the petrographic microscopy instrument which is depicted in photo A of Fig 46. The grinder and polishing machines were facilitated for the sample preparations (photos B and C of Fig 46).

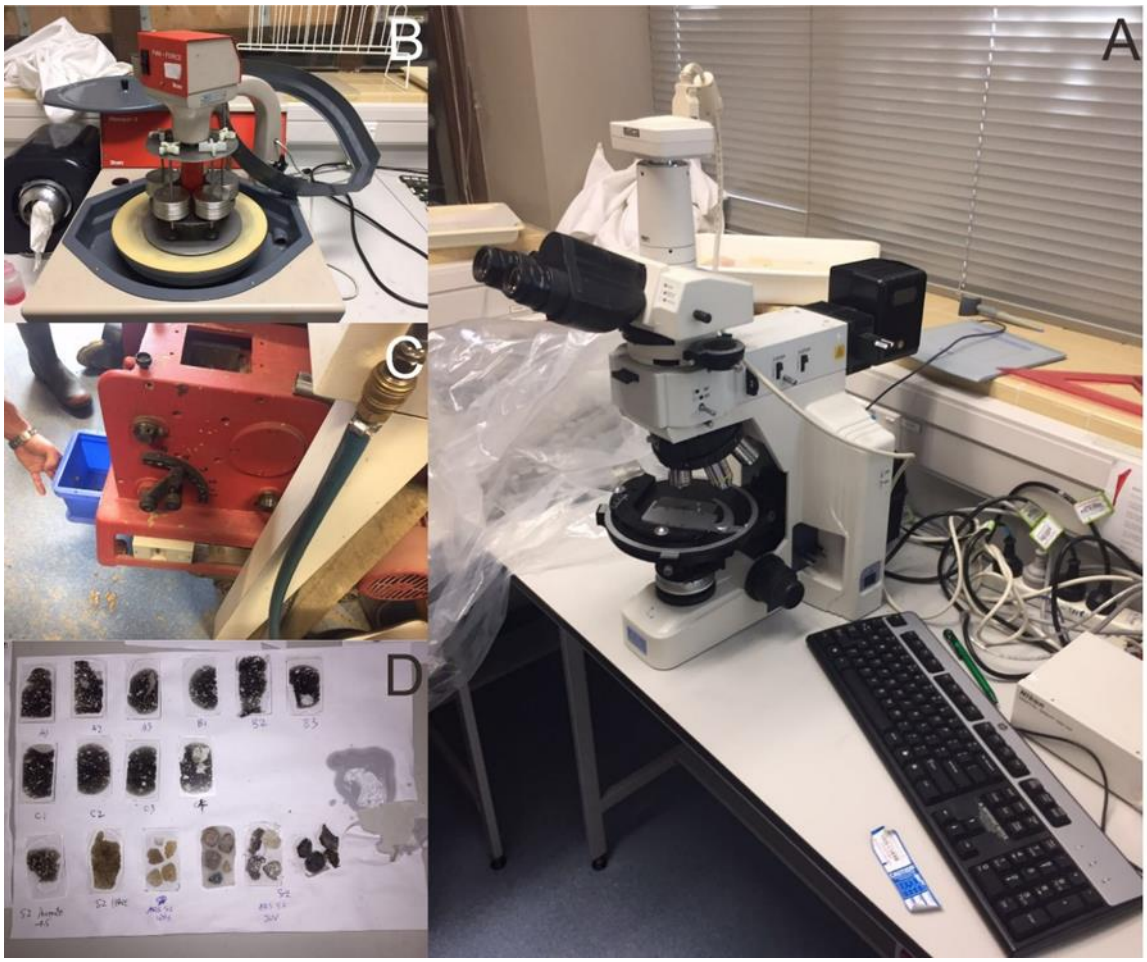

Figure 46: The analytical instruments for petrographic assessment.

The variety of the distribution between juvenile substrates and lithics possibly represents the magnitude of fractional crystallisation and the compositions of the bulk rocks which indicate the lava flow. Although lots of photos were captured, only some give a glimpse of the implications of the properties.

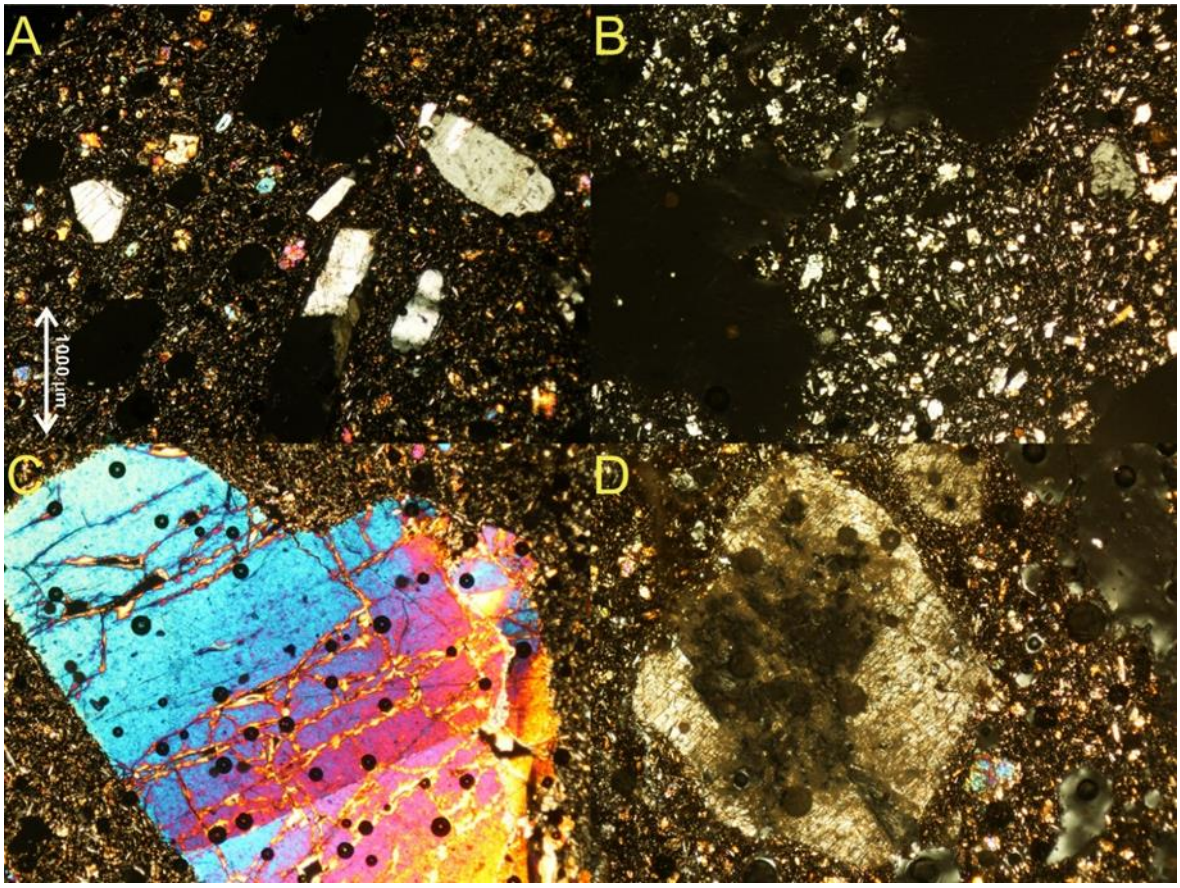

Figure 47: The photos of thin sections captured by petrographic microscope. In these pictures, the cross-polarised observation reveals the detailed relationship between crystals and the surrounding matrix. Note these four photos have the same scale (photos captured at the minerology lab at Massey University).

Fig 47 presents the abundant amount of glassy textures of the matrix with the fractions of plagioclase and a large pyroxene (photo C of Fig 47). Photo A depicts the several vesicle structures (black void areas), plagioclases (white with joints) and other crystals. Photo B represents the plagioclase-dominant glassy matrix textures with a small number of olivine crystals (dark-green particles). Picture C is the above-mentioned pyroxene crystal, and the fractures are recognised on the surface of the pyroxene. The surrounding glassy matrix is dense. Photo D shows a large plagioclase crystal cracked in two parts with well-developed joint structures. This plagioclase is enclosed by the highly-dense matrix with an amount of plagioclase fractions, and the glassy shards are also recognisable (dark-grey with smooth surfaces). The rims of each crystal are sharp and clear. Other observations have shown the high degree of phreatomagmatism during the eruption.

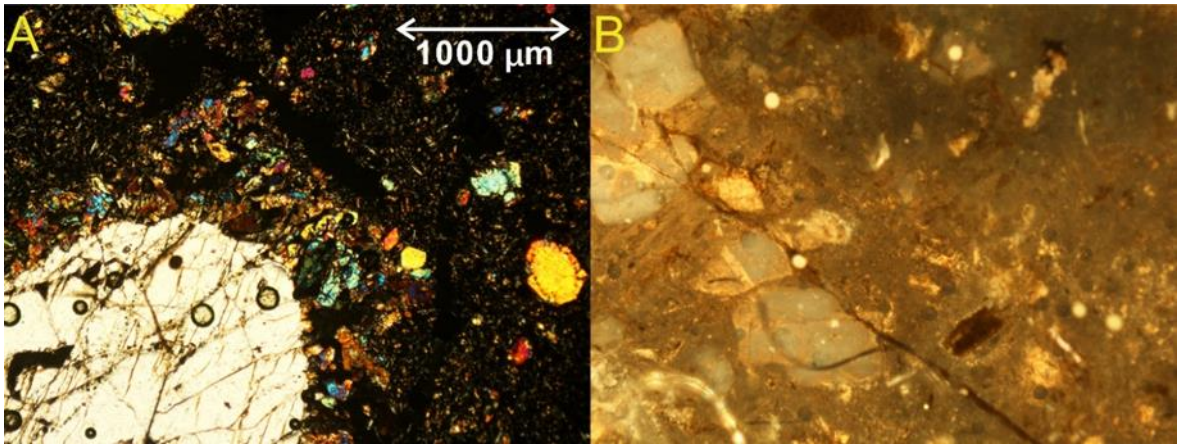

Figure 48: Two photos depict this rare phenomenon – mineral shell in photo A and palagonitisation in photo B – in the observation of the thin section; the scale is same for both photos.

Fig 48 depicts the two infrequent phenomena which indicate the crystallisation processes and magma-water interaction during eruptive phases (Heiken, 1974; Németh and Kereszturi, 2015; Valentine and White, 2012; White and Ross, 2011). Photo A shows a significant plagioclase surrounding a mineral shell. This may indicate the secondary crystallisation contemporarily occurred during the major mineralisation. The mineral shell might compose of pyroxene and olivine. The medium rounded crystal on the right is probably an olivine. As usual, the glassy matrix encloses the rest of the crystals. Photo B depicts the rare phenomenon of palagonitisation which implies a high intensity of water-magma interactions. The large-sized plagioclases are surrounded by the dense-lithic matrix. Generally, the textural characteristic of palagonitisation is a wax-like substance, as well as hydrous, altered basaltic glass textures (Fisher and Schmincke, 1984). As photo B represents, the surface of the plagioclases and matrix is observed as a vitreous lustre with a smooth property.

Back-scattered Electron Microscopy (2D)

The 2D imagery assessments and evaluation were contributed to by Back-scattered Electric Microscopy – FEI Quanta 200 Environmental Scanning Electron Microscope (SEM) with an EDAX module. The 2D BSE imagery can reveal the surface of juvenile and accidental lithics, in association with their shapes, vesicle shapes and internal structures, and thus it may indicate the magnitude of phreatomagmatic interactions and the intensity of magma fragmentation. Massey University has provided the microscope imagery lab to contribute the opportunities for 2D analysis and BSE observation. Three plugs have been produced and polished on the Planopol-3 of Struers (photo B of Fig 46). For both groups of the samples (Sample 1 for Wusulangzi Lake and Sample 2 for Tongxin Crater), choosing the same grain sizes can facilitate the outcomes and require the equal comparison of the analysis and observation.

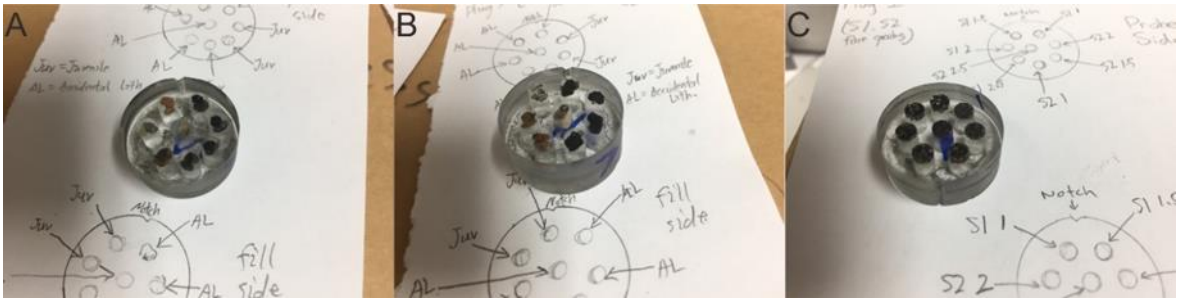

Figure 49: Plugs for BSE 2D analysis.

The grain sizes were chosen from 2.5 to -1 in phi values, while 0 in phi value is an exception. From 2.5 to 1 in phi values implies from fine sand to medium-coarse sand was inserted in the plug which is depicted in photo C of Fig 49. The rest of the two samples with the same grain size in -1 of phi value were plugged into two plugs which are shown in photos A and B of Fig 49.

The following part will illustrate the 2D BSE imageries of Sample 1, i.e. Wusulangzi Lake and Sample 2, i.e. Tongxin Crater. Generally, the vesicles between these two destinations is typically different in porosity density and distribution. However, the intensity of fractional crystallisation is similar. The surface textures are slightly different due to the velocity of solidification. Shapes of total samples are sub-angular to sub-rounded. The xenoliths can rarely be found.

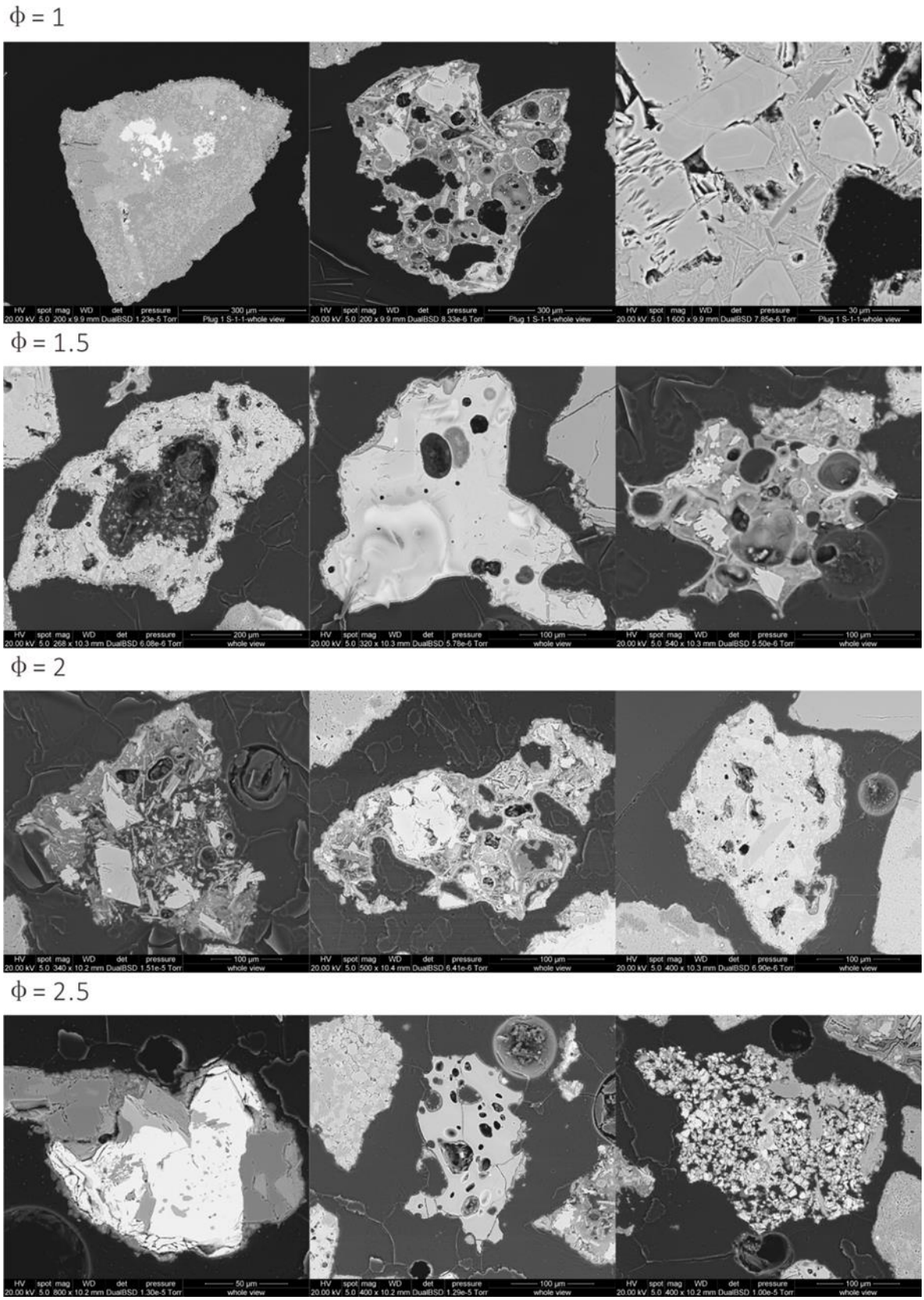

Figure 50: The 2D BSE imageries of Sample 1, i.e. Wusulangzi Lake. Four separated grain sizes were analysed in association with their textures and vesicles.

Fig 50 depicts Sample 1 collected from Wusulangzi Lake with 2D BSE imagery which is held at Massey University. These 12 photos show the relatively sub-angular to sub-rounded shapes for each grain. The first row indicates the grain size is 1 of phi value, the left-side photo depicts an accidental lithic with a sub-angular shape, as well as a poor to non-vesicular structure. The white areas may represent plagioclase. The interaction between water and magma might be at high-level degrees due to the highly-fragmented particles (the second photo of Φ1, the third photo of Φ1.5, and the second photo of Φ2). The vesicles are poorly developed, which is shown in the second and the third photos of Φ1.5 and Φ2 respectively, and it may indicate the gas loaded by the magma is relatively low. Also, the shapes of the vesicles are nearly rounded. Juvenile textures are typical and obvious and crystals are well evolved and developed, especially in the third photo of Φ1. The structures of tree-rings can be clearly seen on the surface of the plagioclases, and this may imply the development and evolution of crystals was experienced over a long range of periods. In the second photo of Φ2.5, the crystal textures are absent on the surface, however the vesicle is poorly developed, thus it may indicate this juvenile particle has experienced a very rapid temperature drop and the processes of crystallisation were too slow to occur. The shape of the vesicles is nearly rounded, which indicates the bubble inflation is probably constant without the sudden alteration of external pressure.

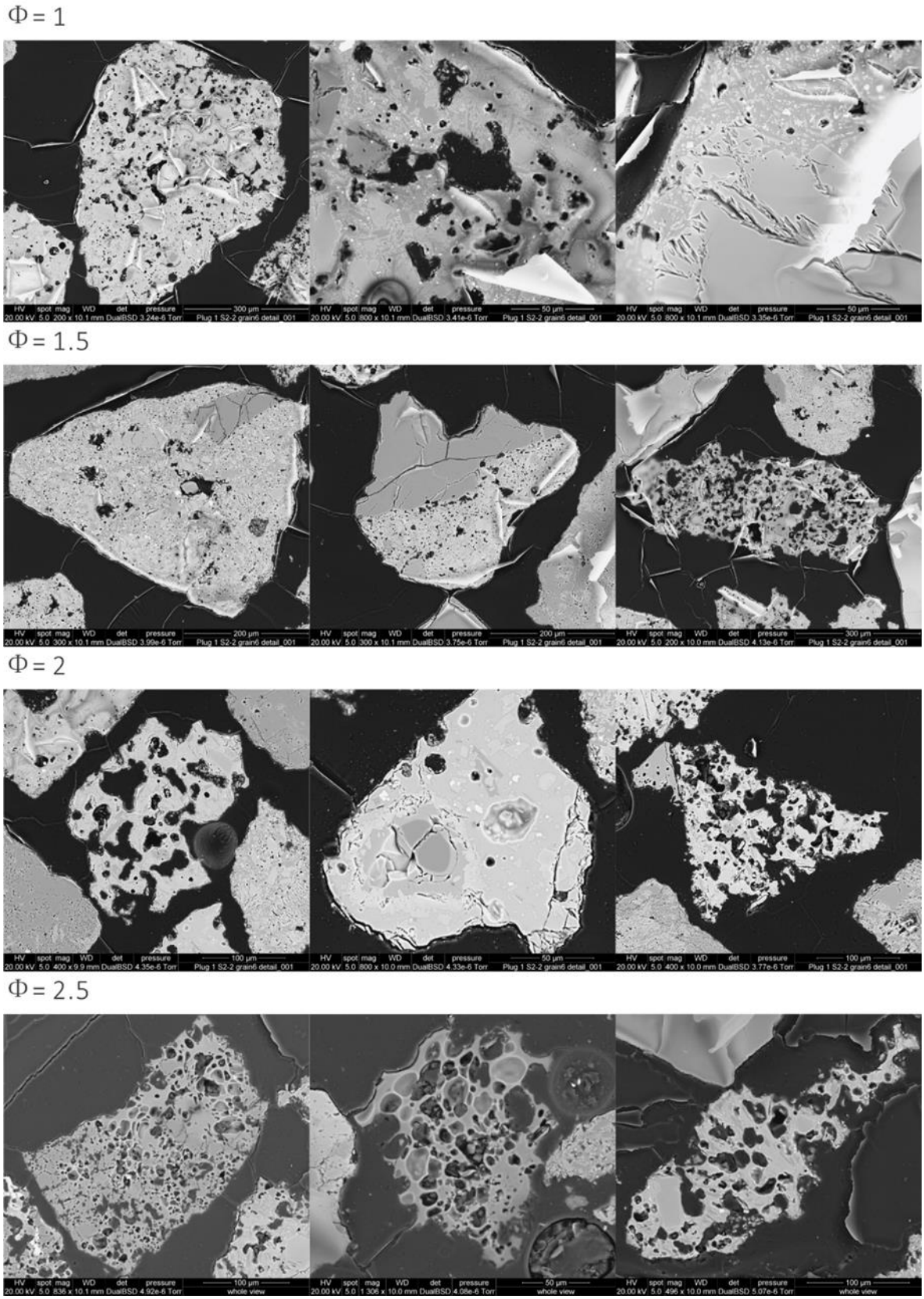

Figure 51: 2D imagery of Sample 2, i.e. Tongxin Crater.

Fig 51 reveals Sample 2, which was collected from the rim of the Tongxin Crater. With similar observation processes, the 2D imagery tech depicts the similar shapes and structures of

Sample 2 in relation to Sample 1. However, the vesicles and the textures of Sample 2 have a range of differences from Sample 1, which may indicate these two sites may have undergone the distinguishing processes of volcanism. The grain sizes are chosen as Sample 1 from Φ1 to Φ2.5 with 0.5 in its interval. Generally, the shapes of particles from Sample 2 range from sub-angular to rounded types, including a slightly sub-rounded style. In other words, the shapes of Sample 2 from the Tongxin Crater rim are diverse. The crystal structures can be observed from the surface of the particles, nevertheless the evolution and development of the crystals are varied. The varieties of crystal evolution may indicate the various cooling times due to the fractional crystallisation with long-time cooling. Similar to Sample 1, the xenoliths are well developed in Sample 2. The vesicles are far more advanced than Sample 1, which implies an intensity of phreatomagmatic eruption is strong at the Tongxin Crater and is more violent than at the Wusulangzi Lake. In observation from the BSE, the average percentage of the vesicles is generally no more than 80%. The shapes of the vesicles are typically sub-rounded to rounded with diversities of size. Xenoliths have highly-developed vesicles but with nearly non-crystal textures. The percentages of vesicles represent the progressive increase in relation to the grain sizes and indicate the intensity of phreatomagmatic eruptions. Also note that the first and the second photos of ϕ2.5 represents the non-crystal texture, which presumably represents the rapid cooling. Compared to Sample 1 (Wusulangzi Lake), the shape of the vesicles of Sample 2 (Tongxin Crater) is sub-angular, even irregular, which means during the inflation of the bubbles rapid or sudden external pressure may have occurred when the magma was ascending.

Averagely, the sizes of the vesicles are various (e.g. the second photo of ϕ1), however compared to Sample 1 (i.e. Wusulangzi Lake), Sample 2 preserves high amount of vesicles with small sizes. This may indicate the intensity of phreatomagmatic eruption is totally obvious and different. The degrees of fragmentation are also various due to the quantities of the vesicles and the shape of the particles, especially in Fig 51, the first and the third photos of ϕ2, as well as the third photo of ϕ2.5, which represent high degrees of fragmentation. The crystals are well developed and evolved, and this may imply both eruptive sites have the same situation of fractional crystallisation.

The following part will be also present the 2D images of Sample 1 and Sample 2 but with the grain size at ϕ-1 meaning the coarse grain size. Photos A and B of Fig 49 depict the two plugs which contain these two groups of samples in ϕ-1. In regard to the same grain size of the different samples, the individual juvenile particle and accidental lithic are observed equally.

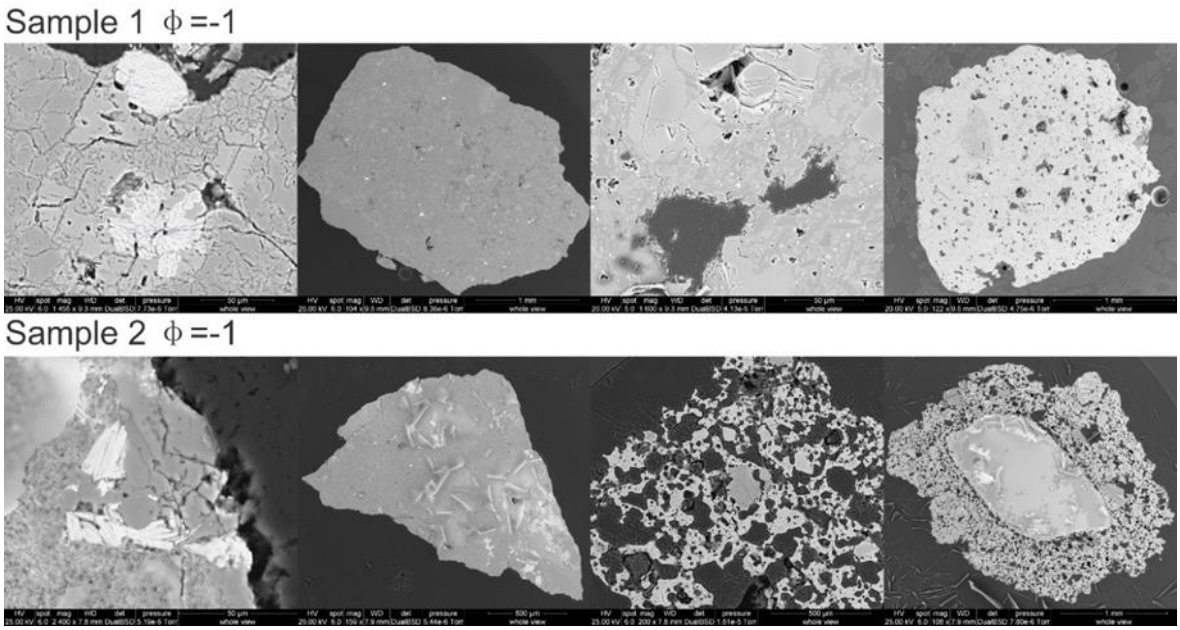

Figure 52: Photos of Sample 1 and 2, i.e. Wusulangzi and Tongxin respectively, with a grain size of -1.

Fig 52 is the group of photos which show the detail of juvenile particles and accidental lithics collected from Sample 1 and 2, i.e. Wusulangzi and Tongxin respectively, with the grain size at -1 of phi value. The first two graphs for each group depict typical accidental lithics. Both of the two groups have similar structures and shapes in accidental lithics, which present as low to non-vesicles, cracks and jointing textures, as well as small amount of clasts (the first photo of each group). The shapes of the accidental lithics are generally angular to sub-angular. The last two photos represent juvenile particles from each group, and similar to the grain size of 1 to 2.5 in phi values, the juvenile particle of Sample 1 shows the poor vesicles and the sub-rounded to rounded shapes. The xenoliths are enclosed by the surrounding juvenile shell, however their quantities are rarely observed. Also assessing from the pictures, the degrees of fragmentation might be low due to the low density of the vesicles. Compared to Sample 1, Sample 2 depicts the various conditions. The surface textures of accidental lithics present as similar to Sample 1, but the amount of cracks is ambiguously more than Sample 1 and the shape of the accidental lithics ranges from sub-angular to sub-rounded categories. The cauliflower-shaped minerals are well preserved as in Sample 1 (the first photo of Sample 2, Fig 52). The juvenile particles have typical and recognisable characteristics compared to Sample 1. As the last two photos of Sample 2 depict, the vesicles are far more advanced and developed than Sample 1. The last photo of Sample 2 shows an intact xenolith, the surrounding juvenile shell has a highly-vesicular structure, and the percentage of the void spaces is approximately more than 55%. As in the third photo of Sample 2, the highly-fragmented juvenile materials indicate the high intensity of phreatomagmatic phases. Basically, the shape of the juvenile particles is nearly rounded, but some of them have sub-rounded shapes.

Scanning Electron Microscopy (3D)

The 3D images of Sample 1 and Sample 2 were processed using scanning electron microscopy – FEI Quanta 200 Environmental Scanning Electron Microscope (SEM) with the EDAX module. 3D imagery observation was utilised for the evaluation and assessment of the particle shapes, and void spaces in various grain sizes, specifically for the fine to very fine-grain sizes. This section will give the 3D SEM images for the grain shapes, vesicles, as well as texture assessments. For each group, microtextures will be specified for the fine to very fine grains which were picked as 2, 2.5 and 3 in phi values.

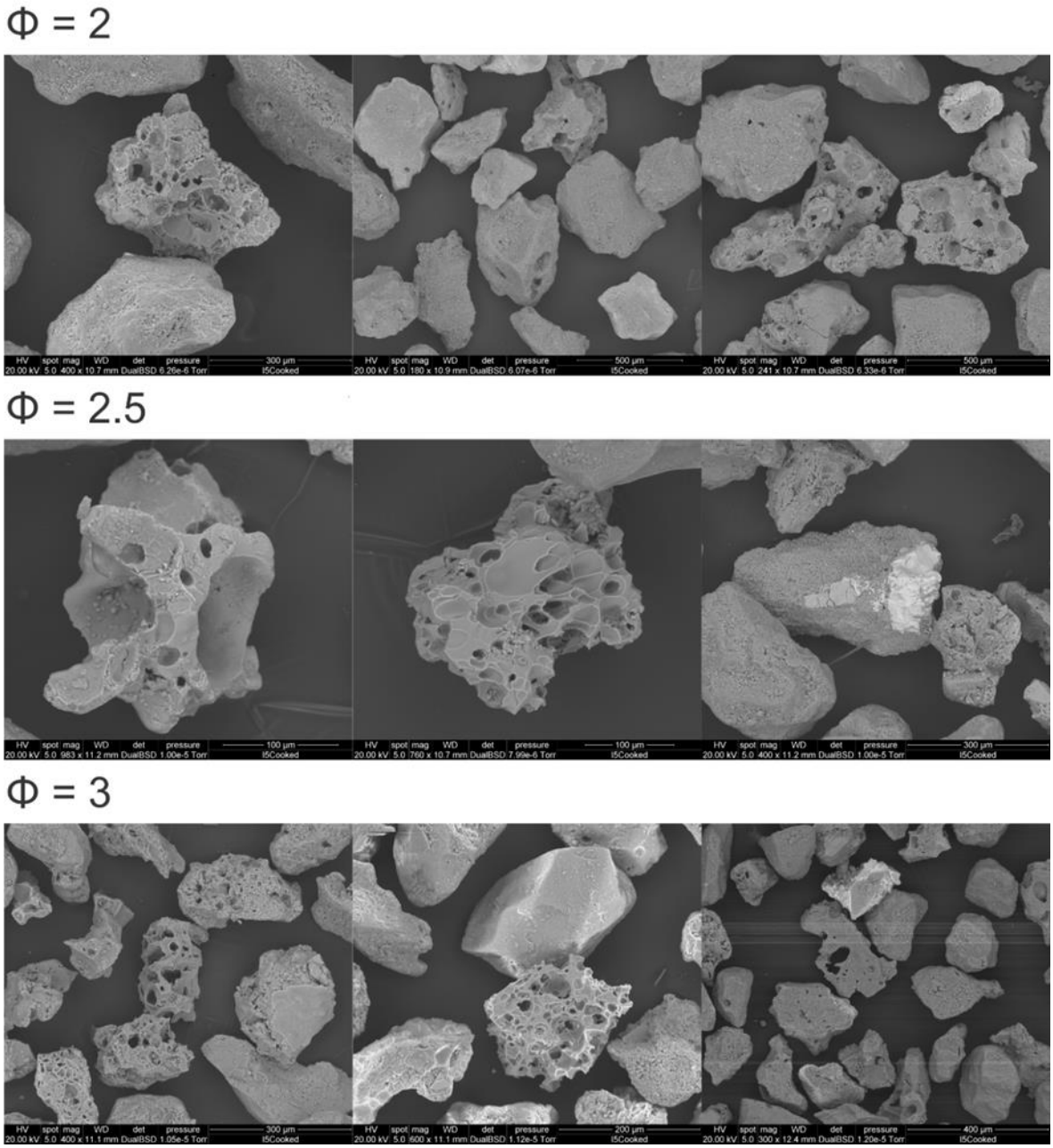

Figure 53: The 3D SEM images of Sample 1, i.e. Wusulangzi Lake.

Fig 53 depicts the 3D images of Sample 1 (i.e. Wusulangzi Lake). The shape of the particles is averagely sub-angular with minor sub-rounded clasts. The vesicles are in intermediate to low

development, and their shape is almost rounded. The first and the third photos of φ2 show the slight varieties for both juvenile particles. Intermediately-developed vesicles with a relatively small volume compared to a relatively large volume, as well as poorly-developed vesicles, indicate the various stages of the phreatomagmatic phases. The second photo of φ 2.5 depicts a juvenile particle without the crystal texture on its surface. This may imply a relatively rapid cooling processes. The shape of vesicles is averagely rounded and well developed. Specifically, the last photo of φ2.5 reveals a mineral-bearing accidental lithic, and the fractional surface is smooth, presumably a plagioclase. The three photos of φ3 represent the various shapes of the juvenile particle with relatively well-developed vesicles. Clasts with irregular shapes are accompanied by the rounded shape of the vesicles. Typically, the second photo of φ3 depicts a fragmented juvenile clast with a nearly non-crystal structure on its surface, and this might also relate to rapid cooling time. The vesicles of Sample 1 reveal a progressive increase in association with the grain sizes. The shape of the vesicles is generally sub-rounded with an occasional sub-angular type. The amount of the vesicles is poor-to-medium, and few of them preserve relatively high amounts of vesicles. The vesicle shape is almost rounded with sub-rounded type in rare particles. The boundaries of the vesicles are relatively thick as shown in the first photo of the ϕ3 group.

Sample 2 group compared to Sample 1 shows slight differences ranging from vesicle shape to surface textures.

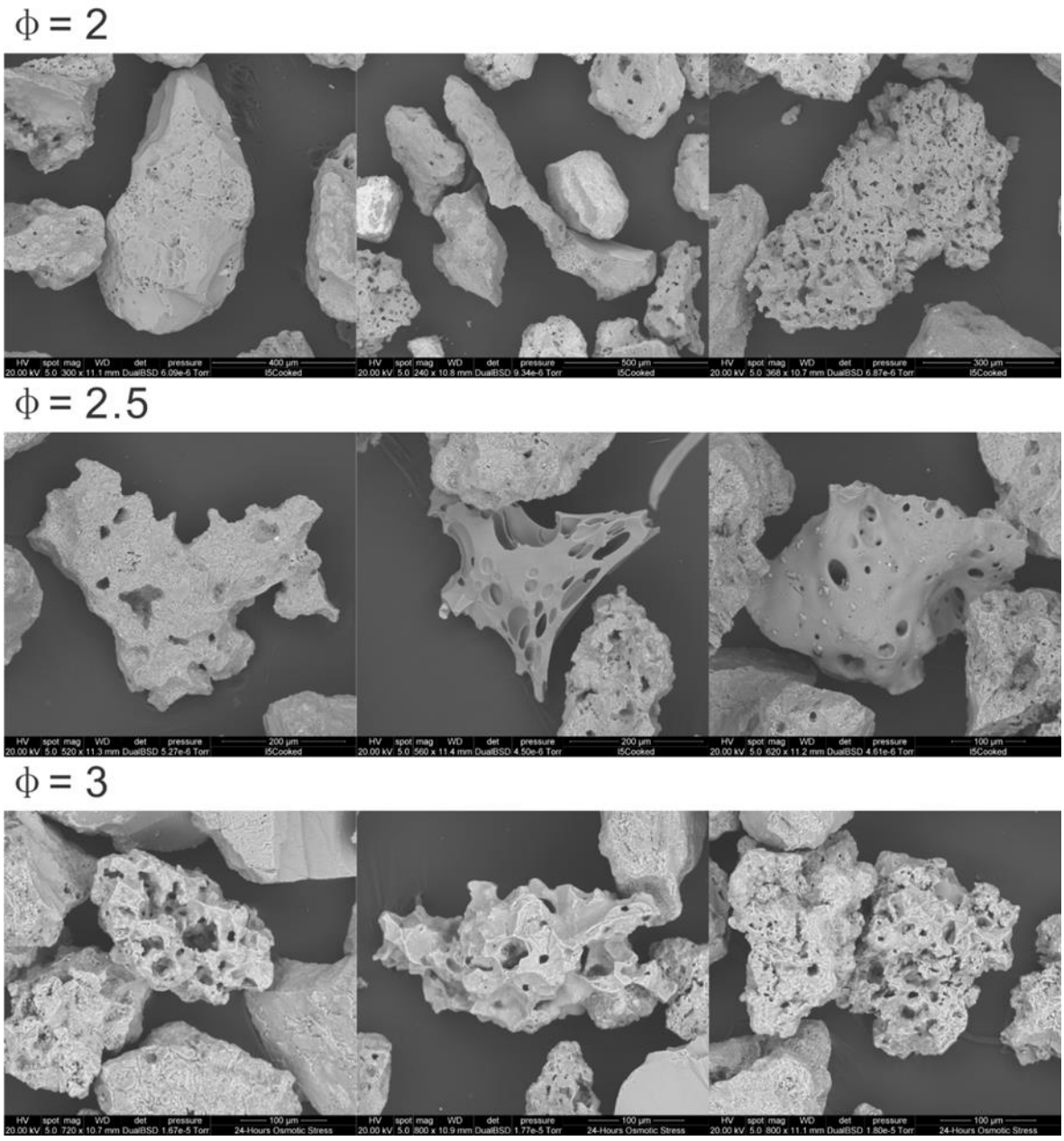

Figure 54: The 3D SEM images of Sample 2; same grain sizes as Sample 1.

Fig 54 depicts the 3D details of Sample 2, i.e. Tongxin Crater. The grain size 2 as a phi value reveals a non-crystal texture particle which has well-evolved vesicles on its surface. The second photo of φ2 shows a long and narrow juvenile clast, vesicles are poorly preserved, and its shape is nearly sub-angular. The last photo of φ2 depicts a highly-fragmented juvenile particle due to the high amount of vesicles, however the shape of the vesicle ranges from sub-angular to sub-rounded types. The grain size of φ2.5 is slightly different with φ2 in association with the surface textures and particle shape. The first photo reveals a sub-angular juvenile clast with relatively large vesicles which are poorly developed. The rest of the two photos present the specific texture of some juvenile clasts, which is a glass-like and non-crystal surface that may indicate the rapid period of cooling processes. The shape is an angular to

sub-angular type. The last row shows the juvenile particles with a high degree of fragmentation and the vesicles are well developed. The shape of these three particles is generally sub-rounded. In observation of the three types of grain sizes of Sample 2, the shape ranges from sub-angular to rounded, and vesicles dominate the juvenile particles at the high stage, which means a high intensity of water-magma interactions. The vesicle's shape is various, i.e. sub-angular, sub-rounded and rounded styles. Glassy textures can be well observed in Sample 2, and this may be other evidence caused by the magma-water interactive eruptions. Also the shapes of Sample 2 range from sub-angular to irregular types, meaning the sudden external pressure may interfere with the bubble development during the magma ascent.

Comparing these two groups, Tongxin Crater may experience more violent eruptions than Wusulangzi Lake, although the qualifications of Wusulangzi still need to be identified. The intensity of magma-water interaction during the eruption phases varies for both sites in association with the density of the vesicles.

Geochemistry of Wusulangzi and Tongxin pyroclastic units

The major and trace elements of the volcanic rocks reveal the essence of volcanism and how it works. Two groups of samples show the varieties of the compositions of major and trace elements in their weight percentages, which can be produced as various diagrams, e.g. Harker diagrams, TAS (total alkali vs silica), the CIPW Norm as well as ternary charts. These charts and diagrams reveal the internal processes of volcanism, such as partial melting, fractional crystallisation and other mineralogical behaviours. This section will depict the preliminary research for both trace and major elements from Wusulangzi Lake and Tongxin Crater, and will present a comparison from other monogenetic volcanic fields around the world. However, as mentioned the bulk rock samples from Wusulangzi Lake are missing, and the geochemical analyses are only held on pyroclastic samples for both of the sites as well as bulk samples from Tongxin Crater. Although lacking data from bulk rocks of Wusulangzi Lake, the analyses can still give a glimpse of the essence and qualified assessments of the ACVF. Also, the comparison between the ACVF and other volcanic fields in the world is necessary and the following part provides the details.

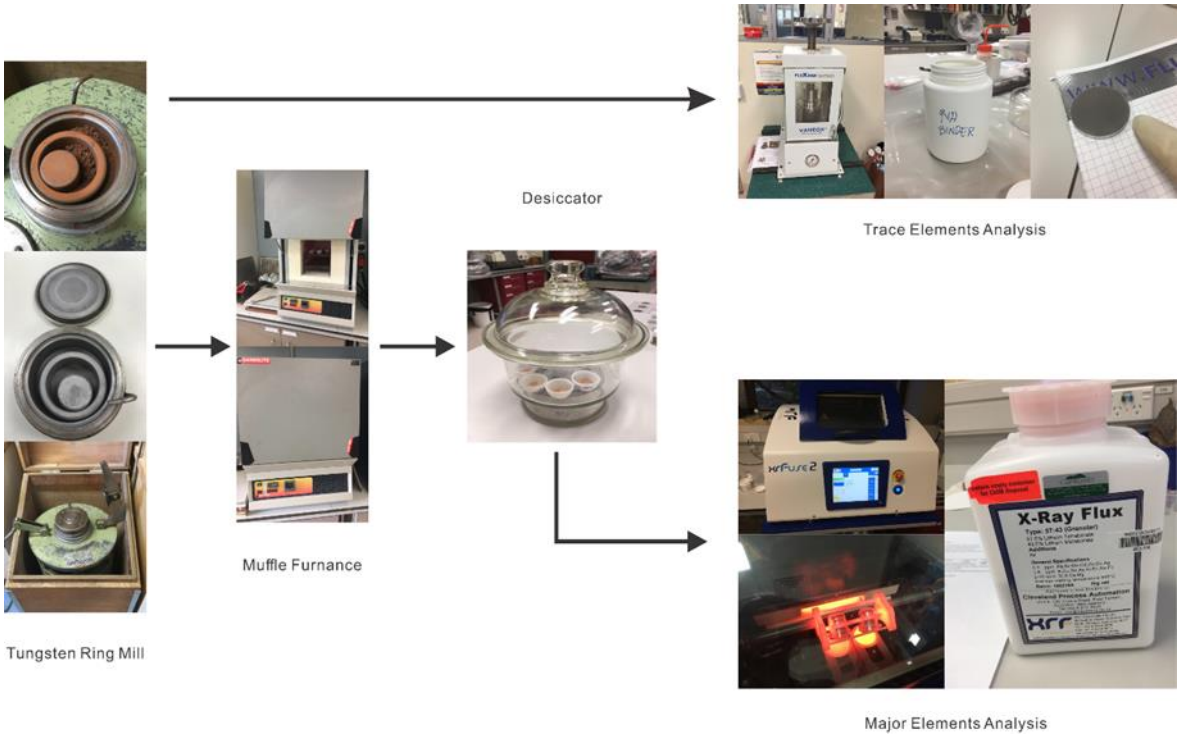

Figure 55: The procedures of the geochemical analyses in terms of major and trace elements (some photos were captured from the instructions of XRF documents at Massey University by Anja Moebis).

Major element chemistry

Like all other research in volcanology, major element geochemistry can be utilised to classify and identify igneous rocks and their processes, and can also reveal the chemical controls on the physical essences such as crystallisation and melting processes (Winter, 2013). In advance, the major element analyses can represent the processes of magma evolution (Winter, 2013). The data of both sample groups is collected from either Waikato or Massey universities. In the powder preparation, the Tungsten ring mills (Fig 55) and the crusher (photo C of Fig 46) were facilitating the procedures, thus the dried rocks and soil can be crushed as the homogeneous powder. After the powder making, the samples were kept in the desiccator (Fig 55) for about 12 hours. After the cooling procedure, the samples contained in the crucibles were heated up to 900° within the Muffle furnace for about 30 minutes in terms of the LOI (loss of ignition). Only by using this step could the samples get rid of the volatile contents, even the water of the crystallisation. Thus, the weight of LOI can be measured through the difference between the sample weight before 900° and after this temperature. By utilising the XRF (X-ray fluorescence analytical instrument), five glass plates were analysed by SPECTRO X-LAB 2000 from Waikato University and BRUKER S8 TIGER from Massey University. These five beads were combined with 0.8 g powder and 8 g flux (Fig 55, the photo of X-Ray Flux) composed by the lithium metaborate and tetraborate, fused in the XrFuse 2 instrument into the glass plates. This part will also show the comparison between concentrated sites and other volcanic fields in the world, as well as the same regional volcanoes in NE China.

1) XRF data presenting

Waikato	SiO2	Al2O3	TiO2	MnO	Fe2O3	MgO	CaO	Na2O	K2O	P2O5	SO3	Sr (PPM)	Ba (PPM)	CO2
S2 Lava A	49.98	12.46	1.752	0.16	11.08153	8.91	7.84	3.102	1.98	0.347	0.04	364	524	0.09
S2 Lava B	49.24	12.09	1.811	0.16	11,20413	9.763	7.828	3.035	2.01	0.38	0.05	401	500	0.11
S2 Lava C	49.79	12.09	1.757	0.16	11.08246	9.328	7.882	2.921	2.01	0.604	0.18	357	507	0.02
S1 Pyroclasts	47.21	12.16	1.81	0.162	11.61564	11.301	7.624	2.911	1.81	0.442	0.06	496	507	1.15
S2 Pyroclasts	49.72	12.13	1.706	0.158	11.1511	9.836	7.823	2.907	1.77	0.331	0.08	329	503	0.25

Table 4: The data of major elements of Sample 1 (S1) and Sample 2 (S2). S1 and S2 were collected from Wusulangzi Lake and Tongxin Crater respectively. Note the measurements were held at Waikato University. There are only two trace elements in this table.

Massey	SiO2	Al2O3	TiO2	MnO	Fe2O3	MgO	CaO	Na2O	K2O	P2O5	SO3	LOI
S2 Lava A	51.92	12.94	1.771	0161	11.127	9.144	8.285	3.488	1.97	0.35	0.01	0.09
S2 Lava B	51.15	12.55	1.821	0.164	11.31679	9.924	8.249	3,169	2.02	0.386	0.01	0.11
S2 Lava C	51.09	12.45	1.755	0.163	10.98118	9.526	8.191	3.481	1.99	0.344	0	0.02
S1 Pyroclasts	49.01	12.61	1.818	0.161	11.52941	11.562	7.965	3.121	1.79	0.451	0.01	1.15
S2 Pyroclasts	51.64	12.56	1.718	0.158	11.24736	10.067	8.239	3.081	1.78	0.32	0.01	0.25

Table 5: The data is the same as for Table 4. Note the measurements were held at Massey University.

These two tables above represent the major elements analysed in the two universities in regard to constraining the deviations during the sample preparations. Generally, the data of major elements can reveal the compositions of volcanic rocks in relation to the magma series, which can define and reveal the origins of the magma in association with partial melting and fractional crystallisation during eruptions. As mentioned, the observation at Wusulangzi Lake lacked of the procedures due to irreversible time schedules. The detailed outcomes can be depicted by a range of diagrams and ternary plots, which will largely represent Tongxin Crater rather than Wusulangzi Lake.

2) TAS (total alkaline vs silica) diagram

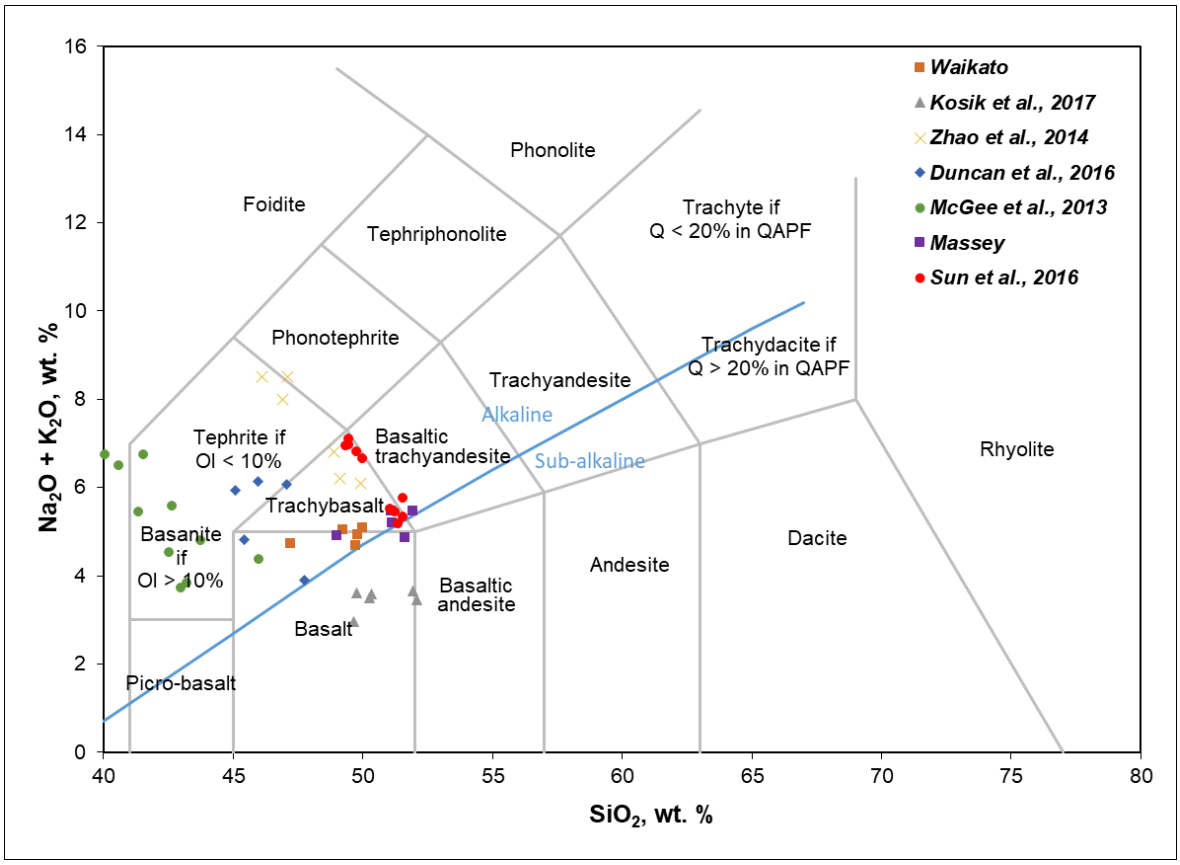

Figure 56: The TAS, i.e. total alkali vs silica diagram (Bas et al., 1986). Note the orange and purple squares mark the samples from the ACVF and others are from Taupo, NZ; AVF, NZ; Nuomin River, China; as well as Saudi Arabia, in association with grey triangles; green dots; yellow crosses; and blue diamonds respectively. The red dots mark the other two vents from the ACVF – Moon Lake and Gaoshan (Sun et al., 2016).

The first qualification is the TAS diagram, also called total alkali vs silica. As Fig 56 depicts, the samples from Wusulangi Lake and Tongxin Crater are marked by orange blocks which lie on the basalt area, and the total alkaline ranges from 4.677 to 5.471 in weight percentages, while the weight percentages of silica are from 49.01 to 51.92, despite the deviation dropping low to the standard values of basalt. Thus the majority of the samples are basalt. The blue line marks the boundary between alkaline and sub-alkaline, and obviously the samples from both Wusulangzi and Tongxin are alkaline basalt, although the deviations have been plotted on this diagram. Combined with the observation of optical and petrographic microscopy, no sign of andesite is identified. Other data from around the world shows the varieties of properties. For instance, the rocks from AVF (McGee et al., 2013) are generally basanites and you may get tephrites in Saudi Arabia (Duncan et al., 2016), and basalts or andesitic basalts may present at the Maroa Volcanic Centre (Kósik et al., 2017), as well as tephrites and trachybasaltic rocks which commonly emerge in the Nuomin Volcanic Field, NE China (Zhao et al., 2014a). Additionally, the other two vents – Moon Lake and Gaoshan in the ACVF – behave with different properties from Wusulangzi and Tongxin in the same volcanic field. The red dots present the trachybasalt at Moon Lake and Gaoshan (Sun et al., 2016). These

variations of the two pairs of samples may deserve further research in association with the magma source diversity.

3) CIPW Norm

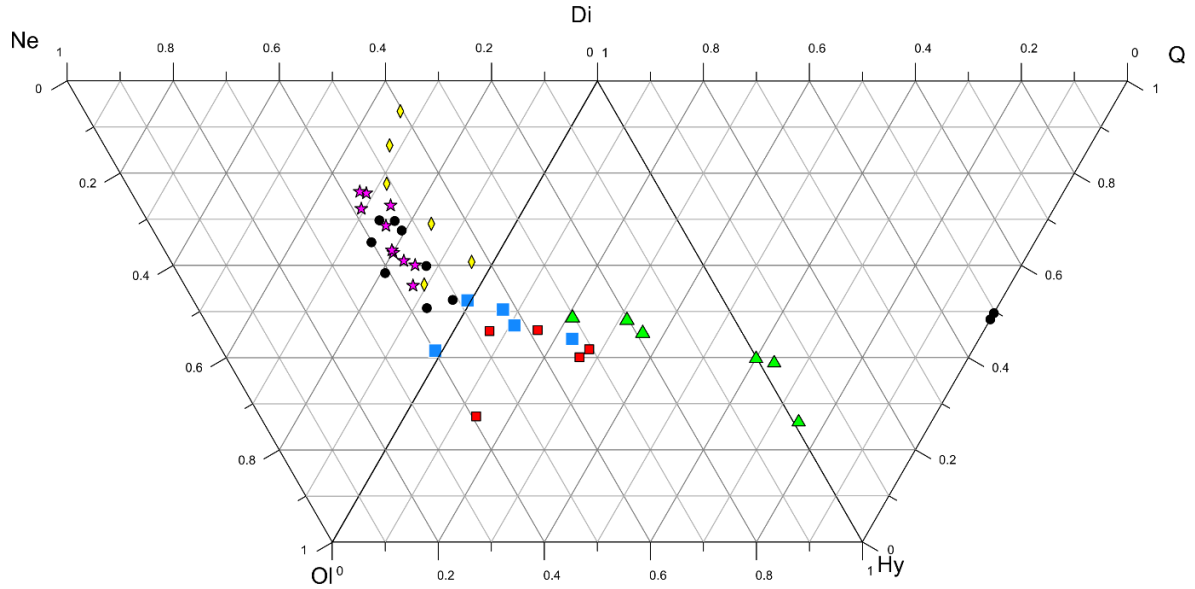

Figure 57: The CIPW Norm ternary plots. Note the data from Wusulangzi and Tongxin are marked by red and blue squares. Other patterns on this chart respectively represent the data of major elements from AVF, Saudi Arabia, TVZ and NE China in turn with purple stars, black dots, green triangles and yellow diamonds (Duncan et al., 2016; Kósik et al., 2017; McGee et al., 2013; Zhao et al., 2014a).

Fig 57 depicts the CIPW Norm potential of the Wusulangzi and Tongxin samples. Due to the normalised data, the major minerals are generally located in the area of Olivine-Hypersthene-Diopside (red and blue blocks). As Tables 4 and 5 depict, the total iron is only composed of $Fe^{3+,}$ no sign of Fe^{2+}, thus during the assessment in the CIPW Norm, the ratio between Fe^{3+} and total iron must be standardised. Three common ratios are utilised for the typical volcanic rocks: 0.1 for basaltic or basaltic andesite, 0.15 for andesite, 0.2 for dacite, and 0.3 for rhyolite. Thus, based on the total alkaline vs silica diagram (Fig 56), the ratio value of Fe^{3+}/total iron should choose 0.1 for basalt. The outcomes of the Norm data are the lack of quantities of quartz, which indicates the samples from the ACVF are silica under-saturated (Winter, 2013). Also, the olivine has been found and observed under the petrographic microscopy, which implies the forsterite is only in the basaltic rocks from the Wusulangzi Lake and Tongxin Crater due to the binary peritectic system (Winter, 2013). Basically, the comparative data from around the world implies nearly all basalts are silica under-saturated. Only the data from the Maroa Volcanic Centre has the sign of quantities of quartz, but normally they are in the minority.

4) *Sodium oxides vs potassium oxides*

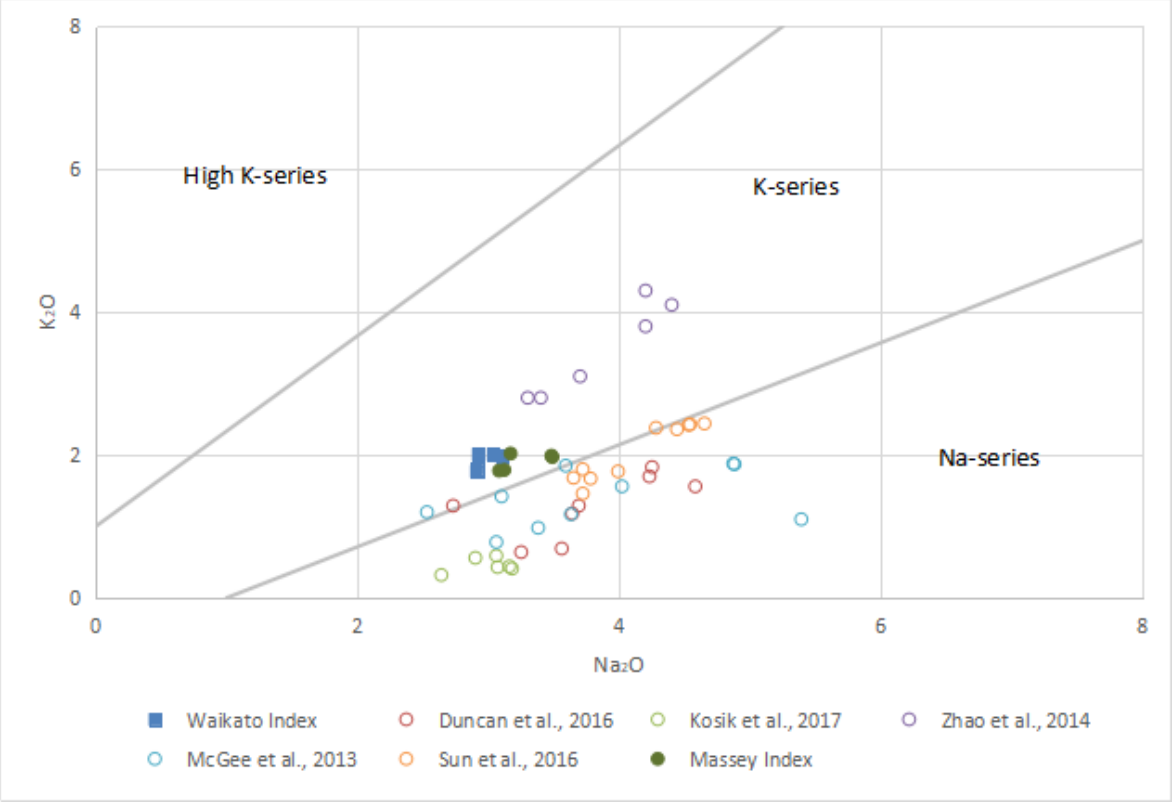

Figure 58: The plot of Na_2O vs K_2O, circles marks the other volcanic field in the world in terms of comparing it with the data from the ACVF. Note the blue blocks and green dots represent the data assessment from both Waikato University and Massey University in the same samples.

Fig 58 represents the ratio between potassium oxides vs sodium oxides in association with the subdivision of the alkaline magma into three series: high-K, K, and Na series (Irvine and Baragar, 1971). As the data reveals, the blue blocks and green dots lie in the area of potassium series due to the percentages of silica ranging from 49.01 to 51.92, and the potassium oxide in 1.77 to 2.02 in weight percentage. This means the sample from both Wusulangzi and Tongxin belong to the alkaline potassium series. Volcanic rocks from the Maroa Volcanic Field (green circles, i.e. (Kósik et al., 2017)), Saudi Arabia (red circles, i.e. (Duncan et al., 2016)), and the AVF in NZ (blue circles, i.e. (McGee et al., 2013)) belong to the sodium series. The two vents in the ACVF have the Na-series rocks distinctive from Wusulangzi and Tongxin (orange circles, i.e. (Sun et al., 2016)). However, the volcanic samples from Nuomin in NE China (purple circles, i.e. (Zhao et al., 2014a)) represent the same chemical properties as Wusulangzi Lake and Tongxin Crater.

5) *The AFM diagram*

In the petrology of igneous rocks, the total alkalis, total iron and MgO can be utilised for the definition of magma stages, as well as the separation between tholeiitic and calc-alkaline rocks. Basically, the AFM diagram includes four cation major elements: Na, Fe, K, and Mg (Winter, 2013). Two analyses were held both in Waikato and Massey, and other data from

around the world have been plotted on this diagram. Each of the data can represent the stages of magma evolution.

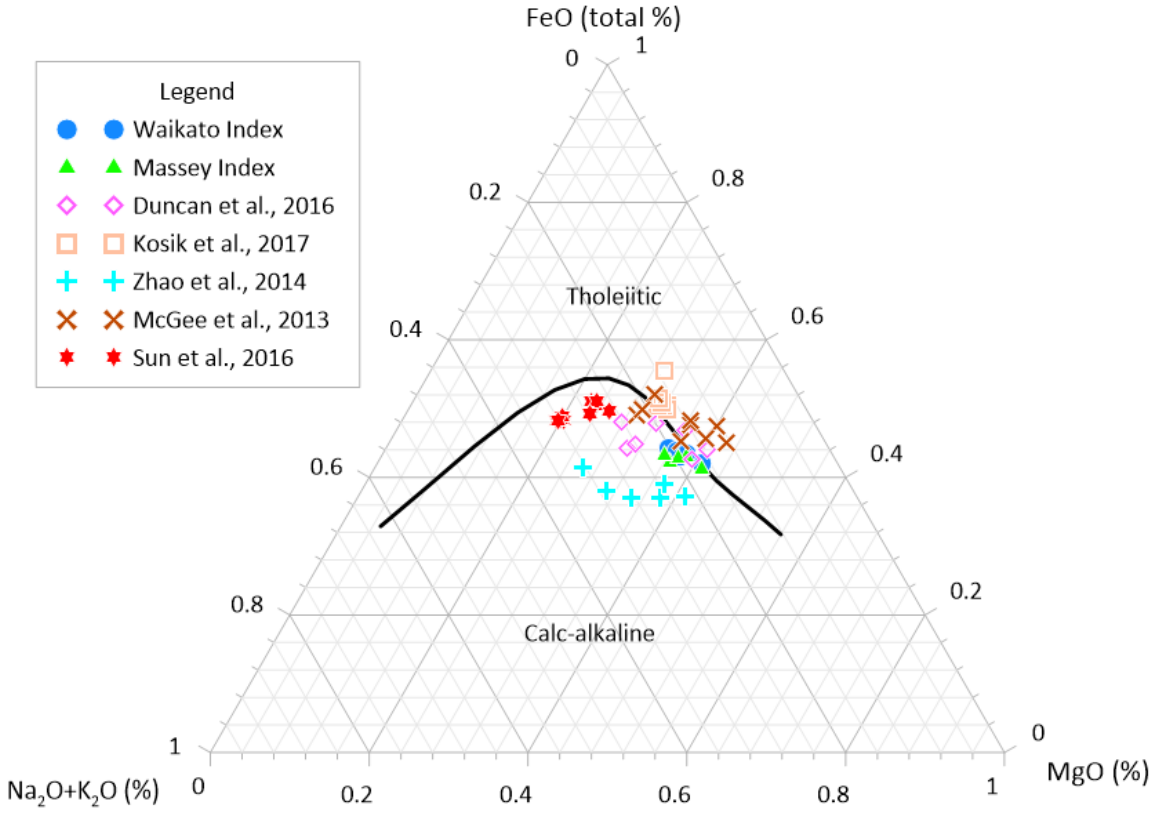

Figure 59: The ternary plots of AFM (alkalis-total iron-MgO); different patterns represent the different data collected worldwide.

In Fig 59, the blue dots and green triangles represent two measurements from both Waikato University and Massey University. The black line shows the trend of the magma evolution; on the right side it represents the primitive stages and on the left side the evolved stages. Two portions of this plot are divided by this trend line, which is the tholeiitic type and calc-alkaline type, which marks the general types of basaltic rocks. As mentioned, the position of the two sets of data marked by blue dots and green triangles is near the end of the right side of the black line, which implies that Wusulangzi Lake and Tongxin Crater erupted amounts of basaltic rocks which were formed in the primitive stages during magma evolution, and also that most of them were generally toward calc-alkaline trends. Light-blue cross-shaped pattern marks were in the volcanic rocks from the Nuomin Volcanic Zone in NE China (Zhao et al., 2014a). Both primitive and slightly-evolved stages of magma batches are presented within this group, also the pure calc-alkaline type of rocks dominate the Nuomin Volcanic Zone. The pink-coloured diamonds show the data from Saudi Arabia (Duncan et al., 2016). Basically, the data indicates the primitive period of the magma evolution, and as always the majority of the data implies a calc-alkaline trend. The incarnadine-coloured squares imply the data was measured from the Maroa Volcanic Zone in New Zealand (Kósik et al., 2017). The data lies on the transition zone between the primitive stage and the evolved stages, which means the rocks

from the Maroa volcano may be formed through magma batches with intermediately ascending velocity in association with the possibly minor assimilation with the lithospheric mantle materials. The majority of the rock type should belong to tholeiitic rocks due to the upper area of the plot. Brown crosses mark the data assessed from the AVF (Auckland Volcanic Field) in New Zealand (McGee et al., 2013). The position of the data also indicates the primitive stage in relation to the magma derivation, as well as the tholeiitic type in the majority of it. Still, some of the data from AVF has a signal of the transition stages during the magma evolution. The red stars reveals the most specific data from the same volcanic field of Wusulangzi Lake and Tonxin Crater, and the samples were collected from Moon Lake and Gaoshan vents from the ACVF (Sun et al., 2016). As the pattern depicts, the position is lying on the evolved magma series accompanied with the calc-alkaline property. Compared to the data from Wusulangzi and Tongxin, the data from Moon Lake and Gaoshan can be assumed to be the subsequent stages of magma evolution in association with Wusulangzi and Tongxin, which are shown to be the distinct primitive magmatic stages.

As mentioned, due to the preliminary stage of the research, the data collected from both sites is limited and one can only hope that the outlines of the interpretation are intact. The detailed plots and data will be assessed in future study.

6) Harker diagram interpretations

This section is about the variation diagrams. Commonly, the variation diagrams are always divided into two types: binary and ternary styles. As mentioned, the CIPW Norm is revealed by the triple ternary plots. The binary diagrams are given in this portion and represent the variation of the major elements during the volcanic procedure, in which the fractional crystallisation and partial melting is indicated. The first section is about the major elements in such a variation diagram – Harker diagrams. Specifically, the data from Ganshan and Moon Lake that are also in the ACVF have totally different trends to Wusulangzi and Tongxin in association with the major elements variation. The preservation of high magnesium is a typical feature of the data from Moon Lake and Gaoshan. However, the three volcanic fields preserve similar MgO in weight percentages to that in the Wusulangzi and Tongxin sites, similar to the trends in the variations. The reason for the utilisation of MgO as abscissa is due to the primitive magma stage during the magma evolution which is revealed in the AFM diagram (Fig 59). Commonly, the Fe or Mg indices are more effective in the early evolution of the mafic rocks than the silica index (Winter, 2013).

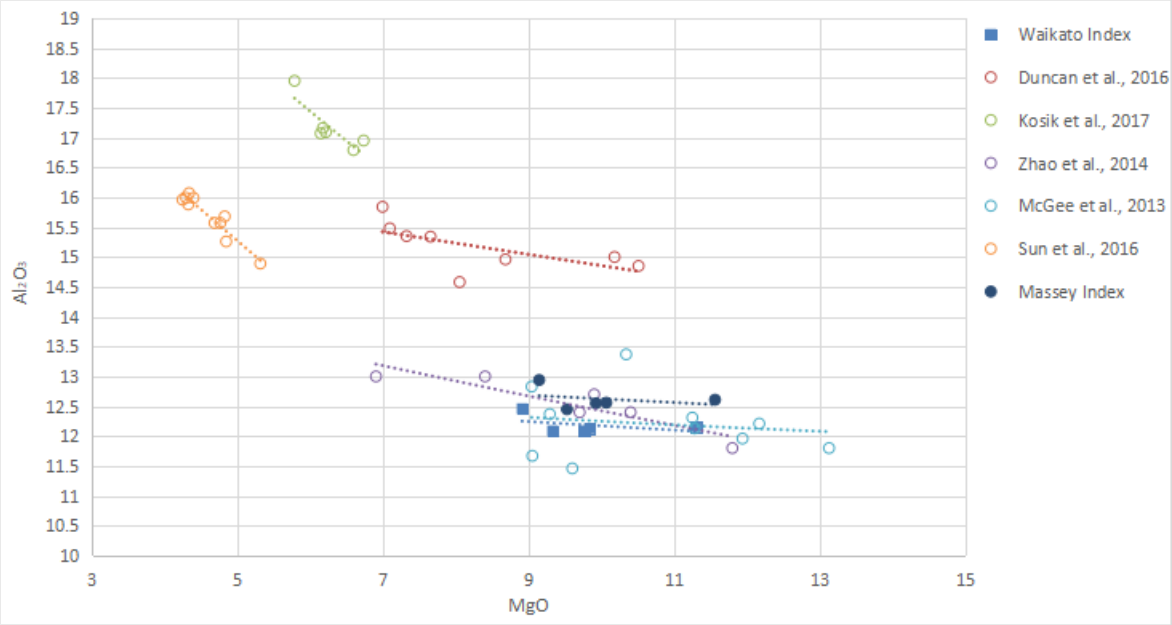

Figure 60: The Harker diagram of MgO vs Al_2O_3. The blue blocks and deep-blue dots represent the sample from Wusulangzi and Tongxin analysed at Waikato University and Massey University respectively.

Fig 60 is one of the several binary variation diagrams and depicts the Al_2O_3 changes in relation to magnesium oxide. Commonly, the index of abscissa is in percentage weights of silica, however due to the properties of basalt the silica under-saturated feature may decide the low-to-none quantities of quartz. In terms of the fractional crystallisation, usually the olivine emerges first, thus the susceptibility of olivine must be higher than the rest of the minerals. Last, but not the least, in the observations from the petrographic microscope and qualified total alkaline vs silica plot as well as the CIPW Norm, no sign of quartz means the olivine can only be forsterite due to the incompatible elements (Winter, 2013). As mentioned, the index of the MgO can variously reveal the variations for each mineral in a large scale. Back to the description of this plot, two analyses reveal a similar potential, although the deviations have been made. Based on the data of the major elements, the variation of MgO ranges from 8.9 to 11.6 wt%. The weight percentages of Al_2O_3 are approximately from 12.09 to 12.84. Generally, the trend of the Al_2O_3 vs MgO is increased, but the variation of Al_2O_3 is not tremendous. Additionally, the data from the AVF has light-blue circles (McGee et al., 2013) and shows the same trend with the Wusulangzi and Tongxin data within the same variation range in terms of increasing the potential for both tendency lines. Typically, the increasing trend is represented in all data from around the world, although with different variation velocities. Judging by the slopes of the trending lines, the same variation occurs between the volcanoes of Saudi Arabia (Duncan et al., 2016) and the Nuomin volcanoes of NE China (Zhao et al., 2014a), and in turn with red circles and purple circles, the variation velocity is relatively intermediate due to the gradual slope. A high variation velocity occurs between Taupo (green circles, i.e. (Kósik et al., 2017)) and two vents from the ACVF (orange circles, i.e. (Sun et al., 2016)).

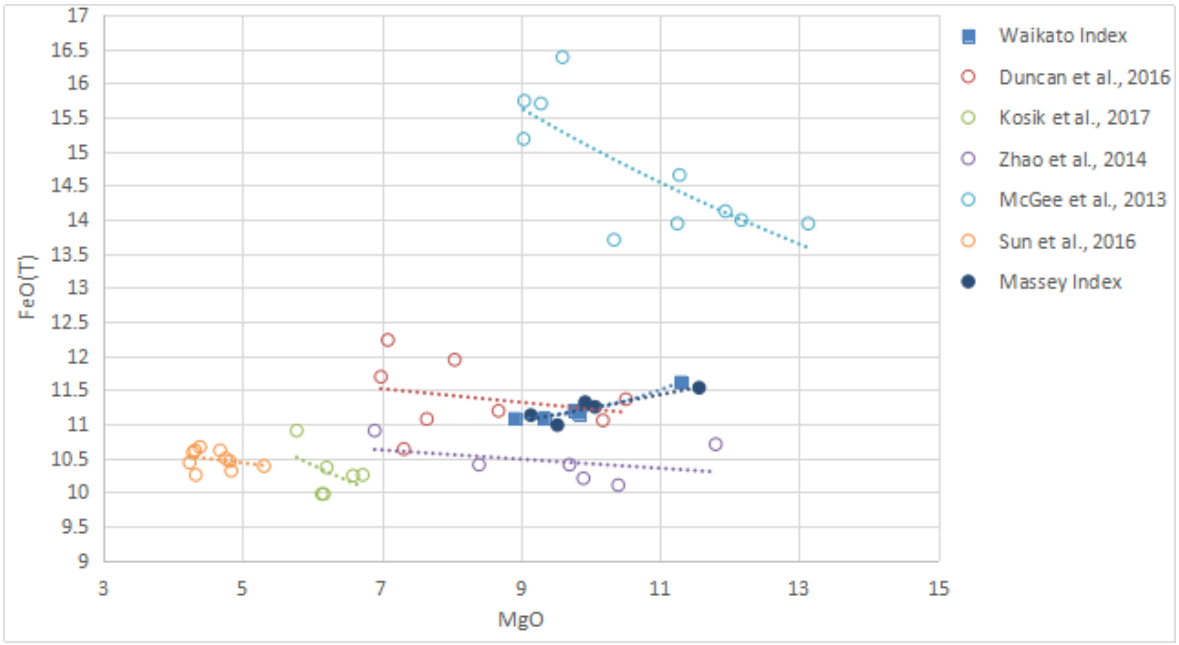

Figure 61: The Harker diagram of MgO vs total iron oxide.

This diagram shows the variations between MgO and total iron oxides, but note in the samples from Tongxin and Wusulangzi that the Fe^{2+} has not been detected from the XRF analyses (Table 4 and 5), thus the total iron oxide only represents the weight percentages of Fe^{3+}. As shown in Fig 61, the iron oxide represents the decreasing trend compared to the aluminium oxides. The variation range for MgO is the same as the previous one. But from approximately 10.98 to 11.53 wt%, the decreasing potential is obvious compared to the variation of Al_2O_3. Other data from around the world shows the total trend variations from Tongxin and Wusulangzi. Increasing is the dominant potential among them. The orange circles represent the data from other vents of the ACVF (Sun et al., 2016), and the trend is obviously contradictory with it representing Tongxin and Wusulangzi. This might indicate the different magma sources in different vents from the ACVF. Otherwise, the slope between volcanoes from Saudi Arabia (red circles, i.e. (Duncan et al., 2016)) and the Nuomin volcanoes from China (purple circles, i.e. (Zhao et al., 2014a)) is the same. The Moon Lake and Gaoshan in the ACVF also depict the same potential as these volcanic fields. Still, high increase rates of total iron oxides occur at Taupo (green circles, i.e. (Kósik et al., 2017)) and AVF (light-blue circles, i.e. (McGee et al., 2013)) in New Zealand. The decreasing trend of samples from Tongxin and Wusulangzi may imply that the olivine was crystalised from the melt during the magma evoluotion.

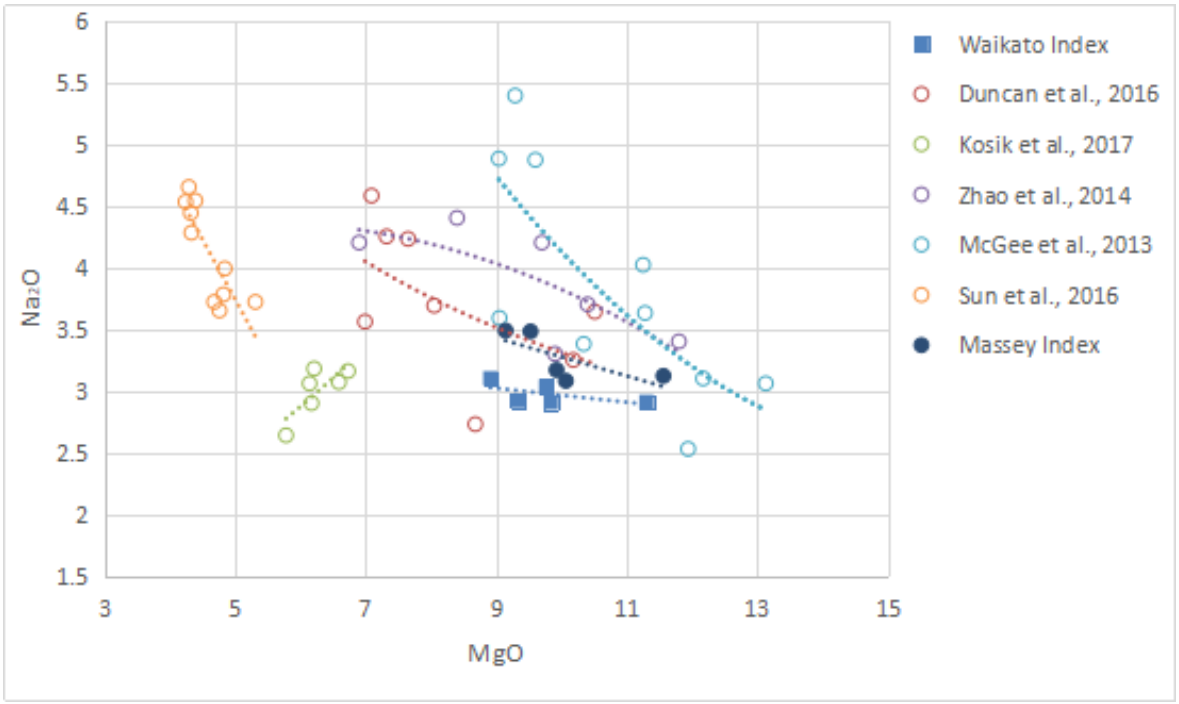

Figure 62: The Harker diagram of MgO vs sodium oxide.

Fig 62 also represents the same property of the mineral variation in volcanic clasts. The MgO vs sodium oxide depicts the increasing trend. The light-blue squares and deep-blue dots represent the data measured from Waikato University and Massey University respectively. The slope is slightly different due to the deviations. However, the trend reveals the same variable rate between Wusulangzi and Tongxin and the Nuomin Volcanic Field (Zhao et al., 2014a), as well as volcanoes from Saudi Arabia (Duncan et al., 2016). The variation range of aluminium oxide is approximately from 12.09 to 12.94 wt% with the same variation of MgO. As with the same area in the ACVF, the potential of Moon Lake and Gaoshan (orange circles, i.e. (Sun et al., 2016)) shows a deeper slope than the trend of Wusulangzi and Tongxin but has the same trend as AVF (McGee et al., 2013), this indicates the high variation of sodium at high variation velocity. Like the plot of Fig 60 and Fig 61, the sources of vents in the ACVF may be different. As an exception, the data from Maroa Volcanic Centre (Kósik et al., 2017), and the TVZ in NZ, depicts the relatively high variation velocity of sodium oxides.

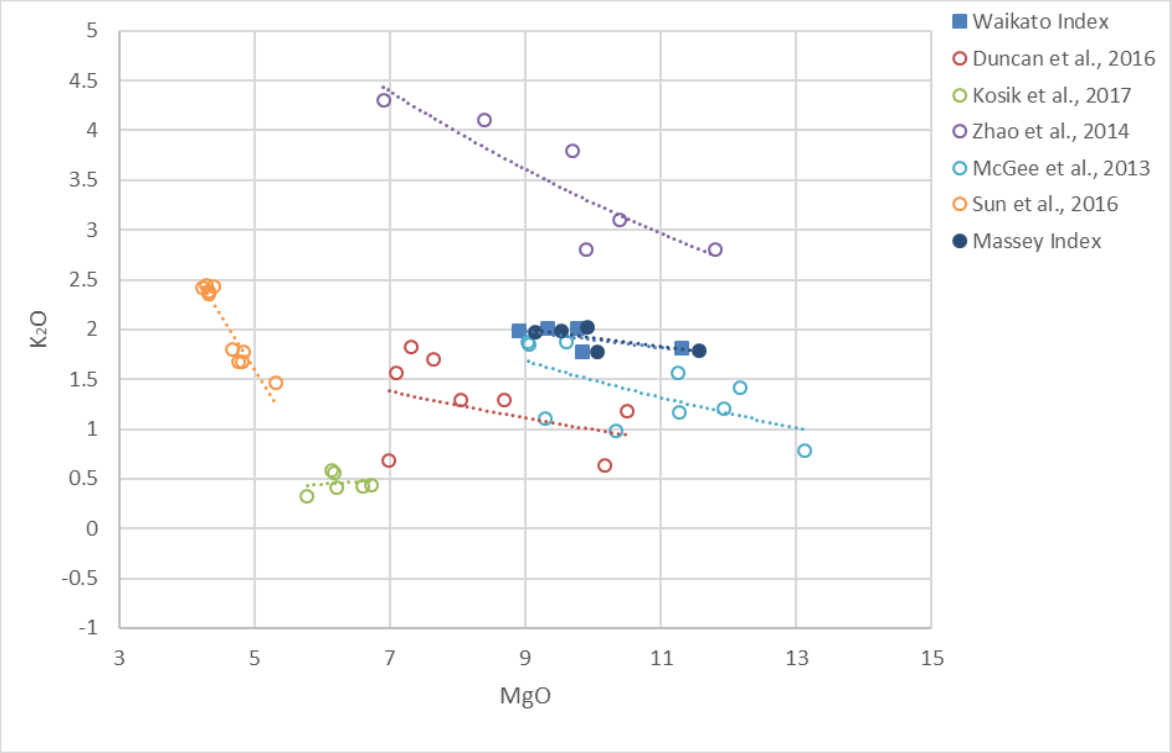

Figure 63: The Harker variation diagram of MgO vs potassium oxides.

Fig 63 is about another major element – potassium as against the magnesium oxides. The variation trend is slightly increased. Two analyses held at Waikato University and Massey University show that there are rarely deviations between them (deep-blue dots and light-blue blocks). As the legends of the figure shows, the potentials for the AVF (light-blue circles, i.e. (McGee et al., 2013)) and volcanoes from Saudi Arabia (red circles, i.e. (Duncan et al., 2016)) reveal the same trend as the data from Wusulangzi and Tongxin. Thus, the possible positive correlations between them happen in the range of 8.91 to 11.6 wt% of MgO. The weight percentages of K_2O is from 1.77 to 3.48 combining both analysed outcomes. Compared to Moon Lake and Gaoshan in the ACVF, the increasing trend of Wusulangzi and Tongxin is much less than the other two vents (orange circles, i.e. (Sun et al., 2016)), compared to their high variation rate (dippest slope). The trend of the Nuomin data is in the intermediate variation rate (purple circles, i.e. (Zhao et al., 2014a)). Only the slightly decreasing trend is being presented in relation to the Maroa volcano data (Kósik et al., 2017).

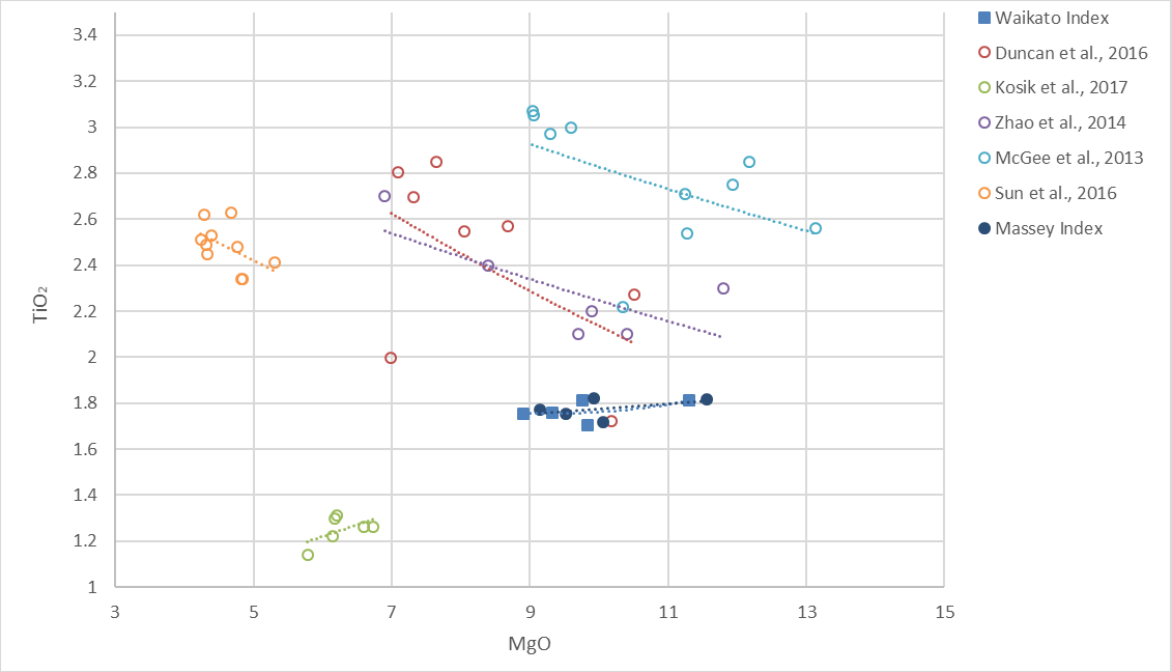

Figure 64: The Harker diagram of MgO vs titanium oxide.

The deep-blue dots and light-blue squares mark the variations of the Wusulangzi and Tongxin samples in terms of MgO against TiO_2 in weight percentages. The variation range is approximately from 1.71 to 1.82 wt%. Thus, the quantities of variation are no more than 0.2 wt%, which means that during the fractional crystallisation the weight of titanium almost keeps the same situation, although with the slightly decreasing trend (Fig 64). As this figure depicts, only the data from Taupo (green circles, i.e. (Kósik et al., 2017)) has a similar potential to data from Wusulangzi and Tongxin. The Nuomin volcanoes (purple circles, i.e. (Zhao et al., 2014a)), the AVF (light-blue circles, i.e. (McGee et al., 2013)), as well as volcanoes from Saudi Arabia (red circles, i.e. (Duncan et al., 2016)) show that their variation trends are the same in increased conditions. However, the other vents from the ACVF that are from Moon Lake and Gaoshan have a totally contradictory trend in regard to the trend of Wusulangzi and Tongxin, but they have a similarly increasing variation trend and slope as with the Nuomin volcanoes (purple circles, i.e. (Zhao et al., 2014a)). Only the data from Taupo (green circles, i.e. (Kósik et al., 2017)) has a decreasing trend as with Wusulangzi and Tongxin. The decreasing trend of TiO_2 indicates that possibly rutile and titanite might be crystallised from the melt.

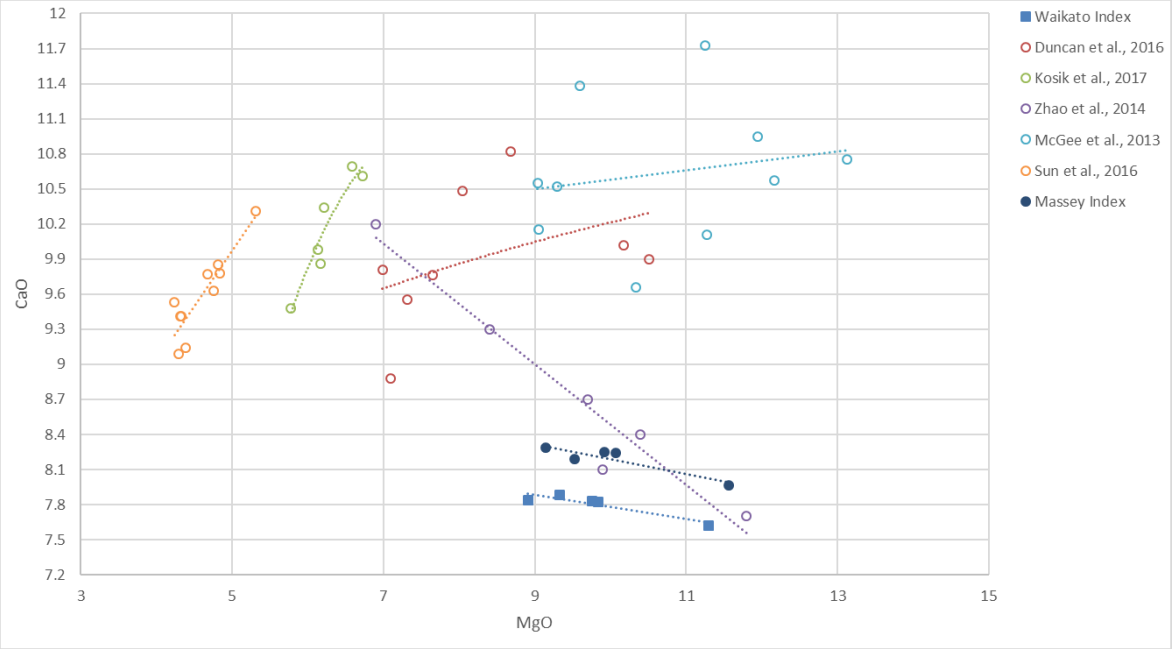

Figure 65: The variation diagram of MgO vs calcium oxides.

The MgO vs CaO diagram reveals the increasing trend for both analyses (deep-blue dots and light-blue squares) which were held at Waikato University and Massey University. The weight percentages of calcium oxide range from 7.62 to 8.28. The increasing trend is gradual compared to the Nuomin Volcanic Field which shows a greatly increasing trend (purple circles, i.e. (Zhao et al., 2014a)). The variation range is approximately 0.66 wt% in relation to the variation range of MgO of about 8.9 to 11.6 wt%. Only the Nuomin Volcanic Field represents a increasing trend with a relatively high variation velocity (purple circles, i.e. (Zhao et al., 2014a)). Another three volcanic fields have decreasing trends, and the data from Saudi Arabi (red circles, i.e. (Duncan et al., 2016)) and the AVF (blue circles, i.e. (McGee et al., 2013)) respectively show a similar increase in trends due to similar slopes. The trending line of green circles (Kósik et al., 2017) represents the high variation velocity of CaO in the Maroa Volcanic Zone with decreased potential. Compared to the data from Wusulangzi and Tongxin, the other two vents in the ACVF emerge with the same trend as the Maroa Volcanic Zone in New Zealand. The data from Moon Lake and Gaoshan (orange circles, i.e. (Sun et al., 2016)) in the ACVF, have a decreasing trend in contradiction to the concentrated data from Wusulangzi Lake and Tongxin Crater which have intermediate increasing potential.

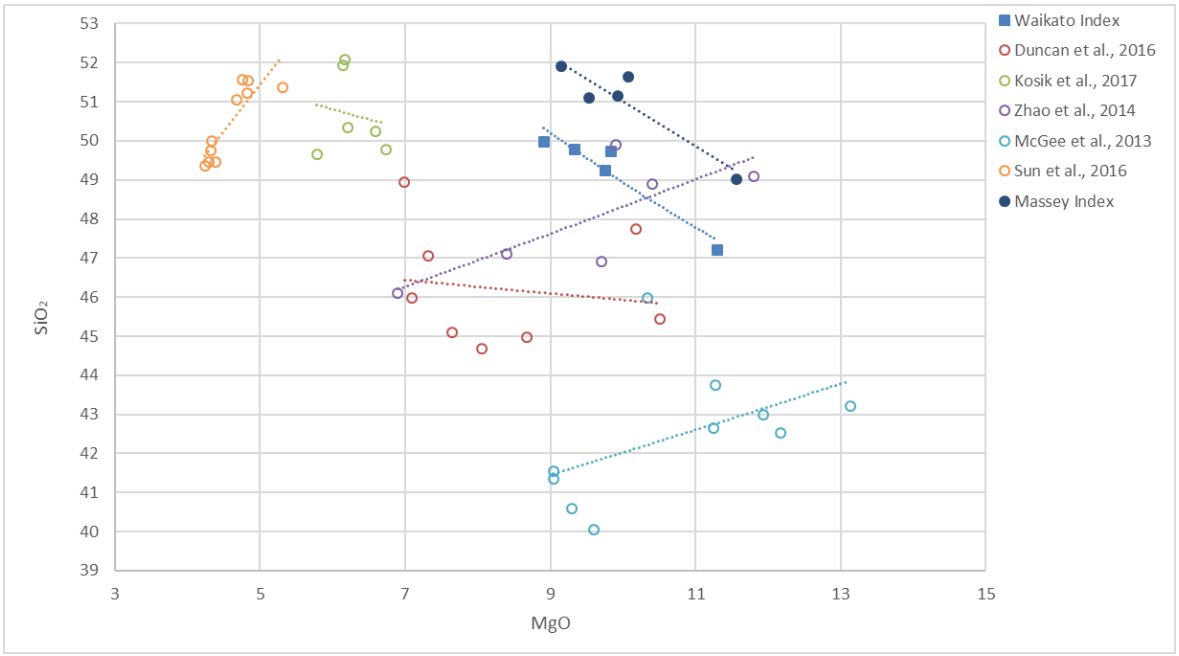

Figure 66: The variation diagram of MgO vs silica.

Fig 66 shows the trend of increase of silica during the magma evolution in terms of the relative decrease of MgO. Two analyses that were measured at Waikato University and Massey University show the same trend in the variations. The weight percentages of silica range from 47.21 to 51.92 in association with 8.9 to 11.6 wt% of MgO. The average range of the silica increase is approximately no more than 3 wt%, which means the relative increase of silica compared to the distinct decrease of the MgO. Another two sites have the same silica increasing trend which is marked by red circles (Duncan et al., 2016) and green circles (Kósik et al., 2017) from Saudi Arabia and the TVZ in New Zealand respectively. The silica variation is shown as intermediate in Saudi Arabia and the TVZ in New Zealand due to the similar slope of the trending lines. In the Nuomin Volcanic Zone (purple circles, i.e. (Zhao et al., 2014a)) and the AVF in NZ (blue circles, i.e. (McGee et al., 2013)), the decreasing trend is obvious with the same velocity of variation in silica weight percentages. The highest decreasing trend is represented as the orange circles, which are marked as Moon Lake and Gaoshan in the same volcanic field of Wusulangzi Lake and Tongxin Crater (Sun et al., 2016). The distinct trends between them also indicate the different magma sources. This diagram precisely shows that the olivine emerged from the melt via fractional crysallisation.

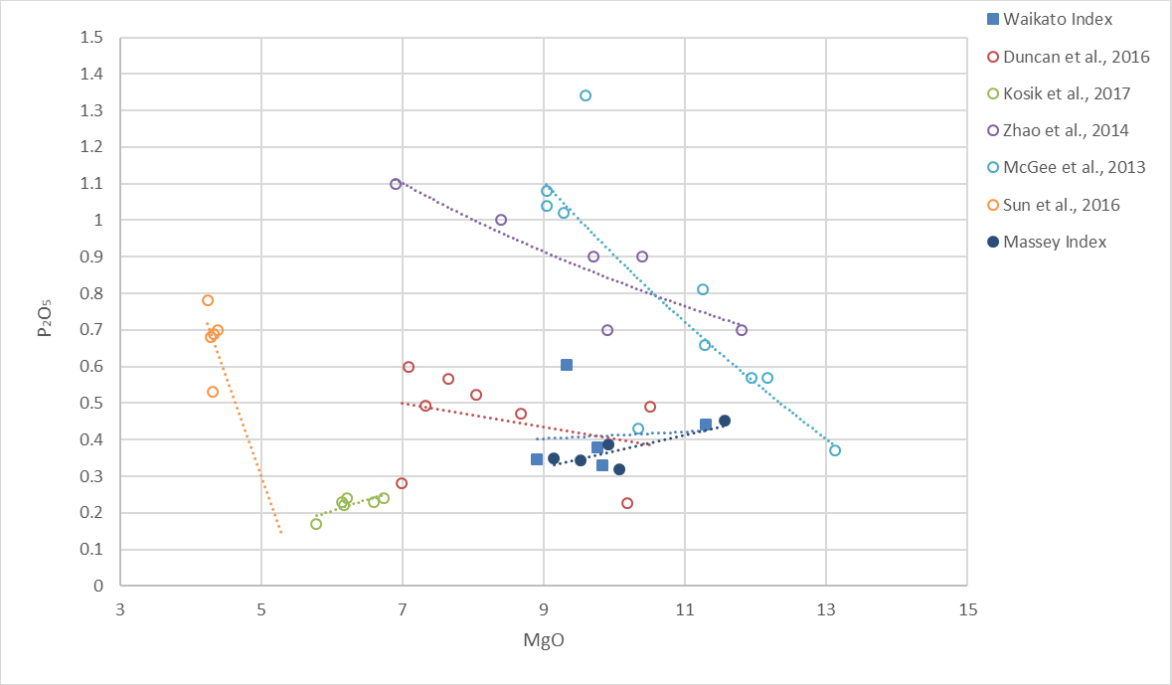

Figure 67: The variation diagram of MgO vs P_2O_5.Note the data of P_2O_5 from Moon Lake is lacking and this plot only depicts the data from Gaoshan marked by orange circles.

Fig 67 shows the amount of the P_2O_5 is in minor quantities without typical variation phenomenon, although it shows that the minor trend is decreasing. Generally, the weight percentages of P_2O_5 hold the same level during fractional crystallisation. The range of variation of the concentrated samples is approximately from 0.33 to 0.6 wt% in relation to the same variation range of MgO which is from 8.9 to 11.6 wt%. The Maroa Volcanic Zone in New Zealand (green circles, i.e. (Kósik et al., 2017)) has a similar variation rate to Wusulangzi and Tongxin in P_2O_5. The data from AVF in New Zealand (blue circles, i.e. (McGee et al., 2013)), the Nuomin Volcanic Field in NE China (purple circles, i.e. (Zhao et al., 2014a)) and Saudi Arabia (red circles, i.e. (Duncan et al., 2016)) emerge with increasing trends, specifically the same trend for the AVF and the Nuomin Volcanic Zone. The Moon Lake and Gaoshan (orange circles, i.e. (Sun et al., 2016)) in the ACVF depict a distinctively increasing potential in terms of the high variation velocity (very deep slope). In terms of a decreasing trend of P_2O_5, the apatite may emerge and be crystallised from the melt during fractional crystallisation.

To sum up, these eight variation diagrams represent the possible fractional crystallisation processes during an eruption. The decreasing trend of iron oxides is probably caused by the silica under-saturated nature of the samples due to the reaction between Fe-bearing minerals with quartz. Another two minerals with a decreasing trend are shown as TiO_2 and P_2O_5, which indicates the possible minor contents of titanite and apatite crystallised from the melt. Specifically, the plot of MgO vs silica (Fig 66) implies an increasing trend of silica with a decreasing potential of MgO in relation to the olivine crystallised from the melt quantitively. This corresponds to the observations made through petrographic microscopy.

Trace element chemistry

The trace elements data was measured from the laboratory at Massey University. Sample preparations were assembled in a range of technical and instrumental processes. The initial preparation of the samples was the same as the procedures of XRF in association with major elements: powder through the ring mill as well as through the oven in terms of dry samples. However, the trace element analysis needs to have the water contents within the pyrogenetic rocks, thus the LOI is unnecessary, which means the procedures of sample heating to 900° in the furnace can be ignored. As Fig 55 depicts, the analyses of trace elements was contributed to by the FLUXANA (Fig 55, the first photo of trace elements analysis) in terms of the pressed powder pellets (Fig 55, the third photo of trace elements analysis). The preparation of the pellets was utilised through the PVA binder (Fig 55, the second photo of trace elements analysis), which is composed of 16% ethanol and deionised H_2O that ensures it is free from any elemental contaminations which are measured by the XRF. The sample powder were combined with the PVA binder with 16 to 20 drops using the pipette. With these above-mentioned procedures, five pellets were measured within the BRUKER S8 TIGER in the utilisation of trace element analyses.

	S1 Pyroclasts	***S2 Pyroclasts***	***S2 Lava A***	***S2 Lava B***	***S2 Lava C***
Sc (PPM)	19	21	19	19	19
V (PPM)	198	213	205	204	207
Cr (PPM)	408	468	326	400	353
Co (PPM)	74	73	61	70	60
Ni (PPM)	411	333	285	308	302
Cu (PPM)	135	155	113	111	96
Zn (PPM)	117	122	118	120	115
Ga (PPM)	18	18	19	19	19
As (PPM)	2	2	2	2	2
Rb (PPM)	50	52	57	56	60
Sr (PPM)	447	330	361	396	362
Y (PPM)	22	24	24	24	27
Zr (PPM)	155	144	151	158	158
Nb (PPM)	41	35	36	38	39
Mo (PPM)	5	5	5	5	5
Sn (PPM)	0	2	0	0	0
Sb (PPM)	0	0	0	0	0

Cs (PPM)	13	12	12	12	12
Ba (PPM)	445	385	440	468	444
La (PPM)	29	21	21	26	22
Ce (PPM)	67	53	51	56	57
Nd (PPM)	28	19	27	25	24
Tl (PPM)	0	0	0	0	0
Pb (PPM)	6	7	7	9	7
Th (PPM)	5	4	4	4	4
U (PPM)	4	4	4	4	4

Table 6: The data of trace elements was analysed at Massey University. Note that S1 and S2 represent the samples from Wusulangzi and Tongxin respectively.

Table 6 presents the data of trace elements (REE) of Sample 1 and Sample 2. In relation to data interpretation, this section will present the analyses of the variations of the trace elements and the multi-element diagram (spider diagram) in terms of the assessments of partial melting and fractional crystallisation during volcanism.

1) *Harker variation diagrams for trace elements*

Like the analyses of the major elements, the binary variation diagrams can be utilised for trace elements in terms of revealing the partial melting styles and fractional crystallisation processes. For some reason, the variation of the trace elements is more susceptible compared to the variation of the major elements due to the incorporation and exclusion of trace elements in different phases being more selective than major elements in the same phases (Winter, 2013). Similar to the major elements in relation to the variation diagram, the Harker-like diagrams of trace elements plots can also reveal the particular partial melting or fractional crystallisation processes. Due to the MgO as the index of the major element analyses, the following trace elements analyses will also utilise the MgO as the same index in terms of the abscissa in the binary plots.

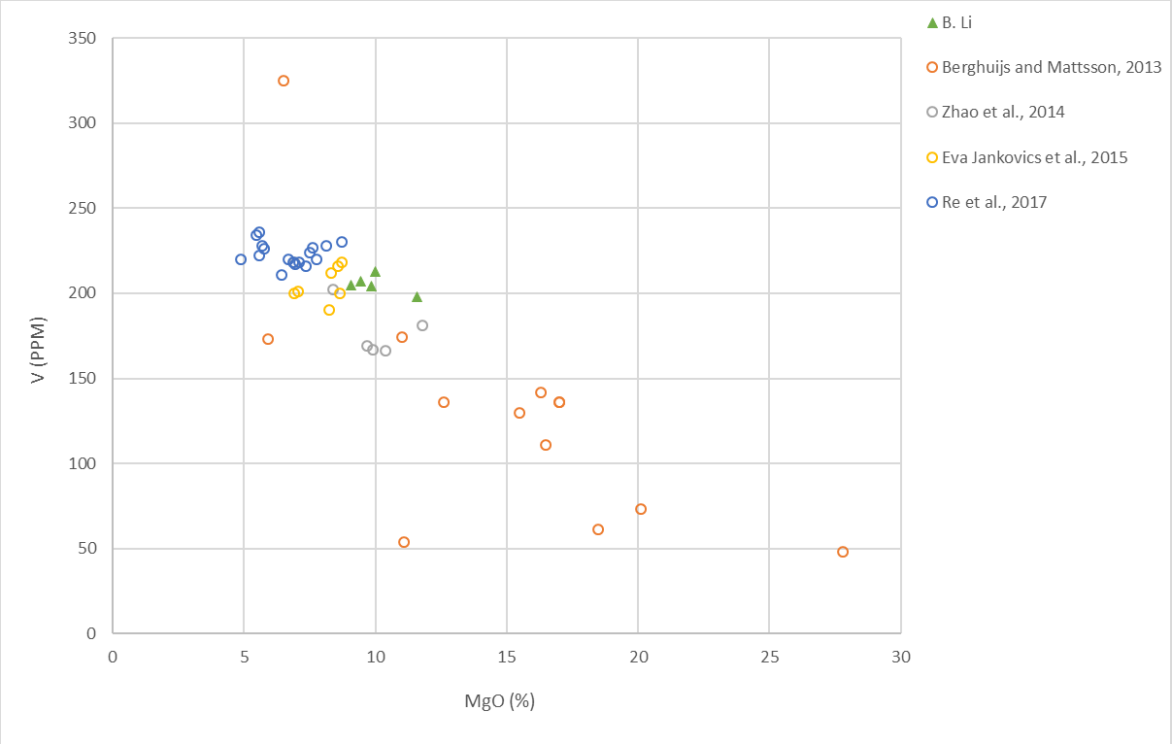

Figure 68: The variation diagram of MgO vs V. Note the MgO is represented by wt%, compared to V as PPM. The following diagrams will obey this rule.

Fig 68 is the plot of MgO vs vanadium. The trend of the data collected from Wusulangzi Lake and Tongxin Crater has relatively increased. Compared to the other data from around the world, the general trend is obvious due to the high slope of the increasing potential. The range of vanadium from Wusulangzi and Tongxin is approximately from 198 to 213 ppm in association with the MgO quantities of 9.1 to 11.6 wt%. Compared to other volcanic sites, the data from both the Kissomlyo volcano (yellow circles, (Jankovics et al., 2015)) and Hopi Buttes volcano (blue circles, (Re et al., 2017)) are higher than the targeted data. On the contrary, the data from Nuomin in NE China (purple circles, (Zhao et al., 2014a)) and Eledoi maar in Tanzania (red circles, (Berghuijs and Mattsson, 2013)) show a lesser value than the targeted samples. Although the trend can rarely be recognised from the plot (green triangles), the general potential is an obviously increasing trend compared to the four volcanic sites.

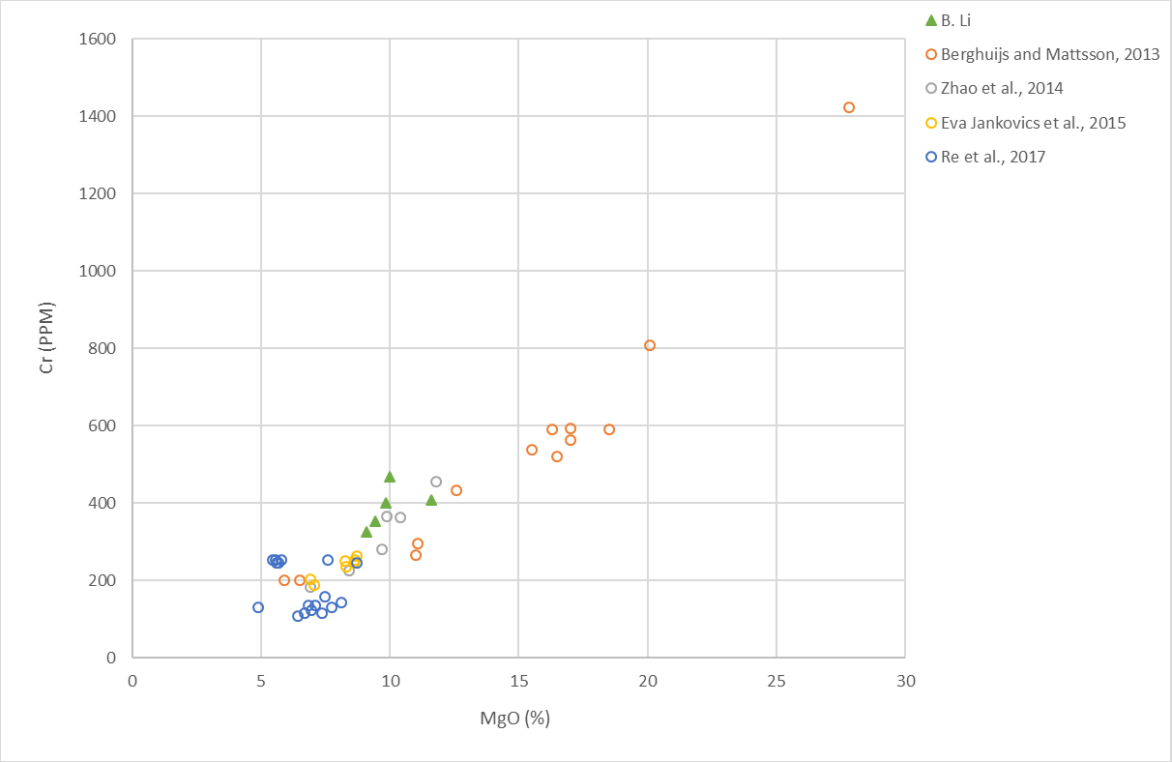

Figure 69: The Harker-like variation diagram of MgO vs chromium. Note the same labels mark the data from various sites.

Fig 69 depicts the variation between MgO and chromium. The data of Wusulangzi and Tongxin ranges from 326 to 468 ppm in plotting the MgO of 9.1 to 11.6 wt%. An increasing trend is obvious, and the other volcano sites represent the various data from approximately 1400 ppm of chromium dropping to near 150 ppm with a tremendous decreasing pattern. The targeted data (green triangles) depicts a similar slope of the total potential, whereas the data from Hopi Buttes in the USA (blue circles, (Re et al., 2017)) shows a relatively lesser trend than the total trend. From this plot, it is clear that the targeted data has a similar decreasing trend to the data from the Eledoi maar volcano in Tanzania (red circles, (Berghuijs and Mattsson, 2013)), the Nuomin Volcanic Field in NE China (purple circles, (Zhao et al., 2014a)), as well as the Kissomlyo monogenetic volcano in Hungary (yellow circles, (Jankovics et al., 2015)). In terms of a decreasing trend of Cr, the clinopyroxene or spinel may be crysallised from the melt (Wilson, 1989).

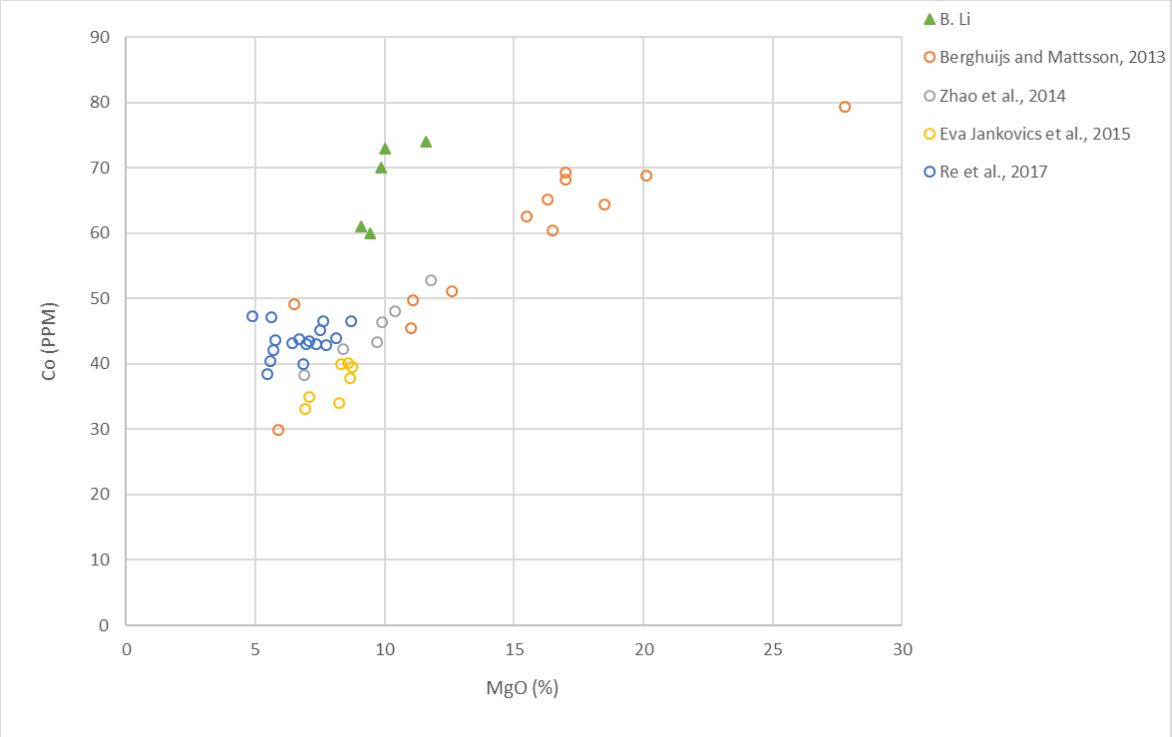

Figure 70: The variation diagram of MgO vs cobalt compared to other volcanic sites.

This diagram is about the variation of cobalt in samples from the Wusulangzi and Tongxin sites. The quantities of cobalt are nearly from 60 to 74 ppm in plotting with the MgO, which is from 9.1 to 11.6 wt%. The total pattern shows a decreased trend, however the targeted data (green triangles) is the deepest slope among them. As shown in Fig 70, the data from the Eledoi maar volcano in Tanzania (red circles, (Berghuijs and Mattsson, 2013)), the Nuomin Volcanic Field in NE China (purple circles, (Zhao et al., 2014a)), and the Kissomlyo monogenetic volcano in Hungary (yellow circles, (Jankovics et al., 2015)) shows a similar decreasing potential compared to the data from Hopi Buttes in the USA (blue circles, (Re et al., 2017)), which has a relatively medium decreasing trend. Moreover, the data from Wusulangzi and Tongxin also represents the highest amount of cobalt compared to the other data in the same range of MgO. The decreasing trend of Co and its quantities, i.e. 60 to 74 ppm reveals the olivine crystallisation and peridotite mantle sourced magma.

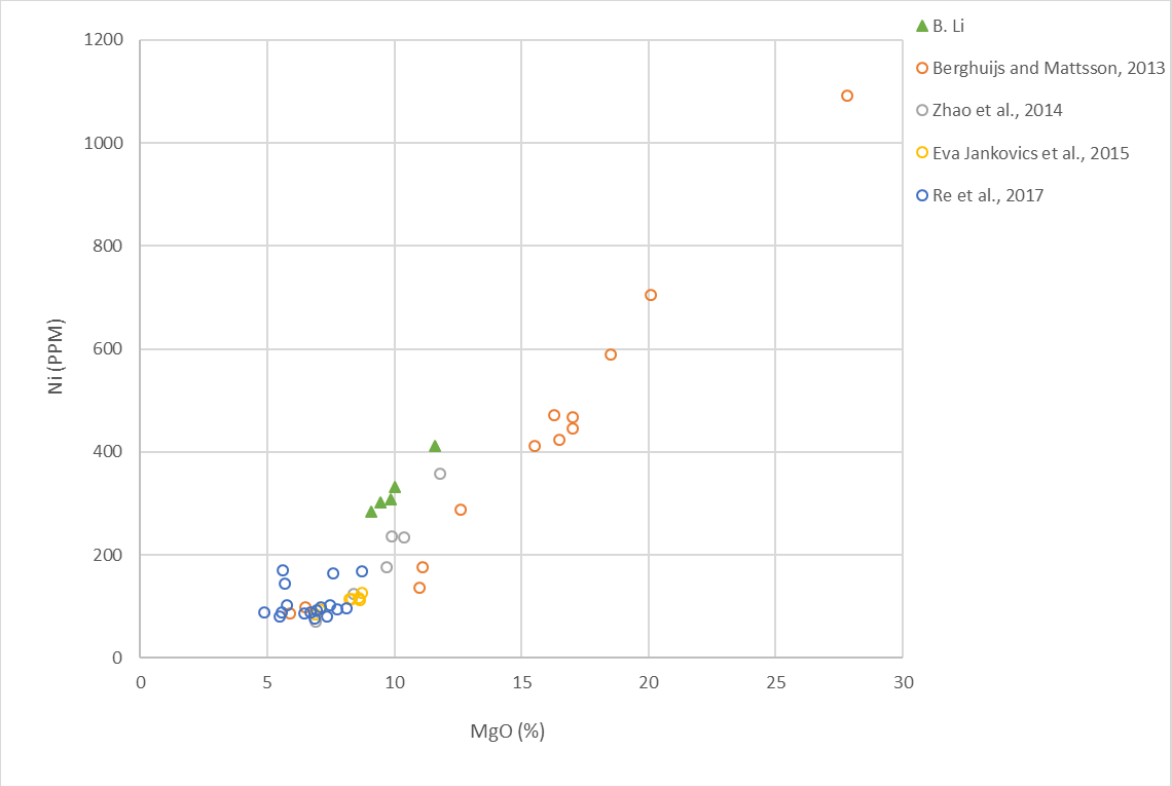

Figure 71: The Harker variation diagram of MgO vs nickel with another four sites.

Fig 71 reveals the variation of nickel from approximately 285 to 411 ppm with the association to MgO about 9.1 to 11.6 wt%. The data from Wusulangzi and Tongxin (green triangles) depicts the medium-to-high decreasing trend of approximately 45° in its slope. The general trend is decreasing almost to zero, and compared to another four sites, the targeted data shows a similar decreasing variation trend to the data from the Eledoi maar volcano in Tanzania (red circles, (Berghuijs and Mattsson, 2013)), and the Nuomin Volcanic Field in NE China (purple circles, (Zhao et al., 2014a)). Whereas, the data from the Kissomlyo monogenetic volcano in Hungary (yellow circles, (Jankovics et al., 2015)) and Hopi Buttes in the USA (blue circles, (Re et al., 2017)) reveals a relatively low variation in the decrease of Ni compared to the targeted data. In addition, the amounts of nickel in the targeted data have the highest values of any others in the same variation range of MgO amounts. The decrease in Ni impies olivine fractionation (Wilson, 1989). Also the quantities of Ni, i.e. 285 to 411 ppm, indicate parental magma batches from a peridotite mantle source (Wilson, 1989).

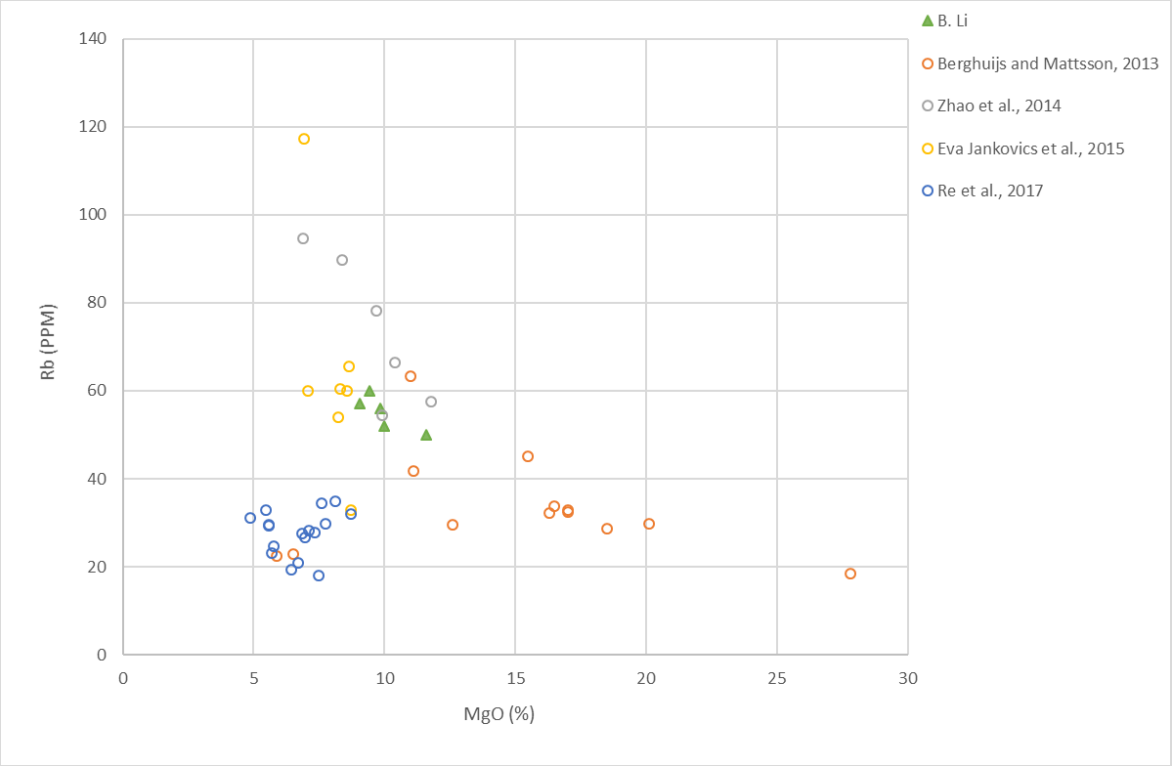

Figure 72: The binary variation diagram of MgO vs rubidium in relation to the four sites of volcanoes.

This Harker-like diagram shows a diverse variation between the different destinations of the volcanoes in association to the amounts of Rb plotting with the amounts of MgO. The targeted samples from Wusulangzi and Tongxin represented by green triangles show the intermediate to high increasing trend, with the quantities of Rb ranging from 50 to 60 ppm with the same range of MgO which is from 9.1 to 11.6 wt%. Fig 72 shows the diversity of the variation trend in terms of these patterns. The data from the Eledoi maar volcano in Tanzania (red circles, (Berghuijs and Mattsson, 2013)) has the initial and relatively low-to-intermediate increasing trend. Followed by the data of the Eledoi maar, the targeted data from Wusulangzi and Tongxin presents the medium-to-rapid increasing trend. Subsequently, the data from the Nuomin Volcanic Field in NE China (purples circles, (Zhao et al., 2014a)) and the Kissomlyo monogenetic volcano in Hungary (yellow circles, (Jankovics et al., 2015)) reveals the high increasing trend compared to the targeted data. Generally, a progressively uprising trend has been plotted on this diagram for these four sites. Specifically, the data from Hopi Buttes in the USA (blue circles, (Re et al., 2017)) has a total contradictory decreasing trend compared to the others.

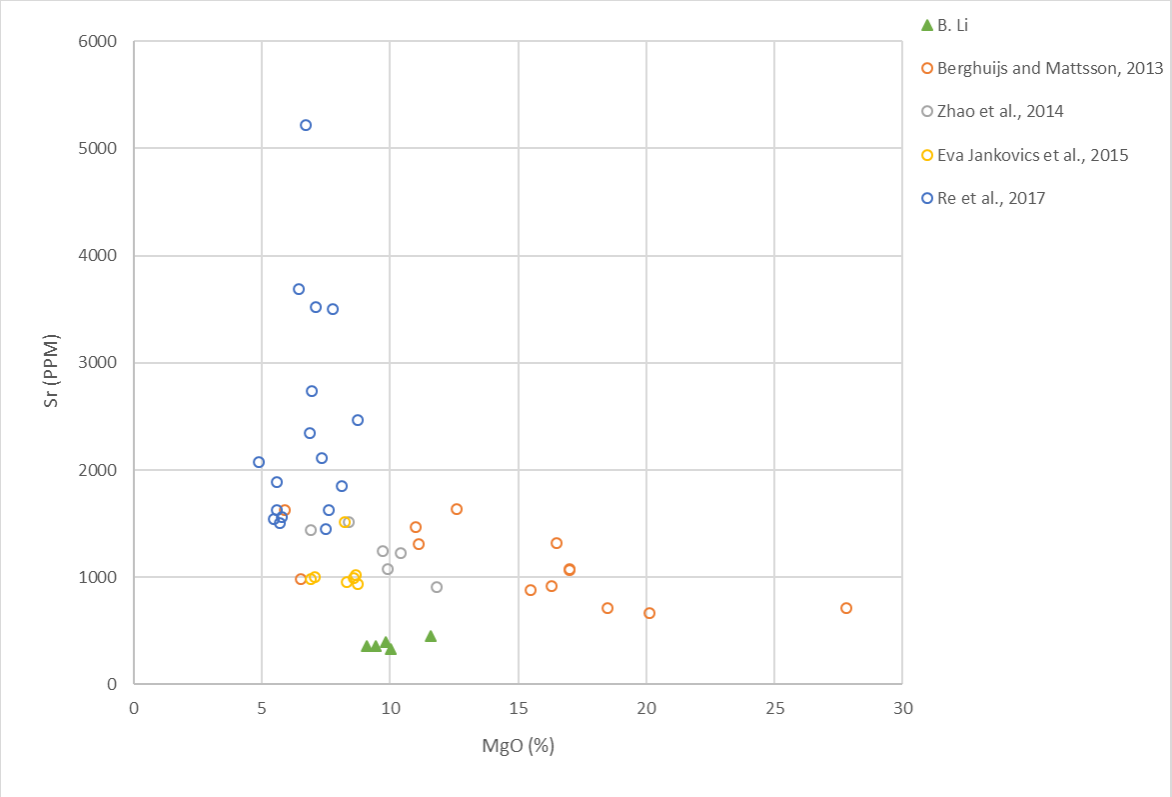

Figure 73: The variation diagram of MgO vs strontium with detailed comparative pattern to other sites.

The binary variation plot of strontium variation is in association with the MgO variation. Green triangles represent the targeted area of Wusulangzi and Tongxin with a relatively ambiguous decrease trend. The amount of strontium is ranges from 330 to 447 ppm in plotting the MgO of about 9.1 to 11.6 wt%. In comparison to other sites, the obviously increasing trend dominates the total potential. The data from the Eledoi maar in Tanzania (red circles, (Berghuijs and Mattsson, 2013)) and the Nuomin Volcanic Zone in NE China (purple circles, (Zhao et al., 2014a)) depict an intermediate increasing variation trend, whereas the subsequent patterns of the Kissomlyo monogenetic volcano in Hungary (yellow circles, (Jankovics et al., 2015)) and Hop Buttes in the USA (blue circles, (Re et al., 2017)) present a tremendous increasing trend. In this binary plot, the amounts of Sr of the targeted data preserve the lowest values amongst all other data in the same range of MgO variation.

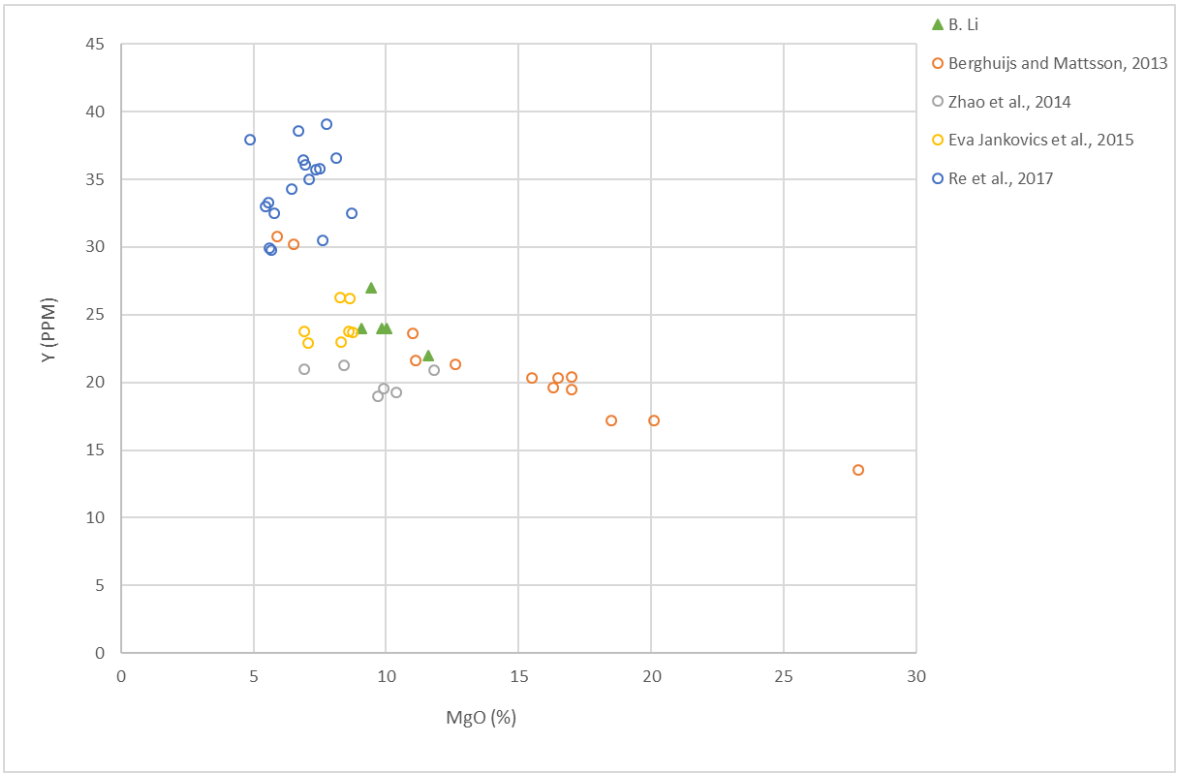

Figure 74: The Harker diagram of MgO vs yttrium for targeted data compared to other sites of volcanoes.

The Harker-like variation diagram depicts the targeted data from Wusulangzi and Tongxin with an intermediate to high increasing trend. The amounts of yttrium are approximately from 22 to 27 ppm with the composition variation of MgO about 9.1 to 11.6 wt%. Observing Fig 74, the entire pattern is an increasing trend in relation to the direction of the fractional crystallisation (from the right side to the left side of the MgO decreasing). Compared to the other sites, the data from the Eledoi maar in Tanzania (red circles, (Berghuijs and Mattsson, 2013)) and the Nuomin Volcanic Zone in NE China (purple circles, (Zhao et al., 2014a)) preserves an intermediate increasing trend. At the MgO depletion side (the left side of abscissa), the increasing trend shows a relatively large variation of yttrium in terms of the variation patterns from both the Kissomlyo monogenetic volcano in Hungary (yellow circles, (Jankovics et al., 2015)) and Hopi Buttes in the USA (blue circles, (Re et al., 2017)). The targeted data shows an intermediate increasing trend between the beginning and end sides of the fractional crystallisation.

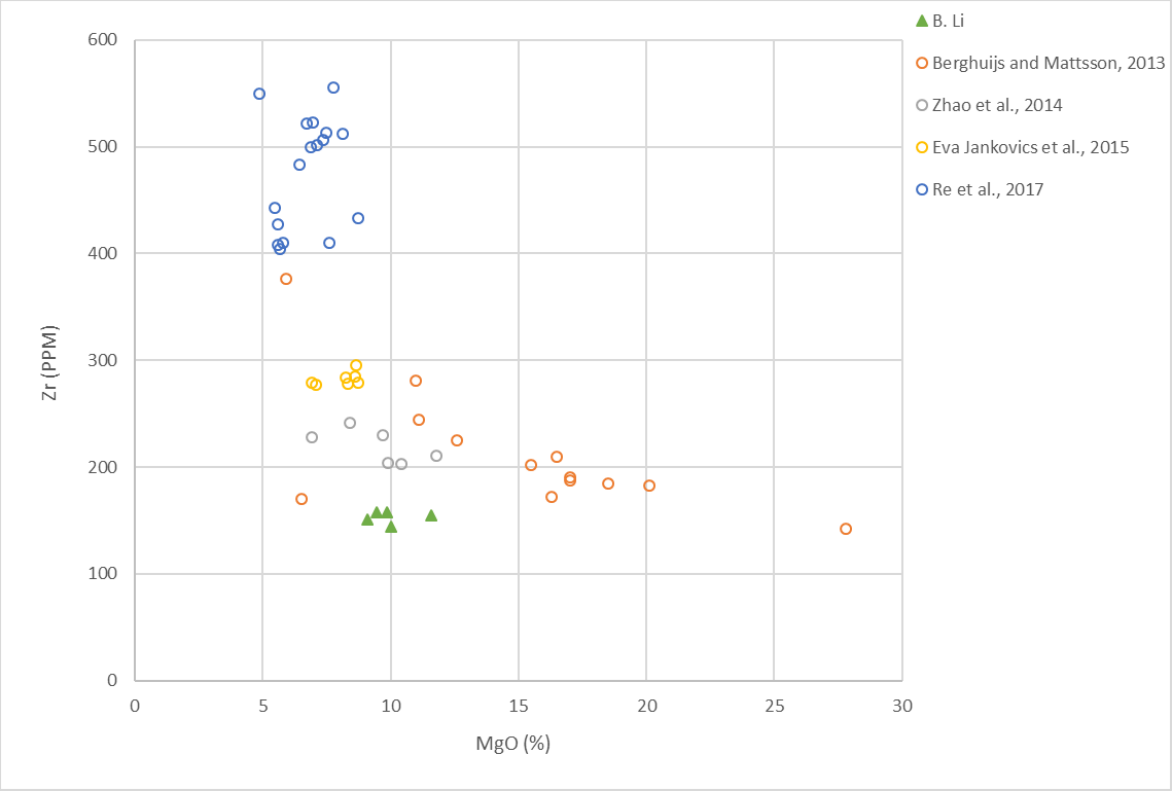

Figure 75: The variation diagram of MgO vs zirconium for the fractional crystallisation direction.

Fig 75 is a binary composition plot between zirconium and MgO. With the variation ranges of Zr (144 to 158 ppm) and MgO (9.1 to 11.6 wt%), the data from Wusulangzi and Tongxin (green triangles) presents an ambiguous decreasing trend compared to other sites. The lower trend is depicted by the data from the Eledoi maar in Tanzania (red circles, (Berghuijs and Mattsson, 2013)) and the Nuomin Volcanic Field in NE China (purple circles, (Zhao et al., 2014a)), whereas a higher increasing trend is revealed by the data from the Kissomlyo monogenetic volcano in Hungary (yellow circles, (Jankovics et al., 2015)) and Hopi Buttes in the USA (blue circles, (Re et al., 2017)). The targeted data preserves the lowest amounts of Zr in relation to the same range of MgO variation compared to the other sites. The data patterns are lying on the medium part of the fractional crystallisation path, which means a sign of MgO depletion during the magma evolution.

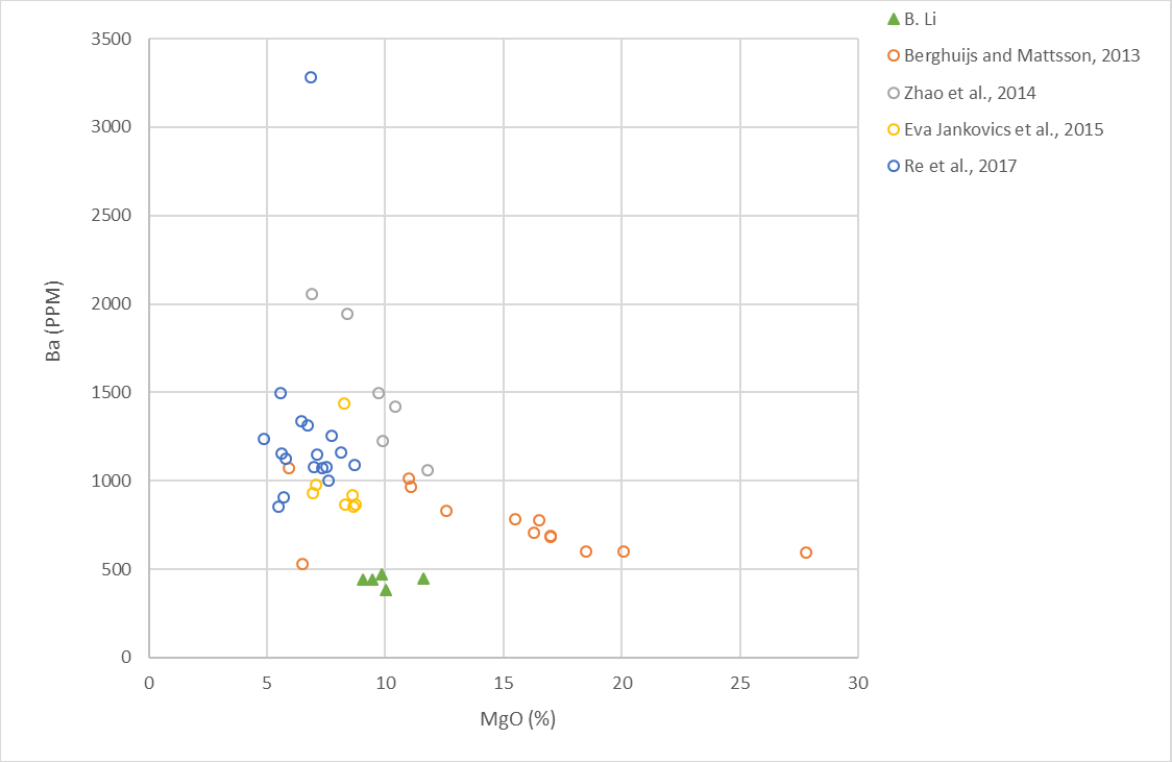

Figure 76: The variation diagram of MgO vs barium in relation to the other sites.

This figure depicts the variation of MgO plotting with the barium for the targeted data from the Wusulangzi and Tongxin areas. The similar ambiguous decrease trend (green triangles) as the plot of MgO vs Zr is obvious compared to other sites of volcanoes. The quantities of Ba are approximately from 385 to 468 ppm with the range of MgO about 9.1 to 11.6 wt%. The other data shows the diverse trends which are the relatively low rates of increasing trends represented by the Eledoi maar in Tanzania (red circles, (Berghuijs and Mattsson, 2013)) and the Kissomlyo monogenetic volcano in Hungary (yellow circles, (Jankovics et al., 2015)), the intermediate variation rate shown by Hopi Buttes in the USA (blue circles, (Re et al., 2017)), as well as the high rates revealed by the Nuomin Volcanic Field in NE China (purple circles, (Zhao et al., 2014a)). From Fig 76, the data from the Eledoi maar occupies the initial stage of the fractional crystallisation process, whereas the data from the Nuomin Volcanic Zone dominates the MgO depletion stage. Thus, the targeted data is lying on the intermediate part of the fractional crystallisation process, with the lowest amounts of Ba in the same variation range of MgO.

The following section represents the REE (rare earth elements) in plotting the MgO in the Harker-like variation diagrams. Due to unexpected and irreversible conditions, the entire REE could not be measured on the ICPMS. Thus only three REE elements can be presented here (lanthanum, cerium and neodymium).

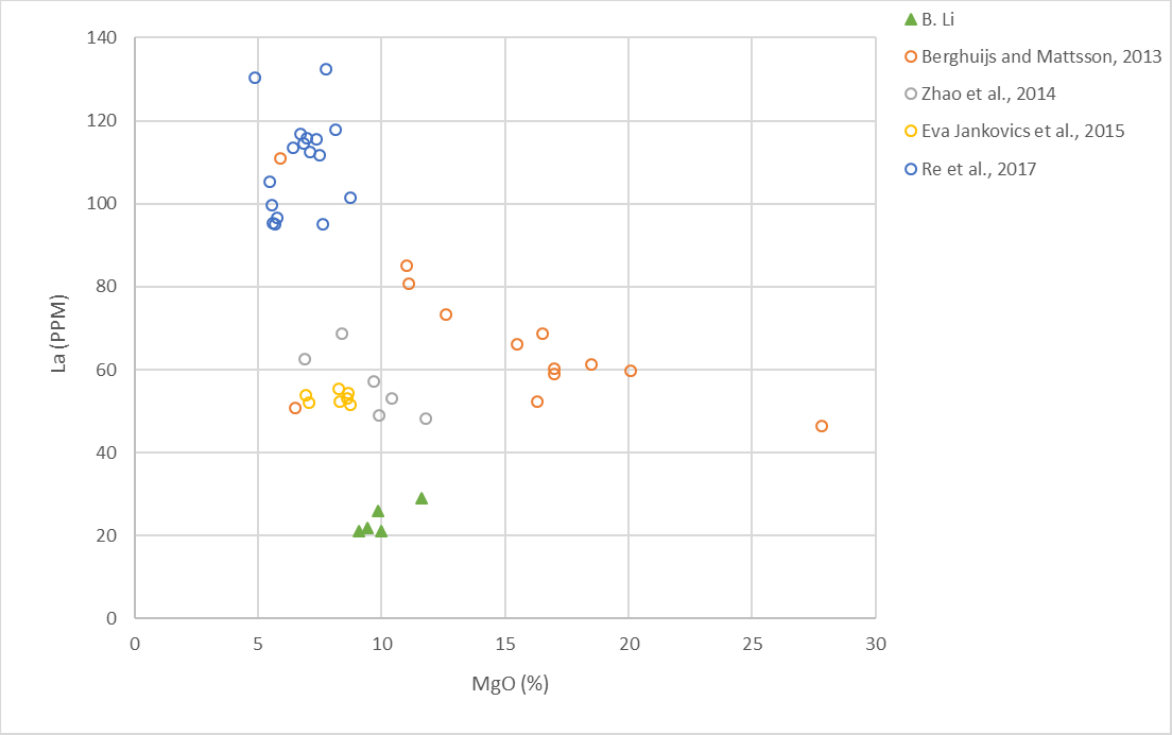

Figure 77: The variation diagram of MgO vs lanthanum in terms of assessments of fractional crystallisation.

The plot of MgO variation and lanthanum composition shows a decreasing trend in the direction of the fractional crystallisation processes of Wusulangzi and Tongxin data (green triangles). The quantities of La are ranging from 21 to 29 ppm, meanwhile MgO is approximately from 9.1 to 11.6 wt% in its amount. The other data for comparison shows a progressive increasing trend in terms of the La quantities along with the direction of fractional crystallisation. The data from the Eledoi maar in Tanzania (red circles, (Berghuijs and Mattsson, 2013)) and the Nuomin Volcanic Zone in NE China (purple circles, (Zhao et al., 2014a)) preserves a similar low-to-medium rate of increasing trend. Nevertheless, the data from Hopi Buttes in the USA (blue circles, (Re et al., 2017)) shows a relatively high rate of increasing trend. Specifically, the data from the Kissomlyo monogenetic volcano in Hungary (yellow circles, (Jankovics et al., 2015)) presents a slightly decreasing trend. The targeted data preserves the lowest amounts of La in the same variation range of MgO compared to others. A slight amount of La, i.e. 21 to 29 ppm, indicates clinopyroxene fractionation (Wilson, 1989).

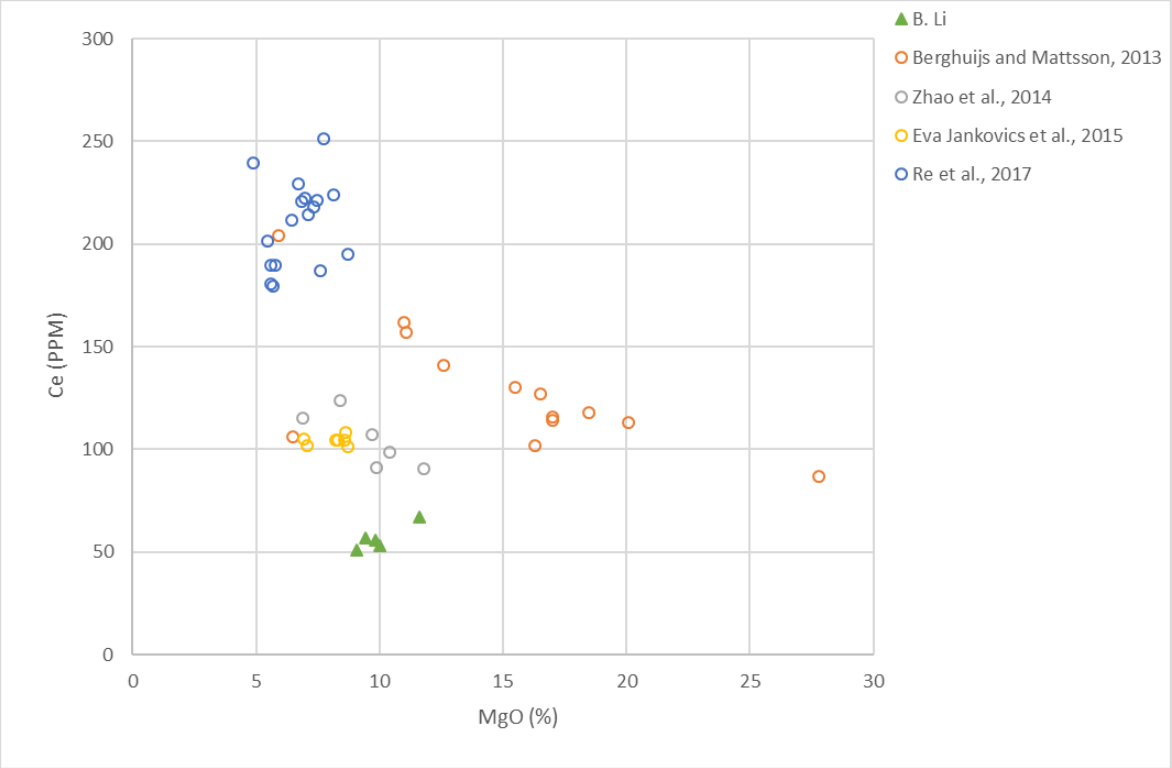

Figure 78: The Harker-like variation diagram of MgO plotting with cerium.

The variation diagram of MgO and cerium shows a decreasing trend along with the direction of fractional crystallisation, and the patterns of the targeted data (green circles) depict a medium rate of decreasing. The range of Ce is from about 51 to 67 ppm with the MgO variation ranging from 9.1 to 11.6 wt%. Along the direction of fractional crystallisation, the data from the Eledoi maar in Tanzania (rec circles, (Berghuijs and Mattsson, 2013)) and the Nuomin Volcanic Zone in NE China (purple circles, (Zhao et al., 2014a)) shows a low rate of increasing variation, whereas the data from Hopi Buttes in the USA (blue circles, (Re et al., 2017)) depicts a tremendously increasing trend with a high variation rate. Specifically, the data from Kissomlyo monogenetic volcano in Hungary (yellow circles, (Jankovics et al., 2015)) reveals an ambiguous increasing trend with a low rate of variation. Compared to the others, the targeted data has the lowest amount of Ce in the same variation range of MgO.

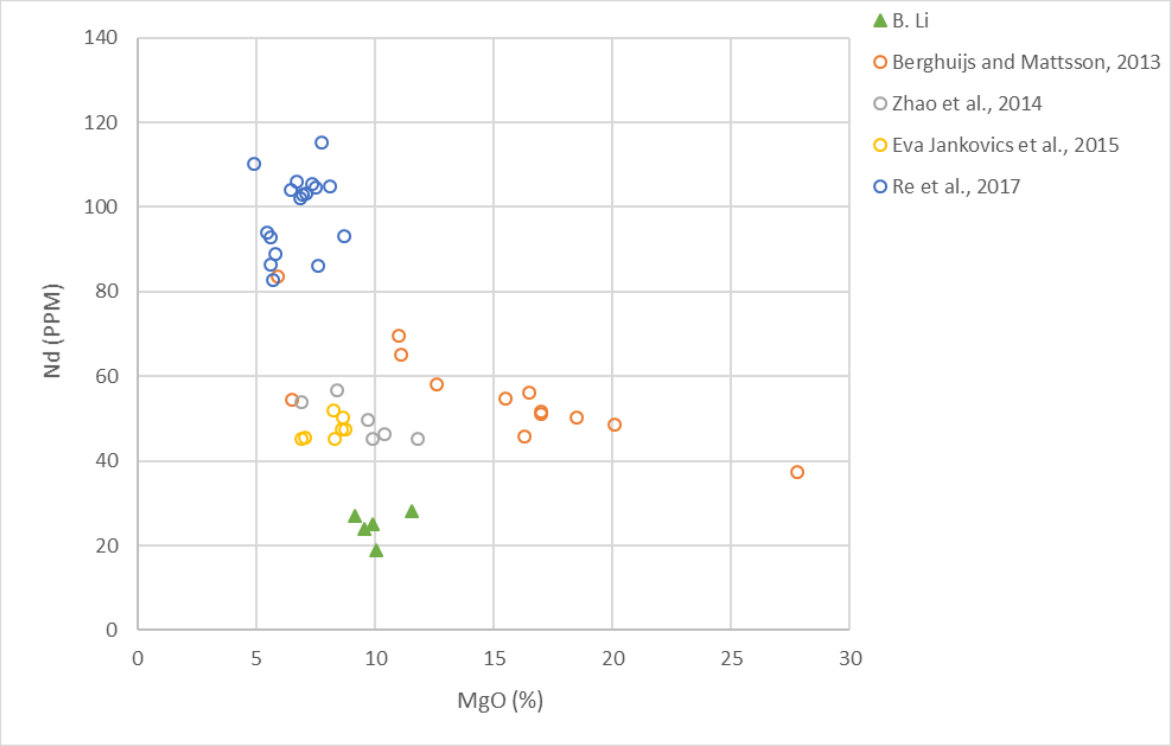

Figure 79: The variation Harker-diagram of MgO plotting with neodymium with other data from around the world.

Fig 79 also depicts the variation plot of MgO and neodymium in association with the assessments of fractional crystallisation. The targeted data from Wusulangzi and Tongxin (green triangles) presents a relatively decreasing trend with a slightly low variation rate. Accordingly, the total pattern of this plot depicts an increasing trend with progressively increasing variation rates throughout the direction of fractional crystallisation. The data from the Eledoi maar in Tanzania (red circles, (Berghuijs and Mattsson, 2013)) that occupy the left side has a similar low variation rate as well as a slightly increasing trend with the data from the Nuomin Volcanic Zone in NE China (purple circles, (Zhao et al., 2014a)) which is dominating the medium part of the trend. The data from Hopi Buttes at the USA (blue circles (Re et al., 2017)) emerges as the near depletion of MgO shows a high variation rate with an increasing trend. However, the yellow circles (Jankovics et al., 2015) that represent the data from the Kissomlyo monogenetic volcano in Hungary preserve a pattern of a decreasing trend and a low variation rate. For a comparison with other volcanic sites, the targeted data from Wusulangzi and Tongxin obtains the lowest amounts of Nd in the same variation range of MgO.

Three REE elements generally present a similar variation trend in relation to the fractional crystallisation, as well as the other data from around the world.

2) Multi-element diagram (spider diagram)

This section will be give the spider diagram which depicts the amounts of each large-ion lithophile elements (LIL) and high field strength elements (HFS) in association with the relative enrichment patterns.

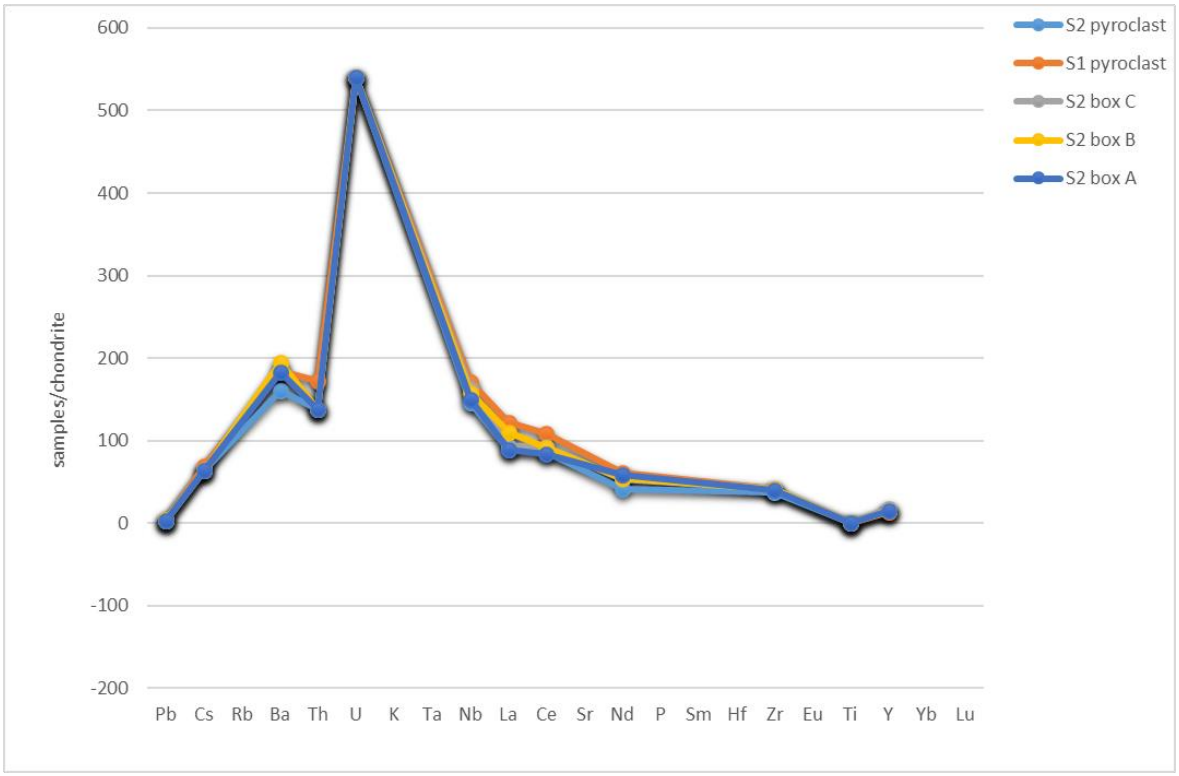

Figure 80: The multi-element diagram of Wusulangzi and Tongxin. Note the order of the whole trace elements is referenced from (Mitchell, 1995; Mitchell and Bergman, 1991).

Fig 80 shows the total trace elements in the multi-element diagram of the five sets of samples from both Wusulangzi and Tongxin at the ACVF in NE China. The order of whole elements on the abscissa is based on continental alkaline magmatism (Winter, 2013) due to the geological settings of volcanic fields in NE China. The ordinate data set is the normative data with chondrite trace elements which are referenced from (McDonough and Sun, 1995). In observation from Fig 80, the right side represents the HFS with an increasing incompatibility from the right to left direction, whereas the LIL shows an increasing incompatibility from the left to right side. As an assessment from HFS elements, Ti is absent amongst the samples; from Zr to La of REE, a steady increasing trend has been preserved with a relatively low amount of Nd. However, the quantities of Nb show a rapid increasing rate. The anomaly occurs with the U, which is much higher than the rest of the trace elements with amounts of 540.5 in normative chondrite values (this is probably not precise due to the very preliminary research). Compared to the Th, the data of Ba depicts another anomaly of all LIL elements with the amount of 182 to 194 in normative chondrite values.

The analyses, evaluations and assessments of trace elements for Wusulangzi and Tongxin in the ACVF show a wide range of variations. In terms of the assessments of Harker-like variation diagrams, the targeted data reveals the magma diversities. The decreasing trends of Ni, Co and Cr indicate the olivine, clinopyroxene and possible spinel fractionations (Wilson, 1989), which corresponds to the observations under petrographic microscopy. The increasing trend of V implies that Fe-Ti fractionation may not happen during the initial process of crystallisation. However, the amounts of Ti are almost zero in the data set (Table 6), which

may indicate there is no substitution of Ti in additional phases (Wilson, 1989), e.g. sphene and rutile, which corresponds to the CIPW Norm outcomes. The slight to non-decreased trend of Zr may imply the substitution of Ti may or may not occur during the fractional crystallisation, which probably corresponds with the non-detection of Ti. The Ba variation shows a rarely decreasing trend, indicating the substitution of K in the potassium feldspar may or may not happen during the process of fractional crystallisation. The increasing trend of Rb reveals the same outcome of no sign of substitution of K in the K-feldspar. The slightly decreasing trend of Sr may imply low amounts of substitution of calcium in plagioclase. The low concentration of Y may indicate the sphene or apatite has very low amounts in the melt. Last, but not the least, the three REE elements depict a similar decreasing trend. For each of the REE, the low amount means the clinopyroxene fractionation occurred during the crystallisation process but only in slight quantities.

Discussion and conclusions

Discussion

The ACVF is one of the massive volcanic fields in the NE of China. The genesis of this area is suspected to be the continental margin rift system, similar to the world-famous East Africa Rift (Liu et al., 2009; Liu et al., 2001). The number of vents in the ACVF is approximately more than 24, with the location of 46°39’-47°50’N, 119°28’-121°23’E (Wang et al., 2014). Compared to other volcanic fields in the world, e.g. in Mexico, the western US, the AVF, and newer volcanic fields, the following table will give a general view in relation to the volcanic types.

Volcanic Fields	Destination	Number of vents	Elevation	Latitude and Longitude	Volcano Types	Rock Types	Tectonic Settings
Newer Volcanic Province	Australia	400	1011 m / 3316 ft	37.77°S 142.5°E	Shield(s) Pyroclastic cone(s) Tuff ring(s)	Trachybasalt / Tephrite Basanite Basalt / Picro-Basalt	Intra-plate Continental crust (> 25 km)
Naolinco Volcanic Field	Mexico	50	2000 m / 6560 ft	19.67°N 96.75°W	Pyroclastic cone(s)	Basalt / Picro-Basalt Andesite / Basaltic Andesite Trachybasalt / Tephrite Basanite	Subduction zone Continental crust (> 25 km)
Auckland Field	New Zealand	50	260 m / 853 ft	36.9°S 174.87°E	Maar-diatreme Scoria cone(s)	Trachybasalt / Tephrite Basanite Basalt / Picro-Basalt Foidite	Subduction zone Continental crust (> 25 km)
Arxan-Chaihe Volcanic Field	NE China	27+	1677 m / 5501 ft	47.45°N 120.8°E	Pyroclastic cone(s) Maar-diatreme Scoria cone(s)	Basalt / Picro-Basalt	Intraplate Continental crust (> 25 km)

Table 7: The volcanic fields around the world compared to the ACVF (Boyce, 2013; McGee et al., 2013; Rodríguez et al., 2010; Wang et al., 2014); http://volcano.si.edu

Table 7 reveals a comparison of four volcanic fields. From the number of vents, the ACVF is relatively small, but the field area ranges from medium to large. Due to the monogenetic features, the rocks types from the ACVF are similar to the other monogenetic volcanic fields, i.e. basalt in common. In contrast with the AVF, the ACVF was formed from the intra-plate continental crust. Also, the continental rift system may play an essential part in the evolution of the ACVF.

The cumulative curve of grain size also indicates the larger particles of pyroclastic materials experienced a very rapid cumulation during the eruption due to the accumulation of grain sizes from -4 to -1 in ϕ values and the relatively deep slope of the curve (Fig 41). This could mean the energy of the eruption was relatively large. Compared to the other destination – Wusulangzi Lake – the accumulation of pyroclastic materials is mainly concentrated on the grain sizes with -2 to 1.5 in ϕ values. Besides, the slope of cumulative curve in relation to the Wusulangzi Lake is less deep than Tongxin's, which may indicate the explosive energy of Wusulangzi was far less than Tongxin. Another observation via the geomorphic and geographic characteristics of Tongxin and Wusulangzi is the area of the lake in Tongxin is more massive than in Wusulangzi, which implies a massive explosive eruption occurred at Tongxin Lake. Meanwhile, the largest vent in the ACVF may be preserved in Tongxin, which is about 1.7 to 2.2 km crossing the geomorphic depression (Németh et al., 2017) (Fig 29).

Along with the proximal sites, the pyroclastic successions and beddings at Tongxin site are highly developed due to it being approximately 30 m thick (Németh et al., 2017). With the coarse clasts inter-bedded by a range of fine grain-sized pyroclastic laminations, the succession around the Tongxin Lake is precisely formed by a high explosive eruption. A set of very fine-grain layers that are shown as chute-and-pool structures, ballistic sags, crossing beds, as well as dune-beddings, indicate the large extent of base surges that developed and flowed through the external slope of the depression. This also definitely points to the phreatomagmatic eruptions in high energy. Water influences in both sites are also considered to have a critical role in how the possible phreatomagmatic eruptions were triggered at Wusulangzi and Tongxin. In terms of the observation under the petrographic microscopy method, the variety of minerals (Fig 47) can be seen and can imply that fractional crystallisation was immense during the magma ascent, and this is also proven by the CIPW Norm in relation to the XRF analyses of major elements (Fig 57). Palaonitisation in the lithic materials (Fig 48B) that was retrieved from Sample 2, i.e. the Tongxin site, means a high reaction of water-magma interactions. The photos from Back-scatter Electron Microscopy (2D) and Scanning Electron Microscopy (3D) depict the irregular or sub-angular vesicles of Sample 2 (Tongxin). This could point to the theory that when magma ascends, the external water generates a sudden external pressure squeezing the bubbles in magma to become such irregular shapes. Otherwise, highly-fragmented particles and a high content of glassy shards are also discovered in Sample 2. Compared to Tongxin, samples from Wusulangzi are out-numbered and depict the low fragmentation and low glass chard content. The pyroclastic successions and beddings in the Wusulangzi proximal area are well preserved meaning the

phreatomagmatic eruption did occur at Wusulangzi Lake. However, due to the lack of observation and sample retrieving at the Wusulangzi site, the energy of explosion and magnitude of phreatomagmatic eruption are still under debate. Thus, this will be another important part for the author's PhD period.

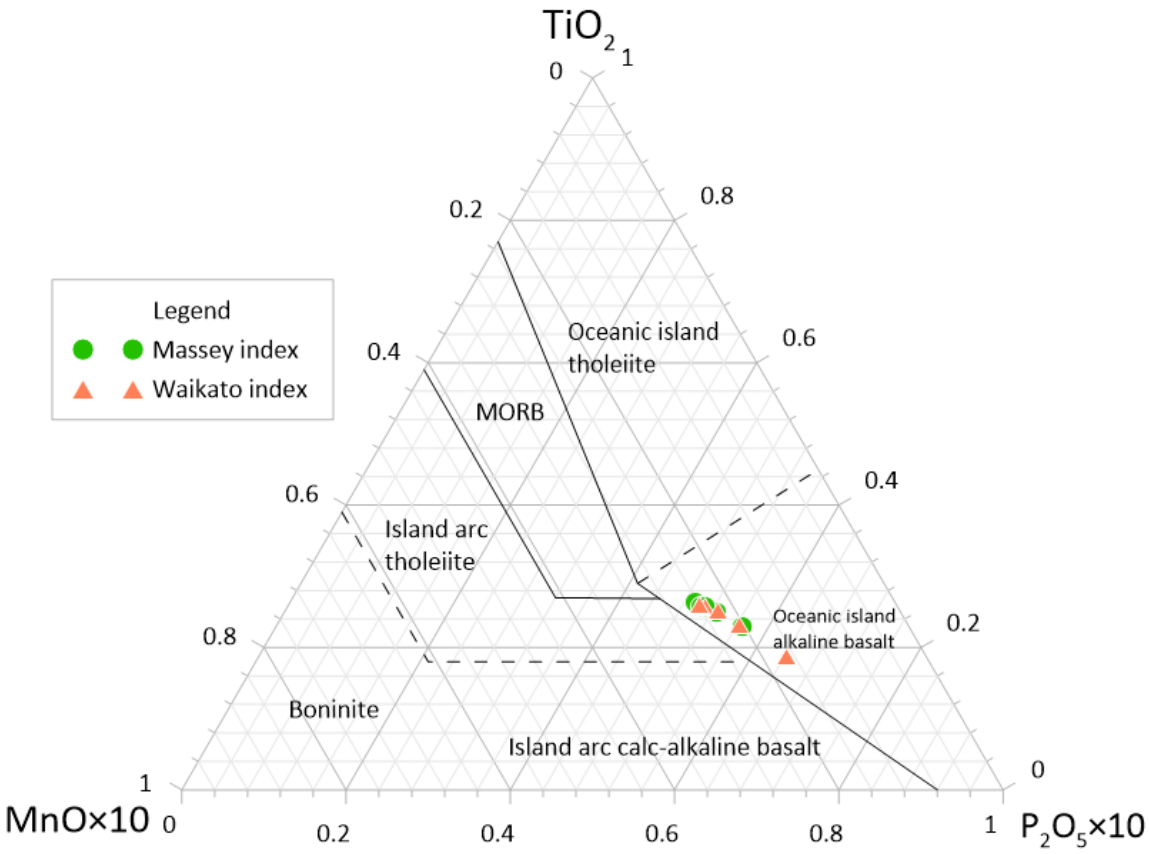

Figure 81: The tectonomagmatic discrimination diagram of basaltic rocks (Mullen, 1983).

Fig 81 depicts the ternary plot of Mno, P_2O_5 and TiO_2 in terms of the recognition of the background tectonic settings, as well as the corresponding source comparing it with the oceanic volcanic rocks. As this plot reveals, both data measured from Massey University and Waikato University are located in the area of oceanic island alkaline basalt. This could mean the possible source of the magma forming the ACVF is similar to the volcanic islands, e.g. Hawaii.

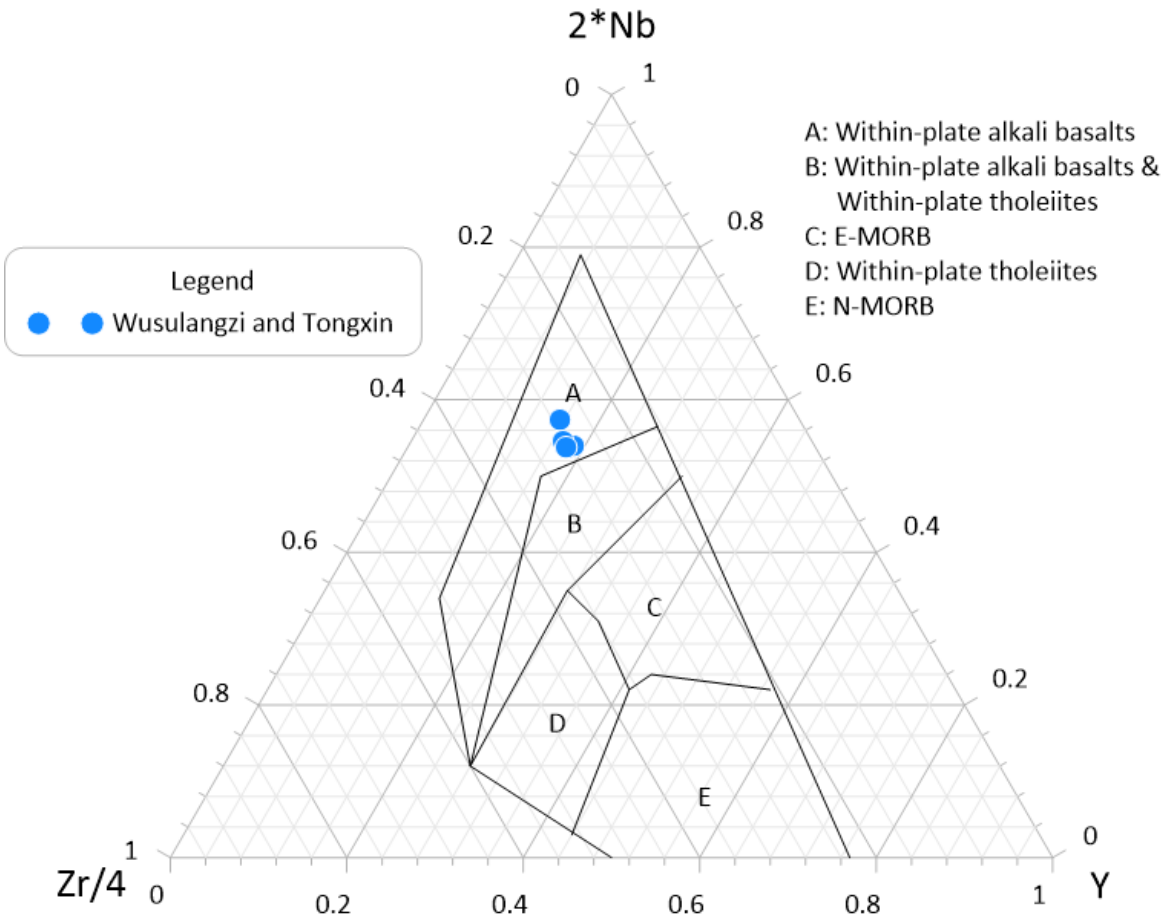

Figure 82: The discrimination plot between oceanic basalts and continental basalts (Meschede, 1986).

Fig 82 is the ternary plot for three trace elements: Nb, Zr and Y, in relation to the distinction of oceanic basalts and continental basalts. The data is lying in the area of "within-plate alkali basalts", which indicates the ACVF was formed in the inland regions of NE China. This corresponds with the geographic, geomorphic and tectonic settings in NE China (Liu et al., 2001; Németh et al., 2017; Wang et al., 2014).

These two plots (Fig 81, 82) also need further research in the author's PhD. Also, for the major and trace elements data, the limitation of the sample quantities has become a barrier for evaluation and estimation in terms of the petrogenesis and derivation of the ACVF. However, due to this preliminary research, the diversity of fractional crystallisation shows a strong magnitude. Harker variation diagrams for both major and trace elements contribute a range of mineral evolutions during the magma evolution processes. In the future, the geochemical analyses will intend to combine large quantities of samples. REE is also required to be more detailed. The pattern of the multi-element (spider diagram) needs to be more precise.

Conclusions

1) The medium-to-high magnitude of phreatomagmatic explosive eruptions did occur at both Wusulangzi Lake and Tongxin Lake due to the presence of abundant surface and ground water system and the relatively humid environment.
2) By calculating the data of major and trace elements measured by the XRF method, the volcanism was controlled by the basaltic magma that produced both pyroclastic deposits and coherent lava in the ACVF in the form of various small monogenetic volcanoes.
3) Observation of every kind of microscopy method, the non-vesicular glass shards, highly-fragmented juvenile particles, well-developed vesicles, tuff lapilli, as well as the highly-evolved pyroclastic beddings in both sample groups from Wusulangzi and Tongxin imply phreatomagmatic origins.
4) The abundance of deep-sourced xenoliths and accidental lithics in both sample groups of Wusulangzi and Tongxin indicate that excavation processes were immense during the eruption phases. Also, the clast componentry of the pyroclastic deposits of the crater rims imply the Tongxin Lake to be a maar crater rather than a caldera.
5) Due to the geographic and geomorphic features of Wusulangzi, especially on the Tongxin site, the depression of Tongxin is covered by a large alluvial fan with a stream via N-S (Fig 29), which indicates surface water in abundant quantities. With the relatively humid to semi-humid environment, it is clear that the water was hosted by this intra-mountain depression and may have triggered the high energy of the phreatomagmatic eruptions.
6) The interaction between water and magma batches may be severe due to the palagonitisation observed from the lithic thin sections of Tongxin samples by petrographic microscopy.
7) The cumulation curves of grain sizes of both Wusulangzi and Tongxin (Fig 41) sample groups give evidence that the explosive energy of Tongxin was far more powerful than the energy at Wusulangzi due to the larger grains being rapidly accumulated on Tongxin site.
8) As same as Tongxin Lake, Wusulangzi Lake is also suspected to be a maar crater. A huge alluvial fan was propagated in the north of the lake. The size of the lake and the pyroclastic successions and beddings which distribute around Wusulangzi also bring evidence in relation to the maar crater. However, due to the limited samples and field observation, only a few analyses can prove Wusulanngzi Lake to be a maar crater. Future research is definitely needed.
9) At Tongxin, abundant pyroclastic successions are well preserved around the Tongxin Depression. The general stratigraphy records a violent explosive phase in the initial stage that was producing base surges that accumulated a tuff ring of over 20 m within the total thickness. Pyroclastic deposits can be traced over 3 km from the crater rim.

In the tuff ring successions, coarse-grained lapilli tuff-dominated and accidental lithic clast rich beds are interpreted to be vent-clearing explosion breccias . The pyroclastic succession is also rich in peridotite iherzolites of up to 20 cm in diameter, indicating a rapid ascent of melt to the surface.

10) The geochemistry data of major and trace elements indicates that fractional crystallisation is varied. Olivine, clinopyroxene and plagioclase phases dominate the major magma evolution. The spider diagram implies the uranium-riched mantle source powers the volcanism in the ACVF. The TAS (total alkali vs silica) and AFM diagrams reveal a basaltic property in relation to the rapid magma ascent with a primitive magma-evolutionary stage.
11) Tongxin Lake was first considered as a caldera (Németh et al., 2017). However, due to the preliminary research and observations, the extent of the Tongxin Depression and the distribution of the pyroclastic successions point to Tongxin Lake being a large maar. Additionally, the composition of the pyroclasts is dominated by tuff lapilli and basaltic materials, as well as non-ignimbrite ashes. Thus, the possibility of a maar crater for Tongxin Lake is highly recommended.

References:

Acocella, V., 2007. Understanding caldera structure and development: An overview of analogue models compared to natural calderas. Earth-Science Reviews, 85(3): 125-160.

Acocella, V., Korme, T., Salvini, F. and Funiciello, R., 2002. Elliptic calderas in the Ethiopian Rift: control of pre-existing structures. Journal of Volcanology and Geothermal Research, 119(1): 189-203.

Affleck, D.K., Cassidy, J. and Locke, C.A., 2001. Te Pouhawaiki Volcano and pre‐volcanic topography in central Auckland: Volcanological and hydrogeological implications. New Zealand Journal of Geology and Geophysics, 44(2): 313-321.

Agustín-Flores, J., Németh, K., Cronin, S.J., Lindsay, J.M. and Kereszturi, G., 2015. Shallow-seated explosions in the construction of the Motukorea tuff ring (Auckland, New Zealand): Evidence from lithic and sedimentary characteristics. Journal of Volcanology and Geothermal Research, 304: 272–286.

Allen, S.R., Bryner, V.F., Smith, I.E.M. and Ballance, P.F., 1996. Facies analysis of pyroclastic deposits within basaltic tuff‐rings of the Auckland volcanic field, New Zealand. New Zealand Journal of Geology and Geophysics, 39(2): 309-327.

Alvarado, G.E., Pérez, W., Vogel, T.A., Gröger, H. and Patiño, L., 2011. The Cerro Chopo basaltic cone (Costa Rica): An unusual completely reversed graded pyroclastic cone with abundant low vesiculated cannonball juvenile fragments. Journal of Volcanology and Geothermal Research, 201(1): 163-177.

Aranda-Gómez, J. and Luhr, J.F., 1996. Origin of the Joya Honda maar, San Luis Potosí, México. Journal of Volcanology and Geothermal Research, 74(1): 1-18.

Aranda-Gómez, J.J., Luhr, J.F. and Pier, G., 1992. The La Breña — El Jagüey Maar Complex, Durango, México: I. Geological evolution. Bulletin of Volcanology, 54(5): 393-404.

Auer, A., Martin, U. and Németh, K., 2007. The Fekete-hegy (Balaton Highland Hungary) “soft-substrate” and “hard-substrate” maar volcanoes in an aligned volcanic complex – Implications for vent geometry, subsurface stratigraphy and the palaeoenvironmental setting. Journal of Volcanology and Geothermal Research, 159(1): 225-245.

Badarch, G., Dickson Cunningham, W. and Windley, B.F., 2002. A new terrane subdivision for Mongolia: implications for the Phanerozoic crustal growth of Central Asia. Journal of Asian Earth Sciences, 21(1): 87-110.

Bai, Z.-D., Tian, M.-Z., Wu, F.-D., Xu, D.-B. and Li, T.-J., 2005. Yanshan, Gaoshan-Two Active Volcanoes of the Volcanic Cluster in Arshan, Inner Mongolia. Earthquake Research in China, 19(4): 402-408.

Bai, Z., Tan, Q., Wang, D. and Wang, Y., 2012. Late Quaternary volcanic activity and neotectonics in the eastern Inner Mongolia. Acta Petrologica Sinica, 28(4): 1099-1107.

Bai, Z., Wang, J., Xu, G., Liu, L. and Xu, D., 2008. Quaternary Volcano Cluster of Wulanhada, Right-back-banner, Chabaer, Inner Mongolia. Acta Petrologica Sinica, 24(11): 2585-2594.

Baker, P.E., Harris, P.G. and REAY, A., 1971. The geology of Tofua island, Tonga. Bull.-R. Soc. NZ, 8: 67-79.

Bao, Q., Zhang, C., Wu, Z., Wang, H., Li, W., Sang, J. and Liu, Y., 2007. SHRIMP U–Pb zircon geochronology of a carboniferous quartz diorite in Baiyingaole area, Inner Mongolia and its implications. Journal of Jilin University (Earth Science Edition), 37(1): 15-23.

Bas, M.J.L., Maitre, R.W.L., Streckeisen, A. and Zanettin, B., 1986. A Chemical Classification of Volcanic Rocks Based on the Total Alkali-Silica Diagram. Journal of petrology, 27(3): 745–750.

BD, B., CM, W. and Anonymous, 2004. Base-surge mechanics and structures, an example from Sinker Butte, ID, western Snake River plain, Rocky Mountain (56th Annual) and Cordilleran (100th Annual) Joint Meeting. Geological Society of America Abstracts with Programs, pp. 84.

Bell, J.W. and House, P.K., 2007. Did Plinian eruptions in California lead to debris flows in Nevada? An intriguing stratigraphic connection. Geology, 35(3): 219-222.

Berghuijs, J.F. and Mattsson, H.B., 2013. Magma ascent, fragmentation and depositional characteristics of “dry” maar volcanoes: Similarities with vent-facies kimberlite deposits. Journal of Volcanology and Geothermal Research, 252: 53-72.

Bitschene, P. and Schüller, A., 2011. Geo-education and geopark implementation in the Vulkaneifel European Geopark. GSA Field Guide, 22: 29-34.

Blaikie, T.N., Ailleres, L., Betts, P.G. and Cas, R.A.F., 2014. Interpreting subsurface volcanic structures using geologically constrained 3-D gravity inversions: Examples of maar-diatremes, Newer Volcanics Province, southeastern Australia. Journal of Geophysical Research: Solid Earth, 119(4): 3857-3878.

Blight, J.H.S., Crowley, Q.G., Petterson, M.G. and Cunningham, D., 2010. Granites of the Southern Mongolia Carboniferous Arc: New geochronological and geochemical constraints. Lithos, 116(1): 35-52.

Boyce, J., 2013. The Newer Volcanics Province of southeastern Australia: a new classification scheme and distribution map for eruption centres. Australian Journal of Earth Sciences, 60(4): 449-462.

Brand, B.D. and Broz, P., 2015. Tuff Cone. In: H. Hargitai and A.k. Kereszturi (Editors), Encyclopedia of Planetary Landforms, Springer, pp. 2197-2204.

Brand, B.D. and White, C.M., 2007. Origin and stratigraphy of phreatomagmatic deposits at the Pleistocene Sinker Butte Volcano, Western Snake River Plain, Idaho. Journal of Volcanology and Geothermal Research, 160(3-4): 319–339.

Brenna, M., Cronin, S.J., Németh, K., Smith, I.E.M. and Sohn, Y.K., 2011. The influence of magma plumbing complexity on monogenetic eruptions, Jeju Island, Korea. Terra Nova: no-no.

Brenna, M., Cronin, S.J., Smith, I.E.M., Maas, R. and Sohn, Y.K., 2012. How Small-volume Basaltic Magmatic Systems Develop: a Case Study from the Jeju Island Volcanic Field, Korea. JOURNALOF PETROLOGY, 53(5): 985-1018.

Broz, P. and Nemeth, K., 2015. Tuff Ring. In: H. Hargitai and A.k. Kereszturi (Editors), Encyclopedia of Planetary Landforms, Springer, pp. 2204-2210.

Büchel, G., 1993. Maars of the Westeifel, Germany. In: J.F.W. Negendank and B. Zolitschka (Editors), Paleolimnology of European Maar Lakes. Springer Berlin Heidelberg, Berlin, Heidelberg, pp. 1-13.

Buck, W.R., 1991. Modes of continental lithospheric extension. Journal of Geophysical Research: Solid Earth, 96(B12): 20161-20178.

Buttner, R., Dellino, P. and Zimanowski, B., 1999. Identifying magma–water interaction from the surface features of ash particles. NATURE, 40(6754): 688-690.

Büttner, R. and Zimanowski, B., 1998. Physics of thermohydraulic explosions. Physical Review E, 57(5): 5726-5729.

Cajz, V., Rapprich, V., Erban, V., Pecskay, Z. and Radon, M., 2009. Late Miocene volcanic activity in the Ceske stredohori Mountains (Ohre/Eger Graben, northern Bohemia). GEOLOGICA CARPATHICA, 60(6): 519-533.

Carey, R.J., Houghton, B.F. and Thordarson, T., 2009. Abrupt shifts between wet and dry phases of the 1875 eruption of Askja Volcano: Microscopic evidence for macroscopic dynamics. Journal of Volcanology and Geothermal Research, 184(3): 256-270.

Carrasco-Núñez, G., Ort, M.H. and Romero, C., 2007. Evolution and hydrological conditions of a maar volcano (Atexcac crater, Eastern Mexico). Journal of Volcanology and Geothermal Research, 159(1): 179-197.

Cas, R. and Wright, J.V., 1987. Volcanic successions, modern and ancient: a geological approach to processes, products, and successions. London; Boston: Allen & Unwin/Chapman & Hall.

Cashman, K.V., Sturtevant, B., Papele, P. and Navon, O., 2000. Magmatic fragmentation. In: H. Sigurdsson, B. Houghton, S. McNutt, H. Rymer and J. Stix (Editors), Encyclopedia of Volcanoes, Academic Press, New York, pp. 421-430.

Cassidy, J., France, S.J. and Locke, C.A., 2007. Gravity and magnetic investigation of maar volcanoes, Auckland volcanic field, New Zealand. Journal of Volcanology and Geothermal Research, 159(1-3): 153–163.

Cebriá, J.M., Martiny, B.M., López-Ruiz, J. and Morán-Zenteno, D.J., 2011. The Paricutin calc-alkaline lavas: new geochemical and petrogenetic modelling constraints on the crustal assimilation process. Journal of Volcanology and Geothermal Research, 201(1): 113–125.

Chao, C.Z., 1992. The classification of the continental plates of China. Bull. Shenyang Inst. Geol. Min. Resour, 1: 45–50.

Chen, B., Jahn, B.-m., Wilde, S. and Xu, B., 2000. Two contrasting paleozoic magmatic belts in northern Inner Mongolia, China: petrogenesis and tectonic implications. Tectonophysics, 328(1): 157-182.

Chen, B., Jahn, B.M. and Tian, W., 2009. Evolution of the Solonker suture zone: Constraints from zircon U–Pb ages, Hf isotopic ratios and whole-rock Nd–Sr isotope compositions of subduction- and collision-related magmas and forearc sediments. Journal of Asian Earth Sciences, 34(3): 245-257.

Chouet, B., Hamisevicz, N. and McGetchin, T.R., 1974. Photoballistics of volcanic jet activity at Stromboli, Italy. Journal of Geophysical Research, 79(32): 4961-4976.

Chough, S.K. and Sohn, Y.K., 1990. Depositional mechanics and sequences of base surges, Songaksan tuff ring, Cheju Island, Korea. Sedimentology, 37(6): 1115-1135.

Christenson, B., Németh, K., Rouwet, D., Tassi, F., Vandemeulebrouck, J. and Varekamp, J.C., 2015. Volcanic Lakes. In: D. Rouwet, B. Christenson, F. Tassi and J. Vandemeulebrouck (Editors), Volcanic Lakes. Springer Berlin Heidelberg, Berlin, Heidelberg, pp. 1-20.

Chu, G., Sun, Q., Rioual, P., Boltovskoy, A., Liu, Q., Sun, P., Han, J. and Liu, J., 2008. Dinocyst microlaminations and freshwater "red tides" recorded in Lake Xiaolongwan, northeastern China. Journal of Paleolimnology, 39(3): 319-333.

Clement, C.R. and Reid, A.M., 1989. The origin of kimberlite pipes: An interpretation based on a synthesis of geological features displayed by southern African occurrences. Kimberlites and related rocks, 1: 632-646.

Cole, J., Milner, D. and Spinks, K., 2005. Calderas and caldera structures: a review. Earth-Science Reviews, 69(1-2): 1-26.

Cook, C., Briggs, R.M., Smith, I.E.M. and Maas, R., 2005. Petrology and geochemistry of intraplate basalts in the South Auckland Volcanic Field, New Zealand: evidence for two coeval magma suites from distinct sources. JOURNAL OF PETROLOGY, 46(3): 473-503.

Courtland, L., Kruse, S. and Connor, C., 2013. Violent Strombolian or not? Using ground-penetrating radar to distinguish deposits of low- and high-energy scoria cone eruptions. Bulletin of volcanology, 75(12): 760.

Crowe, B.M. and Fisher, R.V., 1973. Sedimentary Structures in Base-Surge Deposits with Special Reference to Cross-Bedding, Ubehebe Craters, Death Valley, California. GSA Bulletin, 84(2): 663-682.

Decker, B.B. and Decker, R.W., 1999. Volcano. ENCYCLOPÆDIA BRITANNICA.

DeHon, R., 2015. Maar. In: H. Hargitai and A.k. Kereszturi (Editors), Encyclopedia of Planetary Landforms, Springer, pp. 1295-1299.

DeHon, R.A., 2012. Significance of Maars on Mars: Terrestrial Analogs to Martian Monogenic Volcanism, 43rd Lunar and Planetary Science Conference, Texas State University.

Dellino, P., Isaia, R. and Veneruso, M., 2004b. Turbulent boundary layer shear £ows as an approximation of base surges at Campi Flegrei (Southern Italy). Journal of Volcanology and Geothermal Research, 133(1-4): 211-228.

Dellino, P., Isaia, R., Volpe, L.L. and Orsi, G., 2004a. Interaction between particles transported by fallout and surge in the deposits of the Agnano^Monte Spina eruption (Campi Flegrei, Southern Italy). Journal of Volcanology and Geothermal Research, 133(1-4): 193-210.

Delpit, S., Ross, P.-S. and Hearn, B.C., 2014. Deep-bedded ultramafic diatremes in the Missouri River Breaks volcanic field, Montana, USA: 1 km of syn-eruptive subsidence. Bulletin of Volcanology, 76(7): 832.

Demidjuk, Z., Turner, S., Sandiford, M., George, R., Foden, J. and Etheridge, M., 2007. U-series isotope and geodynamic constraints on mantle melting processes beneath the Newer Volcanic Province in South Australia. Earth and Planetary Science Letters, 261(3): 517–533.

Deng, W., 1978. A preliminary study on the petrology and petrochemistry of the Quaternary volcanic rocks of northern Tibet autonomous region. Acta Geologica Sinica, 52(2): 148-162.

Duncan, R.A., Kent, A.J.R., Thornber, C.R., Schlieder, T.D. and Al-Amri, A.M., 2016. Timing and composition of continental volcanism at Harrat Hutaymah, western Saudi Arabia. Journal of Volcanology and Geothermal Research, 313: 1-14.

Dürig, T., Mele, D., Dellino, P. and Zimanowski, B., 2012. Comparative analyses of glass fragments from brittle fracture experiments and volcanic ash particles. Bulletin of volcanology, 74(3): 691–704.

Elston, W.E., 1984. Mid-Tertiary ash flow tuff cauldrons, southwestern New Mexico. Journal of Geophysical Research: Solid Earth, 89(B10): 8733-8750.

Erlund, E.J., Cashman, K.V., Wallace, P.J., Pioli, L., Rosi, M., Johnson, E. and Granados, H.D., 2010. Compositional evolution of magma from Paricutin Volcano, Mexico: the tephra record. Journal of Volcanology and Geothermal Research, 197(1): 167–187.

Ersoy, E.Y., Helvacı, C. and Palmer, M.R., 2010. Mantle source characteristics and melting models for the early-middle Miocene mafic volcanism in Western Anatolia Implications for enrichment processes of mantle lithosphere and origin of K-rich volcanism in post-collisional settings. Journal of Volcanology and Geothermal Research, 198(1): 112-128.

Ersoy, E.Y. and Palmer, M.R., 2013. Eocene–Quaternary magmatic activity in the Aegean: implications for mantle metasomatism and magma genesis in an evolving orogeny. Lithos, 180: 5-24.

Ersoy, Y.E., Helvacı, C. and Palmer, M.R., 2012a. Petrogenesis of the Neogene volcanic units in the NE–SW-trending basins in western Anatolia, Turkey. Contributions to Mineralogy and Petrology, 163(3): 379-401.

Ersoy, Y.E., Helvacı, C., Uysal, İ., Karaoğlu, Ö., Palmer, M.R. and Dindi, F., 2012b. Petrogenesis of the Miocene volcanism along the Izmir-Bahkesir Transfer Zone in western Anatolia, Turkey: implications for origin and evolution of potassic volcanism in post-collisional areas. Journal of Volcanology and Geothermal Research, 241: 21-38.

Fagents, S.A. and Thordarson, T., 2007. Rootless volcanic cones in Iceland and on Mars, The geology of Mars: evidence from earth-based analogs. Cambridge University Press, Cambridge, pp. 151-177.

Farrand, W.H. and Singer, R.B., 1992. Alteration of hydrovolcanic basaltic ash: Observations with visible and near-infrared spectrometry. Journal of Geophysical Research: Solid Earth, 97(B12): 17393-17408.

Feng, M., G, K. and Wang, F., 1979. Wudalianchi Volcanoes in China. Shanghai Sci Tech Publishers, Shanghai.

Field, M., Gibson, J.G., Wilkes, T.A., Gababotse, J. and Khutjwe, P., 1997. The geology of the Orapa A/K1 kimberlite, Botswana: further insight into the emplacement of kimberlite pipes. RUSSIAN GEOLOGY AND GEOPHYSICS C/C OF GEOLOGIIA I GEOFIZIKA, 38: 24-39.

Fisher, R.V. and Schmincke, H.U., 1984. Pyroclastic rocks. Springer, Berlin.

Fisher, R.V. and Schmincke, H.U., 1994. Volcaniclastic sediment transport and deposition, Sediment Transport and Depositional Processes, Blackwell Scientific, Oxford, pp. 351-388.

Fodor, E.k. and Broz, P., 2015. Cinder Cone. In: H. Hargitai and A. Kereszturi (Editors), Encyclopedia of Planetary Landforms, Springer, pp. 290-295.

Fornaciai, A., Favalli, M., Karátson, D., Tarquini, S. and Boschi, E., 2012. Morphometry of scoria cones, and their relation to geodynamic setting: A DEM-based analysis. Journal of Volcanology and Geothermal Research, 217-218: 56-72.

Francis, P., 1993. Volcanoes. A planetary perspective. Volcanoes. A planetary perspective., by Francis, P.. Clarendon Press, Oxford (UK), 1993, 452 p., ISBN 0-19-854452-9, ISBN 0-19-854033-7 (paper).

Francis, P. and Oppenheier, C., 2004. Volcanoes, Published by OXFORD University Press.

Freundt, A. and Schmincke, H.-U., 1986. Emplacement of small-volume pyroclastic flows at Laacher See (East-Eifel, Germany). Bulletin of Volcanology, 48(1): 39-59.

Funiciello, R., Giordano, G. and De Rita, D., 2003. The Albano maar lake (Colli Albani Volcano, Italy): recent volcanic activity and evidence of pre-Roman Age catastrophic lahar events. Journal of Volcanology and Geothermal Research, 123(1): 43-61.

Gao, W., Li, J., Mao, X. and Li, H., 2013. Geological and Geomorphological Value of the Monogenetic Volcanoes in Wudalianchi National Park, NE China. Geoheritage, 5(2): 73-85.

Gao, W., Li, J., Mao, X. and Zhang, T., 2010. Discussion on genetic mechanism of hornitos in Wudalianchi volcanic field. Acta Petrologica Sinica, 26(1): 309-317.

Gençalioğlu-Kuşcu, G., Atilla, C., Cas, R.A.F. and Kuşcu, İ., 2007. Base surge deposits, eruption history, and depositional processes of a wet phreatomagmatic volcano in Central Anatolia (Cora Maar). Journal of Volcanology and Geothermal Research, 159(1): 198-209.

Gernon, T.M., Field, M. and Sparks, R.S.J., 2009a. Depositional processes in a kimberlite crater: the Upper Cretaceous Orapa South Pipe (Botswana). Sedimentology, 56(3): 623-643.

Gernon, T.M., Fontana, G., Field, M., Sparks, R.S.J., Brown, R.J. and Mac Niocaill, C., 2009b. Pyroclastic flow deposits from a kimberlite eruption: The Orapa South Crater, Botswana. Lithos, 112: 566-578.

Gernon, T.M., Gilbertson, M.A., Sparks, R.S.J. and Field, M., 2009c. The role of gas-fluidisation in the formation of massive volcaniclastic kimberlite. Lithos, 112: 439-451.

Godchaux, M. and Bonnichsen, B., 2002. Syneruptive magma–water and posteruptive lava–water interactions in the Western Snake River Plain, Idaho, during the past 12 million years. Tectonic and magmatic evolution of the Snake River Plain Volcanic Province. Idaho Geol Surv Bull, 30: 387-434.

Godchaux, M.M., Bonnichsen, B. and Jenks, M.D., 1992. Types of phreatomagmatic volcanoes in the western Snake River Plain, Idaho, USA. Journal of Volcanology and Geothermal Research, 52(1): 1-25.

Gong, J., 1997. Xiaogulihe-Keluo-Wudalianchi volcanic belt. Heilongjiang Geology, 8(4): 29-39.

Goto, A., Taniguchi, H., Yoshida, M., Ohba, T. and Oshima, H., 2001. Effects of explosion energy and depth to the formation of blast wave and crater: Field Explosion Experiment for the understanding of volcanic explosion. Geophysical Research Letters, 28(22): 4287-4290.

Graettinger, A.H., Valentine, G.A. and Sonder, I., 2016. Recycling in debris-filled volcanic vents. GEOLOGY, 44(10): 811–814.

Graettinger, A.H., Valentine, G.A., Sonder, I., Ross, P.S. and White, J.D.L., 2015. Facies distribution of ejecta in analog tephra rings from experiments with single and multiple subsurface explosions. Bulletin of Volcanology, 77(8).

Graettinger, A.H., Valentine, G.A., Sonder, I., Ross, P.S., White, J.D.L. and Taddeucci, J., 2014. Maar-diatreme geometry and deposits: Subsurface blast experiments with variable explosion depth. Geochemistry, Geophysics, Geosystems, 15(3): 740-764.

Guilbaud, M.N., Blake, S., Thordarson, T. and Self, S., 2007. Role of Syn-eruptive Cooling and Degassing on Textures of Lavas from the ad 1783–1784 Laki Eruption, South Iceland. Journal of Petrology, 48(7): 1265-1294.

Guo, Y.T., 1992. The minerogenetic geology of Hadamenggou type gold deposits in Wulashan, Inner Mongolia. Jour. Precious Metallic Geology, 1: 191-195.

Gutmann, J.T., 1979. Structure and Eruptive Cycle of Cinder Cones in the Pinacate Volcanic Field and theControls of Strombolian Activity. The Journal of Geology, 87(4): 448-454.

Gutmann, J.T., 2002. Strombolian and ejusive activity as precursors to phreatomagmatism: eruptive sequence at maars of the Pinacate volcanic field, Sonora, Mexico. Journal of Volcanology and Geothermal Research, 113(1-2): 345-356.

Haase, K., Worthington, T. and Stoffers, P., 2004. Variation of the slab input and its effects on partial melting along the Kermadec arc. Geochimica et Cosmochimica Acta, 68(11): A615-A615.

Hack, J.T., 1942. Sedimentation and volcanism in the Hopi Buttes, Arizona. GSA Bulletin, 53(2): 335-372.

Hamilton, C.W., Fagents, S.A. and Thordarson, T., 2010b. Explosive lava–water interactions II: self-organization processes among volcanic rootless eruption sites in the 1783–1784 Laki lava flow, Iceland. Bulletin of Volcanology, 72(4): 469-485.

Hamilton, C.W., Thordarson, T. and Fagents, S.A., 2010a. Explosive lava–water interactions I: architecture and emplacement chronology of volcanic rootless cone groups in the 1783–1784 Laki lava flow, Iceland. Bulletin of Volcanology, 72(4): 449-467.

Harangi, S., Jankovics, M.É., Sági, T., Kiss, B., Lukács, R. and Soós, I., 2015. Origin and geodynamic relationships of the Late Miocene to Quaternary alkaline basalt volcanism in the Pannonian basin, eastern-central Europe. International Journal of Earth Sciences, 104(8): 2007–2032.

Hawthorne, J.B., 1975. 1 - MODEL OF A KIMBERLITE PIPE A2 - AHRENS, L.H. In: J.B. Dawson, A.R. Duncan and A.J. Erlank (Editors), Physics and Chemistry of the Earth. Pergamon, pp. 1-15.

Head, J.W., Bryan, W.B., Greeley, R., Guest, J.E., Schultz, P.H., Sparks, R.S.J., Walker, G.P.L., Whitford-Stark, L.J., Wood, C.A. and Carr, M.H., 1981. Distribution and morphology of basalt deposits on planets. Basaltic volcanism on the terrestrial planets: 702-887.

Head, J.W. and Wilson, L., 1989. Basaltic pyroclastic eruptions: influence of gas-release patterns and volume fluxes on fountain structure, and the formation of cinder cones, spatter cones, rootless flows, lava ponds, and lava flows. Journal of Volcanology and Geothermal Research, 37(3-4): 261-271.

Heiken, G., 1974. An atlas of volcanic ash. Smithsonian Contrib. Earth Sci., 12: 1-101.

Heiken, G.H., 1971. Tuff rings: Examples from the Fort Rock-Christmas Lake Valley Basin, south-central Oregon. Journal of Geophysical Research, 76(23): 5615-5626.

Helo, C., Hegner, E., Kröner, A., Badarch, G., Tomurtogoo, O., Windley, B.F. and Dulski, P., 2006. Geochemical signature of Paleozoic accretionary complexes of the Central Asian Orogenic Belt in South Mongolia: Constraints on arc environments and crustal growth. Chemical Geology, 227(3): 236-257.

Hetényi, G., Taisne, B., Garel, F., Médard, É., Bosshard, S. and Mattsson, H.B., 2012. Scales of columnar jointing in igneous rocks: field measurements and controlling factors. Bulletin of Volcanology, 74(2): 457-482.

Hooper, D.M. and Sheridan, M.F., 1998. Computer-simulation models of scoria cone degradation. Journal of Volcanology and Geothermal Research, 83(3-4): 241-267.

Houghton, B.F., Bonadonna, C., Gregg, C.E., Johnston, D.M., Cousins, W.J., Cole, J.W. and Carlo, P.D., 2006. Proximal tephra hazards: Recent eruption studies applied to volcanic risk in the Auckland volcanic field, New Zealand. Journal of Volcanology and Geothermal Research, 155(1-2): 138-149.

Houghton, B.F., Carey, R.J., Cashman, K.V., Wilson, C.J.N., Hobden, B.J. and Hammer, J.E., 2010. Diverse patterns of ascent, degassing, and eruption of rhyolite magma during the 1.8ka Taupo eruption, New Zealand: Evidence from clast vesicularity. Journal of Volcanology and Geothermal Research, 195(1): 31-47.

Houghton, B.F., Weaver, S.D., Wilson, C.J.N. and Lanphere, M.A., 1992. Evolution of a Quaternary peralkaline volcano: Mayor Island, New Zealand. Journal of Volcanology and Geothermal Research, 51(3): 217-236.

Huang, J.Q., Ren, J.S., Jiang, C.F. and Zhang, Z.K., 1980. Tectonics of China and its Evolution. Science Press, Beijing.

Huang, Z., Cai, F. and Han, Z., 1993. Quaternary Volcanoes of Lei and Qiong Peninsulas. Beijing: Science Press.

Hughes, S.S., Wetmore, P.H. and Casper, J.L., 2002. Evolution of Quaternary Tholeiitic Basalt Eruptive Centers on the Eastern Snake River Plain, Idaho. Tectonic and Magmatic Evolution of the Snake River Plain Volcanic Province: Idaho Geological Survey Bulletin, 30: 363-385.

Inbar, M., Gilichinsky, M., Melekestsev, I., Melnikov, D. and Zaretskaya, N., 2011. Morphometric and morphological development of Holocene cinder cones: A field and remote sensing study in the Tolbachik volcanic field, Kamchatka. Journal of Volcanology and Geothermal Research, 201(1-4): 301-311.

Irvine, T.N. and Baragar, W.R.A., 1971. A Guide to the Chemical Classification of the Common Volcanic Rocks. Canadian Journal of Earth Sciences, 8(5): 523-548.

Jaeger, J.C. and Cook, N., 1979. FUNDAMENTALS OF ROCK MECHANICS. THIRD EDITION. Chapman and Hall Limited, 11 New Fetter Lane, London, England

Jahn, B.M., Auvray, B., Cornichet, J., Bai, Y.L., Shen, Q.H. and Liu, D.Y., 1987. 3.5 Ga old amphibolites from eastern Hebei Province, China: Field occurrence, petrography, Sm-Nd isochron age and REE geochemistry. Precambrian Research, 34(3): 311-346.

Jankovics, M.É., Harangi, S., Kiss, B. and Ntaflos, T., 2012. Open-system evolution of the Füzes-tó alkaline basaltic magma, western Pannonian Basin: Constraints from mineral textures and compositions. Lithos, 140: 25–37.

Jankovics, M.É., Harangi, S., Németh, K., Kiss, B. and Ntaflos, T., 2015. A complex magmatic system beneath the Kissomlyó monogenetic volcano (western Pannonian Basin): evidence from mineral textures, zoning and chemistry. Journal of Volcanology and Geothermal Research, 301: 38-55.

Jian, P., Liu, D., Kröner, A., Windley, B.F., Shi, Y., Zhang, F., Shi, G., Miao, L., Zhang, W., Zhang, Q., Zhang, L. and Ren, J., 2008. Time scale of an early to mid-Paleozoic orogenic cycle of the long-lived Central Asian Orogenic Belt, Inner Mongolia of China: Implications for continental growth. Lithos, 101(3): 233-259.

Jian, P., Liu, D., Kröner, A., Windley, B.F., Shi, Y., Zhang, W., Zhang, F., Miao, L., Zhang, L. and Tomurhuu, D., 2010. Evolution of a Permian intraoceanic arc–trench system in the Solonker suture zone, Central Asian Orogenic Belt, China and Mongolia. Lithos, 118(1): 169-190.

Jurado-Chichay, Z., Rowland, S.K. and Walker, G.P.L., 1996a. The formation of circular littoral cones from tube-fed pāhoehoe: Mauna Loa, Hawai'i. Bulletin of Volcanology, 57(7): 471-482.

Jurado-Chichay, Z., Urrutia-Fucugauchi, J. and Rowland, S.K., 1996b. A paleomagnetic study of the Pohue Bay flow and its associated coastal cones, Mauna Loa volcano, Hawaii: constraints on their origin and temporal relationships. Physics of the Earth and Planetary Interiors, 97(1): 269-277.

Kaiser, T.M., Ansorge, J., Arratia, G., Bullwinkel, V., Gunnell, G.F., Herendeen, P.S., Jacobs, B., Mingram, J., Msuya, C., Musolff, A., Naumann, R., Schulz, E. and Wilde, V., 2006. The maar lake of Mahenge (Tanzania) - unique evidence of Eocene terrestrial environments in sub-Sahara Africa. Zeitschrift der Deutschen Gesellschaft für Geowissenschaften, 157(3): 411-431.

Kereszturi, G., Bebbington, M. and Németh, K., 2017. Forecasting transitions in monogenetic eruptions using the geologic record. Geology, 45(3): 283-286.

Kereszturi, G., Csillag, G., Németh, K., Sebe, K., Balogh, K. and Jáger, V., 2010. Volcanic architecture, eruption mechanism and landform evolution of a Plio/Pleistocene intracontinental basaltic polycyclic monogenetic volcano from the Bakony-Balaton Highland Volcanic Field, Hungary. Central European Journal of Geosciences, 2(3): 362-384.

Kereszturi, G. and Németh, K., 2011. Shallow-seated controls on the evolution of the Upper Pliocene Kopasz-hegy nested monogenetic volcanic chain in the Western Pannonian Basin (Hungary), Geologica Carpathica, pp. 535.

Kereszturi, G. and Németh, K., 2012. Monogenetic Basaltic Volcanoes: Genetic Classification, Growth, Geomorphology and Degradation, Updates in Volcanology - New Advances in Understanding Volcanic Systems.

Kereszturi, G. and Németh, K., 2016. Post-eruptive sediment transport and surface processes on unvegetated volcanic hillslopes – A case study of Black Tank scoria cone, Cima Volcanic Field, California. Geomorphology, 267: 59–75.

Kereszturi, G., Németh, K., Cronin, S.J., Agustín-Flores, J., Smith, I.E.M. and Lindsay, J., 2013. A model for calculating eruptive volumes for monogenetic volcanoes — Implication for the Quaternary Auckland Volcanic Field, New Zealand. Journal of Volcanology and Geothermal Research, 266: 16-33.

Kereszturi, G., Németh, K., Cronin, S.J., Procter, J. and Agustín-Flores, J., 2014. Influences on the variability of eruption sequences and style transitions in the Auckland Volcanic Field, New Zealand. Journal of Volcanology and Geothermal Research, 286: 101-115.

Kereszturi, G., Németh, K., Moufti, M.R., Cappello, A., Murcia, H., Ganci, G., Negro, C.D., Procter, J. and Zahran, H.M.A., 2016. Emplacement conditions of the 1256 AD Al-Madinah lava flow field in Harrat Rahat, Kingdom of Saudi Arabia - Insights from surface morphology and lava flow simulations. Journal of Volcanology and Geothermal Research, 309: 14-30.

Kokelaar, B.P., 1983. The mechanism of Surtseyan volcanism. Journal of the Geological Society, 140(6): 939-944.

Kokelaar, P., 1986. Magma-water interactions in subaqueous and emergent basaltic. Bulletin of Volcanology, 48(5): 275-289.

Kósik, S., Németh, K., Kereszturi, G., Procter, J.N., Zellmer, G.F. and Geshi, N., 2016. Phreatomagmatic and water-influenced Strombolian eruptions of a small-volume parasitic cone complex on the southern ringplain of Mt. Ruapehu, New Zealand: Facies architecture and eruption mechanisms of the Ohakune Volcanic Complex controlled by an unstable fissure eruption. Journal of Volcanology and Geothermal Research, 327: 99-115.

Kósik, S., Németh, K., Procter, J.N. and Zellmer, G.F., 2017. Maar-diatreme volcanism relating to the pyroclastic sequence of a newly discovered high-alumina basalt in the Maroa Volcanic Centre,

Taupo Volcanic Zone, New Zealand. Journal of Volcanology and Geothermal Research, 341: 363-370.

Kovalenko, V.I., Yarmoluyk, V.V., Sal'nikova, E.B., Kozlovsky, A.M., Kotov, A.B., Kovach, V.P., Savatenkov, V.M., Vladykin, N.V. and Ponomarchuk, V.A., 2006. Geology, Geochronology, and Geodynamics of the Khan Bogd alkali granite pluton in southern Mongolia. Geotectonics, 40(6): 450-466.

Kroner, A. and Rojas-Agramonte, Y., 2014. The Altaids as seen by Eduard Suess, and present thinking on the Late Mesoproterozoic to Palaeozoic evolution of Central Asia. Austrian Journal of Earth Sciences, 107(1): 156-168.

Kuntz, M.A., Champion, D.E., Spiker, E.C. and Lefebvre, R.H., 1986. Contrasting magma types and steady-state, volume-predictable, basaltic volcanism along the Great Rift, Idaho. Geological Society of America Bulletin, 97(5): 579-594.

Lajoie, J., Lanzafame, G., Rossi, P.L. and Tranne, C.A., 1992. Lateral facies variations in hydromagmatic pyroclastic deposits at Linosa, Italy. Journal of Volcanology and Geothermal Research, 54(1-2): 135-143.

Lamb, M.A. and Badarch, G., 2001. Paleozoic sedimentary basins and volcanic arc systems of southern Mongolia: New geochemical and petrographic constraints. Geological Society of America Memoirs, 194: 117-149.

Lefebvre, N.S., White, J.D.L. and Kjarsgaard, B.A., 2013. Unbedded diatreme deposits reveal maar-diatreme-forming eruptive processes: Standing Rocks West, Hopi Buttes, Navajo Nation, USA. Bulletin of Volcanology, 75(8).

Li, F., Chu, Y. and Zhong, W., 2003. New remote sensing interpretation of volcanic groups in Gankui and Nuomin-Bilahe, Inner Mongolia. Remote Sensing for Land & Resources, 54(3): 20-24.

Li, F. and Guo, K., 1986. Wudalianchi Volcanoes. Geology Publishing House, Beijing.

Li, S., Liu, X., Jin, W. and Zhang, L., 1990. Characteristics of auriferous ductile shear metamorphic zone, with central Nei Mongol as example. Selected Papers on the Geology of Gold Deposits, 1: 62-72.

Li, S., Mo, X. and Yang, S., 1995. Evolution of circum-Pacific basins and volcanic belts in eastern China and their geodynamics background. Journal of China University of Geosciences, 6(1): 48-58.

Li, S., Yang, S., Wu, C., Huang, J., Cheng, S., Xia, W. and Zhao, G., 1988. LATE MESOZOIC RIFTING IN NORTHEAST CHINA AND NORTHEAST ASIA FAULT BASIN SYSTEM. Science in China Series B-Chemistry, Biological, Agricultural, Medical & Earth Sciences, 31(2): 246.

Lin, C., Li, S., Zhang, Q. and Zhang, Y., 1997. Lithospheric stretching, subsidence and thermal history modeling: application to Yinggehai, Qiongdongnan and Songliao basins in East China. Journal of China University of Geosciences, 8(1): 83-89.

Lindqvist, J.K. and Lee, D.E., 2009. High-frequency paleoclimate signals from Foulden Maar, Waipiata Volcanic Field, southern New Zealand: An Early Miocene varved lacustrine diatomite deposit. Sedimentary Geology, 222(1): 98-110.

Lipman, P.W., 1976. Caldera-collapse breccias in the western San Juan Mountains, Colorado. GSA Bulletin, 87(10): 1397-1410.

Lipman, P.W., 1997. Subsidence of ash-flow calderas: relation to caldera size and magma-chamber geometry. Bulletin of Volcanology, 59(3): 198-218.

Liu, D.Y., Nutman, A.P., Compston, W., Wu, J.S. and Shen, Q.H., 1992. Remnants of ⩾3800 Ma crust in the Chinese part of the Sino-Korean craton. Geology, 20(4): 339-342.

Liu, D.Y., Shen, Q.H., Jahn, B.M. and Auvary, B., 1989. U-Pb geochronology by single zircon stepwise evaporation method : case studies on the Archean rocks from the Sino-Korean Craton. Terra, 1: 351.

Liu, J., 1987. STUDY ON GEOCHRONOLOGY OF THE CENOZOIC VOLCANIC ROCKS IN NORTHEAST CHINA. Acta petrologica sinica, 4: 21-31.

Liu, J., 1989. On the origin and evolution of continental rift system in Northeast China. Chinese Journal of Geology, 3: 209-319.

Liu, J., 1999. Volcanoes in China. Beijing: Science Press.

Liu, J., Chu, G., Han, J., Rioual, P., Jiao, W. and Wang, K., 2009. Volcanic eruptions in the Longgang volcanic field, northeastern China, during the past 15,000 years. Journal of Asian Earth Sciences, 34(5): 645-654.

Liu, J., Han, J. and Fyfe, W.S., 2001. Cenozoic episodic volcanism and continental rifting in northeast China and possible link to Japan Sea development as revealed from K–Ar geochronology. Tectonophysics, 339(3-4): 385-401.

Liu, M., Cui, X. and Liu, F., 2004. Cenozoic rifting and volcanism in eastern China: a mantle dynamic link to the Indo–Asian collision? Tectonophysics, 393(1-4): 29-42.

LIU, R.-x., 2000. Active volcanoes in China. Geological Review, 45: 1-15.

Liu, R., Wei, H. and Li, J., 1998. 长白山天池火山近代喷发. 科学出版社.

Liu, X. and Xiang, T., 1997. 中国东北地区新生代火山和火山碎屑堆积物资源与灾害. 吉林大学出版社.

Lorenz, V., 1970. Some Aspects of the Eruption Mechanism of the Big Hole Maar, Central Oregon. GSA Bulletin, 81(6): 1823-1830.

Lorenz, V., 1973. On the formation of maars. Bulletin Volcanologique, 37(2): 183-204.

Lorenz, V., 1974. Vesiculated tuffs and associated features. Sedimentology, 21(2): 273-291.

Lorenz, V., 1985. Maars and diatremes of phreatomagmatic origin; a review. South African Journal of Geology, 88(2): 459-470.

Lorenz, V., 1986a. On the growth of maars and diatremes and its relevance to the formation of tuff rings. Bulletin of Volcanology, 48(5): 265–274.

Lorenz, V., 1986b. On the growth of maars and diatremes and its relevance to the formation of tuff rings. Bulletin of Volcanology, 48(5): 265-274.

Lorenz, V., 2003a. Maar-Diatreme Volcanoes, their Formation, and their Setting in Hard-rock or Soft-rock Environments. GeoLines, 15: 72-83.

Lorenz, V., 2003b. Syn-and post-eruptive processes of maar–diatreme volcanoes and their relevance to the accumulation of post-eruptive maar–crater sediments. Quaterly Journals of the Geological Survey of Hungary, 40: 13-22.

Lorenz, V., 2007. Syn- and posteruptive hazards of maar–diatreme volcanoes. Journal of Volcanology and Geothermal Research, 159(1): 285-312.

Lorenz, V., 2008. Explosive maar-diatreme volcanism in unconsolidated water-saturated sediments and its relevance for diamondiferous pipes. Zeitschrift der Deutschen Gemmologischen Gesellschaft, 57: 41-60.

Lorenz, V. and Büchel, G., 1980. Zur Vulkanologie der Maare und Schlackenkegel der Westeifel. Mitteilungen der Pollichia, 68: 29-100.

Lorenz, V. and Kurszlaukis, S., 1997. On the last explosions of carbonatite pipe G3b, Gross Brukkaros, Namibia. Bulletin of Volcanology, 59(1): 1-9.

Lorenz, V. and Kurszlaukis, S., 2007. Root zone processes in the phreatomagmatic pipe emplacement model and consequences for the evolution of maar–diatreme volcanoes. Journal of Volcanology and Geothermal Research, 159(1-3): 4-32.

Lorenz, V., Mcbirney, A. and Williams, H., 1970. An investigation of volcanic depressions. Part 3: Maars, tuff-rings, tuff-cones, and diatremes, NASA.

Lorenz, V. and Suhr, P., 2012. On differences and similarities between maar-diatreme volcanoes and explosive collapse calderas, Geoscience Society of New Zealand Miscellaneous Publication, pp. 58.

Lorenz, V., Suhr, P. and Suhr, S., 2017. Phreatomagmatic maar-diatreme volcanoes and their incremental growth: a model. Geological Society, London, Special Publications, 446(1): 29-59.

Luhr, J.F., Simkin, T. and Cuasay, M., 1993. Parícutin: the volcano born in a Mexican cornfield, US Geoscience Press.

Luo, X. and Chen, Q., 1990. Preliminary study on geochronology for Cenozoic basalts from Inner Mongolia. Acta Petrologica et Mineralogica, 9(1): 37-46.

Macdonald, G.A., 1972. Volcanoes, 510 pp.

Martí, J., Geyer, A. and Folch, A., 2009. A genetic classification of collapse calderas based on field studies, and analogue and theoretical modelling, Volcanology: the Legacy of GPL Walker. London, IAVCEI-Geological Society of London, pp. 249-266.

Martí, J., Planagumà, L., Geyer, A., Canal, E. and Pedrazzi, D., 2011. Complex interaction between Strombolian and phreatomagmatic eruptions in the Quaternary monogenetic volcanism of the Catalan Volcanic Zone (NE of Spain). Journal of Volcanology and Geothermal Research, 201(1): 178-193.

Martin, U. and Nemeth, K., 2005. Eruptive and depositional history of a Pliocene tuff ring that developed in a fluvio-lacustrine basin: Kissomlyo´ volcano (western Hungary). Journal of Volcanology and Geothermal Research, 147(3-4): 342-356.

Martin, U. and Németh, K., 2004. Mio/Pliocene phreatomagmatic volcanism in the western Pannonian Basin. GEOLOGICA HUNGARICA, 26: 1-191.

Martin, U. and Németh, K., 2006. How Strombolian is a "Strombolian" scoria cone? Some irregularities in scoria cone architecture from the Transmexican Volcanic Belt, near Volcán Ceboruco, (Mexico) and Al Haruj (Libya). Journal of Volcanology and Geothermal Research, 155(1-2): 104-118.

Martin, U., Németh, K., Lorenz, V. and White, J.D.L., 2007. Introduction: Maar-diatreme volcanism. Journal of Volcanology and Geothermal Research, 159(1-3): 1-3.

Mattox, T.N. and Mangan, M.T., 1997. Littoral hydrovolcanic explosions: a case study of lava–seawater interaction at Kilauea Volcano. Journal of Volcanology and Geothermal Research, 75(1): 1-17.

McDonough, W.F. and Sun, S.-s., 1995. The composition of the Earth. Chemical Geology, 120(3-4): 223-253.

McGee, L.E. and Smith, I.E.M., 2016. Interpreting chemical compositions of small scale basaltic systems: A review. Journal of Volcanology and Geothermal Research, 325: 45-60.

McGee, L.E., Smith, I.E.M., Millet, M.-A., Handley, H.K. and Lindsay, J.M., 2013. Asthenospheric Control of Melting Processes in a Monogenetic Basaltic System: a Case Study of the Auckland Volcanic Field, New Zealand. Journal of Petrology, 54(10): 2125-2153.

McGreger, A.D. and Lees, J.M., 2004. Vent discrimination at Stromboli Volcano, Italy. Journal of Volcanology and Geothermal Research, 137(1): 169-185.

Mège, D. and Masson, P., 1996. A plume tectonics model for the Tharsis province, Mars. Planetary and Space Science, 44(12): 1499-1546.

Meschede, M., 1986. A method of discriminating between different types of mid-ocean ridge basalts and continental tholeiites with the Nb-Zr-Y diagram. Chemical Geology, 56(3): 207-218.

Miao, L., Fan, W., Liu, D., Zhang, F., Shi, Y. and Guo, F., 2008. Geochronology and geochemistry of the Hegenshan ophiolitic complex: Implications for late-stage tectonic evolution of the Inner Mongolia-Daxinganling Orogenic Belt, China. Journal of Asian Earth Sciences, 32(5): 348-370.

Miao, L., Zhang, F., Fan, W.-M. and Liu, D., 2007. Phanerozoic evolution of the Inner Mongolia–Daxinganling orogenic belt in North China: constraints from geochronology of ophiolites and associated formations. Geological Society, London, Special Publications, 280(1): 223-237.

Miller, L.D., 1998. North China gold : a product of multiple orogens. Soc. Econ. Geol. Newsletter, 33: 6-12.

Mingram, J., Allen, J.R.M., Brüchmann, C., Liu, J., Luo, X., Negendank, J.F.W., Nowaczyk, N. and Schettler, G., 2004. Maar- and crater lakes of the Long Gang Volcanic Field (N.E. China)—overview, laminated sediments, and vegetation history of the last 900 years. Quaternary International, 123-125: 135-147.

Mitchell, R.H., 1995. Kimberlites, orangeites, and related rocks. Springer Science & Business Media.

Mitchell, R.H. and Bergman, S.C., 1991. Petrology of lamproites. Springer Science & Business Media.

Morrissey, M.M., Zimanowski, B., Wohletz, K. and Büttner, R., 2000. Phreatomagmatic fragmentation. In: H. Sigurdsson, B.F. Houghton, S.R. McNutt, H. Rymer and J. Stix (Editors), Encyclopedia of Volcanoes, Academic Press, pp. 421-430.

Moufti, M.R. and Németh, K., 2016. Geoheritage of Volcanic Harrats in Saudi Arabia, Published by Springer.

Mouginis-Mark, P.J. and Robinson, M.S., 1992. Evolution of the Olympus Mons Caldera, Mars. Bulletin of Volcanology, 54(5): 347-360.

Muirhead, J.D., Van Eaton, A.R., Re, G., White, J.D.L. and Ort, M.H., 2016. Monogenetic volcanoes fed by interconnected dikes and sills in the Hopi Buttes volcanic field, Navajo Nation, USA. Bulletin of Volcanology, 78(2): 11.

Mullen, E.D., 1983. MnO/TiO2/P2O5: a minor element discriminant for basaltic rocks of oceanic environments and its implications for petrogenesis. Earth and Planetary Science Letters, 62(1): 53-62.

Murcia, H., Németh, K., El-Masry, N.N., Lindsay, J.M., Moufti, M.R.H., Wameyo, P., Cronin, S.J., Smith, I.E.M. and Kereszturi, G., 2015. The Al-Du'aythah volcanic cones, Al-Madinah City: implications for volcanic hazards in northern Harrat Rahat, Kingdom of Saudi Arabia. Bulletin of Volcanology, 77(6): 54.

Murcia, H., Németh, K., Moufti, M.R., Lindsay, J.M., El-Masry, N., Cronin, S.J., Qaddah, A. and Smith, I.E.M., 2014. Late Holocene lava flow morphotypes of northern Harrat Rahat, Kingdom of Saudi Arabia: Implications for the description of continental lava fields. Journal of Asian Earth Sciences, 84: 131-145.

Németh, K., 2010a. Monogenetic volcanic fields: Origin, sedimentary record, and relationship with polygenetic volcanism, What Is a Volcano? Geological Society of America Special Papers, pp. 43-66.

Németh, K., 2010b. Volcanic glass textures, shape characteristics and compositions of phreatomagmatic rock units from the Western Hungarian monogenetic volcanic fields and their implications for magma fragmentation. Open Geosciences, 2(3).

Németh, K., 2012. An Overview of the Monogenetic Volcanic Fields of the Western Pannonian Basin: Their Field Characteristics and Outlook for Future Research from a Global Perspective. Updates in Volcanology-A Comprehensive Approach to Volcanological Problems.

Németh, K. and Cronin, S.J., 2007. Syn- and post-eruptive erosion, gully formation, and morphological evolution of a tephra ring in tropical climate erupted in 1913 in West Ambrym, Vanuatu. Geomorphology, 86(1): 115-130.

Németh, K. and Cronin, S.J., 2011. Drivers of explosivity and elevated hazard in basaltic fissure eruptions: The 1913 eruption of Ambrym Volcano, Vanuatu (SW-Pacific). Journal of Volcanology and Geothermal Research, 201(1): 194-209.

Németh, K., Cronin, S.J., Haller, M.J., Brenna, M. and Csillag, G., 2010. Modern analogues for Miocene to Pleistocene alkali basaltic phreatomagmatic fields in the Pannonian Basin: "soft-substrate" to "combined" aquifer controlled phreatomagmatism in intraplate volcanic fields. Geosciences, 2(3): 339-361.

Németh, K., Cronin, S.J., Smith, I.E.M. and Agustin Flores, J., 2012. Amplified hazard of small-volume monogenetic eruptions due to environmental controls, Orakei Basin, Auckland Volcanic Field, New Zealand. Bulletin of Volcanology, 74(9): 2121-2137.

Németh, K., Goth, K., Martin, U., Csillag, G. and Suhr, P., 2008. Reconstructing paleoenvironment, eruption mechanism and paleomorphology of the Pliocene Pula maar, (Hungary). Journal of Volcanology and Geothermal Research, 177(2): 441-456.

Németh, K. and Kereszturi, G., 2015. Monogenetic volcanism: personal views and discussion. International Journal of Earth Sciences, 104(8): 2131-2146.

Németh, K., Manville, V. and Kano, K., 2009. Source to sink — Volcaniclastic sedimentation in and around the Pacific. Sedimentary Geology, 220(3): 135.

Németh, K. and Martin, U., 1999. Late Miocene paleo-geomorphology of the Bakony-Balaton Highland Volcanic Field (Hungary) using physical volcanology data. Zeitschrift fur Geomorphologie, 43(4): 417-438.

Németh, K. and Martin, U., 2007. Practical Volcanology, Geological Institute of Hungary.

Németh, K., Risso, C., Nullo, F. and Kereszturi, G., 2011. The role of collapsing and cone rafting on eruption style changes and final cone morphology: Los Morados scoria cone, Mendoza, Argentina. Central European Journal of Geosciences, 3(2): 102-118.

Németh, K. and White, J.D.L., 2009. Miocene phreatomagmatic monogenetic volcanism of the Waipiata Volcanic Field, Otago, New Zealand: Field Guide, Oamaru Conference, 2009. GSNZ, Oamaru, New Zealand, pp. 1-52.

Nemeth, K., White, J.D.L., Reay, A. and Martin, U., 2003. Compositional variation during monogenetic volcano growth and its implications for magma supply to continental volcanic fields. Journal of the Geological Society, 160(4): 523–530.

Németh, K., Wu, J., Sun, C. and Liu, J., 2017. Update on the Volcanic Geoheritage Values of the Pliocene to Quaternary Arxan–Chaihe Volcanic Field, Inner Mongolia, China. Geoheritage, 9(3): 279-297.

Ngwa, C.N., Suh, C.E. and Devey, C.W., 2010. Phreatomagmatic deposits and stratigraphic reconstruction at Debunscha Maar (Mt Cameroon volcano). Journal of Volcanology and Geothermal Research, 192(3): 201-211.

Nie, F.-J., 1997a. An Overview of the Gold Resources of China. International Geology Review, 39(1): 55-81.

Nie, F.-J., 1997b. Type and Distribution of Gold Deposits along the Northern Margin of the North China Craton, People's Republic of China. International Geology Review, 39(2): 151-180.

Ognjanova-Rumenova, N. and Vass, D., 1998. Palaeoecology of the Late Miocene Maar Lakes, Podrecany Basalt Formation, Southern Slovakia, on the basis of siliceous microfossils, 351-368 pp.

Ohba, T., Taniguchi, H., Oshima, H., Yoshida, M. and Goto, A., 2002. Effect of explosion energy and depth on the nature of explosion cloud: A field experimental study. Journal of Volcanology and Geothermal Research, 115(1): 33-42.

Ollier, C., 1988. Volcanoes. Basil Blackwell, Oxford.

Ort, M.H., Elson, M.D., Anderson, K.C., Duffield, W.A. and Samples, T.L., 2008. Variable effects of cinder-cone eruptions on prehistoric agrarian human populations in the American southwest. Journal of Volcanology and Geothermal Research, 176(3): 363-376.

Otterloo, J.v., Cas, R.A.F. and Scutter, C.R., 2015. The fracture behaviour of volcanic glass and relevance to quench fragmentation during formation of hyaloclastite and phreatomagmatism. Earth-Science Reviews, 151: 79–116.

Otterloo, J.V., Raveggi, M., Cas, R.A.F. and Maas, R., 2014. Polymagmatic Activity at the Monogenetic Mt Gambier Volcanic Complex in the Newer Volcanics Province, SE Australia: New Insights into the Occurrence of Intraplate Volcanic Activity in Australia. JOURNAL OF PETROLOGY, 55(7): 1317-1351.

Ou, X. and Fu, Q., 1984. The relationship between the Longgang Volcanic Group and Tectonic activity. Jiling Geology, 1: 76-81.

Palladino, D.M., Gaeta, M., Giaccio, B. and Sottili, G., 2014. On the anatomy of magma chamber and caldera collapse: The example of trachy-phonolitic explosive eruptions of the Roman Province (central Italy). Journal of Volcanology and Geothermal Research, 281: 12-26.

Palladino, D.M., Valentine, G.A., Sottili, G. and Taddeucci, J., 2015. Maars to calderas: end-members on a spectrum of explosive volcanic depressions. Frontiers in Earth Science, 3.

Pardo, N., Macias, J.L., Giordano, G., Cianfarra, P., Avellán, D.R. and Bellatreccia, F., 2009. The ~1245 yr BP Asososca maar eruption: The youngest event along the Nejapa–Miraflores volcanic fault, Western Managua, Nicaragua. Journal of Volcanology and Geothermal Research, 184(3): 292–312.

Parfitt, E.A., 2004. A discussion of the mechanisms of explosive basaltic eruptions. Journal of Volcanology and Geothermal Research, 134(1-2): 77-107.

Pedrazzi, D., Bolós, X. and Martí, J., 2014. Phreatomagmatic volcanism in complex hydrogeological environments: La Crosa de Sant Dalmai maar (Catalan Volcanic Zone, NE Spain). Geosphere, 10(1): 170-184.

Pei, R.F. and Nie, F.J., 1993. Volcanism and metallogeny at the ancient continental margin of south–central Inner Mongolia, P.R. China. In: E.S.s. Verlagsbuchhandlung and N.Ž.u. Obermiller (Editors), The 8th Quadrennial IAGOD Symposium, Stuttgart, pp. 737-752.

Pirrung, M., BÜChel, G., Lorenz, V. and Treutler, H.-C., 2008. Post-eruptive development of the Ukinrek East Maar since its eruption in 1977 A.D. in the periglacial area of south-west Alaska. Sedimentology, 55(2): 305-334.

Porritt, L.A. and Cas, R.A.F., 2009. Reconstruction of a kimberlite eruption, using an integrated volcanological, geochemical and numerical approach: A case study of the Fox Kimberlite, NWT, Canada. Journal of Volcanology and Geothermal Research, 179(3): 241-264.

Raue, H., 2004. A new model for the fracture energy budget of phreatomagmatic explosions. Journal of Volcanology and Geothermal Research, 129(1): 99-108.

Rayner, R.J., Waters, S.B., McKay, I.J., Dobbs, P.N. and Shaw, A.L., 1991. The mid-Cretaceous palaeoenvironment of central Southern Africa (Orapa, Botswana). Palaeogeography, Palaeoclimatology, Palaeoecology, 88(1): 147-156.

Re, G., Palin, J.M., White, J.D.L. and Parolari, M., 2017. Unravelling the magmatic system beneath a monogenetic volcanic complex (Jagged Rocks Complex, Hopi Buttes, AZ, USA). Contributions to Mineralogy and Petrology, 172(11-12).

Ren, J., Li, S. and Lin, C., 1997. Late Mesozoic intracontinental rifting and basin formation in eastern China. Journal of China University of Geosciences, 8(1): 40-44.

Ren, J., Tamaki, K., Li, S. and Junxia, Z., 2002. Late Mesozoic and Cenozoic rifting and its dynamic setting in Eastern China and adjacent areas. Tectonophysics, 344(3-4): 175– 205.

Reynolds, D.L., 1954. Fluidization as a geological process, and its bearing on the problem of intrusive granites. American Journal of Science, 252(10): 577-613.

Riedel, C., Ernst, G.G.J. and Riley, M., 2003. Controls on the growth and geometry of pyroclastic constructs. Journal of Volcanology and Geothermal Research, 127(1-2): 121-152.

Rittmann, A., 1962. Volcanoes and their activity, Interscience Publishers.

Rodríguez, S.R., Morales-Barrera, W., Layer, P. and González-Mercado, E., 2010. A quaternary monogenetic volcanic field in the Xalapa region, eastern Trans-Mexican volcanic belt: Geology, distribution and morphology of the volcanic vents. Journal of Volcanology and Geothermal Research, 197(1): 149-166.

Ross, P.-S., Carrasco Núñez, G. and Hayman, P., 2017. Felsic maar-diatreme volcanoes: a review. Bulletin of Volcanology, 79(2): 20.

Ross, P.-S. and White, J.D.L., 2006. Debris jets in continental phreatomagmatic volcanoes: A field study of their subterranean deposits in the Coombs Hills vent complex, Antarctica. Journal of Volcanology and Geothermal Research, 149(1): 62-84.

Rottas, K.M. and Houghton, B.F., 2012. Structure, stratigraphy, and eruption dynamics of a young tuff ring: Hanauma Bay, O'ahu, Hawai'i. Bulletin of Volcanology, 74(7): 1683-1697.

Schmincke, H.-U., Fisher, R.V. and Waters, A.C., 1973. Antidune and chute and pool structures in the base surge deposits of the Laacher See area, Germany. Sedimentology, 20(4): 553-574.

Scott Smith, B.H., 2008. Canadian kimberlites: Geological characteristics relevant to emplacement. Journal of Volcanology and Geothermal Research, 174(1): 9-19.

Self, S. and Healy, J., 1987. Wairakei Formation, New Zealand: Stratigraphy and correlation. New Zealand Journal of Geology and Geophysics, 30(1): 73-86.

Self, S. and Sparks, R.S.J., 1978. Characteristics of widespread pyroclastic deposits formed by the interaction of silicic magma and water. Bulletin Volcanologique, 41(3): 196.

Şengör, A.M.C., Natal'in, B.A. and Burtman, V.S., 1993. Evolution of the Altaid tectonic collage and Palaeozoic crustal growth in Eurasia. Nature, 364: 299.

Shao, J. and Zhang, W., 2008. The evolving rift belt—Wudalianchi volcanic rock belt. Earth Science Frontiers, 15(6): 241-250.

Sheridan, M.F. and Wohletz, K.H., 1981. Hydrovolcanic Explosions: The Systematics of Water-Pyroclast Equilibration. Science, 212(4501): 1387-1389.

Sheridan, M.F. and Wohletz, K.H., 1983. HYDROVOLCANISM: BASIC CONSIDERATIONS AND REVIEW. Journal of Volcanology and Geothermal Research, 17(1-4): 1-29.

Shi, Y., Liu, D., Zhang, Q., Jian, P., Zhang, F., Miao, L., Shi, G., Zhang, L. and Tao, H., 2004. SHRIMP geochronology of dioritic-granitic intrusions in Sunidzuoqi area, inner Mongolia. Acta Geologica Sinica, 78: 789-799.

Shoemaker, E.M., Roach, C.H. and Byers Jr, F.M., 1962. Diatremes and Uranium Deposits in the Hopi Buttes, Arizona, Petrologic Studies: A volume to Honor A.F. Buddington, Geological Society of America. Boulder, Colorado, pp. 327–356.

Skilling, I.P., White, J.D.L. and McPhie, J., 2002. Peperite: a review of magma–sediment mingling. Journal of Volcanology and Geothermal Research, 114(1): 1-17.

Skinner, E.M.W. and Marsh, J.S., 2004. Distinct kimberlite pipe classes with contrasting eruption processes. Lithos, 76(1): 183-200.

Smith, I.E.M., Blake, S., Wilson, C.J.N. and Houghton, B.F., 2008. Deep-seated fractionation during the rise of a small-volume basalt magma batch: Crater Hill, Auckland, New Zealand. Contributions to Mineralogy and Petrology, 155(4): 511-527.

Smith, I.E.M. and Németh, K., 2017. Source to surface model of monogenetic volcanism: a critical review. Geological Society, London, Special Publications, 446(1): 1-28.

Smith, R.M.H., 1986. Sedimentation and palaeoenvironments of Late Cretaceous crater-lake deposits in Bushmanland, South Africa. Sedimentology, 33(3): 369-386.

Sohn, Y.K., 1996. Hydrovolcanic processes forming basaltic tuff rings and cones on Cheju Island, Korea. GSA Bulletin, 108(10): 1199-1211.

Sottili, G., Palladino, D.M., Gaeta, M. and Masotta, M., 2012. Origins and energetics of maar volcanoes: examples from the ultrapotassic Sabatini Volcanic District (Roman Province, Central Italy). Bulletin of Volcanology, 74(1): 163-186.

Sparks, R.S.J., Baker, L., Brown, R.J., Field, M., Schumacher, J., Stripp, G. and Walters, A., 2006. Dynamical constraints on kimberlite volcanism. Journal of Volcanology and Geothermal Research, 155(1): 18-48.

Stiefenhofer, J. and Farrow, D.J., 2004. Geology of the Mwadui kimberlite, Shinyanga district, Tanzania. Lithos, 76(1): 139-160.

Stroncik, N.A. and Schmincke, H.-U., 2002. Palagonite - a review. International Journal of Earth Sciences, 91(4): 680–697.

Suhr, P., Goth, K., Lorenz, V. and Suhr, S., 2006. Long lasting subsidence and deformation in and above maar-diatreme volcanoes – a never ending story
[Lang anhaltende Subsidenz und Deformation in und über Maar-Diatrem-Vulkanen – eine unendliche Geschichte]. Zeitschrift der Deutschen Gesellschaft für Geowissenschaften, 157(3): 491-511.

Sui, J., Fan, Q. and Cao, J., 1999. A preliminary study of eruption features and petrochemistry of volcanic rocks from the Longgang volcanoes. Geological Review, 45: 319-324.

Sulpizio, R., Bonasia, R., Dellino, P., Di Vito, M.A., La Volpe, L., Mele, D., Zanchetta, G. and Sadori, L., 2008. Discriminating the long distance dispersal of fine ash from sustained columns or near ground ash clouds: The example of the Pomici di Avellino eruption (Somma-Vesuvius, Italy). Journal of Volcanology and Geothermal Research, 177(1): 263-276.

Sulpizio, R. and Dellino, P., 2008. Chapter 2 Sedimentology, Depositional Mechanisms and Pulsating Behaviour of Pyroclastic Density Currents. In: J. Gottsmann, Mart, iacute and Joan (Editors), Developments in Volcanology. Elsevier, pp. 57-96.

Sun, C., Liu, Q., Wu, J., Németh, K., Wang, L., Zhao, Y., Chu, G. and Liu, J., 2016. The first tephra evidence for a Late Glacial explosive volcanic eruption in the Arxan-Chaihe volcanic field (ACVF), northeast China. Quaternary Geochronology, 40: 109-119.

Tao, K.Y., Xing, G.F., Ji, S.X., Yang, Z.L., Zhao, Y. and Shen, J.L., 1999. A review of volcano (volcanic rock) tourism resources. Volcanology & Mineral Resources, 20(2): 78-86.

Thorarinsson, S., 1953. The crater groups in Iceland. Bulletin Volcanologique, 14(1): 3-44.

Thordarson, T. and Self, S., 1993. The Laki (Skaftár Fires) and Grímsvötn eruptions in 1783–1785. Bulletin of Volcanology, 55(4): 233-263.

Thouret, J.C., 1999. Volcanic geomorphology—an overview. Earth-Science Reviews, 47(1): 95-131.

Tian, Z.-Y., Han, P. and Xu, K.-D., 1992. The Mesozoic-Cenozoic East China rift system. Tectonophysics, 208(1): 341-363.

Valentine, G.A., Doronzo, D.M., Dellino, P. and de Tullio, M.D., 2011. Effects of volcano profile on dilute pyroclastic density currents: Numerical simulations. Geology, 39(10): 947-950.

Valentine, G.A., Graettinger, A.H., Macorps, É., Ross, P.-S., White, J.D.L., Döhring, E. and Sonder, I., 2015. Experiments with vertically and laterally migrating subsurface explosions with applications to the geology of phreatomagmatic and hydrothermal explosion craters and diatremes. Bulletin of Volcanology, 77(3).

Valentine, G.A. and Gregg, T.K.P., 2008. Continental basaltic volcanoes — Processes and problems. Journal of Volcanology and Geothermal Research, 177(4): 857-873.

Valentine, G.A., Krier, D., Perry, F.V. and Heiken, G., 2005. Scoria cone construction mechanisms, Lathrop Wells volcano, southern Nevada, USA. Geology, 33(8): 629-632.

Valentine, G.A., Krier, D.J., Perry, F.V. and Heiken, G., 2007. Eruptive and geomorphic processes at the Lathrop Wells scoria cone volcano. Journal of Volcanology and Geothermal Research, 161(1-2): 57-80.

Valentine, G.A., Perry, F.V., Krier, D., Keating, G.N., Kelley, R.E. and Cogbill, A.H., 2006. Small-volume basaltic volcanoes: Eruptive products and processes, and posteruptive geomorphic evolution in Crater Flat (Pleistocene), southern Nevada. Geological Society of America Bulletin, 118(11-12): 1313-1330.

Valentine, G.A. and van Wyk de Vries, B., 2014. Unconventional maar diatreme and associated intrusions in the soft sediment-hosted Mardoux structure (Gergovie, France). Bulletin of Volcanology, 76(3).

Valentine, G.A. and White, J.D.L., 2012. Revised conceptual model for maar-diatremes: Subsurface processes, energetics, and eruptive products. Geology, 40(12): 1111-1114.

Vazquez, J.A. and Ort, M.H., 2006. Facies variation of eruption units produced by the passage of single pyroclastic surge currents, Hopi Buttes volcanic field, USA. Journal of Volcanology and Geothermal Research, 154(3-4): 222-236.

Vespermann, D. and Schmincke, H.U., 2000. Scoria cones and tuff rings, Encyclopedia of Volcanoes, Academic Press.

Walker, G.P.L., 1988. Three Hawaiian calderas: An origin through loading by shallow intrusions? Journal of Geophysical Research: Solid Earth, 93(B12): 14773-14784.

Wang, C.P., 1989. Genetic relation of various granitoid rocks and gold mineralization in central Inner Mongolia. Geol. Soc. Inner Mongolia Bull, 11: 23-30.

Wang, K. and Guo, F., 1982. THE STRUCTURAL AND PETROLOGICAL CHARACTERISTICS OF LAOHEI HILL AND HUOSHAO HILL, WUDALIANCHI, HEILONGJIANG PROVINCE [J]. Geological Review, 4: 004.

Wang, L. and Tian, M., 2013. The volcanic tourism development research based on the SWOT analysis, in northeastern Inner Mongolia, China. International Proceedings of Chemical, Biological and Environmental Engineering (IPCBEE), 52: 75-79.

Wang, L., Tian, M., Wen, X., Zhao, L., Song, J., Sun, M., Wang, H., Lan, Y. and Sun, M., 2014. Geoconservation and geotourism in Arxan-Chaihe Volcano Area, Inner Mongolia, China. Quaternary International, 349: 384-391.

Wang, Y., 1979. Volcanic geology and volcanic landform of Wudalianchi area. Heilongjiang Geol, 1(3): 33-43.

Wang, Y., 1996. 中国东部内蒙古-燕山造山带晚古生代晚期-中生代的造山作用过程. 地质出版社.

Wang, Y., 1998. 中生代以来华北地区造山带与盆地的演化及动力学. 地质出版社.

Wang, Y., Li, C. and Chen, H., 1999. Tectonic settings of Cenozoic volcanism in northeastern China. Geological Review, 45: 180-189.

Wayne Peter, B., 2008. The rock mechanics of kimberlite volcanic pipe excavation. Journal of Volcanology and Geothermal Research, 174(1): 29-39.

Webb, K.J., Scott Smith, B.H., Paul, J.L. and Hetman, C.M., 2004. Geology of the Victor Kimberlite, Attawapiskat, Northern Ontario, Canada: cross-cutting and nested craters. Lithos, 76(1): 29-50.

Wei, H., Liu, R., Fan, Q., Jin, B., Liu, X. and Zhang, C., 1999. Monogenetic volcanism in Longgang volcano clusters. Geological Review, 45(3252): 325-331.

Wei, H., Liu, R., Fan, Q. and Li, N., 1998a. Active volcanoes in China and their relevant hazards. Ziran Zazhi, 20(4): 196-200.

Wei, H., Liu, R., Jin, B., Liu, X., Zhang, C., Yang, Q. and Li, N., 1998b. 核电站选址中的火山灾害评价, 海峡两岸地质环境与天然灾害学术讨论会, Beijing, pp. 160-163.

Wei, H., Sparks, R.S.J., Liu, R., Fan, Q., Wang, Y., Hong, H., Zhang, H., Chen, H., Jiang, C., Dong, J., Zheng, Y. and Pan, Y., 2003. Three active volcanoes in China and their hazards. Journal of Asian Earth Sciences, 21(5): 515–526.

Wentworth, C.K., 1922. A scale of grade and class terms for elastic sediments. J. Geol., 30(5): 377-392.

White, J.D., 1991a. Maar-diatreme phreatomagmatism at Hopi Buttes, Navajo Nation (Arizona), USA. Bulletin of Volcanology, 53(4): 239-258.

White, J.D., 1991b. The depositional record of small, mono-genetic volcanoes within terrestrial basins. Sedimentation in Vol-canicl Setting, SEPM Spec Publ, 45: 155-171.

White, J.D.L., 1992. Pliocene subaqueous fans and Gilbert-type deltas in maar crater lakes, Hopi Buttes, Navajo Nation (Arizona), USA. Sedimentology, 39(5): 931-946.

White, J.D.L., 1996. Impure coolants and interaction dynamics of phreatomagmatic eruptions. Journal of Volcanology and Geothermal Research, 74(3-4): 155-170.

White, J.D.L., McPhie, J. and Skilling, I., 2000. Peperite: a useful genetic term. Bulletin of Volcanology, 62(1): 65-66.

White, J.D.L. and Ross, P.S., 2011. Maar-diatreme volcanoes: A review. Journal of Volcanology and Geothermal Research, 201(1-4): 1-29.

White, J.D.L. and Schmincke, H.-U., 1999. Phreatomagmatic eruptive and depositional processes during the 1949 eruption on La Palma (Canary Islands). Journal of Volcanology and Geothermal Research, 94(1): 283-304.

Williams, H. and McBirney, A., 1979. Volcanology, 397 pp. Free man, Cooper & Co., San Francisco.

Williams, S.N., 1983. Plinian airfall deposits of basaltic composition. Geology, 11(4): 211-214.

Wilson, B.M., 1989. Igneous petrogenesis a global tectonic approach. Springer Science & Business Media.

Wilson, C.J.N., Houghton, B.F., McWilliams, M.O., Lanphere, M.A., Weaver, S.D. and Briggs, R.M., 1995. Volcanic and structural evolution of Taupo Volcanic Zone, New Zealand: a review. Journal of Volcanology and Geothermal Research, 68(1): 1-28.

Wilson, L. and Head Iii, J.W., 2007a. An integrated model of kimberlite ascent and eruption. Nature, 447: 53.

Windley, B.F., Alexeiev, D., Xiao, W., Kröner, A. and Badarch, G., 2007. Tectonic models for accretion of the Central Asian Orogenic Belt. Journal of the Geological Society, 164(1): 31-47.

Winter, J.D., 2013. Principles of igneous and metamorphic petrology. Pearson Education.

Wohletz, K.H., 1986. Explosive magma-water interactions: Thermodynamics, explosion mechanisms, and field studies. Bulletin of Volcanology, 48(5): 245-264.

Wohletz, K.H. and McQueen, R.G., 1984a. Experimental studies of hydromagmatic volcanism. Explosive volcanism: inception, evolution, and hazards: 158-169.

Wohletz, K.H. and McQueen, R.G., 1984b. Volcanic and stratospheric dustlike particles produced by experimental water-melt interactions. Geology, 12(10): 591-594.

Wohletz, K.H. and Sheridan, M.F., 1983. Hydrovolcanic explosions II. Evolution of basaltic tuff rings and tuff cones. American journal of science, 283(5): 385-413.

Wood, C.A., 1979a. Monogenetic volcanoes of the terrestrial planets, Lunar and Planetary Science Conference Proceedings, pp. 2815-2840.

Wood, C.A., 1979b. Morphometric studies of planetary landforms: impact craters and volcanoes, Harvard.

Wood, C.A., 1980. Morphometric evolution of cinder cones. Journal of Volcanology and Geothermal Research, 7(3-4): 387-413.

Wood, S.H. and Clemens, D.M., 2004. Tectonic and magmatic evolution of the Snake River Plain volcanic province. In: B. Bonnichsen, M. McCurry and C. White (Editors). Idaho Geological Survey, Moscow, Idaho, pp. 69-103.

Wu, F.-y., Sun, D.-y., Li, H., Jahn, B.-m. and Wilde, S., 2002. A-type granites in northeastern China: age and geochemical constraints on their petrogenesis. Chemical Geology, 187(1): 143-173.

Xiao, L. and Wang, C., 2009. Geologic features of Wudalianchi volcanic field, northeastern China: Implications for Martian volcanology. Planetary and Space Science, 57(5-6): 685-698.

Xiao, W., Windley, B.F., Hao, J. and Zhai, M., 2003. Accretion leading to collision and the Permian Solonker suture, Inner Mongolia, China: Termination of the central Asian orogenic belt. Tectonics, 22(6): n/a-n/a.

Xiao, W.J., Windley, B.F., Huang, B.C., Han, C.M., Yuan, C., Chen, H.L., Sun, M., Sun, S. and Li, J.L., 2009. End-Permian to mid-Triassic termination of the accretionary processes of the southern Altaids: implications for the geodynamic evolution, Phanerozoic continental growth, and metallogeny of Central Asia. International Journal of Earth Sciences, 98(6): 1189-1217.

Xie, Y., Liu, X. and Xiang, T., 1993. The researches on cenozoic volcanoes and volcanic rocks in the middle district of northeast China. Northeast Normal University Press, Changchun.

Xu, D. and Bai, Z., 2009. Oroqen nuomin volcanic geological heritage investigation. Beijing: China University of Geosciences (Beijing).

Xu, T., Sun, H.Y. and Tian, M.Z., 2011. A Discussion on the Concept and Taxonomic Hierarchies of Geological Heritages. Acta Geoscientica Sinica, 32(2): 211-216.

Yang, J., 1988. Petrology of Cenozoic basalts from Simen, Inner Mongolia. Acta Petrologica Sinica, 4(2): 13-32.

Yarmolyuk, V.V., Kovalenko, V.I., Kozlovsky, A.M., Kovach, V.P., Sal'nikova, E.B., Kovalenko, D.V., Kotov, A.B., Kudryashova, E.A., Lebedev, V.I. and Eenzhin, G., 2008. Crust-forming processes in the Hercynides of the Central Asian Foldbelt. Petrology, 16(7): 679-709.

Zhang, C., Liu, S., Han, B. and Li, D., 2006. Characteristics of ultramafic xenoliths from Cenozoic basalts in Abagaqi area, Inner Mongolia. Acta Petrologica Sinica, 22(11): 2801-2807.

Zhang, H.-T., So, C.-S. and Yun, S.-T., 1999. Regional geologic setting and metallogenesis of central Inner Mongolia, China: guides for exploration of mesothermal gold deposits. Ore Geology Reviews, 14(2): 129–146.

Zhang, H.T., 1991. Granitoid Magma Series and Gold Metallogeny of the Baotou-Bayan Obo District, Inner Mongolia. PhD Thesis, Graduate School, Chinese Academy of Geological Sciences.

Zhang, J.e., Xiao, W., Han, C., Ao, S., Yuan, C., Sun, M., Geng, H., Zhao, G., Guo, Q. and Ma, C., 2011a. Kinematics and age constraints of deformation in a Late Carboniferous accretionary complex in Western Junggar, NW China. Gondwana Research, 19(4): 958-974.

Zhang, J.e., Xiao, W., Han, C., Mao, Q., Ao, S., Guo, Q. and Ma, C., 2011b. A Devonian to Carboniferous intra-oceanic subduction system in Western Junggar, NW China. Lithos, 125(1): 592-606.

Zhang, L., 1989. Distribution and geologic features of gold deposits along northern margin of North China platform (within Inner Mongolian Autonomous Region). Bulletin of Geological Society of lnner Mongolia, 11: 1-6.

Zhang, L., Chen, Z., Zhou, X., Wang, F. and Zhang, Y., 2009. Geochemistry and tectonic settings of Early Tertiary volcanic rocks in the east depression, Liaohe Basin. Journal of Earth Sciences and Environment, 31(4): 368-375.

Zhang, S.-H., Zhao, Y., Liu, X.-C., Liu, D.-Y., Chen, F., Xie, L.-W. and Chen, H.-H., 2009a. Late Paleozoic to Early Mesozoic mafic–ultramafic complexes from the northern North China Block: Constraints on the composition and evolution of the lithospheric mantle. Lithos, 110(1): 229-246.

Zhang, S.-H., Zhao, Y., Song, B., Hu, J.-M., Liu, S.-W., Yang, Y.-H., Chen, F.-K., Liu, X.-M. and Liu, J., 2009b. Contrasting Late Carboniferous and Late Permian–Middle Triassic intrusive suites from the northern margin of the North China craton: Geochronology, petrogenesis, and tectonic implications. Geological Society of America Bulletin, 121(1-2): 181-200.

Zhang, X. and Zhai, M., 2010. Magmatism and its metallogenetic effects during the Paleozoic continental crustal construction in northern North China: an overview. Acta Petrologica Sinica, 26(5): 1329-1341.

Zhang, X., Zhang, H., Jiang, N., Zhai, M. and Zhang, Y., 2010. Early Devonian alkaline intrusive complex from the northern North China craton: a petrological monitor of post-collisional tectonics. Journal of the Geological Society, 167(4): 717-730.

Zhao, D., 2009. Multiscale seismic tomography and mantle dynamics. Gondwana Research, 15(3): 297-323.

Zhao, T. and Zhao, X., 2009. Geoheritage taxonomy and its application. Acta Geoscientica Sinica, 30(3): 309-324.

Zhao, Y.-W., Fan, Q.-C., Zou, H. and Li, N., 2014a. Geochemistry of Quaternary basaltic lavas from the Nuomin volcanic field, Inner Mongolia: Implications for the origin of potassic volcanic rocks in Northeastern China. Lithos, 196-197: 169-180.

Zhao, Y.-W., Li, N., Fan, Q.-C., Zou, H. and Xu, Y.-G., 2014b. Two episodes of volcanism in the Wudalianchi volcanic belt, NE China: Evidence for tectonic controls on volcanic activities. Journal of Volcanology and Geothermal Research, 285: 170-179.

Zhao, Y., Fan, Q., Bai, Z., Sun, Q., Li, N., Sui, J. and Du, X., 2008. Preliminary study on Quaternary volcanoes in the Halaha River and Chaoer River area in Daxing'an Mountain range. Acta Petrologica Sinica, 24(11): 2569-2575.

Zhao, Z., Zhao, X., Liu, C., Yi, X. and Chen, X., 2015. Geoparks in China. In: E. Errami, M. Brocx and V. Semeniuk (Editors), From Geoheritage to Geoparks: Case Studies from Africa and Beyond. Springer International Publishing, Cham, pp. 215-232.

Zhizhong, Z., Xun, Z., Changxing, L., Xiaohong, Y. and Xiaoning, C., 2015. Geoparks in China. In: E. Errami, M. Brocx and V. Semeniuk (Editors), From Geoheritage to Geoparks: Case Studies from Africa and Beyond. Springer International Publishing, Cham, pp. 215-232.

Zimanowski, B., 1998. Phreatomagmatic explosions. In: A. Freundt and M. Rosi (Editors), From magma to tephra, Elsevier, Amsterdam, pp. 25-53.

Zimanowski, B. and Buttner, R., 2002. Dynamic mingling of magma and liqueˆed sediments. Journal of Volcanology and Geothermal Research, 114(1-2): 37-44.

Zimanowski, B., Büttner, R. and Lorenz, V., 1997. Premixing of magma and water in MFCI experiments. Bulletin of Volcanology, 58(6): 491-495.

Zimanowski, B., Fröhlich, G. and Lorenz, V., 1995. Experiments on steam explosion by interaction of water with silicate melts. Nuclear Engineering and Design, 155(1): 335-343.

Zimanowski, B., Wohletz, K., Dellino, P. and Buttner, R., 2003. The volcanic ash problem. Journal of Volcanology and Geothermal Research, 122(1-2): 1-5.

Zimanowski, B. and Wohletz, K.H., 2000. Physics of phreatomagmatism; Part 2: Eruption physics. Terra Nostra, 6: 535-544.

Zolitschka, B., 1992. Climatic change evidence and lacustrine varves from maar lakes, Germany. Climate Dynamics, 6(3): 229-232.

Zou, H., Reid, M.R., Liu, Y., Yao, Y., Xu, X. and Fan, Q., 2003. Constraints on the origin of historic potassic basalts from northeast China by U–Th disequilibrium data. Chemical Geology, 200(1): 189-201.